



**CHARACTERIZATION OF PARTICULATE
EMISSIONS: SIZE FRACTIONATION AND
CHEMICAL SPECIATION
CP1106**

OCTOBER 2003

**ADEL F. SAROFIM & JOANN S. LIGHTY
UNIVERSITY OF UTAH**

Report Documentation Page

Form Approved
OMB No. 0704-0188

Public reporting burden for the collection of information is estimated to average 1 hour per response, including the time for reviewing instructions, searching existing data sources, gathering and maintaining the data needed, and completing and reviewing the collection of information. Send comments regarding this burden estimate or any other aspect of this collection of information, including suggestions for reducing this burden, to Washington Headquarters Services, Directorate for Information Operations and Reports, 1215 Jefferson Davis Highway, Suite 1204, Arlington VA 22202-4302. Respondents should be aware that notwithstanding any other provision of law, no person shall be subject to a penalty for failing to comply with a collection of information if it does not display a currently valid OMB control number.

1. REPORT DATE OCT 2003		2. REPORT TYPE		3. DATES COVERED 00-00-2003 to 00-00-2003	
4. TITLE AND SUBTITLE Characterization of Particulate Emissions: Size Fractionation and Chemical Speciation				5a. CONTRACT NUMBER	
				5b. GRANT NUMBER	
				5c. PROGRAM ELEMENT NUMBER	
6. AUTHOR(S)				5d. PROJECT NUMBER	
				5e. TASK NUMBER	
				5f. WORK UNIT NUMBER	
7. PERFORMING ORGANIZATION NAME(S) AND ADDRESS(ES) University of Utah, 201 Presidents Circle, Salt Lake City, UT, 84112				8. PERFORMING ORGANIZATION REPORT NUMBER	
9. SPONSORING/MONITORING AGENCY NAME(S) AND ADDRESS(ES)				10. SPONSOR/MONITOR'S ACRONYM(S)	
				11. SPONSOR/MONITOR'S REPORT NUMBER(S)	
12. DISTRIBUTION/AVAILABILITY STATEMENT Approved for public release; distribution unlimited					
13. SUPPLEMENTARY NOTES					
14. ABSTRACT					
15. SUBJECT TERMS					
16. SECURITY CLASSIFICATION OF:			17. LIMITATION OF ABSTRACT	18. NUMBER OF PAGES	19a. NAME OF RESPONSIBLE PERSON
a. REPORT unclassified	b. ABSTRACT unclassified	c. THIS PAGE unclassified			

CLEARANCE REQUEST FOR PUBLIC RELEASE OF DEPARTMENT OF DEFENSE INFORMATION

(See Instructions on back.)

(This form is to be used in requesting review and clearance of DoD information proposed for public release in accordance with DoDD 5230.9.)

TO: Director, Freedom of Information & Security Review, Rm. 2C757, Pentagon

1. DOCUMENT DESCRIPTION

a. TYPE Final Report	b. TITLE Characterization of Particulate Emissions: Size Fractionation and Chemical Speciation (CP-1106)
c. PAGE COUNT 53	d. SUBJECT AREA Strategic Environmental Research & Development Program (SERDP)

2. AUTHOR/SPEAKER

a. NAME (Last, First, Middle Initial) Sarafin, Adel; Lighty, Joanne	b. RANK	c. TITLE
d. OFFICE	e. AGENCY University of Utah, Salt Lake City, UT	

3. PRESENTATION/PUBLICATION DATA (Date, Place, Event)

**CLEARED
FOR OPEN PUBLICATION**

MAR 31 2004 8

SECURITY REVIEW

DEPARTMENT OF DEFENSE

4. POINT OF CONTACT

a. NAME (Last, First, Middle Initial) Kelly, Amy	b. TELEPHONE NO. (Include Area Code) 910-579-8052 or 703-696-2124
---	--

5. PRIOR COORDINATION

a. NAME (Last, First, Middle Initial) Smith, Bradley Holst, Robert	b. OFFICE/AGENCY SERDP Executive Director SERDP Compliance Program Manager	c. TELEPHONE NO. (Include Area Code) 703-696-2121 703-696-2125
--	--	--

6. REMARKS

THE INFORMATION CONTAINED IN THIS REPORT FALLS UNDER THE PURVIEW OF THIS OFFICE.

WHEN CLEARED, PLEASE FAX DD-1910 TO 703-478-0526. ATTN: Lucia (phone: 703-736-4549)

7. RECOMMENDATION OF SUBMITTING OFFICE/AGENCY

a. THE ATTACHED MATERIAL HAS DEPARTMENT/OFFICE/AGENCY APPROVAL FOR PUBLIC RELEASE (qualifications, if any, are indicated in Remarks section) AND CLEARANCE FOR OPEN PUBLICATION IS RECOMMENDED UNDER PROVISIONS OF DODD 5320.9. I AM AUTHORIZED TO MAKE THIS RECOMMENDATION FOR RELEASE ON BEHALF OF:

Strategic Environmental Research & Development Program

b. CLEARANCE IS REQUESTED BY 20040325 (YYYYMMDD).

c. NAME (Last, First, Middle Initial) Smith, Bradley P.	d. TITLE Executive Director, Strategic Environmental R&D Program
e. OFFICE SERDP	f. AGENCY USD (AT&L)

g. SIGNATURE 	h. DATE SIGNED (YYYYMMDD) 20040305
---	---------------------------------------

Handwritten notes: m.e. 1024

This report was prepared under contract to the Department of Defense Strategic Environmental Research and Development Program (SERDP). The publication of this report does not indicate endorsement by the Department of Defense, nor should the contents be construed as reflecting the official policy or position of the Department of Defense. Reference herein to any specific commercial product, process, or service by trade name, trademark, manufacturer, or otherwise, does not necessarily constitute or imply its endorsement, recommendation, or favoring by the Department of Defense.

TABLE OF CONTENTS

SECTION 1: INTRODUCTION 1-1

 1.1 Performing Organizations 1-1

 1.2 Project Background 1-1

 1.3 Objectives 1-1

 1.4 Technical Approach 1-2

 1.5 Project Accomplishments 1-2

 1.6 SERDP Action Items 1-3

 1.7 SERDP List of Publications 1-4

SECTION 2: DEVELOPMENT AND EVALUATION OF THE ATOFMS 2-1

 2.1 Instrument Description 2-1

 2.1.1 Improving the sensitivity of ATOFMS to smaller particles 2-2

 2.2 Evaluation of the ATOFMS for DoD sources 2-4

 2.3 Summary 2-6

SECTION 3: DETAILED CHEMICAL ANALYSIS OF PARTICULATE MATTER 3-1

 3.1 Abstract 3-1

 3.2 Introduction 3-1

 3.3 Sampling 3-2

 3.4 Summary of the Results 3-2

SECTION 4: DEVELOPMENT AND EVALUATION OF THE PHOTOACOUSTIC ANALYZER 4-1

 4.1 Instrument Description 4-1

 4.2 Evaluation of the PA for DoD Sources 4-2

 4.3 Summary 4-5

SECTION 5: DEVELOPMENT AND EVALUATION OF THE PHOTOELECTRIC AEROSOL SENSOR 5-1

 5.1 Description of the Photoelectric Aerosol Sensor 5-1

 5.2 Evaluation of the PAS for DoD Sources 5-2

 5.3 Summary 5-4

SECTION 6: AIRCRAFT EMISSIONS AT NORTH ISLAND NAVAL AIR STATION 6-1

 6.1 Executive Summary 6-1

 6.2 Objectives 6-2

 6.3 Experimental Approach 6-3

 6.4 AIMD Experiments 6-5

 6.4.1 AIMD Real-Time Data Time Series 6-6

 6.4.2 Summary of Real-Time Results 6-19

6.4.3	Evaluation of Photoelectric Aerosol Sensor (Objective #1)	6-20
6.4.4	Evaluation of Photoacoustic Instrument (Objective #2)	6-23
6.4.5	Evaluation of DustTrak Instrument (Objective #3)	6-27
6.4.7	Supporting Measurements: Emission Rates	6-30
6.4.8	Conclusions Regarding Objectives #1-#3 at AIMD Site	6-32
6.4.9	Conclusions for all Real-Time Instruments	6-33
6.5	Flightline Measurements	6-34
6.5.1	Summary of Flightline Observations	6-41
6.5.2	Evaluation of the Photoelectric Aerosol Sensor (Objective #1)	6-42
6.5.3	Evaluation of the Photoacoustic Instrument (Objective #2)	6-43
6.5.4	Conclusions Regarding Objectives #1-#3 at Flightline Site	6-46
6.6	Overall Conclusions from North Island Experiments	6-47
6.6.1	Evaluation of PAS (Objective #1)	6-48
6.6.2	Evaluation of PA (Objective #2)	6-48
6.6.3	Evaluation of DT (Objective #3)	6-49
SECTION 7:	EMISSIONS FROM ROCKET FIRINGS	7-1
SECTION 8:	EVALUATION OF DIESEL SOOT FILTERS	8-9
SECTION 9:	COMPARISON OF THE EFFECT OF DIESEL AND JP8 FUELS ON PARTICULATE EMISSIONS	9-1
9.1	Objectives	9-1
9.2	Experimental Methods	9-1
9.2.1	Engine and Test Conditions	9-1
9.2.2	Dilution	9-2
9.2.3	Emission Measurement Methods	9-3
9.3	Results and Discussion	9-4
9.3.1	Real-Time Measurements of PM	9-4
9.3.2	Gas-Phase Emissions	9-6
9.3.3	Particle-Size Distributions	9-7
9.3.4	Denuder and MOUDI Results for PAHs	9-8
9.3.5	MOUDI Mass and Elemental Carbon Results	9-12
9.4	Conclusions	9-13
SECTION 10:	SIMULATION OF THE EVOLUTION OF PARTICLE SIZE DISTRIBUTION IN A VEHICLE EXHAUST PLUME	10-1
10.1	Introduction	10-1
10.2	Methods	10-2
10.2.1	Model Vehicle and Conditions	10-2
10.2.2	Computational Fluid Dynamics Methods	10-3
10.2.3	Aerosol Dynamics Modeling	10-5
10.3	Results and Discussion	10-6
10.3.1	CFD Results	10-6
10.3.2	Aerosol Dynamics Simulation Results	10-10
10.4	Conclusions	10-14

- Appendix 1: USER GUIDE FOR CHARACTERIZING PARTICULATE MATTER
- Appendix 2: EVALUATION OF 1047 NM PHOTOACOUSTIC INSTRUMENTS AND PHOTOELECTRIC AEROSOL SENSORS IN SOURCE-SAMPLING OF BLACK CARBON AEROSOL AND PARTICLE BOUND PAH'S FROM GASOLINE AND DIESEL POWERED VEHICLES
- Appendix 3: PHASE AND SIZE DISTRIBUTION OF POLYCYCLIC AROMATIC HYDROCARBONS IN DIESEL AND GASOLINE VEHICLE EMISSIONS
- Appendix 4: NORTH ISLAND PAH RESULTS
- Appendix 5: EVALUATION OF DIESEL SOOT FILTERS
- Appendix 6: SUMMARY OF EMISSION FACTORS

LIST OF FIGURES

Figure 2-1. Schematic of a field transportable ATOFMS. 2-2

Figure 2-2. Mass scaling curves for the ATOFMS..... 2-2

Figure 2-3. The focusing dynamics of an aerodynamic lens system. 2-3

Figure 2-4. Single-particle mass spectra sampled using the aerodynamic lenses. 2-3

Figure 2-5. Single-particle mass spectrum sampled from used sandblasting material. ... 2-5

Figure 2-6. Size-resolved composition of diesel exhaust from the ATOFMS. 2-5

Figure 2-7. Temporal and size distributions representing particles that contain
magnesium, top, and organic carbon, bottom..... 2-6

Figure 3-1. Size-resolved chemical composition of PM emissions from a diesel truck,
FTP cycle. 3-2

Figure 3-2. Recoveries of metals for the analysis of standard reference materials. 3-4

Figure 3-3. Comparison of INAA and ICP-MS analyses for fine PM emitted from
combustion of Illinois and Utah coal in a pulverized coal combustor..... 3-5

Figure 3-4. Comparisons of bulk concentrations measured from PM2.5 and the sum of
the MOUDI impactor fine particle stages for mass and chemical species. 3-5

Figure 3-5. Chemical composition fractions of PM2.5 emitted from coal combustion.
BF: batch furnace. PB: pulverized boiler..... 3-6

Figure 3-6. Size-resolved chemical compositions of coal combustion emissions..... 3-8

Figure 3-7. Size-segregated chemical composition of PM emissions from coal
combustion. 3-9

Figure 3-8. Size distributions measured for diluted rocket exhaust..... 3-10

Figure 4-1. Schematic of the new photoacoustic instrument..... 4-2

Figure 4-2. PA and DustTrack signal for a F-404-GE-400, aircraft engine 4-3

Figure 4-3. PA and DustTrack results for a TF-34 engine 4-4

Figure 4-4. PA signal during three CBD driving cycles..... 4-4

Figure 4-5. Comparison of MOUDI EC and PA results for aircraft and aircraft ground
support equipment..... 4-5

Figure 5-1. Schematic of the PAS..... 5-1

Figure 5-2. PAS signal during three CBD driving cycles..... 5-3

Figure 5-3. Correlation between the PAS signal and particle-bound PAHs as measured
with a Gundel denuder for four military aircraft. 5-3

Figure 5-4. Correlation between the PAS signal and particle-bound PAHs measured with
a Gundel denuder for military aircraft ground support equipment. 5-4

Figure 6-1. AIMD dilution and sampling setup..... 6-6

Figure 6-2. AIMD run #1, TF-34 engine, unit #1..... 6-7

Figure 6-3. AIMD run #1, TF-34, unit #1..... 6-9

Figure 6-4. AIMD run #2, TF-34, unit #1..... 6-10

Figure 6-5. Particle size distribution for AIMD run #2, TF-34, unit#1..... 6-11

Figure 6-6. AIMD run #3, TF-34 unit #2. 6-12

Figure 6-7. Particle size distribution for AIMD run #3, TF-34 unit#2..... 6-13

Figure 6-8. Dynamic blank of the augmentor chamber (run#4). 6-14

Figure 6-9. Particle size distribution for dynamic blank of augmentor chamber. 6-15

Figure 6-10. AIMD run #5, TF-34 unit #3.....	6-16
Figure 6-11. AIMD run #5, TF-34 unit #3.....	6-17
Figure 6-12. AIMD run #6, T-700 engine.	6-18
Figure 6-13. Particle size distribution for Run #6, T-700 engine.	6-19
Figure 6-14. PAS signal versus denuder Siegmann sum of particle-bound PAHs.....	6-21
Figure 6-15. PAS signal versus MOUDI Siegmann sum of PAH.	6-22
Figure 6-16. Comparison of PA and DT data for AIMD, run #1	6-24
Figure 6-17. Comparison of PA and DT data for AIMD, run #3.	6-24
Figure 6-18. Comparison of PA and DT data for AIMD Run #5.....	6-25
Figure 6-19. Comparison of PA and DT data for AIMD Run #6.....	6-25
Figure 6-20. PA data and quartz filter and MOUDI measurements of EC.....	6-27
Figure 6-21. Comparison of average DT, filter and MOUDI mass concentrations.....	6-28
Figure 6-22. MOUDI, Teflon filter, and SMPS mass concentrations for AIMD.	6-30
Figure 6-23. Portable sampling pallet.....	6-34
Figure 6-24. Flightline run #1, F-404-GE-400, right engine, plane 164037.	6-35
Figure 6-25. Flightline run #2, F-404-GE-400, right engine, plane 164037.	6-36
Figure 6-26. Flightline run #3, F-404-GE-400, right engine, plane 164037.	6-37
Figure 6-27. Particle size distribution, run #3, right engine, plane 164037.....	6-38
Figure 6-28. Flightline run#4, right engine, plane 164257.....	6-39
Figure 6-29. Flightline run#5, left engine, plane 164037.	6-40
Figure 6-30. Particle size distribution, run#5, left engine, plane 164037.....	6-41
Figure 6-31. Correlation between PA BC results with PAS PAHs results.....	6-42
Figure 6-32. Comparison of PA and DT data, run #1.....	6-43
Figure 6-33. Comparison of PA and DT data, run #2.....	6-43
Figure 6-34. Comparison of PA and DT data, run #3.....	6-44
Figure 6-35. Comparison of PA and DT data, run #4.....	6-44
Figure 6-36. Comparison of PA and DT data, run #5.....	6-45
Figure 6-37. Comparison of PA and DT data for all flightline runs.....	6-46
Figure 6-38. Calculated mass scattering efficiency for spherical particles	6-4650
Figure 7-1a. Representative spectra for Aerotech Blue Thunder model rocket.	7-2
Figure 7-1b. Representative spectra for Aerotech Blue Thunder model roc	7-2
Figure 7-2a. Representative spectra for Aerotech White Lightning model rocket.	7-3
Figure 7-2b. Representative spectra for Aerotech White Lightning model rocket.	7-3
Figure 7-3. Representative spectra for Aerotech Blackjack model rocket.	7-4
Figure 7-4. Representative spectra for Estes black powder model rocket.	7-4
Figure 7-5a. Representative spectra for Minuteman SR19 II rocket motor.....	7-6
Figure 7-5b. Representative spectra for Minuteman SR19 II rocket motor.	7-7
Figure 7-6a. Representative spectra of HAFB soil in rocket wake zone.	7-8
Figure 7-6b. Representative spectra of soil within sampled rocket wake.....	7-8
Figure 9-1. Dilution and sampling system.....	9-3
Figure 9-2. Comparison of real-time results for two diesel and two JP8 tests at 2200 rpm and 4 ft-lb. The error bars show the standard deviation.	9-5
Figure 9-3. Comparison of real-time results for two diesel and two JP8 tests at 2200 rpm and 8 ft-lb. The error bars show the standard deviation.	9-5
Figure 9-4. Particle size distributions for idle, 1500 rpm.	9-7
Figure 9-5. Particle size distributions for 4 ft-lb.....	9-8

Figure 9-6. Particle size distributions for 8 ft-lb..... 9-8

Figure 9-7. The sum of PAH collected on XAD-coated denuder section, filter and PUF/XAD/PUF section of the annual denuder for all diesel and JP8 fuel runs..... 9-10

Figure 9-8. The gas-particle phase distribution of semi-volatile PAH..... 9-11

Figure 9-9. PAH contents on different particle sizes, as measured by MOUDI, for diesel fuel and JP8 fuel..... 9-15

Figure 9-10. Comparison of Siegman sum PAH collected by MOUDI and denuder... 9-16

Figure 10-1. Bobtail geometry as modeled..... 10-2

Figure 10-2. Model particle size distribution for the Dodge bobtail..... 10-3

Figure 10-3. Computational domain for the CFD simulations..... 10-4

Figure 10-4. Diagram showing the starting positions of the various points in the tailpipe for streamline calculations..... 10-5

Figure 10-5. Contours of the natural log of dilution ratio for the vehicle moving at 5 mph..... 10-7

Figure 10-6. Contours of the natural log of dilution ratio for the vehicle moving at 25 mph..... 10-7

Figure 10-7. Contours of the natural log of dilution ratio for the vehicle moving at 5, 15, and 25 mph..... 10-8

Figure 10-8. Natural log of dilution ratio for the vehicle moving at 5 mph for three elevations..... 10-9

Figure 10-9. Natural log of dilution ratio for the vehicle moving at 25 mph for three elevations..... 10-9

Figure 10-10. Flow streamlines beginning in the center of the tailpipe for three vehicle speeds..... 10-10

Figure 10-11. Comparison of the five streamlines for case 1 and case 2, slow and rapid dilution, respectively..... 10-11

Figure 10-12. Bobtail particle size distributions at 50 m downwind, dilution with particle-free air..... 10-12

Figure 10-13. Bobtail particle size distributions at 50 m downwind, dilution with ambient air..... 10-12

Figure 10-14. Bobtail particle size distributions at 50 m downwind, dilution with double-concentration ambient air..... 10-13

Figure 10-15. Simulation results for case 1 showing the effects of dilution with particle-free and ambient air..... 10-13

Figure 10-16. Simulation results for case 2 showing the effects of dilution with particle-free and ambient air..... 10-14

LIST OF TABLES

Table 3-1. Trace components of diesel PM. 3-3

Table 3-2. Composition of fine particle emissions from diluted rocket exhaust (weight percent). 3-11

Table 6-1. Instruments deployed at AIMD and flightline sites. 6-4

Table 6-2. SERDP experiment conditions at AIMD site. 6-5

Table 6-3. Engine Power Settings for AIMD Run #1. 6-8

Table 6-4. Engine Power Settings for AIMD Run #2. 6-10

Table 6-5. Engine power settings for AIMD Run #3. 6-12

Table 6-6. Engine Power Settings for AIMD Run #5. 6-16

Table 6-7. Engine power settings for AIMD Run #6. 6-18

Table 6-8. Comparison of PA and EC data from quartz filter and MOUDI. 6-26

Table 6-9. Mass concentrations from the DustTrak, MOUDI, and the Teflon filter. 6-28

Table 6-10. AIMD emission factors derived from Teflon and Quartz filter data. 6-31

Table 6-11. SERDP experiments conducted at flightline site. 6-34

Table 9-1. Experimental conditions. 9-2

Table 9-2. Measurement methods. 9-3

Table 9-3. Summary of real-time results. 9-6

Table 9-4. Conditions where JP8 produced significantly lower emissions, denoted with an x. 9-6

Table 9-5. Average gas-phase emission results. 9-7

Table 9-6. MOUDI elemental carbon (EC) and total mass concentrations. 9-12

Table 10-1. Vehicle/wind conditions for the aerosol dynamics simulations. 10-10

SECTION 1: INTRODUCTION

1.1 Performing Organizations

University of Utah: Adel Sarofim, JoAnn Lighty, Pengzhi Jiang, Kerry Kelly, and David Wagner

Desert Research Institute: W. Patrick Arnott, Mark McDaniel, C. Fred Rogers, John Sagebiel, and Barbara Zielinska

University of California at Riverside: Kimberly Prather, Phil Silva, David Sodeman, David Suess, Steve Toner

University of Wisconsin: James Schauer, Charles Christensen, and June-Soo Park

California Institute of Technology: Glen R. Cass*

Air Force Research Laboratory, AEF Technology Division: Major Michael Calidonna

Hill Air Force Base: Glenn Palmer

Reaction Engineering International: Chris Montgomery

1.2 Project Background

This study developed and validated innovative techniques for characterizing the amount and composition of PM₁₀, PM_{2.5}, and smaller particles for four major classes of DoD emission sources: aircraft ground support vehicles, rocket motors, aircraft, and sandblasting operations. The techniques include the coupling of dilution samplers with advanced measurement techniques for composition and size that provide detailed analyses sufficient to complete a material balance. The size-classified analyses include measurement made with the cascade impactor and aerosol time-of-flight mass spectrometer (ATOFMS). A photoelectric aerosol sensor (PAS) was being evaluated for use in rapidly evaluating field emissions of particle-bound polycyclic aromatic hydrocarbons (PAH). In addition, a photoacoustic spectrometer was investigated for use in measuring soot particle concentrations. The objective was to calibrate and enhance these instruments for DOD use. To this end, the devices are being demonstrated at DoD facilities, and the methodologies developed will be transferred to personnel responsible for monitoring emissions at DoD facilities.

1.3 Objectives

The objectives of this project were to develop advanced methods for the measurement of the size distribution and composition of particulate matter (PM) emitted from mobile and stationary sources in order to provide the DoD with the tools needed to characterize and control the emissions from DoD facilities. This information is needed for compliance with the new ambient particulate standards and for the assessment of the risks associated with PM emissions at DoD facilities. Combustion sources are significant contributors to PM emissions at DoD facilities, and a comprehensive discussion of combustion particle

* deceased

formation, composition, and measurement can be found in (Lighty et al., 2000). The feasibility of using advanced analytical measurements to characterize the chemical composition and size of particulate emissions from a diverse range of sources operated by the DoD was determined. The data obtained during the evaluation of the instruments will provide a measure of the relative importance of different DoD sources and will be useful for guiding the strategies for controlling the emissions from DoD facilities. The cost effectiveness of different measurement methods was assessed and recommendations made for the best protocols for measurement of the fine particle emissions.

1.4 Technical Approach

Three innovative techniques for rapid measurement of fine particles were used in combination with a dilution sampler. The first is an aerosol time-of-flight mass spectrometer (ATOFMS), which measures the size and composition of individual particles. The second is the photoacoustic (PA) detector, which provides a method for rapidly measuring elemental carbon. The third is a photoelectric PAH detector (PAS), which provides rapid measurement of the PAH-laden carbonaceous particles that dominate the emissions from combustion sources. The approach was to apply these devices in parallel with more conventional measurement techniques to establish their validity for characterizing the particle emissions from DoD sources. Optical particle counters (OPC) and differential mobility analyzers (DMA) were used to obtain detailed size distributions in order to calibrate the ATOFMS.

1.5 Project Accomplishments

This SERDP program successfully enhanced the capabilities of the ATOFMS, PAS, and PAS and evaluated their performance on numerous DoD sources, as highlighted below:

1. ATOFMS

- Enhanced the ability of the ATOFMS to analyze ultrafine particles.
- Calibrated the ATOFMS with advanced chemical analysis of filter samples.
- Applied the ATOFMS to DoD sources including: coal combustors, vehicles, rocket firings, sandblasting operations, and ambient PM concentrations at Hill Air Force Base.

2. PA

- Developed a compact system for measuring PA, PAS, CO₂ and particle concentrations that permitted the development of fuel-based emission factors.
- Compared the PA to impactor measurements of elemental carbon for aircraft ground support vehicles, aircraft, and a study of the effect of diesel and JP8 fuels on PM emissions.
- Applied the PAS to DoD sources and studies including: aircraft ground support vehicles, aircraft, the evaluation of diesel PM filters, and a comparison of diesel and JP8 fuels.

3. PAS

- Developed a compact system for measuring PA, PAS, CO₂ and particle concentrations that permitted the development of fuel-based emission factors.
- Compared the PAS to denuder and impactor measurements of particle-bound PAHs for aircraft ground support vehicles, aircraft, and a study of the effect of diesel and JP8 fuels on PM emissions.
- Applied the PAS to DoD sources and studies including: aircraft ground support vehicles, aircraft, the evaluation of diesel PM filters, and a comparison of diesel and JP8 fuels.

The following sections of the final report summarize the highlights of the SERDP program and discuss the results of studies performed in 2002. Summaries of the work performed in previous years can be found in previous years annual reports. This report includes the following sections:

2. *Development and Evaluation of the ATOFMS.*
3. *Detailed Chemical Analysis of Particulate Matter.*
4. *Development and Evaluation of the PA.*
5. *Development and Evaluation of the PAS.*
6. *Aircraft Emissions at North Island Naval Air Station.*
7. *Emissions from Rocket Firings.*
8. *Evaluation of Diesel Soot Filters.*
9. *Comparison of the Effect of Diesel and JP8 fuels on Particulate Emissions.*
10. *Simulation of the Evolution of Particle Size Distribution in a Vehicle Exhaust Plume.*

1.6 SERDP Action Items

During the project's annual in-progress review, the SERDP reviewers requested that our team address a series of issues in this final report. These issues are addressed in the relevant sections of this report, and the locations of the response are listed below.

1. Explain how information regarding concentrations vs. operation mode vs. source will be used for air permit questions, e.g. AP-42 or APIMS. Appendix 6 contains a summary of the fuel based emission factors developed during this program for compounds of regulatory interest.
2. Provide guidance for bag sampling including coagulation and diffusion, which is important for ultrafine particles (e.g., in diesel exhaust). This is discussed in the User's Guide (Appendix 1).

3. If time allows, please consider performing a quick ATOFMS experiment to verify P. LaPuma's results on the size dependence of chromium content in paint deposits (Contact Joe Wander). Unfortunately, time and budget constraints did not allow for this.
4. Please identify how the data collected can be made available to future researchers. Many of the results from this program have been published, presented or are in the process of being published (See list below). A summary of emission factors is presented in Appendix 6. ATOFMS data sets obtained during the SERDP project will be put on a web site that will allow public access. Prof. Prather's group adopted the NARSTO data format to allow relatively fast searches and general display of their spectra. Other mass spectrometry groups are using this format, and information can be found at: eosweb.larc.nasa.gov/PRODOCS/narsto/table_narsto.html). The Prather group will start working on archiving the source datasets from this project in the near future.

1.7 SERDP List of Publications

Published or in press

- S. Angelino, D.T. Suess and K.A. Prather, Formation of Aerosol Particles in the Presence of Secondary and Tertiary Alkylamines. Characterization by Aerosol Time-of-Flight Mass Spectrometry, *Environ. Sci. Tech.*, 35:3130-3138 (2001).
- W.P. Arnott, H. Moosmüller, and J. W. Walker. Nitrogen Dioxide and Kerosene-Flame Soot Calibration of Photoacoustic Instruments for Measurement of Light Absorption by Aerosols. *Review of Scientific Instruments*. 71(7) (2000) 4545.
- W.P. Arnott, H. Moosmüller, C.F. Rogers, T. Jin, and R. Bruch, Photoacoustic Spectrometer for Measuring Light Absorption by Aerosol: Instrument Description, *Atmospheric Environment* [33 \(17\)](#) (1999) 2845.
- P.V. Bhave, D.P. Fergenson, K.A. Prather, G.R. Cass, Source Apportionment of Fine Particulate Matter by Clustering Single Particle Data: Tests of Receptor Model Accuracy, *Environ. Sci. Tech.*, 35:2060-2072 (2001).
- P.V. Bhave, J.O. Allen, B.D. Morrical, D.P. Fergenson, G.R. Cass, K.A. Prather, A Field-Based Approach for Determining ATOFMS Instrument Sensitivities to Ammonium and Nitrate, *Environ. Sci. & Technol.* 36:4868-4879 (2002).
- P.V. Bhave, M.J. Kleeman, J.O. Allen, L.S. Hughes, K.A. Prather, G.R. Cass, Evaluation of an air quality model for the size and composition of source-oriented particle classes, *Environ. Sci. & Technol.*, 36:2154-2163 (2002).
- D.P. Fergenson, X.-H. Song, Z. Ramadan, J.O. Allen, L. Hughes, G.R. Cass, P.K. Hopke, K.A. Prather, Quantitation of ATOFMS Data Using Multivariate Methods, *Anal. Chem.*, 73:3535-3541 (2001).
- M. Gälli, S.A. Guazzotti and K.A. Prather, Improved Lower Particle Size Limit for Aerosol Time-of-Flight Mass Spectrometry, *Aerosol Sci. Tech.*, 34:381-385 (2001).
- S.A. Guazzotti, Suess, D.T., Coffee, K.R., Quinn, P.K., Bates, T.S., Wisthaler, A., Hansel, A., Ball, W.P., Dickerson, R. R., Neusüß, C., Crutzen, P.J., Prather, K. A. Characterization of carbonaceous aerosols outflow from India and Arabia: Biomass/biofuel burning and fossil fuel combustion, *J. Geophys. Res.*, 108: 4485 (2003).
- D.S. Gross, E.E. Gälli, P.J. Silva, S.H. Wood, D.Y. Liu and K.A. Prather, Single Particle Characterization of Automobile and Diesel Truck Emissions in the Caldecott Tunnel, *Aerosol Sci. Tech.*, 32:152-163 (2000).

K.E. Kelly, D.A. Wagner, J. S. Lighty, A.F. Sarofim, C.F. Rogers, J. Sagebiel, B. Zielinska, W. P. Arnott, and G. Palmer Characterization of Exhaust Particles from Military Vehicles Fueled with Diesel, Gasoline, and JP-8, *J. Air & Waste Management Assoc.* (2003) 53, 273-282.

K.E. Kelly, D.A. Wagner, B. Bretecher, B. Holden, K. Sahay, Z. Nardi, J.S. Lighty, A.S. Sarofim, N. Helgeson Evaluation of Catalyzed and Electrically Heated Soot Filters for Removal of Particulate Emissions from Diesel and JP-8 Fueled Engines, *J. Air & Waste Management Assoc.*, *in press*.

J. S. Lighty, J. M. Veranth, and A.F. Sarofim. Combustion Aerosols: Factors Governing their Size and Composition and Implications to Human Health. *J. Air & Waste Management Assoc.* (2000) 50, 1565-1618.

B.D. Morrical, D.P. Fergenson, K.A. Prather, Coupling Two-Step Laser Desorption/Ionization with Aerosol in Near Real-Time," *J. Amer. Soc. Mass Spec.*, 9:1068-1073 (1998).

B.D. Morrical. The Design and Application of a Field Transportable Time-of-Flight Mass Spectrometer (ATOFMS) and Use of Two Step Laser Desorption/Ionization (L2MS) to Determine PAH in Single Particles. Ph.D. Thesis, University of California, Riverside, 2000.

C.F. Rogers, J.C. Sagebiel, B. Zielinska, W.P. Arnott, E.M. Fujita, J.D. McDonald, J.B. Griffin, K. Kelly, D. Overacker, D., Wagner, J. Lighty, A. Sarofim, and G. Palmer. Characterization of Submicron Exhaust Particles from Engines Operating Without Load on Diesel and JP-8 Fuels. *Aerosol Sci. Technol.* 37 (4) (2003) 355.

P.J. Silva, K.A. Prather, Interpretation of Mass Spectra from Organic Compounds in Aerosol Time-of-Flight Mass Spectrometry *Anal. Chem.*, 72:3553-3562 (2000).

X.H. Song, N.M. Faber, P.K. Hopke, D.T. Suess, D.P. Fergenson and K.A. Prather, Source Apportionment of Gasoline and Diesel by Multivariate Calibration Based on Single Particle Mass Spectral Data, *Anal. Chim. Acta.* 446 (2001) 329-343.

X-H. Song, D.P. Fergenson, P.K. Hopke, K.A. Prather, Classification of Single Particles Analyzed by ATOFMS Using An Artificial Neural Network, ART-2a, *Anal. Chem.*, 71:860-865 (1999).

In progress

W. P. Arnott, B. Zielinska, C. F. Rogers, and J. Sagebiel, K. Kelly, D. Wagner, A. Sarofim, J. Lighty, G. Palmer, Evaluation of 1047 nm Photoacoustic Instruments and Photoelectric Aerosol Sensors in Source-Sampling of Black Carbon Aerosol and Particle Bound PAH's from Gasoline and Diesel Powered vehicles, In progress.

P. Jiang, C. Montgomery, A. Sarofim, K. Kelly, J. Lighty. Predicting the effect of dilution on particle size distributions in an exhaust plume. In progress.

J.S. Park, M.M. Shafer, J.J. Schauer, D. Wagner, A. F. Sarofim, J. Lighty, and G.R. Cass. Impact of Combustion Technology on the Composition Size Distribution of Fine Particulate Matter Emitted from the Combustion of Coal. In progress.

C.F. Rogers, J.C. Sagebiel, B. Zielinska, W.P. Arnott, K. Kelly, D., Wagner, J. Lighty, A. Sarofim. Evaluation of aircraft emissions at North Island Naval Air Station. In progress.

J. J. Schauer, C. G. Christensen, and G.R. Cass. The Composition and Size Distribution of Fine Particulate Matter Emitted from Model Rockets. In progress.

B. Zielinska¹, J. Sagebiel, W. P. Arnot¹, C.F. Rogers, K.E. Kelly², D.A. Wagner, J. S. Lighty, A.F. Sarofim, G. Palmer, Phase and Size Distribution of Polycyclic Aromatic Hydrocarbons in Diesel and Gasoline Vehicle Emissions. Submitted *Environ. Sci. Technol.*

Presentations

Arnot, W.P., C.F. Rogers, H. Moosmuller, J. B. Griffin, 2000: Evaluation of Aerosol-Bound PAHs and Elemental Carbon Aerosol in Diesel and Gasoline Vehicles. Presented at Tenth Coordinating Research Council (CRC) On-Road Vehicle Emissions Workshop, San Diego, CA, March 27-29, 2000.

- Jiang P., J.S. Lighty, A.F. Sarofim, E.G. Eddings, 2002, Coagulation Simulation and Inference of Initial Particle Size Distributions Annual Meeting, American Association for Aerosol Research.
- Kelly K.E., A.F. Sarofim, J.S. Lighty, D.A. Wagner, W.P. Arnott, C.F. Rogers, J. Sagebiel, B. Zielinska, G. Palmer, J. Schauer, K. Prather, D. Suess, M. Calidonna (2002) Characterization of Fine Particulate Matter from Military Sources with Real-Time Instruments. *SERDP, Technical Symposium*, December 3-5, Washington D.C.
- Kelly K.E., D. A. Wagner, A.F. Sarofim, J.S. Lighty, W.P. Arnott, E. Fujita, C.F. Rogers, J. Sagebiel, B. Zielinska, K.A. Prather, D.T. Suess, J. Schauer, G. Palmer (2001) Characterization of fine particulate emissions from vehicles using real-time instruments, *222nd ACS National Meeting -Chicago, IL August 26-30, Paper 122*.
- Kelly K.E., D.A. Wagner, P. Kiang, A.F. Sarofim, J.S. Lighty, W.P. Arnott, E. Fujita, C.F. Rogers, J. Sagebiel, B. Zielinska, G. Palmer, M. Calidonna (2001) Using Real-Time Instruments to Characterize Fine Particles from a Variety of Combustion Sources. *Seventh International Congress on Combustion By-Products*, Research Triangle Park, NC June 4-6.
- Kelly K.E., D.A. Wagner, A.F. Sarofim, J.S. Lighty, W.P. Arnott, E. Fujita, C.F. Rogers, J. Sagebiel, B. Zielinska, K. A. Prather and D. T. Suess, J. Schauer, G. Palmer, M. Calidonna (2001) Characterization of Particulate Matter from Aircraft Ground Support Equipment. *Real World Clean Air Conference*, San Diego, CA, April 23-25.
- Lighty J.S., A.F. Sarofim, D.A. Wagner, K.E. Kelly, C.F. Rogers, B. Zielinska, J.Sagebiel, W.P. Arnott, Evaluation of real-time instruments for the characterization of aircraft particulate matter emissions. Phase and Size Distribution of Polycyclic Aromatic Hydrocarbons in Gasoline and Diesel Vehicle Emissions, 2002 Annual Meeting, American Association for Aerosol Research.
- Rogers, C.F., B. Zielinska, J. Sagebiel, P. Arnott, E. Fujita, J.McDonald, A. Sarofim, J. Lighty, K. Kelly, J.B. Griffin, D. Overacker, D. Wagner, G. Palmer, and B. Armstrong, 2001: Characterization of Exhaust Particles Generated by Engines Operating on Gasoline, Diesel, and JP-8 Fuels. Eleventh Coordinating Research Council On-Road Vehicle Emissions Workshop, San Diego, CA, March 26-28, 2001.
- Suess D.T., K.A. Prather, Characterization of Aerosol Combustion Sources: Road to Single Particle Source Apportionment, Analytical Chemistry Department Seminar, University of California at Riverside, March 15, 2001.
- Suess D.T., K.A. Prather, G.R. Cass (2001) Single Particle Source Profiles of Gasoline and Diesel Powered Biomass Burning and Coal Combustion Emissions. *American Geophysical Union*, San Francisco, CA.
- Suess D.T., K.R. Coffee, K.A. Prather, Annual Research Progress of the ATOMS, Strategic Environmental Research and Development Program (SERDP): Source of Coal Combustion Particulate Emissions, Implementation of Aerodynamic Lenses, on ATOFMS and Hill Air Force Base Sandblasting and Ambient Results, *SERDP Advisory Panel Meeting*, San Diego CA, December 15, 2001.
- Suess D.T., B. Morrical, K.A. Prather, J.Schauer, Z. Chowdury, P. Fine, G.R. Cass, Source Characterization of Biomass Burning Particulate Emissions Investigated by Single Particle Chemical Analysis. *American Association for Aerosol Research*, St. Louis, MO, November 10, 2000.
- Suess D.T., P. Silva, K.A. Prather, J. Schauer, Z. Chowdury, P. Mayo, G.R. Cass, D. Wagner, J.S. Lighty, A.F. Sarofim, Source Characterization of Coal Combustion Particulate Emissions Investigated by Single Particle Chemical Analysis, *Society for mass Spectrometry*, Long Beach, CA, June 12, 2000.
- Suess D.T., K.A. Prather, Characterization of Aerosol Combustion Sources: A Single Particle Source Apportionment, Analytical Chemistry Department Seminar, University of California at Riverside, Riverside, CA March 15, 2001.
- Suess D.T., D.Y. Lui, M.Gaelli, K.A. Prather, Real-Time Single Particle Analysis at the Grand Canyon Utilizing an Aerosol Time-of-Flight Mass Spectrometer (ATOFMS), Western Regional ACS Meeting, Ontario, CA, October 8, 1999.
- Suess D.T., K.A. Prather, Novel Applications of Chemically Suppressed Ion Chromatography, Chemistry Departmental Seminar, University of California At Riverside, Riverside, CA, February 25, 1999.

D.T. Suess, P. Silva, K.A. Prather, J. Schauer, G.R. Cass, Application of a Combustion Source Study to Ambient Freeway Data Using Aerosol Time-of-Flight Mass Spectrometry,. Association for Aerosol Research Annual Conference, Tacoma, WA, October 14, 1999.

D.T. Suess, P. Silva, K.A. Prather, J. Schauer, G.R. Cass, Application of a Combustion Source Study to Ambient Freeway Data Using Aerosol Time-of-Flight Mass Spectrometry. Department of Chemistry Seminar, University of California at Riverside, Riverside, CA, February 27, 1998.

Wagner D.A., A.F. Sarofim, J.S. Lighty, D.A. Wagner, W.P. Arnott, C.F. Rogers, J. Sagebiel, B. Zielinska, G. Palmer, J. Schauer, K. Prather, D. Suess, M. Calidonna (2001) Characterization of Fine Particulate Matter from Military Sources with Real-Time Instruments. *SERDP, Technical Symposium*, December, Arlington, VA.

B. Zielinska , J. Sagebiel, C.F. Rogers, W. P. Arnott, K.E. Kelly, D.A.Wagner, J. S. Lighty, A.F. Sarofim, and G. Palmer, 2002: Phase and Size Distribution of Polycyclic Aromatic Hydrocarbons in Gasoline and Diesel Vehicle Emissions, 2002 Annual Meeting, American Association for Aerosol Research.

SECTION 2: DEVELOPMENT AND EVALUATION OF THE ATOFMS

The aerosol time-of-flight mass spectrometer (ATOFMS) measures the size and chemical composition of individual particles in real time. The ATOFMS is a powerful tool because it provides associations between compounds within single particles, and this information can be used to identify a particle's source. The ATOFMS also provides PM composition for transient conditions, which bulk techniques, such as filters, cannot.

2.1 Instrument Description

A schematic of the transportable ATOFMS is shown in Figure 2-1. A brief description will be given here, but a more in depth description of the instrument, as well as the field of single-particle mass spectrometry can be found elsewhere (Gard et al., 1997; Suess and Prather, 1999). The aerosol is introduced into the instrument through a converging nozzle where individual particles are accelerated, reaching different terminal velocities depending on their aerodynamic diameters. Larger particles are accelerated less effectively and thus achieve slower velocities than smaller ones. These particles then pass through two skimmers, which help to achieve lower mass spectrometric pressures ($\sim 10^{-7}$ Torr) as well as to collimate the particle beam. The particles then travel into the optical sizing region of the instrument where two continuous wave diode lasers are located a known distance apart, perpendicular to one another and the incoming particle beam. A single particle passes through the first diode laser and a photomultiplier tube (PMT) detects the scattered light, which starts a clock within the instrument's timing circuit. The same particle traverses a known distance to the second diode laser and again scatters light, which is detected by a second PMT. Measuring the time taken for a single particle to travel a fixed distance allows for the single particle's velocity determination. The aerodynamic size of that individual particle can be determined by an external size calibration using polystyrene latex spheres (PSLs) of known sizes. The particle then traverses another fixed distance into the ion source region of the instrument where a timing circuit fires the desorption/ionization (DI) laser used to create ions from a single particle. These ions are then accelerated in opposite directions down two flight tubes depending on their charge. Positive ions are accelerated in one direction and negative ions are accelerated in the opposite direction. A reflectron in each flight tube is utilized to reverse the ion's flight path, but more importantly greatly enhance the resolution of the mass spectrometer. Microchannel plates (MCPs), located just outside the source region of the TOFMS, are used as ion detectors that allow for the acquisition of the mass spectra.

Although the ATOFMS can determine the composition of single particles, the instrument does not sample all particles from a given sample. Therefore, bulk techniques, such as a micro-orifice uniform deposit impactor (MOUDI), which do sample all particles, are used to scale ATOFMS data. Figure 2-2 gives an example scaling for combustion tests of coal, diesel, and tires. It also illustrates that the ATOFMS is less sensitive to smaller particles than larger ones.

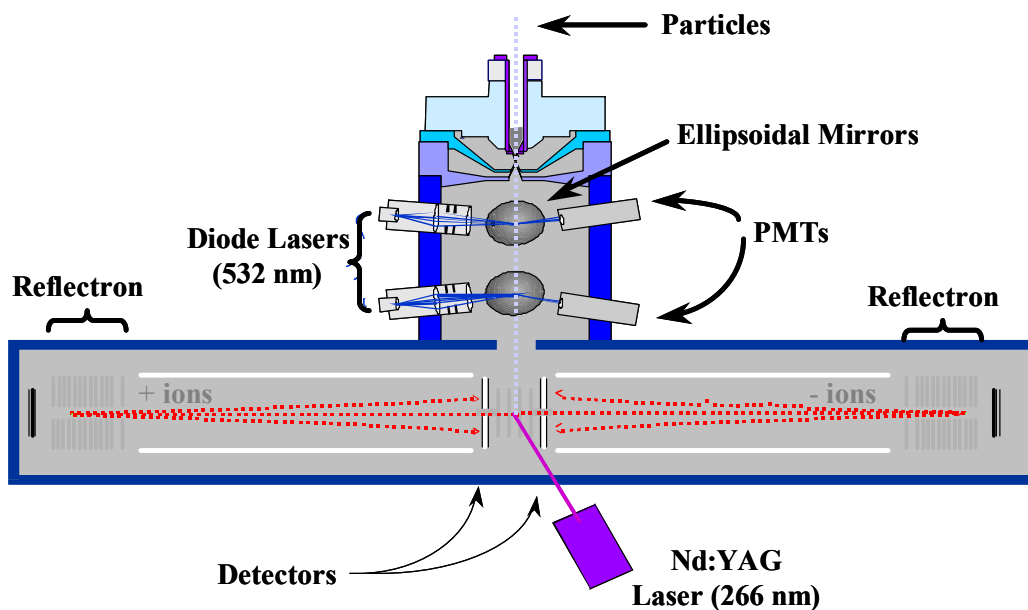


Figure 2-1. Schematic of a field transportable ATOFMS.

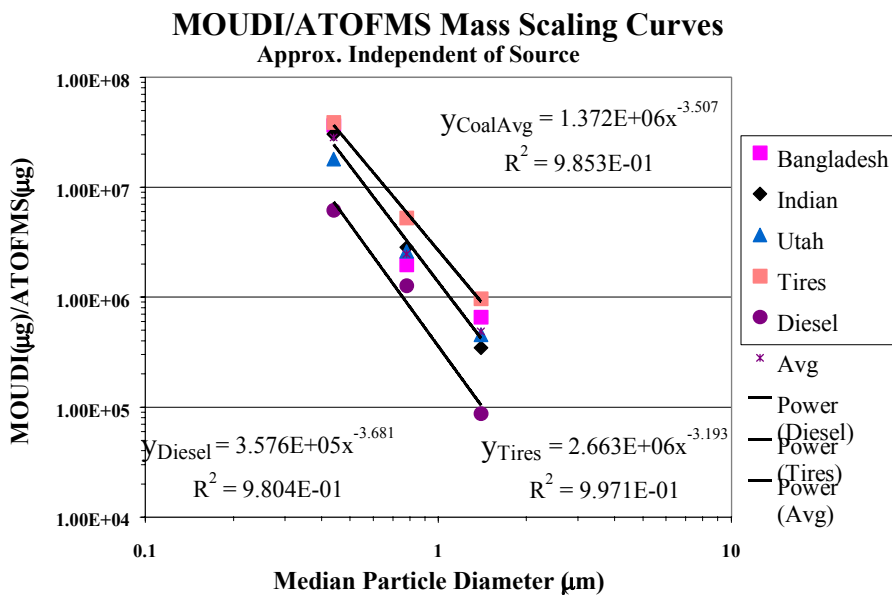


Figure 2-2. Mass scaling curves for the ATOFMS.

2.1.1 Improving the sensitivity of ATOFMS to smaller particles

One of the biggest accomplishments in the SERDP program was improving the ability ATOFMS to analyze ultrafine particles, from an original detection limit of 300 nm to the current limit of 20 nm. These particles are known to play a significant role in the

atmospheric chemistry field and having the ability to analyze them will greatly extend the applicability of ATOFMS. This was accomplished using an aerodynamic lens, which focuses the incoming particle stream into a tight beam (Figure 2-3). The aerodynamic lens improves the transmission efficiency to a level where particles as small as 30-40nm in aerodynamic diameter can be analyzed (Jayne et al., 2000). In contrast, the original ATOFMS particle transmission efficiency allows for analysis of particles between 200nm – 3 μ m in aerodynamic diameter. Figure 2-4 illustrates the use of the ATOFMS on two ultrafine particles. Figure 2-4a represents a 20nm laboratory-generated gold colloid particle indicative of the gold ion and cluster ion at m/z 197 and 394, respectively. Figure 2-4b shows an ambient particle sampled through a differential mobility analyzer for particle sizing.

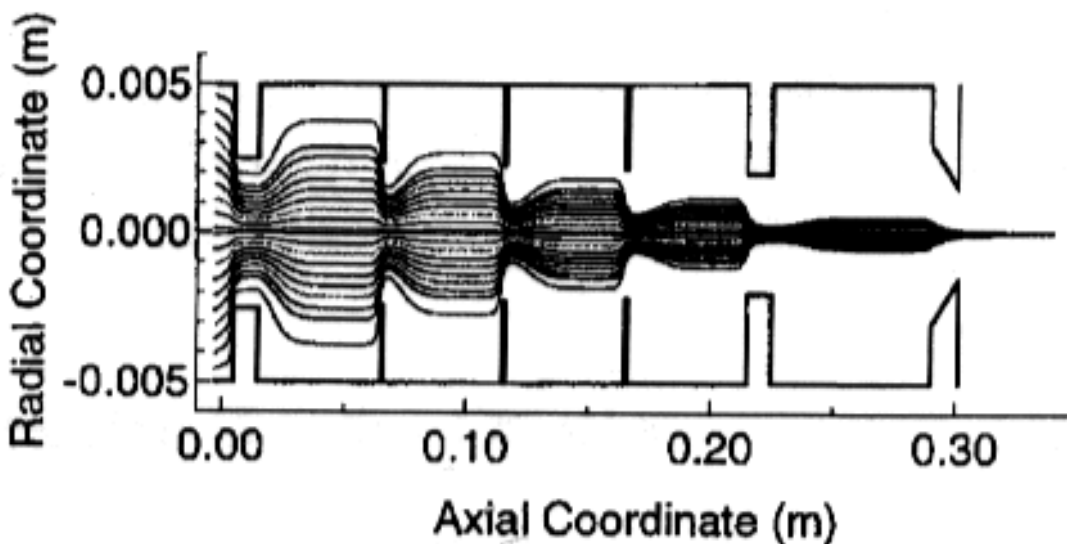


Figure 2-3. The focusing dynamics of an aerodynamic lens system that allows for the transformation of an uncollimated polydisperse particle stream to a tightly focused particle beam (Ziemann, 1998).

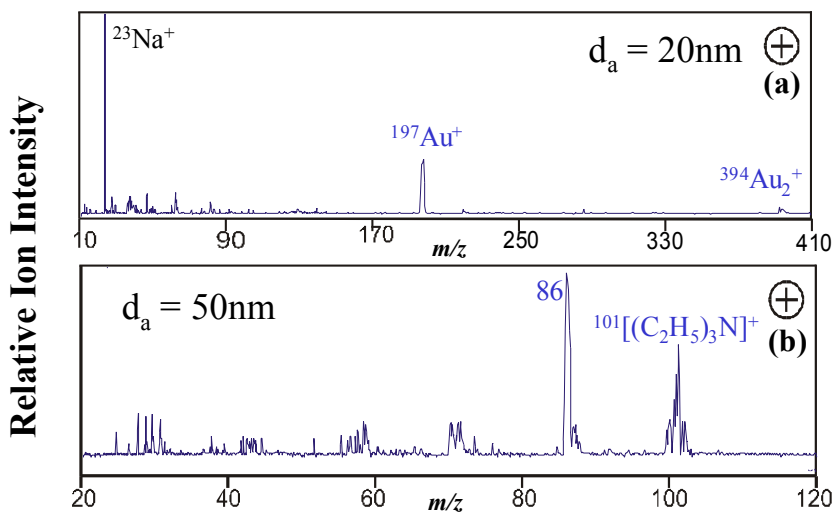


Figure 2-4. Single-particle mass spectra sampled using the aerodynamic lenses.

2.2 Evaluation of the ATOFMS for DoD sources

The results of the SERDP evaluation of the ATOFMS are detailed in this final report and previous annual reports. Briefly during the SERDP program, the ATOFMS was deployed to measure PM size and composition in the following studies:

- Sandblasting operations at Hill Air Force Base (HAFB, Annual Report 2001)
- Ambient PM from Hill Air Force Base and Salt Lake City (Annual Report 2000, 2001)
- Coal combustion studies (Annual Report 2000, 2001)
- A dynamometer study of ten gasoline vehicles and one diesel truck (Annual Report 2000)
- Emissions from rocket firings (Final Report)

The ATOFMS performed well for all of the DoD sources, including testing emissions from a rocket motor. ATOFMS data sets obtained during the SERDP project will be put on a web site that will allow public access. Prof. Prather's group adopted the NARSTO data format to allow relatively fast searches and general display of their spectra. Other mass spectrometry groups are using this format, and information can be found at: eosweb.larc.nasa.gov/PRODOCS/narsto/table_narsto.html). The Prather group will start working on archiving the source datasets from this project in the near future.

Figure 2-5 and 2-6 show examples of ATOFMS results for two different sources, sandblasting and diesel exhaust. Figure 2-5 shows spectra for PM from sandblasting operations at HAFB. The particles contained both chromium and strontium, which are most likely from the paint that had been stripped off planes within the facility. Importantly, these metals are extremely rare in terms of traditional ATOFMS ambient sampling and may be valuable chemical markers to identify particles emitted from the facility. Figure 2-6 summarizes ATOFMS results for diesel emissions from the ATOFMS, and it illustrates how particle composition varies with size.

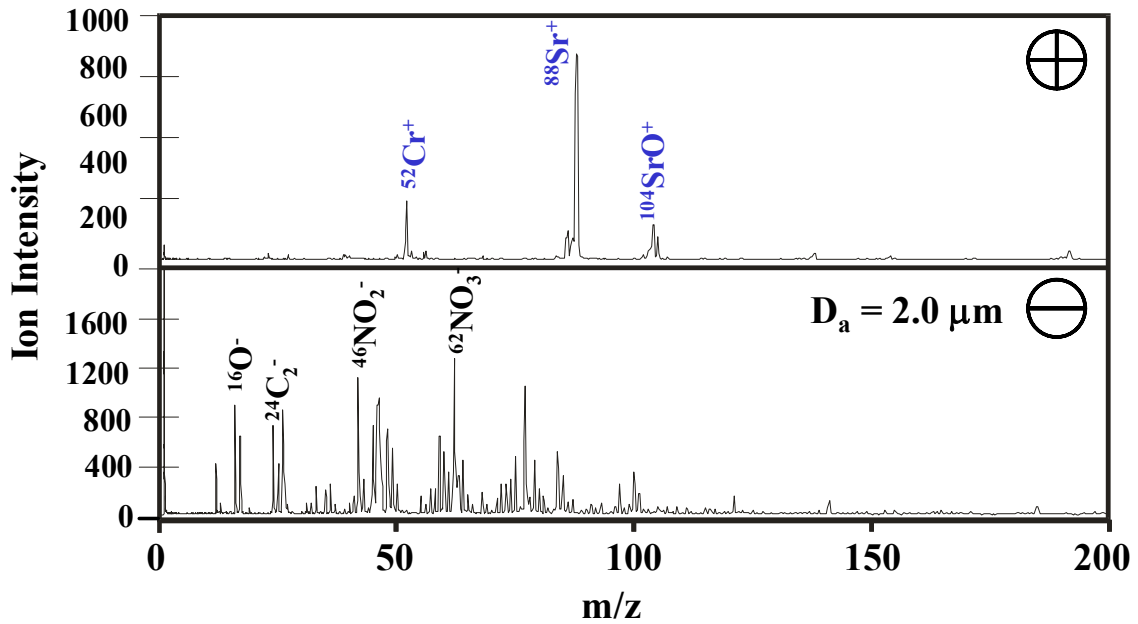


Figure 2-5. A single-particle mass spectrum sampled from used sandblasting material.

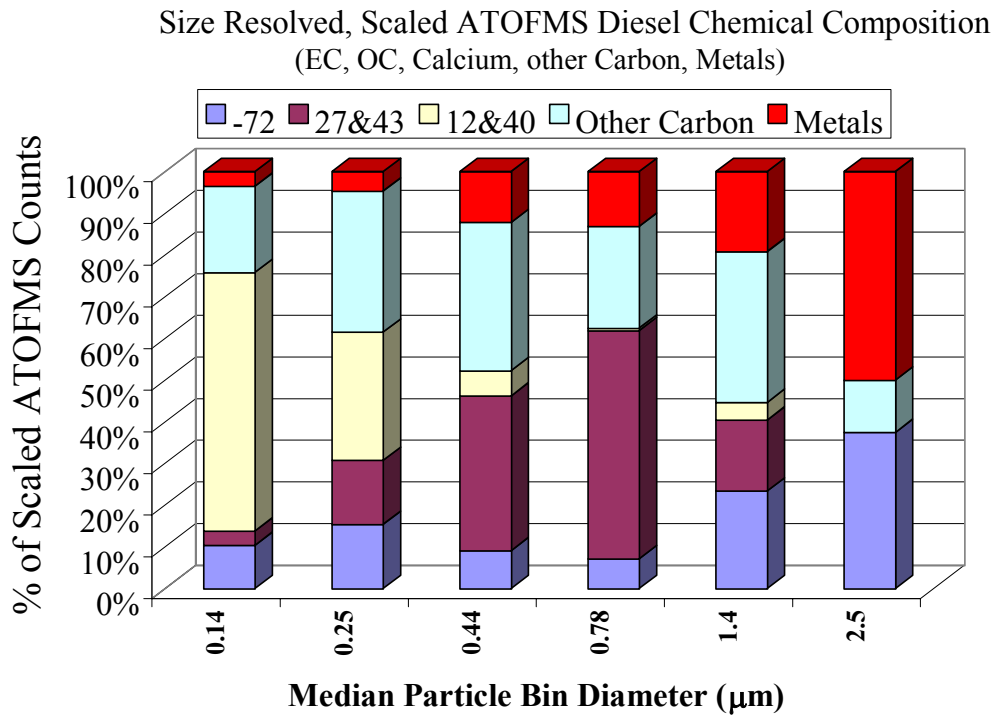


Figure 2-6. Size-resolved composition of diesel exhaust from the ATOFMS.

The SERDP team also collected ambient PM for one week at HAFB, where the week began with a snowstorm followed by warmer stagnant weather. During the snowstorm,

the team identified two interesting particle types containing magnesium. One contained positive water-cluster ions, and the other contains negative chloride cluster ions. Both of these particle types were only present during the winter snowstorm. The associated size distribution of these magnesium containing particles are nearly all greater than $1\mu\text{m}$ which indicates they were mechanically generated particles. During the course of the week, the abundance of particles containing organic carbon increased (Figure 2-7). The warmer weather allowed the overall particle concentrations to increase along with the organic carbon containing particles emitted from local combustion sources.

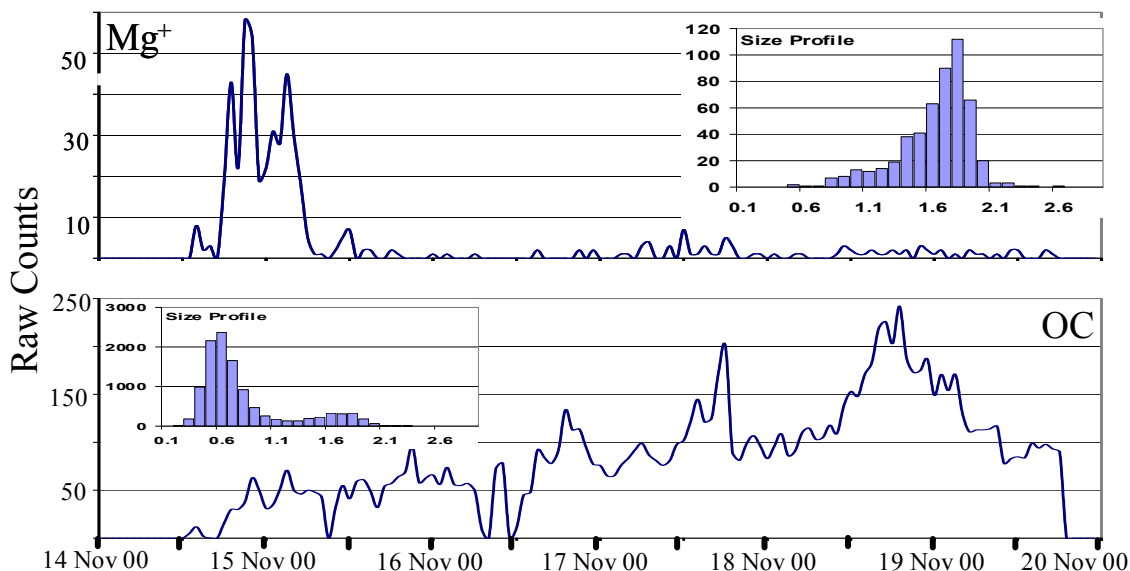


Figure 2-7. Temporal and size distributions representing particles that contain magnesium, top, and organic carbon, bottom.

2.3 Summary

The ATOFMS performed well for all DoD sources tested during this SERDP program, and it provided signatures for a variety of DoD sources. One of the biggest accomplishments during SERDP was improving the sensitivity of the ATOFMS to characterize ultrafine particles. The User Guide (Appendix 1) provides a more complete description of the ATOFMS and comparison with other methods for determining PM size and composition.

The most obvious applications for DoD users would be source apportionment and detection of signature compounds, including biowarfare detection. Biological particles can easily be discriminated from other atmospheric particles on a continuous basis. These instruments conceivably could detect individual bacteria and discriminate between them and particles from other sources. ATOFMS could acquire this information continuously so the particles of concern could be detected instantaneously for early warning. This has serious defense ramifications.

References

Gard E., J.E. Mayer, B.D. Morrical, T. Dienes, D.P. Fergenson, K.A. Prather (1997). *Anal. Chem.* 69, 4083-4091.

Suess D.T., K.A. Prather (1999) *Chem. Rev.* 99, 3007-3035.

Ziemann P.J. (1998). *Trends Anal. Chem.* 17, 322-328.

SECTION 3: DETAILED CHEMICAL ANALYSIS OF PARTICULATE MATTER

3.1 Abstract

In order to facilitate the development of real-time chemical speciation measurements of particulate matter emissions from air pollution sources, a series of source tests were conducted that employed a dilution source sampler. The sampler allowed hot exhaust emissions to be diluted with purified dilution air, which was sampled by an Aerosols Time of Flight Mass Spectrometer (ATOFMS) and on substrates for detailed chemical analysis in the laboratory. Fine particle (PM_{2.5}) filter samples along with cascade impactor samples were collected using a variety of substrates to allow detailed chemical analysis of organic and inorganic particulate matter constituents. A series of tests were conducted over the course of the project. In Year 1, motor vehicles were tested using a chassis dynamometer. Emissions from the gasoline-powered motor vehicles were too low to be quantified with the sampling system employed but the emissions from a diesel vehicle operating over the FTP cycle were characterized. In Year 2, emissions from combustion of coal were characterized at the University of Utah Coal Combustion Research Facility. Emissions from a pulverized coal burner and a laboratory batch under-fired grate burner were measured. In Year 3, particulate matter measurements were conducted in a sandblasting facility and near a jet aircraft runway at Hill Air Force Base. Fine particle mass loadings on the sampling substrates were too low for chemical characterization. In Year 4, diluted emissions from model rocket combustion emissions were collected and analyzed to simulate aerosols generated from Open Burn and Detonation operations used to decommission bombs. The measurements provide the traditional chemical analysis of particulate matter to help further develop and calibrate the ATOFMS and provide an important foundation for future tests of this nature.

3.2 Introduction

In the past several decades, significant advances have been made in the development of instruments to characterize atmospheric particulate matter and to employ advanced chemical and physical analysis tools to characterize atmospheric aerosols. As there is increased pressure to understand the impact of emissions from different air pollution sources on air quality by regulatory and health effects communities, there is a great need to apply the tools that have been developed for atmospheric aerosols to the characterization of primary emissions from sources. Although instruments have been developed that allow the measurements of particulate matter in the stacks of air pollution sources, it is clear that non-volatile and semi-volatile components of particulate matter evolve significantly in the dilution process. To this end, measurements directed at understanding the impact of emissions on air quality should sample and analyze aerosols after the dilution and cooling processes that occur in plumes downwind of stack emissions. For this reason, the current project employs a dilution source sampler originally developed at Caltech (Hildemann, et al., 1991a) and has been extensively used by other research teams in recent years. In the present project, the sampler is employed

as presented by Schauer et al. (Schauer, et al., 1999a; Schauer, et al., 1999b) and is operated with an ATOFMS. The ATOFMS measurements are reported separately.

3.3 Sampling

The motor vehicle tests were conducted at the California Air Resources Board Vehicle Testing Laboratory in El Monte, California. The tests were describe as reported by Schauer et al. (Schauer, et al., 1999a; Schauer, et al., 1999b). The only major modification was the connection of the ATOFMS at the residence time chamber of the sampler, which was used for continuous measurements during the tests. A similar sampling system was used for the coal combustion tests except that a primary dilution sampler was not used. The measurements were collected from the hot stack emissions of the University of Utah Coal Combustion facility. The rocket tests were performed using a similar sampling scheme as previously described by Fine et al. (Fine, et al., 1999).

3.4 Summary of the Results

As previously reported, particulate matter from diesel vehicles are predominately carbonaceous materials with trace levels of inorganic species (Hildemann, et al., 1991a; Kleeman, et al., 2000). Figure 3-1 presents the size resolved chemical composition of particulate matter emitted from the diesel vehicle tested. These results are consistent with previous measurements by represent the first measurements of this nature that integrate a collocated ATOFMS instrument. Table 3-1 presents the contribution of inorganic species to particulate matter emissions from the diesel vehicles. Although these measurements do not provide new insights into the emission from motor vehicles, they provided the foundation for the integration of the ATOFMS with the dilution source sampling system.

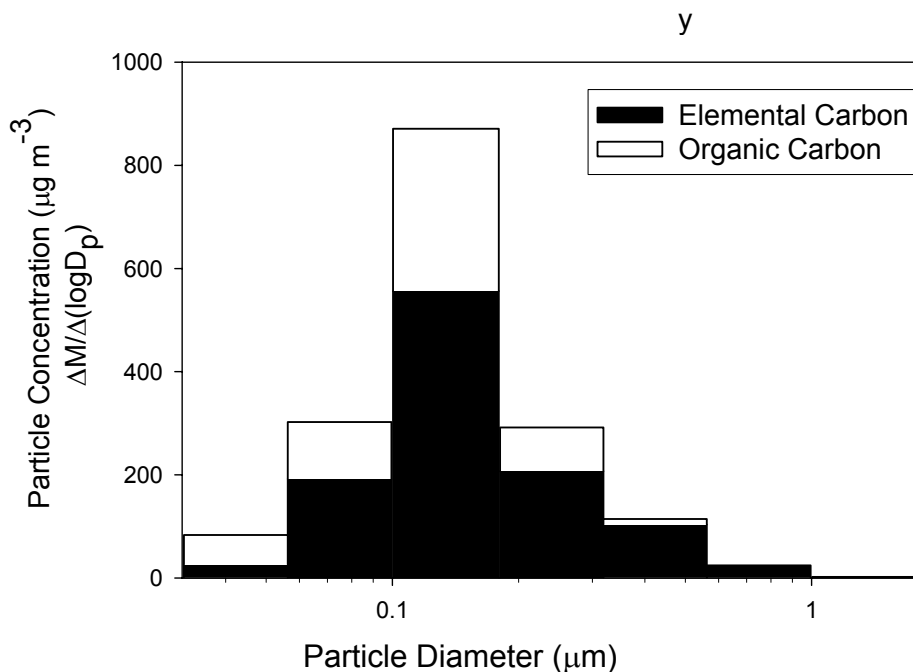


Figure 3-1. Size-resolved chemical composition of PM emissions from a diesel truck, FTP cycle.

Table 3-1. Trace components of diesel PM.

Compound	Percent of Mass		Compound	Percent of Mass		Compound	Percent of Mass	
	Average	Uncertainty		Average	Uncertainty		Average	Uncertainty
Sulfate ion	0.55	0.16	Fe	0.06	0.06	Pd	0.02	0.29
Ammonium Ion	0.21	0.08	Co	0.00	0.04	Ag	0.00	0.35
Nitrate Ion	0.01	0.20	Ni	0.00	0.04	Cd	0.00	0.37
Al	0.39	0.12	Cu	0.00	0.05	In	0.00	0.41
Si	1.23	0.09	Zn	0.76	0.02	Sn	0.38	0.53
P	0.68	0.06	Ca	0.00	0.07	Sb	0.00	0.62
S	1.02	0.06	As	0.00	0.08	Ba	1.15	2.16
Cl	0.29	0.07	Se	0.00	0.04	La	1.05	3.19
K	0.17	0.17	Br	0.02	0.04	Au	0.00	0.12
Ca	1.13	0.08	Rd	0.02	0.03	Hg	0.02	0.09
Ti	0.00	0.88	Sr	0.01	0.04	Tl	0.00	0.09
V	0.00	0.34	Y	0.00	0.05	Pb	0.02	0.11
Cr	0.00	0.08	Zr	0.00	0.05	U	0.00	0.09
Mn	0.01	0.06	Mo	0.00	0.10			

Note: Values in bold are statistically different from zero with a 95% confidence interval.

In order to facilitate more accurate measure of metals present in the particulate matter emissions from coal combustion, samples were for detailed trace metals by using Inductively Coupled Plasma Mass Spectrometry that utilized a microwave-assisted acid digestion. Particulate matter samplers were digested in a mixture of 1.5 mL HNO₃, 0.5 mL HF, and 0.5 mL HCl. The samples were digested in the microwave programmed for a 9-minute heating ramp to the final digestion temperature (180 °C) and were held at this temperature for 10 minutes. After digestion the samplers were cooled for 1 hour and diluted with Milli-Q water to a final volume of 30 ml. All Teflon tubes and vessels used in the microwave were soaked in 50 v/v hot nitric acid baths for at least 24 hours. 60 mL polybottles for the final solution were cleaned by 30 HCl for 48 hours and then 20 HNO₃ for 48 hours. The methods and protocols developed for this study have been validated through the analysis of Standard Reference Materials: San Joaquin Soil (NIST 2706), Auto Catalyst (NIST 2556), and Urban Dust (NIST 1649a) which are presented in Figure 3-2.

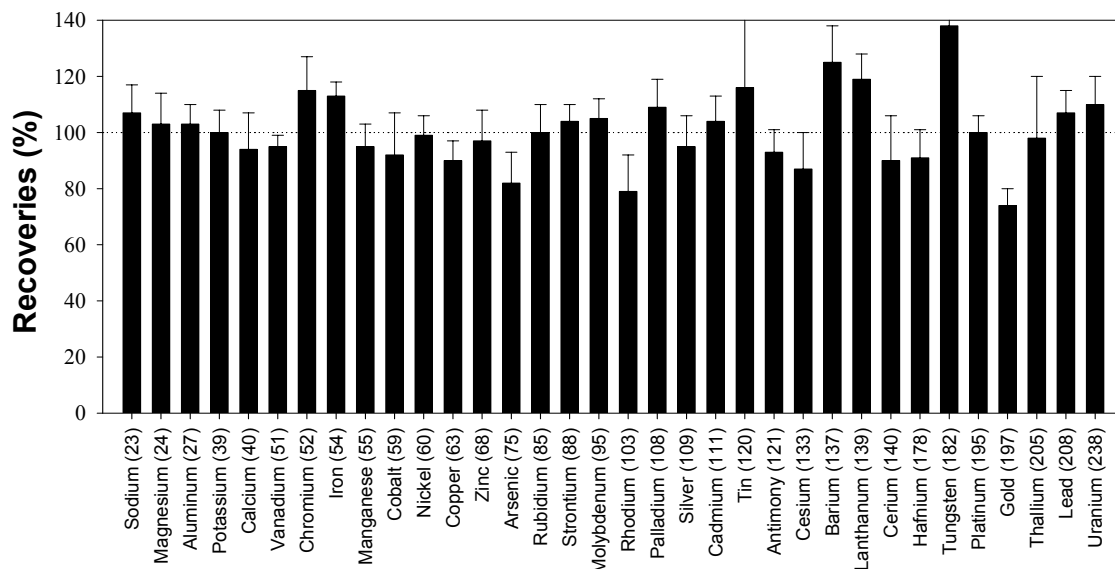


Figure 3-2. Recoveries of metals for the analysis of standard reference materials (SRM). San Joaquin Soil (NIST 2706), Used Auto Catalyst (NIST 2556), and Urban Dust (NIST 1649a) were used for this recovery study.

The measurement of trace elements using ICP-MS was evaluated by comparing with INAA measurements conducted in the Massachusetts Institute for Technology. Particulate matter samples collected from coal combustions were cut in half and analyzed by using both ICP-MS and INAA techniques. As, Ba, Mg, Ce, Zn, Cr, Co, Mo, V, La, Ti, and Sb were relatively consistent between these two techniques (Figure 3-3). However, the measurement of other elements between these two techniques showed some discrepancies. Teflon substrate from MOUDI impactors were also cut in half and analyzed by both techniques. However, data were not comparable since most elements measured by INAA were below detection. In addition, toxic trace elements (e.g., Pb and Cd) were well quantified by the ICP-MS technique. However, Si and Se, which may be important elements in particulate matter emission from coal combustion, have not been measured accurately in ICP-MS, due to major interferences from matrices and argon dimmers, respectively.

Co-located PM_{2.5} samplers and MOUDI impactors collected fine particulate matter emissions from three types of coal combustions. The measurements obtained from the PM_{2.5} samples and MOUDI impactor samples were compared to evaluate the performance of the current sampling and chemical analyses methodology used in this study. The sum of six MOUDI impactor stages (0.06–1.8 μm) and the Teflon after-filter (<0.06 μm) were compared to the PM_{2.5} samples for mass, organic and elemental carbons, inorganic ions (sulfate, nitrate, ammonium, and chloride), and trace elements (Figure 3-4). Typically, mass and trace elements measured from PM_{2.5} showed good agreement with a slight elevation over the sum of the MOUDI stages. The slight elevations of chemical species on PM_{2.5} are likely a result of the difference in particle size cut between the PM_{2.5} samples (0–2.5 μm particle diameter) and the impactor samples (0–1.8 μm particle diameter).

batch furnace. Particulate sulfate was a dominant chemical component in Utah and Illinois coal emissions from pulverized coal furnace.

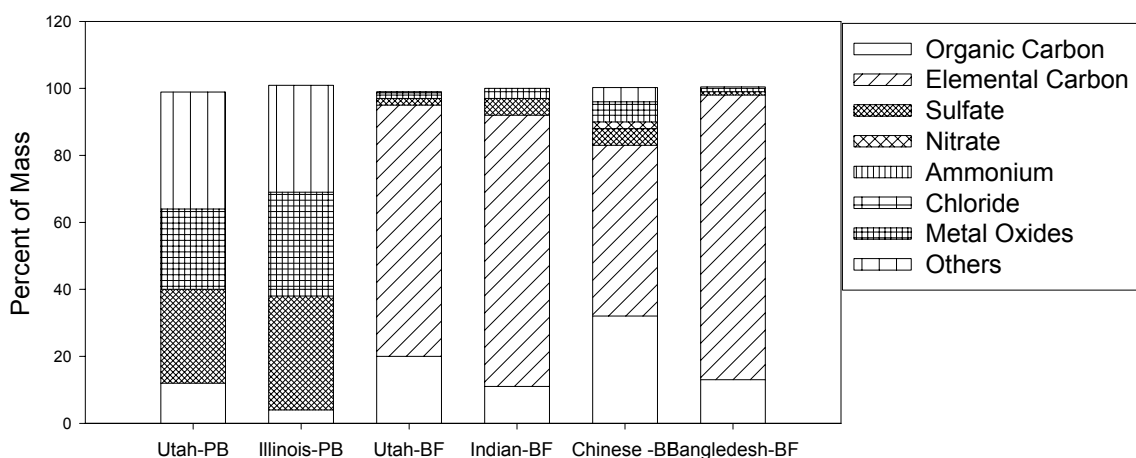


Figure 3-5. Chemical composition fractions of PM_{2.5} emitted from coal combustion. BF: batch furnace. PB: pulverized boiler.

To assess the size-resolved chemical composition of emissions, particulate matter emissions from Utah and Illinois coal combustion at pulverized furnace and from Bangladesh coal combustion at batch furnace were collected by using 6 stages MOUDI impactors and after filter. Fine particulate matter distributions in a function of size were shown in Figure 3-6. Fractions of unknown compounds and metal oxides were also large in all size ranges of particulate matter emission from Utah and Illinois coal combustion at pulverized furnace, which is consistent to the results from PM_{2.5} chemical species distribution shown in Figure 3-5. Size and composition distribution in coal combustion emissions was, however, quite different from other contributors to urban air pollution including automobiles, wood combustion, meat smoke, paved road dust, food frying, and natural gas combustion (Hildemann, et al., 1991b; Kleeman, et al., 1999). In contrast to the single peaked size distribution observed from other studies above, the bimodal distribution was typical in size and composition distribution of particulate matter emission from coal combustion at pulverize boiler. The peaks at 1.0–1.8, and 0.18–0.32 μm and sometimes 0.10–0.18 μm were generally shown at size distribution of particulate matter mass in pulverized boiler experiment. However, these bimodal trends were also variable depending on the chemical species in this study. No simple correlations were found between the ash content and particulate matter emission (McElroy, et al., 1982). Reportedly, bimodal distribution with a submicron mode is a general feature of pulverized combustion with a very high flame temperature where particle formation involves with volatilization of ash components and then condensation and coagulation of the volatile material in the dilution sampling system with cool condition (McElroy, et al., 1982; Quann, et al., 1982; Markowski and Filby, 1985; Amdur, et al., 1986; Kauppinen and Pakkanen, 1990).

The size distributions of chemical compositions were not uniform in particulate matter emissions from coal combustions. In Utah coal emission, size distribution of organic and elemental carbons, ammonium and chloride showed a peak at 0.10–0.18 μm while sulfate showed a peak in 0.18–0.32 μm (Figure 3-7). About 40 trace elements were detected over instrumental detection limits and almost all elements are continuously distributed over the entire size ranges. However, only some elements significantly higher than the calculated uncertainties were presented in Figure 3-6 to more clearly explain the overall trends. As shown in Figure 3-6, Ca, V, Sr, and Ba showed bimodal distribution with a primary peak at 0.18–0.32 and then at 0.56–1.0 μm as a secondary peak. It may be indicative that these elements experienced some volatilization and recondensation to form fine particles during the combustion process. In contrast, Mg, Al, K, Ti, Fe, Cr, and Co were strongly distributed over size range larger than 0.56 μm and then sometimes at 0.18–0.32 μm as a secondary peak, which tend to follow the size distribution of particulate matter mass. This may indicate that these elements were relatively refractory during combustion process and thus non-vaporized part of coal fly ash were predominant in the chemical size distribution above 0.56 μm . In other word, incombustible mineral component of the coal fly ash were carried over. Especially, Al showed a flat distribution over particle size smaller than 0.56 μm . More volatile elements such as Cu, Zn, As, Ni, and Sn were strongly observed at after filter ($< 0.06 \mu\text{m}$). Interestingly, As and in some degree Sn showed a increment tendency as the size range decreases.

Figure 3-8 and Table 3-2 summarize the results of the rocket tests, which were used as preliminary tests to obtain fingerprints for the ATOFMS to identify particles from stationary rocket firing operations at the Hill Air Force Base.

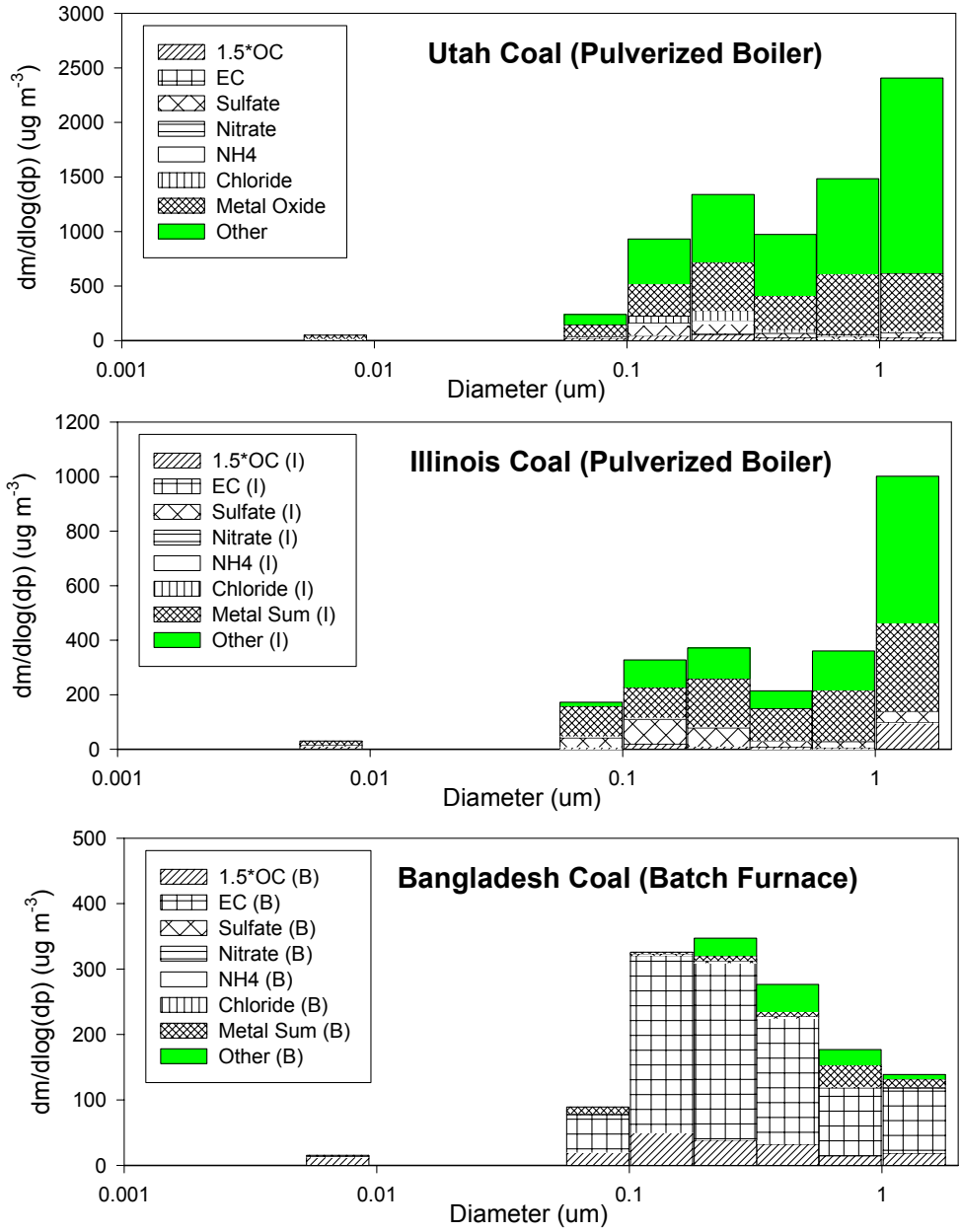


Figure 3-6. Size-resolved chemical compositions of coal combustion emissions. Measured organic carbon was multiplied by 1.5 to approximate organic compound mass.

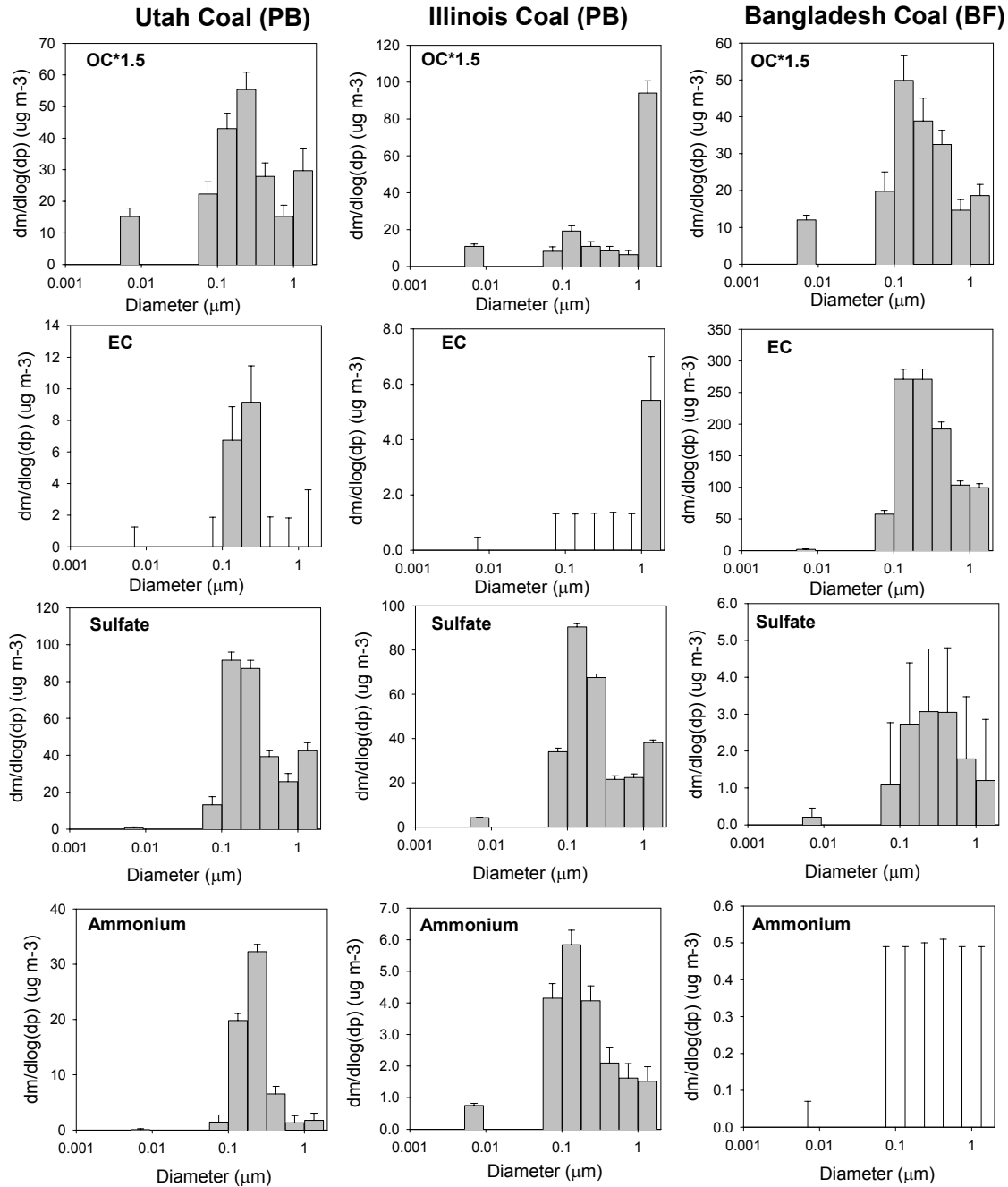


Figure 3-7. Size-segregated chemical composition of PM emissions from coal combustion.

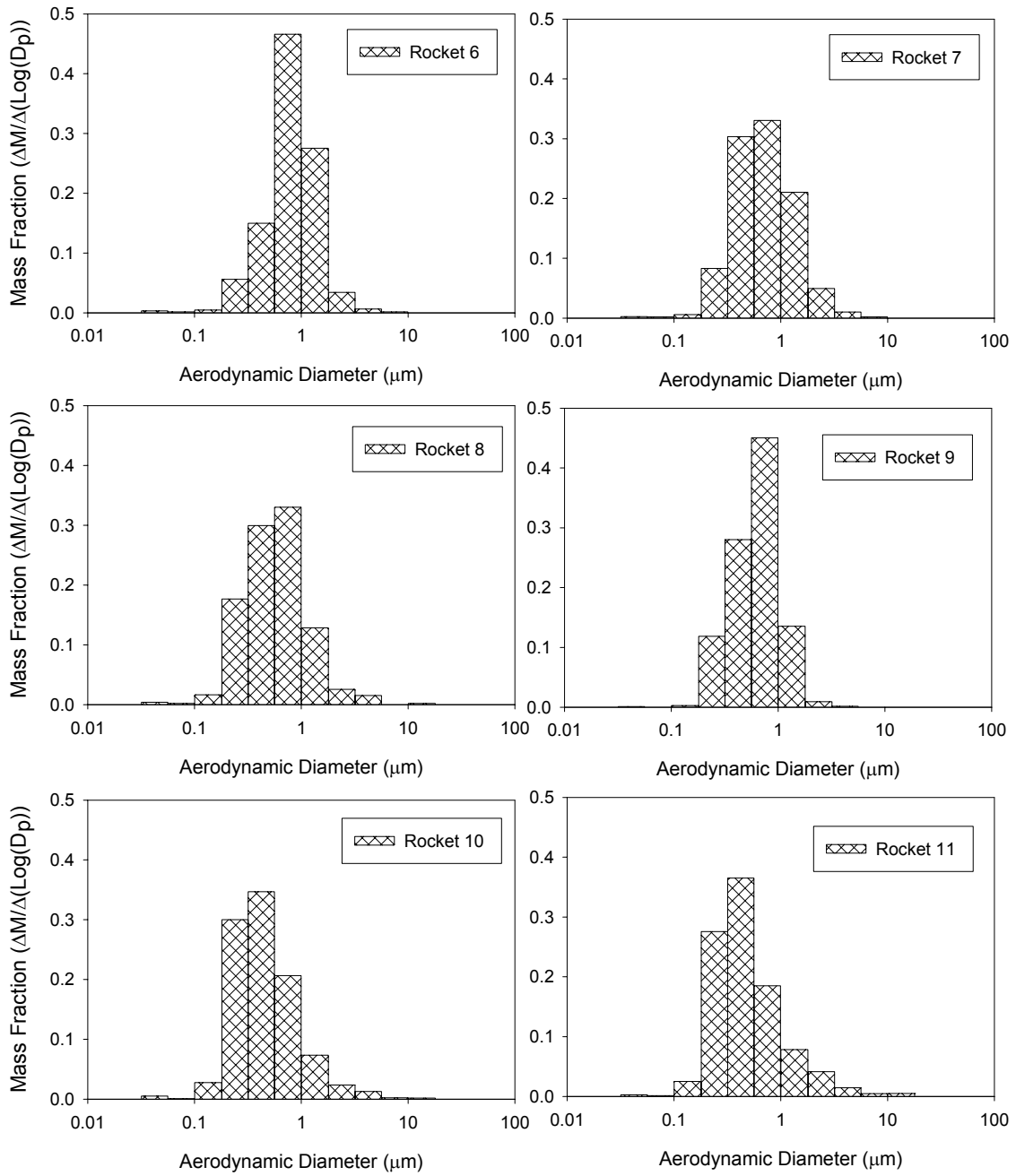


Figure 3-8. Size distributions measured for diluted rocket exhaust.

Table 3-2. Composition of fine particle emissions from diluted rocket exhaust (weight percent).

Rocket	Rocket Type	OC	EC	Chloride	Nitrate	Sulfate	NH4 ⁺	Other
1	White Lightning F20-7W	1.4	4.0	16.9	0.0	0.3	0.3	76
2	Blue Thunder G-80-4T	8.2	1.2	30.6	0.1	2.5	3.3	54
3	Blackjack F12-5	5.5	2.0	22.4	0.1	0.0	2.8	66
4	Blackjack F12-5	105	10.8	25.8	19.1	0.0	2.1	0
5	White Lightning F20-7W	4.8	1.5	23.0	0.1	0.3	3.9	66
6	Blue Thunder G-80-4T Composite of 4	7.4	1.7	0.2	0.2	0.1	4.6	86
7	White Lightning F20-7W Composite of 2	6.0	0.9	23.5	0.2	0.0	3.7	65
8	BlackJack F12-5 Composite of 2	12.6	4.7	26.6	1.9	0.0	2.2	54
9	Blue Thunder G-80-4T	8.0	1.8	27.9	0.2	0.0	4.1	58
10	White Lightning F20-7W	5.7	1.0	21.4	0.3	0.0	1.5	70
11	Blackjack F12-5	6.5	2.7	23.7	0.4	0.0	2.0	65
12	Estes Composite of 4	1.5	0.2	0.1	0.3	0.0	0.0	98

OC: organic carbon; EC: elemental carbon

Note: Values in bold are statistically different from zero with a 95 confidence interval

Publications

The following manuscripts are in preparation and are planned to be submitted for publication in the near future:

J. J. Schauer, C. G. Christensen, and G.R. Cass. The Composition and Size Distribution of Fine Particulate Matter Emitted from Model Rockets. *In progress*.

J.S. Park, M.M. Shafer, J.J. Schauer, D. Wagner, A. F. Sarofim, J. Lighty, and G.R. Cass. Impact of Combustion Technology on the Composition Size Distribution of Fine Particulate Matter Emitted from the Combustion of Coal. *In progress*.

References

Amdur MO, Sarofim AF, Neville M, Quann RJ, Mccarthy JF, Elliott JF, Lam HF, Rogers AE, Conner MW. 1986. Coal Combustion Aerosols and So₂ - an Interdisciplinary Analysis. *Environmental Science & Technology*. 20: 138-145.

Fine PM, Cass GR, Simoneit BRT. 1999. Characterization of fine particle emissions from burning church candles. *Environmental Science & Technology*. 33: 2352-2362.

Hildemann LM, Markowski GR, Cass GR. 1991a. Chemical-Composition of Emissions from Urban Sources of Fine Organic Aerosol. *Environmental Science & Technology*. 25: 744-759.

Hildemann LM, Markowski GR, Jones MC, Cass GR. 1991b. Submicrometer aerosol mass distributions of emissions from boilers, fireplaces, automobiles, diesel trucks, and meat cooking operations. *Aerosol Science and Technology*. 14: 138-152.

Kauppinen EI, Pakkanen TA. 1990. Coal Combustion Aerosols - a Field-Study. *Environmental Science & Technology*. 24: 1811-1818.

Kleeman MJ, Schauer JJ, Cass GR. 1999. Size and composition distribution of fine particulate matter emitted from wood burning, meat charbroiling, and cigarettes. *Environmental Science & Technology*. 33: 3516-3523.

Kleeman MJ, Schauer JJ, Cass GR. 2000. Size and composition distribution of fine particulate matter emitted from motor vehicles. *Environmental Science & Technology*. 34: 1132-1142.

Markowski GR, Filby R. 1985. Trace-Element Concentration as a Function of Particle-Size in Fly-Ash from a Pulverized Coal Utility Boiler. *Environmental Science & Technology*. 19: 796-804.

McElroy MW, Carr RC, Ensor DS, Markowski GR. 1982. Size Distribution of Fine Particles from Coal Combustion. *Science*. 215: 13-19.

Quann RJ, Neville M, Janghorbani M, Mims CA, Sarofim AF. 1982. Mineral Matter and Trace-Element Vaporization in a Laboratory-Pulverized Coal Combustion System. *Environmental Science & Technology*. 16: 776-781.

Schauer JJ, Kleeman MJ, Cass GR, Simoneit BRT. 1999a. Measurement of emissions from air pollution sources. 1. C-1 through C-29 organic compounds from meat charbroiling. *Environmental Science & Technology*. 33: 1566-1577.

Schauer JJ, Kleeman MJ, Cass GR, Simoneit BRT. 1999b. Measurement of emissions from air pollution sources. 2. C-1 through C-30 organic compounds from medium duty diesel trucks. *Environmental Science & Technology*. 33: 1578-1587.

SECTION 4: DEVELOPMENT AND EVALUATION OF THE PHOTOACOUSTIC ANALYZER

The photoacoustic analyzer (PA) detects and quantifies light-absorbing particles in real time. This process occurs with the particles suspended in a flowing sample air stream, without the need to collect the particles on a filter (i.e., it is an “in-situ” method). It offers advantages over filter collection, which may alter the characteristics of the particles with respect to light absorption. The DRI photoacoustic instrument has been described in detail in recent publications (e.g., Arnott et al. 1999, 2000, 2003; Moosmüller et al., 1997, 1998, 2001a), and the results of the SERDP studies are described in a draft paper (Appendix 2).

Light absorbing particles in the atmosphere are usually composed of “black” carbon, although in dusty areas some light absorbing mineral oxides may be present. Black carbon is a major component of motor vehicle exhaust, especially that from diesel vehicles, and the term “black” carbon is nearly synonymous with the “elemental” carbon that is measured by the Thermal-Optical Reflectance (TOR) method (Chow et. al., 1993). The photoacoustic method has the major advantages of real time and in-situ detection compared to the TOR method.

4.1 Instrument Description

During the course of SERDP, the DRI team made some improvements to the instrument including reducing its size, increasing its field robustness, and developing use with a laser wavelength of 1047 nm for optimal sensing of combustion particles free from gaseous interference. Figure 3-1 shows the new photoacoustic instrument design. The instrument comprises two identical coupling sections, and a third resonator section. These parts are manufactured out of aluminum. The coupling sections allow the laser beam to enter the instrument through windows well separated from the resonator section. The sample inlets and outlets are followed by cavities that are tuned to reduce the coupling of noise into the resonator section. The resonator section has a horizontal tube that is 1/2 of an acoustic wavelength long, and two vertical tubes that are 1/4 of an acoustic wavelength long. In previous designs, the vertical tubes were at an angle of 45 degrees to the horizontal instead of 90 degrees as they are now, and the tubes were formed from pipe rather than machined with precision. The 90 degrees angles allow for symmetry when deciding where the holes in the resonator are placed to allow for laser beam and sample air passage. The piezoelectric transducer is used as a sound source to occasionally scan the resonator resonance frequency and quality factor for use in calibrating the instrument from an acoustical perspective. The microphone and piezoelectric transducer sit at pressure antinodes of the acoustic standing wave, and the holes in the resonator are at pressure nodes. The instrument is bolted together in three parts for easy disassembly in case it needs to be cleaned. The laser beam passes through the windows and the holes in the resonator section. The laser beam pumps the acoustic wave through light absorption, and the transfer of the associated heat to the surrounding air, in the resonator section.

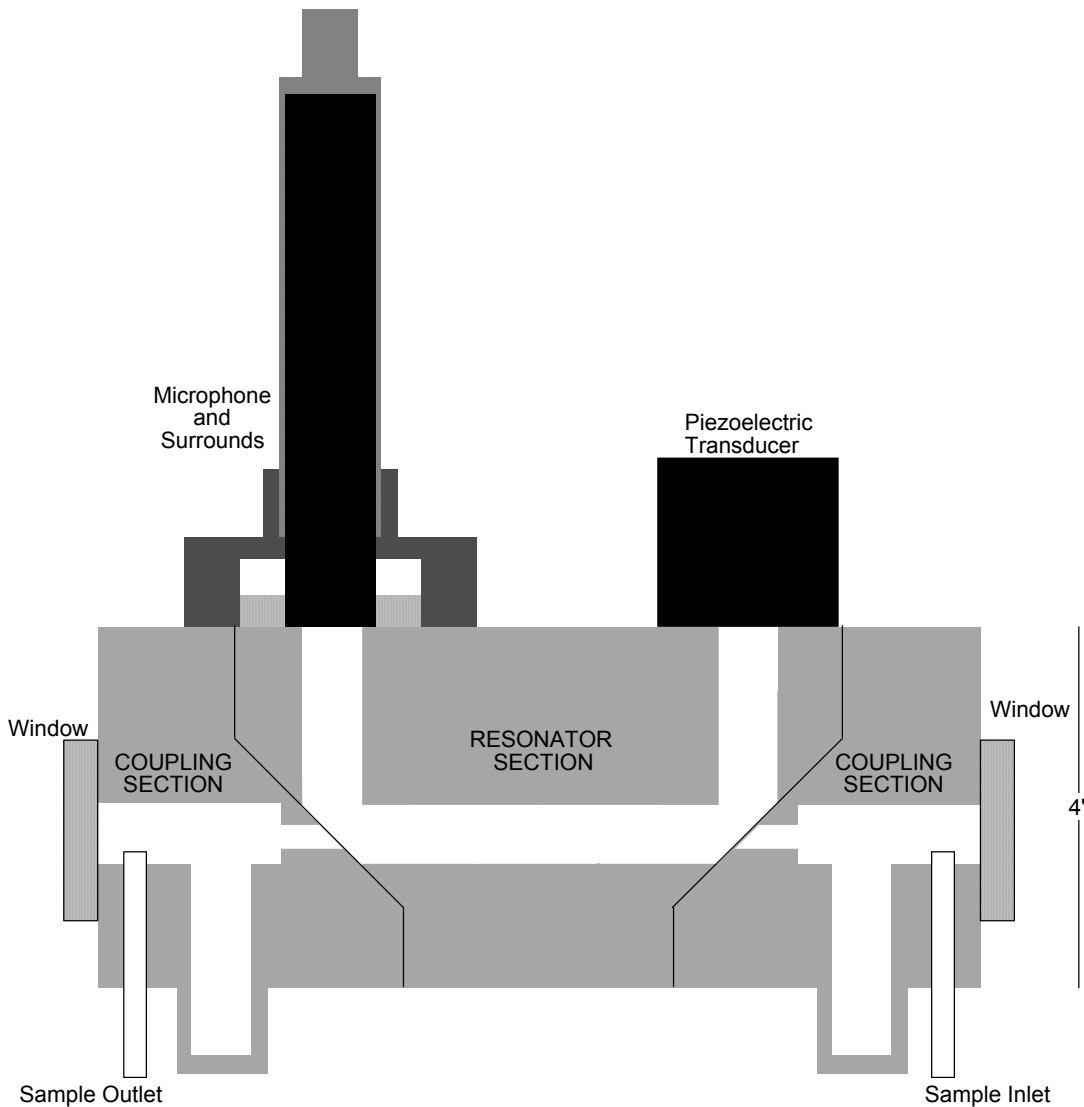


Figure 4-1. Schematic of the new photoacoustic instrument.

4.2 Evaluation of the PA for DoD Sources

The results of the SERDP evaluation of the PA are detailed in a draft paper (Appendix 2) and in previous SERDP annual reports. Briefly during the SERDP program, the SERDP team employed the PA to measure black carbon in the following studies:

- Emissions from aircraft ground support vehicles (Appendix 2)
- Evaluation of diesel soot filters for removal of PM (Section 7)
- Evaluation of the effect of JP8 and diesel fuels on PM emissions (Section 8)
- Emissions from aircraft (Section 6)

The PA performed well for all of the DoD sources, including aircraft (Figure 3-2 and 3-3). Figure 3-2 demonstrates that the PA can perform in challenging environments like a flightline, where aircraft are tethered for testing and the instruments are located within ten

feet of the engine. In Figure 3-3, the PA and other instruments were located just outside of an engine test cell. Figure 3-4 shows an example of how the PA signal can provide emissions information for transient events. It illustrates how BC concentration varies during three City Bus Driving (CBD) cycles performed at California Air Resources Laboratory Heavy Duty Test Facility. Note that the BC shows a similar trend to PM mass as measured by a DustTrack (TSI, Inc.). In contrast, an impactor or filter sample would only provide an average emission concentration. The DustTrak measures PM using light scattering. Its measurements are uncalibrated, but they provide an estimate of total PM mass. Moosmüller et al. (2001b) showed that DustTrack measurements correlated well with total PM mass from a diesel engine measured using filter collection methods according to the Code of Federal Regulations. However, they also observed some sensitivity of the DustTrack to aerosol composition and size.

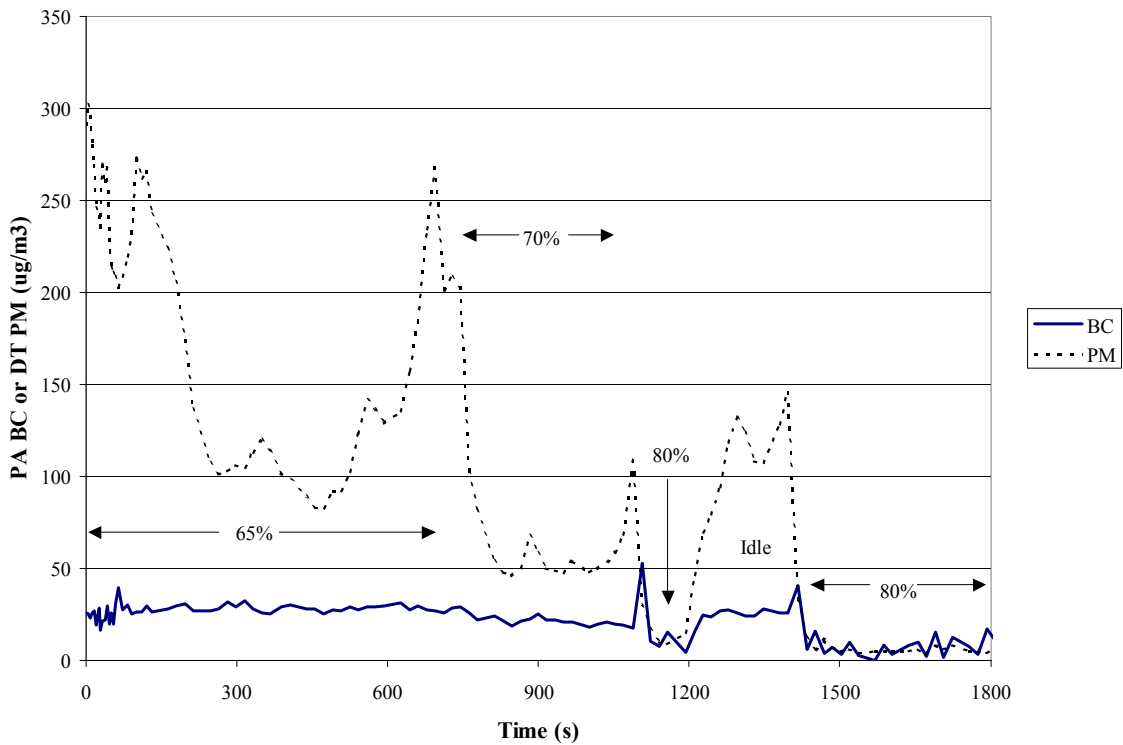


Figure 4-2. PA and DustTrack signal for a F-404-GE-400, aircraft engine, at several different engine settings, noted as percentages in the figure. These measurements were collected on the flightline at North Island Naval Air Station. PM concentration was measured using a DustTrack.

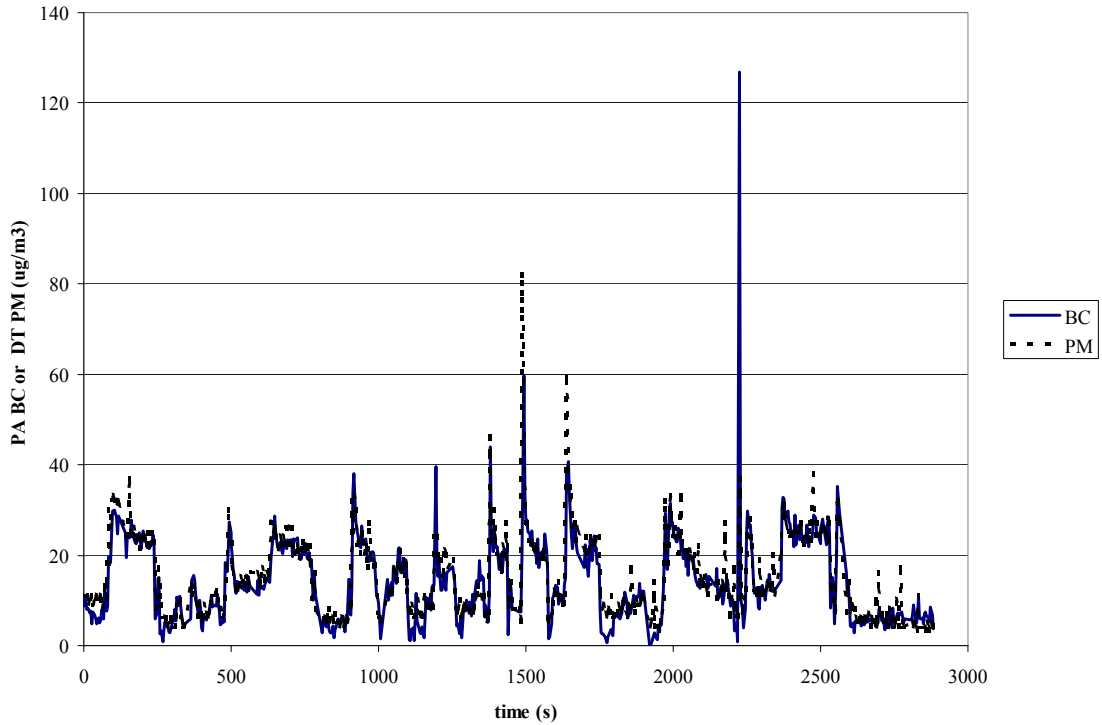


Figure 4-3. PA and DustTrack results for a TF-34 engine at the aircraft intermediate maintenance department, North Island Naval Air Station. PM concentration was measured using a DustTrack.

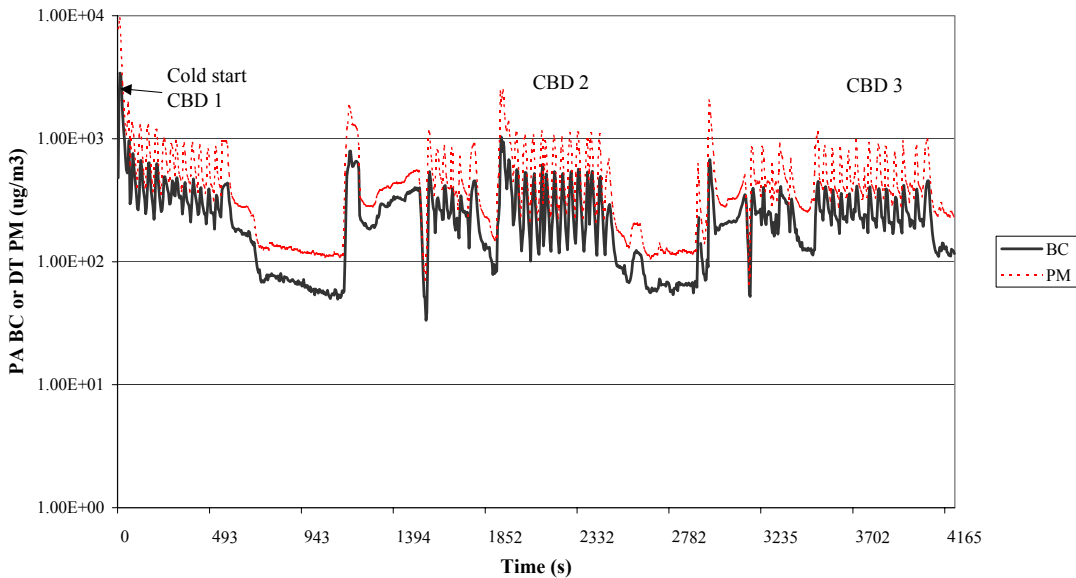


Figure 4-4. PA signal during three CBD driving cycles.

For the studies of aircraft ground support equipment, diesel/JP8 fuels, and aircraft, corresponding impactor measurements of elemental carbon (EC) were collected. Figure

4-5 shows the correlation of black carbon measurements with elemental carbon measurements by the thermal optical reflectance method for aircraft ground support equipment and aircraft. The EC data was obtained from the sum of all data from the stages of the MOUDI sampler. Note the high degree of correlation and the slope of the line for aircraft and aircraft ground support equipment. The black carbon measurement is evidently very close to the elemental carbon measurement when the efficiency factor of 5 m²/g is used to go between the light absorption measurement at 1047 nm laser wavelength and the black carbon mass concentration. This factor was indicated by our previous SERDP work with an older photoacoustic instrument, and provides confirmation that the new instrument is performing satisfactorily.

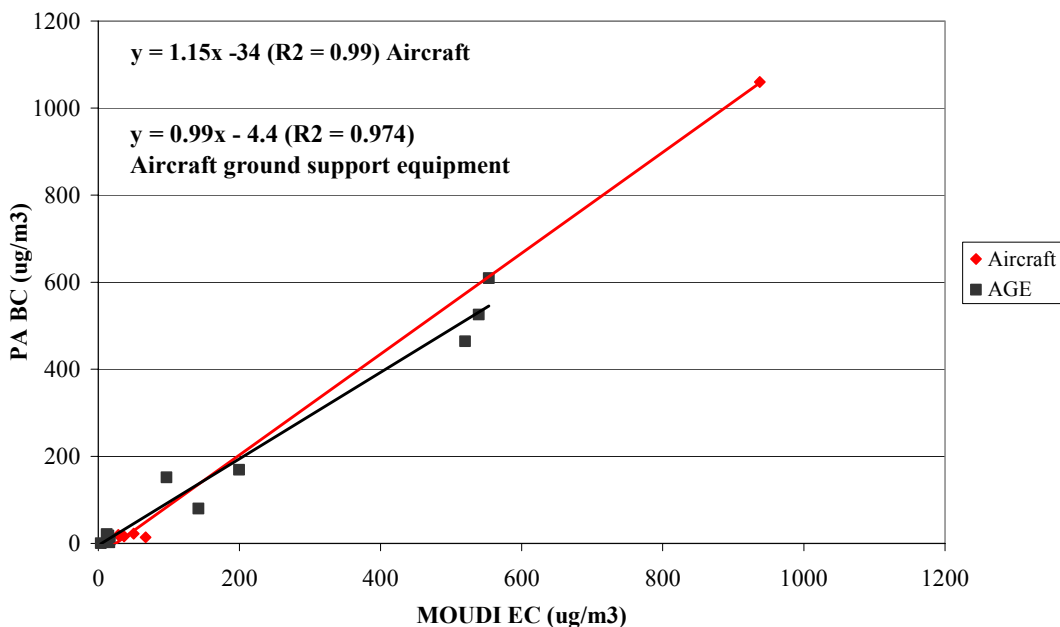


Figure 4-5. Comparison of MOUDI EC and PA results for aircraft and aircraft ground support equipment.

4.3 Summary

The PA performed well for all DoD sources tested during this SERDP program, and its results correlated highly with TOR measures of elemental carbon from impactor samples. In addition, it offers several advantages over traditional measurements including rapid response, rapid analysis of results, relative insensitivity to humidity, and a large dynamic range. The User Guide (Appendix 1) provides a more complete comparison of the PA with other methods.

DoD users should look to the PA for many of their black carbon mass concentration needs. It is useful for collecting ambient measurements at fixed locations, such as in air quality measurements at military bases. It is useful for profiling sources at DoD locations, as demonstrated in this SERDP program, and it is also useful for instrumented

vehicles to measure emissions from the vehicle, other vehicles, or as a function of time and space. In related work, it has also been utilized successfully to measure black carbon aloft from meteorological aircraft.

References

- Arnott, W. P., H. Moosmüller, C. F. Rogers, T. Jin and R. Bruch (1999). "Photoacoustic spectrometer for measuring light absorption by aerosols: Instrument description." *Atmospheric Environment* 33: 2845-2852.
- Arnott, W. P., H. Moosmüller, P. J. Sheridan, J. A. Ogren, R. Raspet, W. V. Slaton, J. L. Hand, S. M. Kreidenweis and J. L. Collett (2003). Photoacoustic and filter-based ambient aerosol light absorption measurements: Instrument comparisons and the role of relative humidity. *Journal of Geophysical Research* D1: 4034.
- Arnott, W. P., H. Moosmüller and J. W. Walker (2000). Nitrogen dioxide and kerosene-flame soot calibration of photoacoustic instruments for measurement of light absorption by aerosols. *Review of Scientific Instruments* 71(7): 4545-4552.
- Chow, J. C., J. G. Watson, L. C. Pritchett, W. R. Pierson, C. A. Frazier and R. G. Purcell (1993). The DRI thermal/optical reflectance carbon analysis system: Description, evaluation and applications in U.S. air quality studies. *Atmospheric Environment* 27A: 1185-1201.
- Moosmüller H., W.P. Arnott, C.F. Rogers (1997). Methods for Real Time *In Situ* Measurements of Aerosol Light Absorption. *J. Air & Waste Manage. Assoc.*, **47**, 157-166.
- Moosmüller H., W.P. Arnott, C.F. Rogers, J.C. Chow, and C.A. Frazier (1998). Photoacoustic and Filter Measurements Related to Aerosol Light Absorption During the Northern Front Range Air Quality Study (Colorado 1996/1997). *J. Geophys. Res.*, **103**, 28,149-28,157.
- Moosmüller, H., W. P. Arnott, C. F. Rogers, J. L. Bowen, J. A. Gillies, W. R. Pierson, J. F. Collins, T. D. Durbin and J. M. Norbeck (2001a). Time resolved characterization of particulate emission: 2. Instruments for elemental and organic carbon measurements. *Environmental Science & Technology* 35: 1935-1942.
- Moosmüller H.; Arnott W.P.; Rogers C.F.; Bowen J.L.; Gillies J.A.; Pierson W.R.; Collins J.F.; Durbin T.D.; Norbeck J.M. (2001b) Time Resolved Characterization of Diesel Particulate Emissions 1. Instruments for Particle Mass Measurements; *Environ. Sci. Technol.* 35, 781-787.

SECTION 5: DEVELOPMENT AND EVALUATION OF THE PHOTOELECTRIC AEROSOL SENSOR

The measurement of particle-bound polycyclic aromatic hydrocarbons is a challenging, time consuming, and expensive process. The photoelectric aerosol sensor (PAS) is designed to measure particle-bound PAHs rapidly offers several potential benefits including cost savings, rapid-response time, and reduced analysis time.

5.1 Description of the Photoelectric Aerosol Sensor

Details about the PAS can be found in EPA (1997) and Burtscher (1992). Figure 5-1 shows a schematic of the PAS. Briefly, an aerosol sample passes through the PAS instrument at a constant flow of 2 l/min. As the sample passes through the eximer lamp ionization region, the particle-bound PAH molecules are ionized, and the electron that is stripped from the PAH molecule has a probability of escaping the particle that is dependent on the particle size and composition. The photon energy of the lamp is chosen so that no gas-phase molecules are ionized. The photoelectric ionization and subsequent electron loss leaves the particle with a net positive charge that is detected by measuring the charge that collects on an isolated filter element. Because this charge is exceedingly small, an electrometer is used to detect the change in potential from the filter element to ground. The change in potential can be attributed to a charge and is integrated over time to give the photoelectric current (in femto or pico amps). This current should be proportional to a specific loading of PAH on a particle and related to a specific PAH mass/volume of surrounding gas.

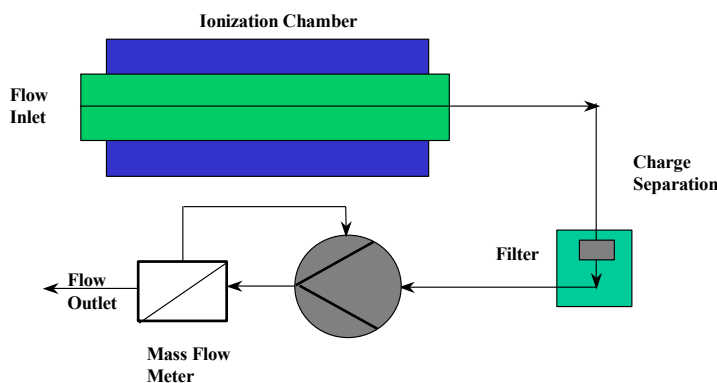


Figure 5-1. Schematic of the PAS.

The PAS was originally calibrated to fifteen individual PAHs (called the Siegmann sum) from several sources, with a universal conversion factor of $1\text{-}3 \mu\text{g}/\text{m}^3 \text{ picoamp}^{-1}$ (Wilson and Barbour, 1994; Wilson et al., 1991; EPA, 1997). Because PAHs are such a complex

mix of vapor and particle-phase compounds, the PAS responds differently to each type of source, and calibration factors can vary widely. Therefore, the PAS requires a calibration curve for each source in order to provide any quantitative results. Without an appropriate calibration curve, the PAS will only give you a relative measure of particle-bound PAH levels.

5.2 Evaluation of the PAS for DoD Sources

The results of the SERDP evaluation of the PAS are detailed in a draft paper (Appendix 2) and in previous SERDP annual reports. Briefly during the SERDP program, the SERDP team employed the PAS to measure particle-bound PAHs in the following studies:

- Emissions from aircraft ground support vehicles (Appendix 2)
- Evaluation of diesel PM filters (described in Section 7)
- Evaluation of the effect of JP8 and diesel fuels on PM emissions (Section 9)
- Emissions from aircraft (Section 6)

Figure 5-2 illustrates how the PAS signal varies during three City Bus Driving (CBD) cycles performed at California Air Resources Laboratory Heavy Duty Test Facility. Note that the PAS shows a similar trend to PM mass as measured by a DustTrack (TSI, Inc.). In contrast, an impactor or filter sample would only provide an average emission concentration for this entire time period.

Figures 5-3 and 5-4 compare PAS to denuder measurements of particle-bound PAHs for military vehicles and aircraft. The PAH sampling and analysis methods are described in Appendix 3. The PAS results correlate reasonably well with filter measurements for military vehicles ($R^2 = 0.753$) and better for military aircraft ($R^2=0.99$), but the aircraft correlation is heavily weighted by one data point. For aircraft ground support equipment, it is interesting to note that the PAS correlates better with black carbon concentration ($R^2=0.97$) than with particle-bound PAH concentrations. Other researchers report similar results for diesel emissions (Baltensperger et al., 2001; Matter et al., 1999).

During the evaluation of the PAS for DoD sources, the SERDP team learned that the PAS has some limitations. For example, the PAS periodically gave erratic negative responses, which were reduced by the use of a heated line (300 F) for source samples. The negative responses tended to occur during conditions of high emissions, such as an increase in engine load. In addition, the PAS response varied with temperature; therefore the PAS inlet must be maintained at a constant temperature. Finally, the response of each PAS instrument varies, so a calibration curve for each instrument should be developed for each source.

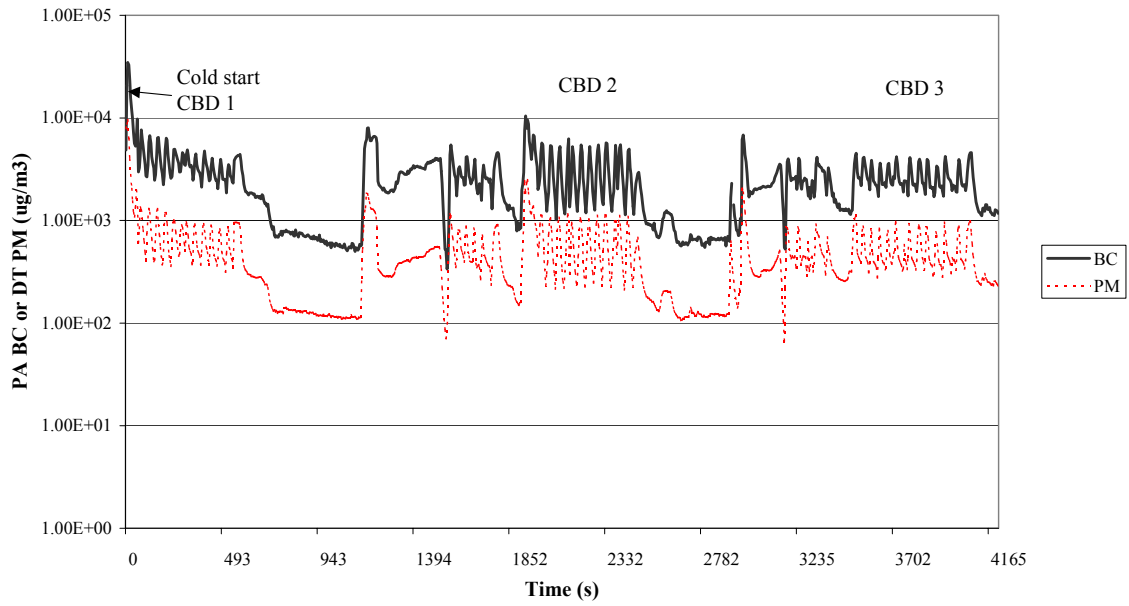


Figure 5-2. PAS signal during three CBD driving cycles.

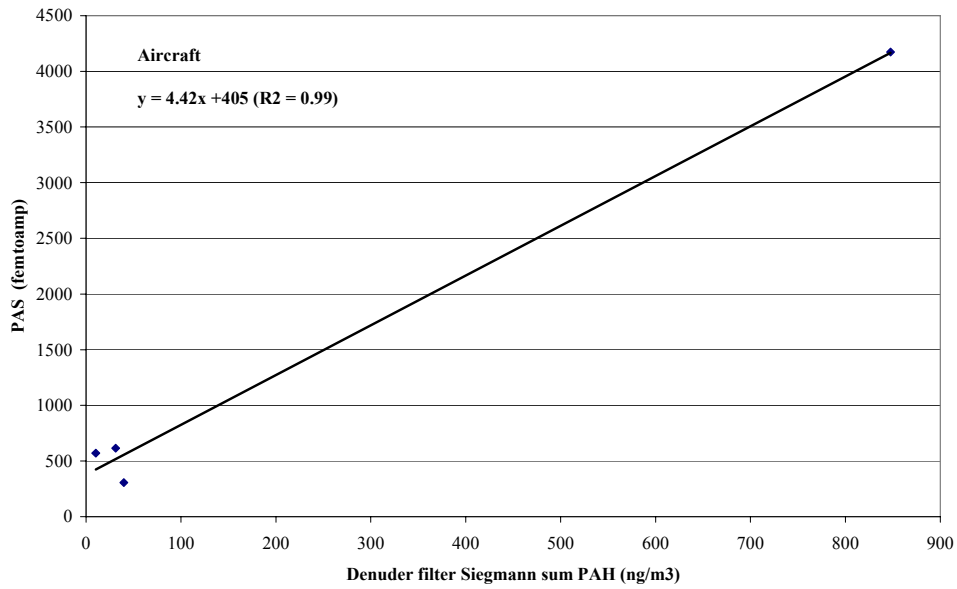


Figure 5-3. Correlation between the PAS signal and particle-bound PAHs as measured with a Gundel denuder for four military aircraft.

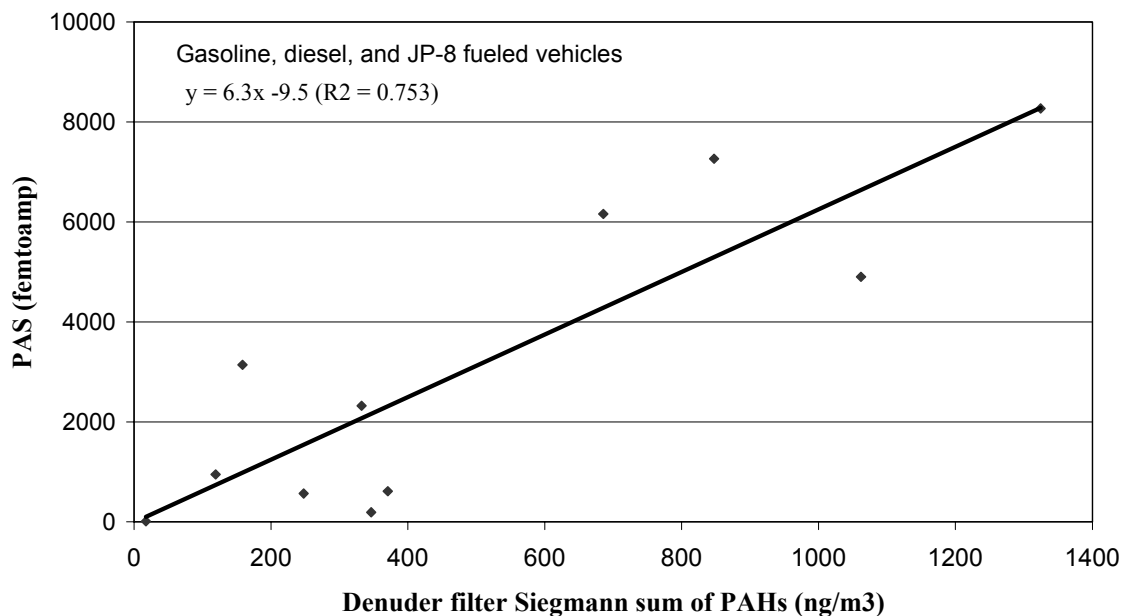


Figure 5-4. Correlation between the PAS signal and particle-bound PAHs measured with a Gundel denuder for military aircraft ground support equipment.

5.3 Summary

The PAS provided a qualitative measure of particle-bound PAH concentration for all DoD sources tested during this SERDP program. Its results correlated somewhat with traditional measurements of particle-bound PAH for all sources, and for some sources the PAS signal correlated well with black carbon measurements. The PAS also periodically produces erratic negative signals although this was reduced with the use of a heated inlet. PAS measurements can be less expensive than traditional filter or denuder measurements, and they provide information about transient conditions. However, calibration of the PAS is challenging, and without calibration the PAS provides only qualitative results. The User Guide (Appendix 1) provides a more complete comparison of the PAS with other methods.

The PAS is a good choice when a relative measure of particle-bound PAHs is desired or when transient conditions are studied. For example, it would be useful for the preliminary evaluation of a control device, for screening sources for further analysis, or for studying transient conditions. The PAS is a relatively new instrument, and with additional study and independent calibration it may produce more valuable results.

References

Baltensperger, U. E. Weingartner, H. Burtscher, J. Keskiönen, Dynamic mass and surface area measurements. In: P.A. Baron and K. Willeke (eds.) *Aerosol Measurement*, 2001 New York:Wiley, pp. 387-418.

Burtscher, H. Measurement and Characteristics of Combustion Aerosols with Special Consideration of Photoelectric Charging and Charging by Flame Ions; *J. Aerosol Sci.*, **1992**, 23 (6) 549-595.

EPA. *Field and Laboratory Analyses of a Real-Time PAH Analyzer*, EPA/600/R-97/034; EPA Office of Research and Development, **1997**.

Matter U., H.C. Siegmann, H. Burtscher, Dynamic Field Measurements of Submicron Particles from Diesel Engines, *Environ. Sci. Technol.* **1999**, 33 1946-1952.

Wilson N.K., Barbour, R.K., Evaluation of a real-time monitor for fine particle-bound PAH in air, *Polycyclic Aromatic Compounds*, **1994**, 5, 167-174.

Wilson N.K., Chuang, J.C., MR. Sampling polycyclic aromatic hydrocarbons and related semivolatile organic compounds in indoor air. *Indoor Air*, **1991**, 4 513-512.

SECTION 6: AIRCRAFT EMISSIONS AT NORTH ISLAND NAVAL AIR STATION

6.1 Executive Summary

The goal of this study was to evaluate the performance of three real-time instruments, the photoacoustic analyzer (PA), the photoelectric aerosol sensor (PAS), and the DustTrack (DT), for characterizing particulate matter (PM) emissions from jet exhaust and to provide supporting PM characterization results using more traditional methods. The PA measures black carbon, which is closely related to elemental carbon and soot. The PAS is designed to measure particle-bound polycyclic aromatic hydrocarbons (PAHs), and the DT measures particle mass concentration. The SERDP team collected PM emissions at two locations at the North Island Naval Air Station, the flightline and the aircraft intermediate maintenance depot (AIMD). At the flightline, F/A-18C aircraft equipped with F-404-GE-400 engines undergo maintenance testing, and emissions were collected directly from the engine exhaust. The SERDP team deployed a portable pallet containing a compact dilution system, a PA, PAS, and DT at the flightline. At AIMD, aircraft engines undergo testing after being overhauled, and two types of engines were tested, the TF-34-GE-400 and the T-700-GE-401. PM emissions were collected from an engine test cell (TF-34-GE-400) or a test pad (T-700-FE-401). In addition to the real-time instruments at AIMD, the SERDP team deployed a more comprehensive set of measurement techniques including: a microorifice uniform deposit impactor (MOUDI) to provide PM mass, elemental and organic carbon content, and individual particle-bound PAH concentrations; a Gundel denuder sampler to provide gas- and particle-phase concentration of individual PAHs; a scanning mobility particle sizer to provide particle size distributions; and a canister sampler to provide CO, CO₂, and CH₄ concentrations. At both locations, North Island's Aircraft Environmental Support Office provided assistance in developing the testing plan and provided additional particle size data.

In general, the real-time instruments performed well at AIMD and at the flightline. For the most part, the PA signals tracked the changes in the TF-34 and T-700 engine settings. The PA provided little information on the F-404 engine because the exhaust appeared to contain little black carbon. The PA's signal also correlated well with MOUDI elemental carbon results. Although the data were heavily weighted by the T-700 emissions, the slope of the regression line was approximately one, nearly the same as a similar comparison of PA results and MOUDI elemental carbon for military vehicles. In addition, on average the PA and DT results correlated well, and the real-time results show that the instruments respond to the same variations in engine setting.

The PAS instrument was designed to measure particle-phase PAHs in real time, which has important health and exposure applications. Because traditional measurements of PAHs are expensive and time consuming, a real-time PAH detector would be a valuable tool. During much of the testing, the PAS signal tracked the engine settings for the TF-34, T-700, and F-404 engines. However, the PAS did not always respond as expected. For example, during an increase in engine setting the PAS signal sometimes decreased

while all other real-time signals increased. In studies of other types of combustion sources, the PAS tended to track the PA and PAS signals. However, these periodic unexpected signals have been observed during other source tests and tend to occur during periods of high emissions. The average PAS results in femptoamps show a reasonable agreement with the Gundel's particle-phase PAH concentration (slope of 4.4 femptoamps/ng PAH) although the correlation was heavily weighted by the T-700 emissions. The correlation between the PAS and Gundel results also differs from a similar correlation for military vehicles (6.5 femptoamps/ng PAH) and from results reported by others (1-3 femptoamps/ng PAH). Overall, the PAS results indicate that further evaluation is needed.

The DT is a relatively inexpensive instrument that provides an empirical measure of the mass concentrations of particles in the approximate diameter range of 0.1 to a few micrometers. The DT can be calibrated by comparison to filter samples taken from a given aerosol source. During these experiments, the DT responded reasonably to most of the source variations, with a few exceptions, and it tracked the PA response well.

The secondary goal of characterizing PM emissions from aircraft also provided a number of findings. For the TF-34, T-700, and F404 engines, low power settings generally produced greater mass concentrations of PM. For the T-700 and F404 studies for which undiluted exhaust was sampled, the measured mass emissions ranged from about 100 $\mu\text{g}/\text{m}^3$ to about 4 $\mu\text{g}/\text{m}^3$ (corrected for dilution). For all engines tested, there is evidence that power-setting changes cause brief emissions spikes.

6.2 Objectives

Following earlier measurement and instrument evaluations conducted on aircraft and aircraft ground support vehicles at Hill Air Force Base, near Ogden, Utah, in 1999 and 2000 (Rogers, et al., 2003, Kelly et al., 2003), a new experiment was conducted at the North Island Navy Base, San Diego, California, in January, 2002. The North Island measurements and instrument evaluations focused on Navy jet engine exhaust emissions, both from engine maintenance test cells and from tethered aircraft. North Island's Aircraft Environmental Support Office (AESO) assisted with the development of the testing plan, assisted with designing sampling systems, collaborated with the SERDP team during the tests, and collected complimentary data.

Given this new category of DoD combustion source, the three main objectives of the North Island experiment were:

1. To evaluate the performance of the photoelectric aerosol sensor (PAS 2000, Ecochem Inc.) in providing real-time measurements of particle-phase PAH compounds emitted from a selection of jet engines at North Island;
2. To evaluate the performance of the photoacoustic sensor (PA) in providing real-time measurements of light-absorbing particles (generally black carbon, or "soot") emitted by a selection of jet engines at North Island;

3. To evaluate the performance of the DustTrak (DT, TSI Inc.) particle mass monitor in providing real-time measurements of exhaust particle mass concentrations;

Objective #3 was added to Objectives #1 and #2 following encouraging experience with the DustTrak, a portable, robust commercial device.

Measurements conducted in support of the main objectives were as follows:

- Phase-resolved PAH data was obtained from a non-real time instrument, the Gundel denuder sampler, in support of Objective #1 (presented in Appendix 4);
- Non-real time, size-resolved total particulate mass, carbon species mass, particulate sulfate mass, and PAH compound mass was obtained in support of all three objectives, using a cascade impactor (PAH data presented in Appendix 4);
- Near-real time particulate size distribution data was in diagnostic support of all three objectives, using a Scanning Mobility Particle Sizer (SMPS).

6.3 Experimental Approach

The experiment objectives were addressed at two North Island sites. With the cooperation of the North Island staff, the SERDP project instruments were deployed at the North Island Aircraft Intermediate Maintenance Department (AIMD), a facility in which newly overhauled jet engines are tested at varying power levels before they are certified for flight use. Measurements were also taken at a “flightline” site, where measurements were taken directly from the exhausts of tethered aircraft. The AIMD tests utilized turbofan TF-34-GE-400 engines, found in S-3A, Viking anti-submarine, and KS-3A tanker aircraft, as well as one turboshaft T-700-GE-401 engine, found in Seahawk, Super Cobra, and Jayhawk helicopters. The flightline site tests utilized F404-GE-400 engines, found in F-18 aircraft. All engines burned JP-5 aviation fuel; for emissions estimates, JP-5 is regarded to contain 86.9% carbon by weight (Paetow, 2003).

The two sites allowed deployment of a full complement of instruments and a range of tests that would not have been possible had only one or the other site been available. The AIMD site allowed an investigation that was somewhat similar to the previous efforts in this project. The experimental instruments were set up in a fixed arrangement, sampling from a fixed test facility, analogous to the SERDP dynamometer tests reported by Kelly et al., (2003). The AIMD site was therefore compatible with the use of the non-real-time devices like the Gundel denuder and the MOUDI cascade impactor. These instruments are also sensitive to mechanical disturbances and require various kinds of support structures. All of the project objectives listed above were addressed at the AIMD site

The flightline site required that instruments be mounted on a rolling pallet that could be deployed rapidly out onto the tarmac, and just as rapidly rolled back in order to avoid any interference with the Navy’s ongoing operations. This situation may more realistically simulate the rigorous requirements of measurements at some kinds of DoD facilities,

where the instruments must operate robustly despite motions and extreme noise environments, and must provide measurements in real time. Therefore, the instruments deployed at the flightline included only the real-time and near-real-time devices. The main project objectives were addressed at the flightline site, in addition to showing that a rapidly portable instrument pallet could successfully be designed and used.

Table 6-1 shows the instruments deployed at each site.

Table 6-1. Instruments deployed at AIMD and flightline sites.

Instrument	Purpose	Reference	Site
PAS 2000	Real-time PAH detection and quantification	Burtscher , 1992	Flightline and AIMD
Photoacoustic Spectrometer	Real-time detection and quantification of light-absorbing particles	Arnott et al., 2000	Flightline and AIMD
DustTrack	Real-time estimation of particulate mass concentration	Manufacturer’s web site, www.tsi.com ; Moosmuller et al., 2001.	Flightline and AIMD
Scanning Mobility Particle Sizer (SMPS, TSI, Inc.)	Near-real time measurement of particle size distributions	Wang and Flagan, 1990	Flightline and AIMD
Gundel Denuder Sampler	Bulk measurement of PAH compounds in both gas and condensed phases	Gundel et al. 1995	AIMD only
MOUDI (Microorifice Uniform Deposit Impactor, MSP Corp.)	Bulk measurement of particulate mass and carbon	Marple, et al., 1991	AIMD only
Teflon and quartz filter sampler	Bulk measurement of particle-phase mass, carbon species, ions	Built for project	AIMD only
Canister sampler	Measurement of CO ₂ , CO, CH ₄ integrated over each test run	Built for project	AIMD only

Operating principles for the PA and PAS are described in Section 4 (PA) and Section 5 (PAS) of this report, and operating principles for the other instruments are documented in the references listed in Table 6-1.

6.4 AIMD Experiments

Table 6-2 details the five experimental runs conducted at the AIMD site.

Table 6-2. SERDP experiment conditions at AIMD site.

AIMD				
Run Number	Date and Time (PST)	Jet Engine Type	Eductor Dilution Factor	Comments
1	1/29/02 0851-1003	TF-34-GE-400	3.4: 1	
2	1/29/02 1112-1137	TF-34-GE-400	3.4: 1	Engine same unit as Run #1
3	1/30/02 1308-1412	TF-34-GE-400	3.4:1	Engine new unit
4	1/30/02 1535-1610	Blank	3.4: 1	
5	1/31/02 1248-1336	TF-34-GE-400	3.1: 1	Engine a new unit and test ended early due to engine leaks
6	2/1/02 0808-0900	T-700-GE-401	4.1:1	Moved measurement setup to helicopter test pad

Note 1: Dilution factors are given as dilution air-to-sample air in volumetric ratios.

The first five AIMD site experiments utilized an existing discharge (“augmentor”) chamber into which the test engine’s exhaust is directed. This chamber dilutes and cools the exhaust with an unquantified amount of entrained ambient air, and the SERDP team’s sampling port was located after this primary dilution. The chamber consisted of a large horizontal steel cylinder, approximately three meters in diameter and six meters in length. Engines undergoing tests are mounted at one end of the chamber, and the other end is connected to a vertical tunnel that directs the exhaust upward and into the atmosphere.

The SERDP tests utilized an existing port located about one meter from the connection between the horizontal and vertical sections of this exhaust discharge system. A stainless steel tube, 0.95 cm in diameter, extended into the augmentor chamber about 59 cm and, by means of a gentle bend, faced into the exhaust stream. The last in the AIMD series of experiments, Run #6, utilized a separate test pad designed for helicopter engine tests. At this site, a dynamometer simulates the load that would normally be applied by a helicopter’s rotors. This helicopter test location did not contain a discharge chamber.

The AIMD aerosol samples were obtained using an eductor-based dilution system (Figure 6-1), which mixes the sample air with dry, clean, particle-free dilution air. Dilution prevents spurious water condensation. Eductors are air-driven devices similar to laboratory aspirators. The sample from the discharge chamber flows through a critical orifice, which controls the sample flow, and into the eductor (Fox Inc. axial mini-eductor) where it is mixed with compressed, dehumidified and particle-free air. The pressure drop between the compressed air and sample causes the sample to flow through the orifice. The flows were checked with a Gilibrator (Gillian Inc.) flow meter and a dry gas meter. Table 6-2 gives the sample dilution ratios for the AIMD experiments.

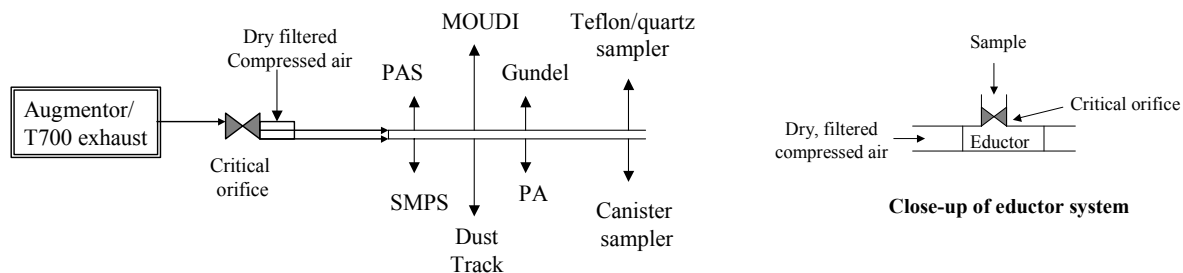


Figure 6-1. AIMD dilution and sampling setup.

For AIMD Runs #1 through #5, the diluted sample flowed from the eductor through a 4.2-meter line (1.2 cm diameter stainless steel tubing) back to a system of tees that distributed flow to the instruments listed in Table 4-1. For Run #5, the MOUDI impactor, Gundel denuder, and Teflon/quartz sample flow was withdrawn directly from the discharge chamber, bypassing the eductor.

For AIMD Run #6, the eductor system was employed with a one-meter stainless steel sample inlet probe that was inserted into the helicopter engine exhaust plume. The sampling instruments were positioned close to the engine test stand, and a 2-meter line conveyed diluted sample from the eductor to the instrument distribution tees. It is possible that this configuration caused some particle deposition in the sample lines.

During each AIMD test, engine power was raised from an idle value to approximately 97% of maximum power, and back down to the idle value in several cycles. Although the North Island engine test operators provided us with summary descriptions of each test, there were variations from one test to another as the operator exercised discretion in evaluating each engine. The engine power settings varied significantly during each run. The cycles over which these variations occurred were not necessarily identical from one run to the next. The non-real-time data from each run are integrated over the entire run, while the real-time data will vary with the changes in power settings.

6.4.1 AIMD Real-Time Data Time Series

Project Objective #1 called for evaluation of the performance of the PAS in providing real-time measurements of particle-phase PAH compounds emitted from the two types of engines that were available at the AIMD site during the experiment period. Objective #2 called for evaluation of the performance of the PA in providing real-time measurements of light-absorbing particles (generally black carbon, or “soot”) emitted by the same engines. Objective #3 called for evaluation of the DustTrak monitor in providing real-time particle mass concentration data. Examination of the real-time data from each of the six AIMD test runs allows the first approach to these objectives. Supporting data from the SMPS instrument at AIMD also assisted in the interpretation of the results.

Run #1

Figure 6-2 presents a time series plot of the real-time data from the PA, DT, and PAS real-time instruments taken during AIMD Run #1.

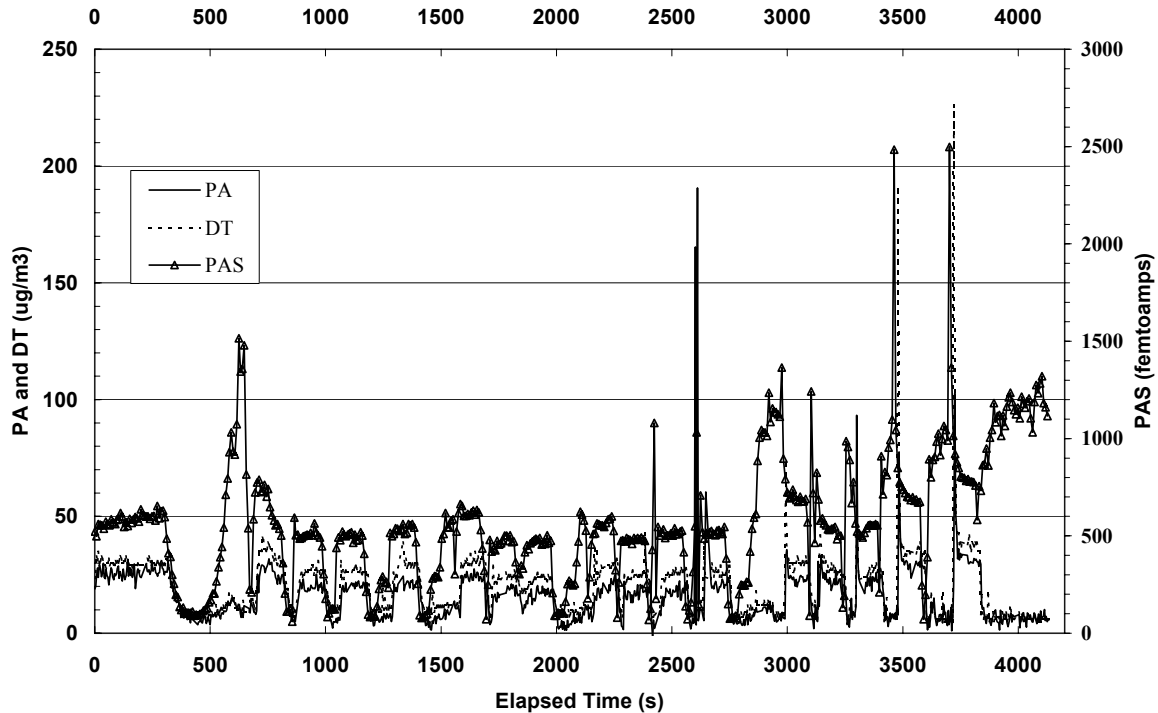


Figure 6-2. AIMD run #1, TF-34 engine, unit #1.

Figure 6-2 displays the PA output in units of light absorbing particle concentrations (left-hand scale), and the DT output is proportional to particle mass concentration (left-hand scale). The PAS data is plotted in units of femptoamps; the instrument's signal is proportional to the concentrations of particle-phase PAH compounds (right-hand scale). This figure demonstrates the instruments' responses to changing exhaust particle concentrations in the augmentor chamber, which appear to vary frequently and on time scales of a few seconds. We hypothesize that the data series varied as engine power settings were changed by the AIMD technicians. Detailed records of the engine power settings were not available, but the AIMD technicians often provided information over a radio link as a courtesy to the SERDP experiment team. These verbal quantifications were recorded in the SERDP field notes. Table 6-3 lists the engine power setting data available for Run #1.

Table 6-3. Engine Power Settings for AIMD Run #1.

Time (PST)	Test Elapsed Time (seconds)	Power Setting
09:28	2016	Idle (64%)
09:33	2320	96%
09:42	2855	80%
09:45	3040	96%
09:49	3279	setting changed but not specified
09:53	3515	96%
09:54	3575	64%
09:55	3650	96%
10:01	3995	64%

In general, the PAS, PA, and DT data traces exhibit maxima and minima at about the same elapsed times. All three instruments generally, but not always, appear to be responding to the same changes in particle concentrations. The low-power data segment following 2016 seconds elapsed time is clearly identifiable, as is the increase in readings after 2320 seconds. Noticeable data spikes follow the power setting notes of 2855 and 3040; our information doesn't indicate whether the power was raised or lowered at these times, but it appears that spikes in the exhaust particle concentrations may have resulted. Similar observations apply to the "power setting changed" note at 3279 seconds, and the "96%" note at 3515 seconds. Power was reduced to 64% at 3575 seconds and raised to 96% at 3650 seconds. These changes seemed to correspond to decreasing data signals at about 3575 seconds, and increasing signals at about 3650 to 3750 seconds. (Response time lags may be due to sample travel time in the inlet lines, and/or to instruments' response-time characteristics.)

The field notes at 2320, 2855, and 3040 seconds elapsed time show that the engine power settings were 96%, 80%, and 96%, respectively. However, the PAS data at these times show different trends than the PA and DT. The PAS readings were about 500, 700, and about 700 femptoamps, respectively, while the PA readings were 16, 9, and 22 $\mu\text{g}/\text{m}^3$. The Dust Track showed trends similar to the PA readings: 24, 12, and 30 $\mu\text{g}/\text{m}^3$.

SMPS measurements provided useful diagnostic information; for example, variations in particle mass concentrations can often be attributed to the presence or absence of larger particles as quantified by size distribution measurements (e.g., Rogers et al., 2003). SMPS particle size distributions were measured at both North Island sites using the Scanning Mobility Particle Sizer (SMPS, Table 6-1). The SMPS requires two to three minutes to complete one size distribution measurement, so the instrument is not a real-time device. At the AIMD site, every effort was made to coordinate the SMPS measurements with the verbal advisories from the engine test cell operators, in order to be able to classify the resulting data in terms of engine power setting. However, the first priority of the test cell operators was to set the power levels according to their protocols, their minute-to-minute judgments regarding getting the data necessary to either certify the engine or else call for additional repairs, and their judgments regarding safety. Therefore the engine power settings were sometimes changed while the SMPS was involved in a measurement cycle. In post-analysis of the SMPS data, we have chosen the SMPS cases that are least subject to uncertainty regarding engine power settings.

Figure 6-3 shows SMPS distribution for AIMD Run #1, for three power settings.

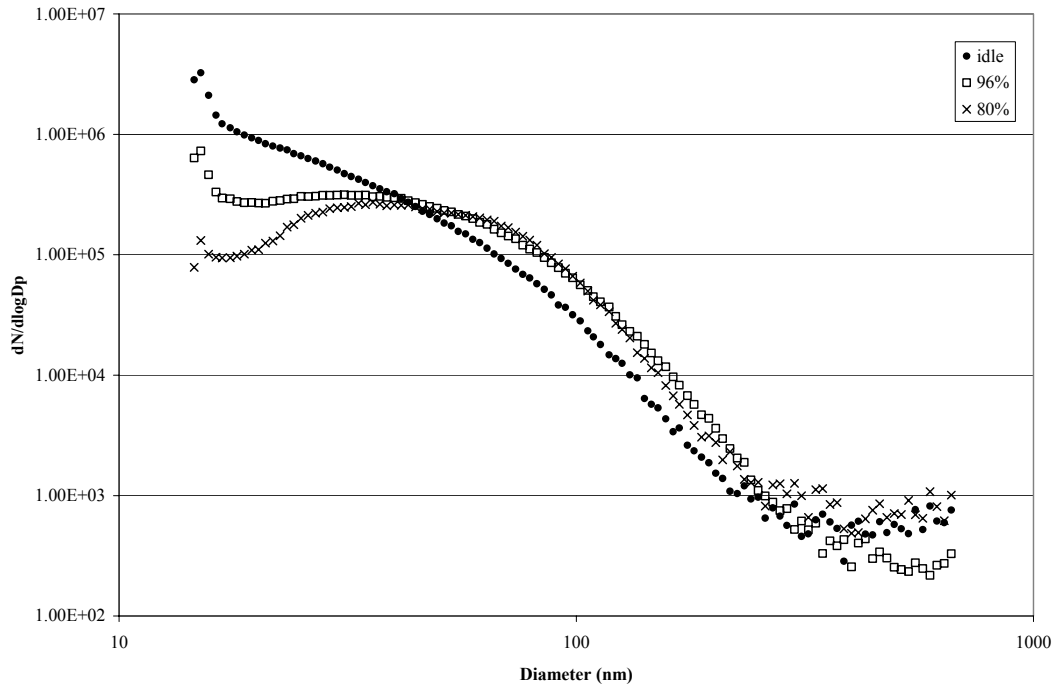


Figure 6-3. AIMD run #1, TF-34, unit #1.

Figure 6-3 shows that the idle distribution exhibits the greatest differential particle concentrations and peaks at or below the small particle detection limit of the SMPS, approximately 10 nanometers (nm). The 80% and 96% power distributions peak at larger particle sizes, in the 20 to 50 nm range. All distributions exhibit a single broad maximum, unlike other types of sources such as heavy-duty diesel engines, which usually exhibit two maxima.

Run #2

Figure 6-4 presents the PAS data from AIMD Run #2. The PA and DustTrak data were lost from this run due to a data acquisition system failure. However, Run #2 provides an opportunity to examine the PAS response in detail.

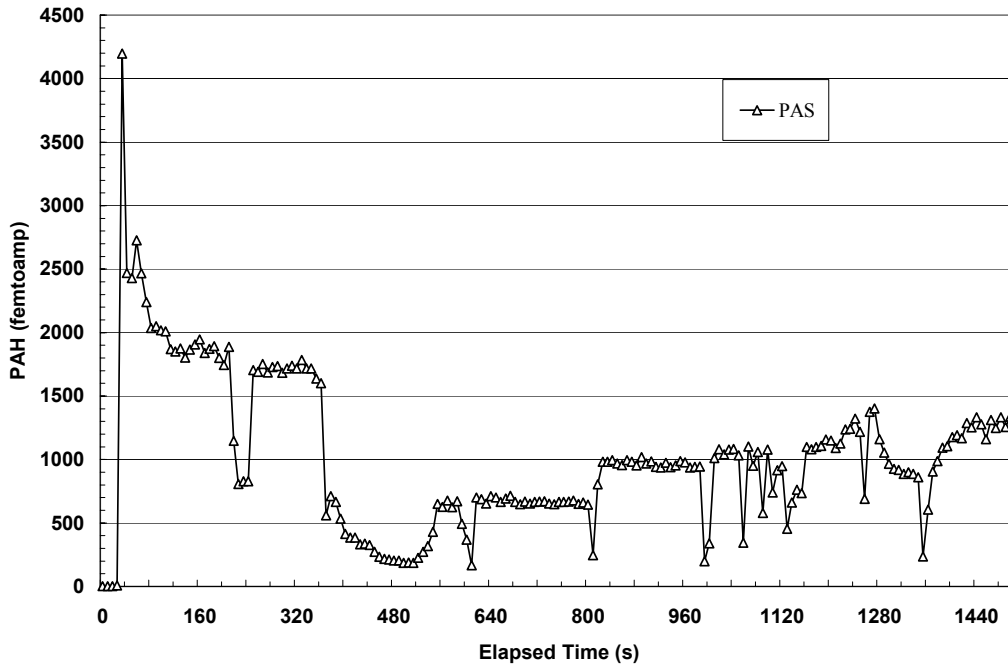


Figure 6-4. AIMD run #2, TF-34, unit #1.

Table 6-4 lists the engine power setting information that is available for Run #2.

Table 6-4. Engine Power Settings for AIMD Run #2.

Time (PST)	Elapsed Time, Seconds	Power Setting
11:14	67	Idle (64%)
11:19	367	96%
11:21	487	80% and decreased to 67%
11:22	547	raise to 96%
11:23	622	96.4%
11:28	922	67%
11:30	1027	raise to 96%
11:30:30	1057	67%
11:32:30	1177	96%
11:34	1282	67%

The signal decrease shown in Figure 6-4 as beginning at about 360 seconds is questionable because the field notes indicate that the engine power setting was 96% at 367 seconds. The relative magnitudes of the PAS signals do not always correspond to the magnitudes of the engine power settings, as given in the field notes, which in turn are transcriptions of the radio information from the AIMD test operators. For example, the field notes indicate that the power setting in the 550-580 second interval was 96%, 67% in the 922-970- second interval, and 96% from 1027-1056 seconds. However, the PAS signal was successively greater for each of these settings, so either the PAH particulate concentrations, or the PAS signal, or both, did not respond in proportion to the power

setting. One would expect the PAS signals for the two 96% power settings to be similar although they differed by almost a factor of two. Under high PM loads, such as during a rapid rise in engine setting, the PAS sometimes exhibits decreasing signals. The SERDP team identified this trend at the flightline and AIMD as well as during separate diesel studies.

The PAS signal increased at about 544 seconds, corresponding to the field note “raise to 96%” at 547 seconds. The signal also increased at about 1000 seconds, apparently corresponding an identical field note at 1027 seconds. A power setting decrease to 67% at 1057 is also reflected in the data as a negative spike. The decrease to 67% at 1282 is also fairly clearly reflected in the PAS data although the signal decrease resembles an exponential decay rather than a sharp drop.

Figure 6-5 displays the SMPS particle size distribution data for two power settings for Run #2.

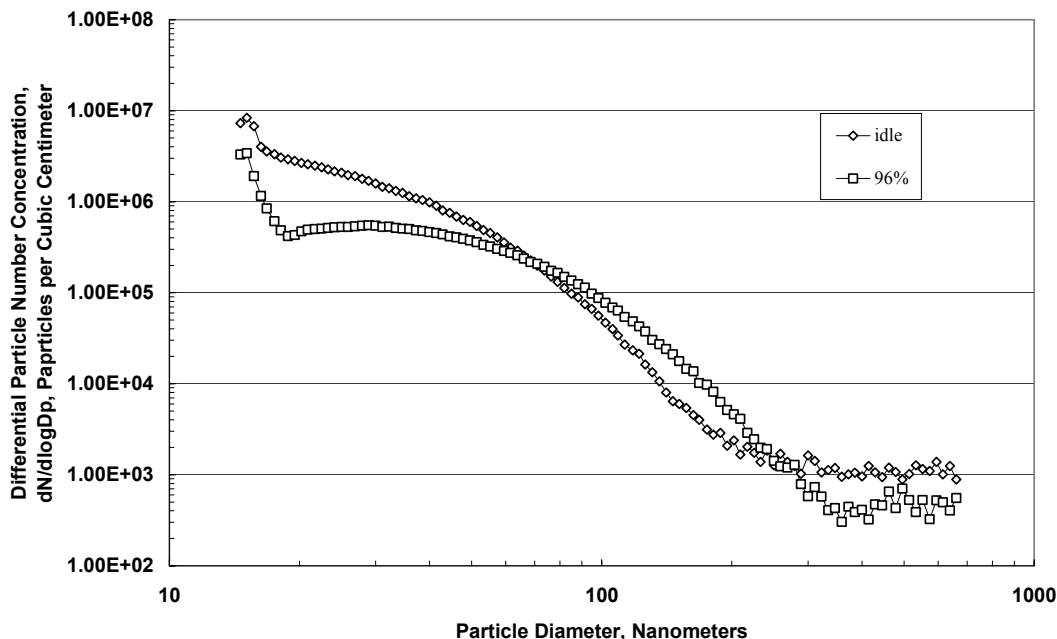


Figure 6-5. Particle size distribution for AIMD run #2, TF-34, unit#1.

The distributions in Figure 6-5 are generally similar to the equivalent power setting cases shown in Figure 6-3. Some similarity to Run #1 is expected, given that the same engine was tested in Run #2. The idle case again peaks near the lower size limit of the data, and the 96% case again exhibits lesser differential particle concentrations at small particle sizes than the idle case. The 96% case may also be bimodal, with a peak below the detection limit of the SMPS and another peak in the 20 to 50 nm range.

Run #3

Figure 6-6 presents the PAS data from AIMD Run #3. This run utilized a second TF-34 engine that replaced the unit used for Runs #1 and #2.

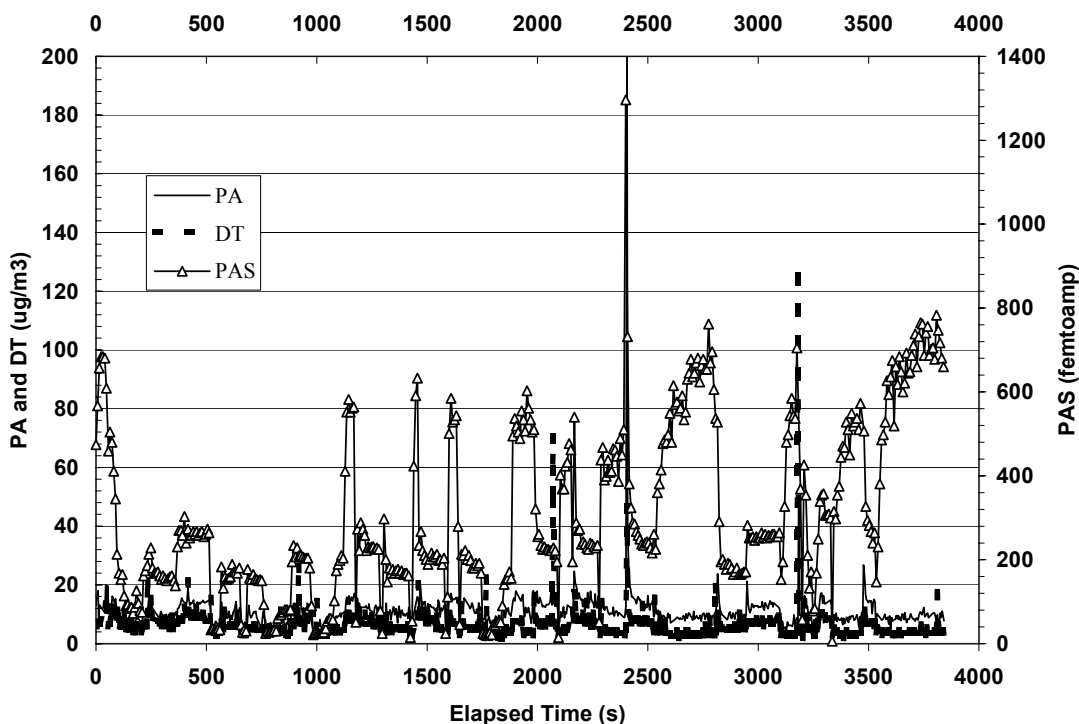


Figure 6-6. AIMD run #3, TF-34 unit #2.

Table 6-5 presents the engine power setting information that is available for Run #3. The field notes also indicate that there was a prolonged period of operation at 80% power corresponding to the note at 13:46:10.

Table 6-5. Engine power settings for AIMD Run #3.

Time (PST)	Elapsed Time, Seconds	Power Setting
13:20	166	80%
13:22:46	332	80%
13:28	646	80%
13:46:10	1736	80%

The PAS data from Run #3 indicate variations that were not reflected in the DT and PA data. Aside from a few spikes, the DT and PA signals seem nearly indicative of constant settings. The field notes are incomplete for this run; it is apparent that a power setting of 80% was frequently employed, but power setting changes were not noted. In previous studies, the PAS signals tended to follow the PA and DT signals. This could be due to the PAS or differences in the size and composition of aircraft exhaust.

Figure 6-7 shows an SMPS distribution obtained for the 80% power setting during Run #3.

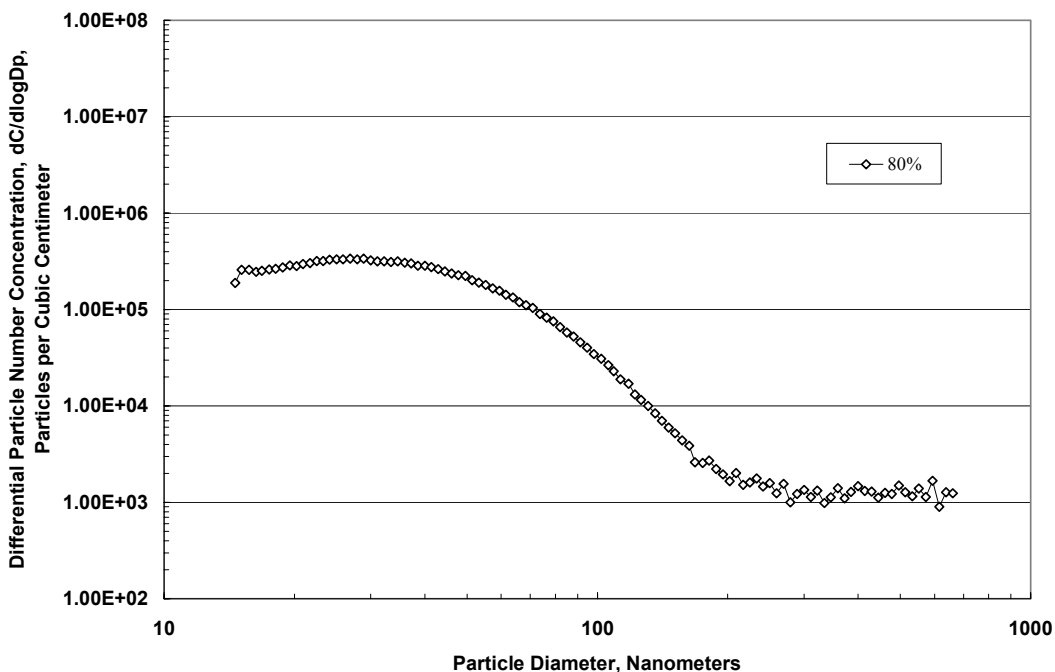


Figure 6-7. Particle size distribution for AIMD run #3, TF-34 unit#2.

The 80% distributions in Figures 6-7 and 6-3 are very similar, with a single broad mode peaking between about 20 and 50 nm. The differential particle concentration values in these two distributions are also very similar; particle mass concentrations estimated on the basis of these two distributions would be of similar magnitudes.

Run #4

Figure 6-8 presents the PAS data from AIMD Run #4. This run was an intentional dynamic blank. All instruments operated according to the procedures applied in Runs 1-3, but no engine exhaust was present in the discharge chamber. Run #4 began with a “HEPA” filter attached to the eductor’s sample inlet. At 1543, eight minutes into the run, the HEPA filter was disconnected and the eductor sample inlet was connected to the usual sampling port on the AIMD discharge chamber, in order to provide a more realistic dynamic blank.

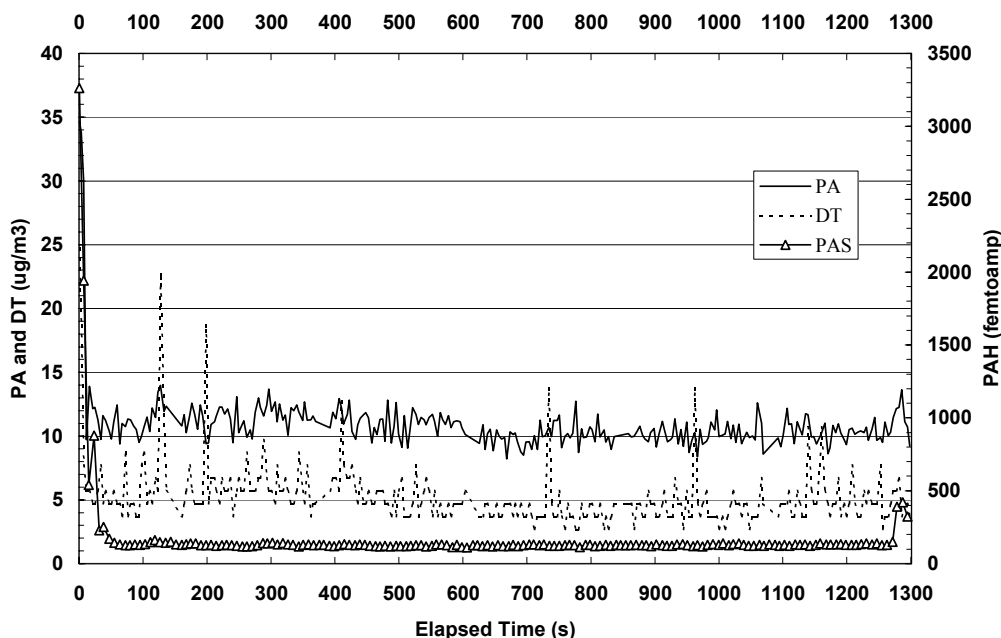


Figure 6-8. Dynamic blank of the augmentor chamber (run#4).

Figure 6-8 shows that the PAS signal remained nearly constant at just above 100 femptoamps for most of the run. The DustTrak and PA signals held mostly constant at about 5 and 10 $\mu\text{g}/\text{m}^3$, respectively. The AIMD augmentor chamber contains at least two sources of vapor and particle-phase material in the absence of jet engine exhaust: (1), vapors that outgas from wall deposits, and possibly condensed-phase material resulting from those vapors; (2) ambient air that enters the chamber under the influence of ambient wind.

Figure 6-9 shows an SMPS distribution obtained during Run #4. These distributions are very similar to the higher-power setting cases shown in Figures 6-5 and 6-7; the differential concentration values shown in Figure 6-9 are only slightly reduced compared to those in Figures 6-5 and 6-7. Run #4 was initiated about one hour and twenty minutes after the end of Run #3, so it is possible that the chamber was not completely flushed, and that significant amounts of the aerosol from Run #3 were still present. Particles in the 10 to 100 nm range have very small gravitational fall speeds and require times longer than a few hours for complete removal. This dynamic blank therefore fulfilled its purpose by demonstrating that each test run in the augmentor chamber would, at its onset, flush out the aerosol remaining from the previous run if that run had occurred only a matter of a few hours previously.

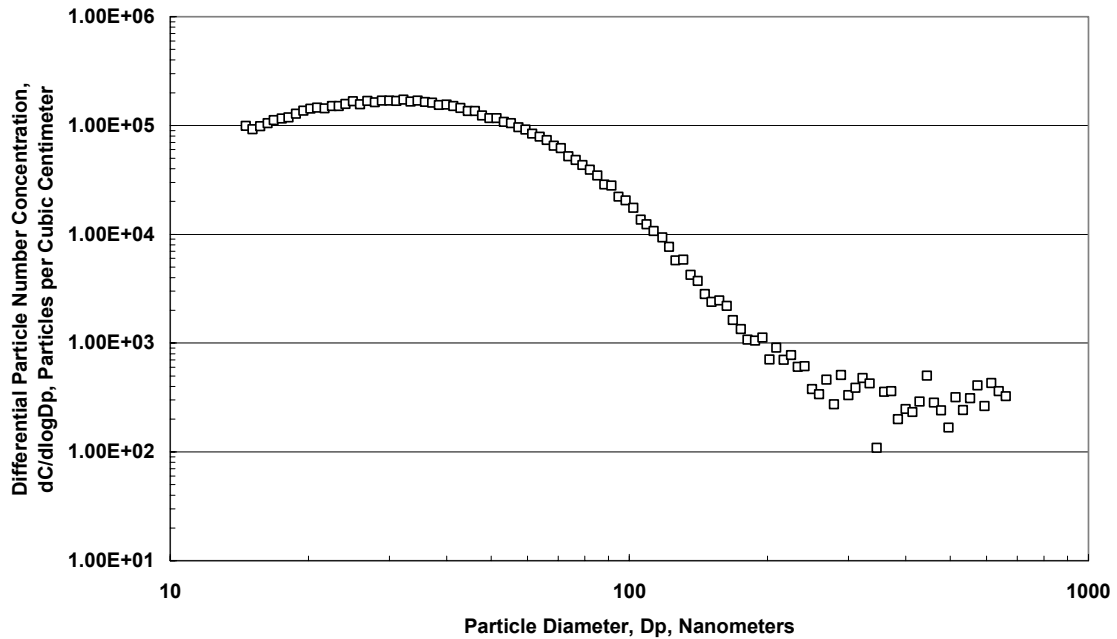


Figure 6-9. Particle size distribution for dynamic blank of augmentor chamber.

Run #5

Figure 6-10 presents the real-time data from AIMD Run #5. This run utilized a TF-34 engine, the third unit involved in this series of tests. The run was terminated at 1336 due to mechanical problems with the engine. For Run #5, the MOUDI, Gundel, and Teflon/quartz samplers were disconnected from the eductor system and connected directly to the sampling port in the augmentor chamber. This change was made in order to eliminate the sample dilution associated with the eductor system for one run.

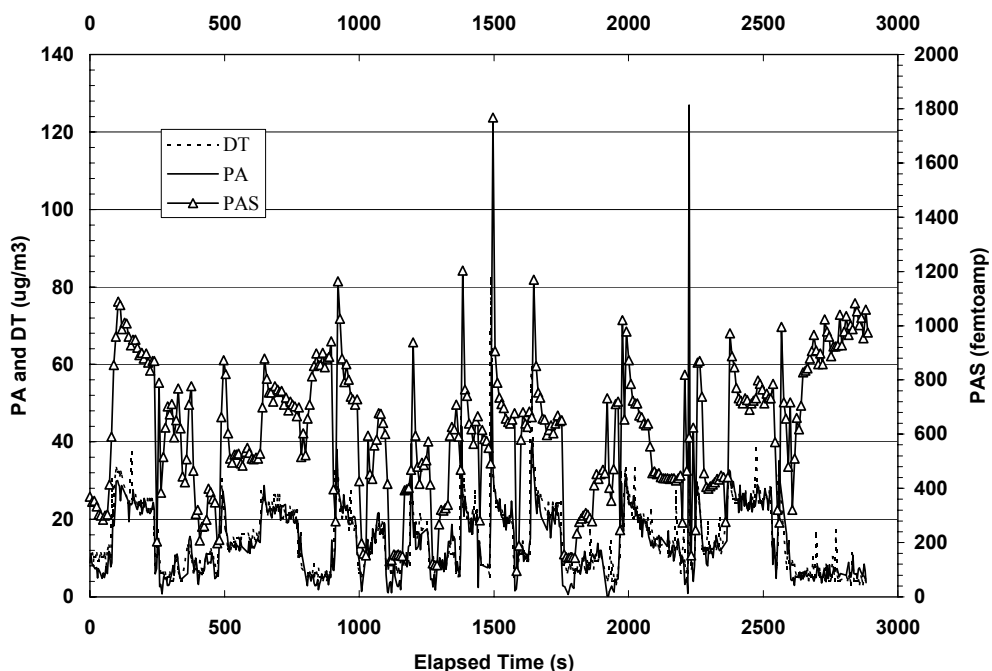


Figure 6-10. AIMD run #5, TF-34 unit #3.

Table 6-6 presents the engine power setting information that is available for Run #5.

Table 6-6. Engine Power Settings for AIMD Run #5.

Time (PST)	Elapsed Time, Seconds	Power Setting
13:11:56	1403	“high”
13:12:41	1448	“powered down”
13:14:50	1577	“high”
13:14:58	1585	“cut way down”
13:16:05	1652	“way back up”
13:21:35	1982	“high”
13:25:25	2212	“setting changing frequently”
13:31:37	2584	“setting changing frequently”

Possibly because of the mechanical problems encountered with this TF-34 engine, Unit #3, we do not have quantitative information regarding engine power settings. The entries in the third column of Table 6-6 reflect the SERDP team’s best effort to characterize the power setting on the basis of its sound. Figure 6-10 shows once again that the PAS signal, often, but not always, tracked closely with the PA and DT signals. The spike at 1400 in the PAS data seems to correspond to the noted high power setting at 1403 followed by the reduction at 1448. The PAS data between about 1575 and 1650 seconds also seems to correspond to the noted power reduction at 1585 seconds followed by the increase at 1652 seconds. The PA and DT data also seem to show this relationship

between 1585 and 1650 seconds. The noted high power setting at 1982 seconds seems to be reflected by the spikes in the PAS signal at about 1980 seconds, although the PA and DT data steadily decrease in this region of the time series.

Figure 6-11 provides an SMPS distribution for Run #5. This “high power” distribution is quite similar to the 80% and 96% distributions shown in Figures 6-3, 6-5, and 6-7. It is also similar to the residual aerosol distribution shown in Figure 6-9, although the differential concentrations are generally greater for this “live” run. Bimodality may be indicated at the small size limit of the data.

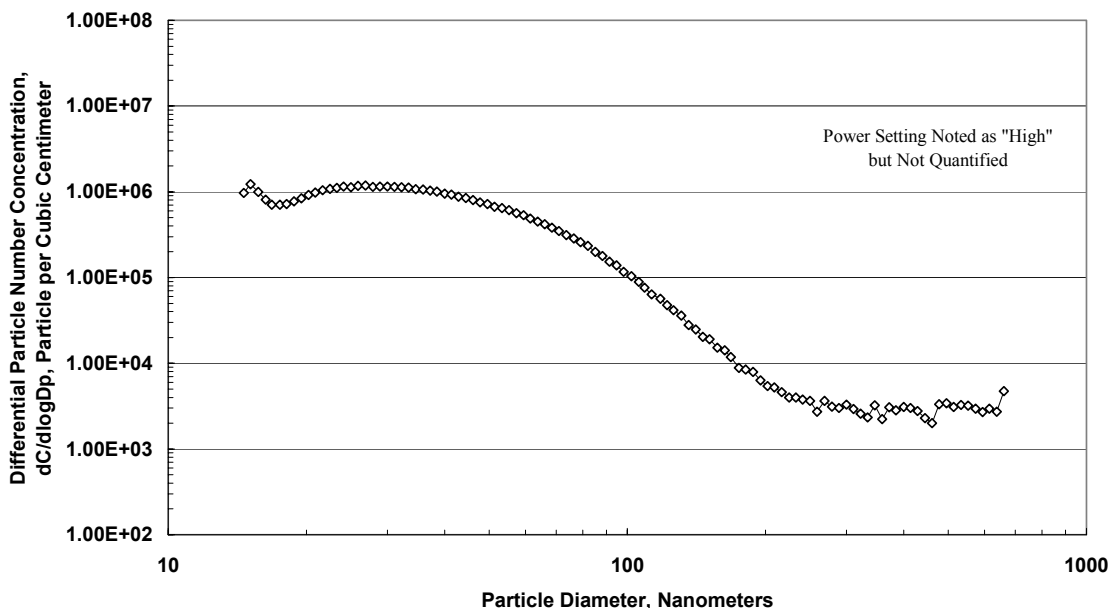


Figure 6-11. AIMD run #5, TF-34 unit #3.

Run #6

Figure 6-12 presents the PAS data from AIMD Run #6. This run utilized a helicopter engine test pad close to the AIMD augmentor chamber that was used for Runs #1 through #5. However, at this site, no augmentor chamber was available and the SERDP sampling system was positioned so the eductor inlet was directly exposed to the engine exhaust stream as described previously. Table 6-7 shows the available engine power setting information for Run #6.

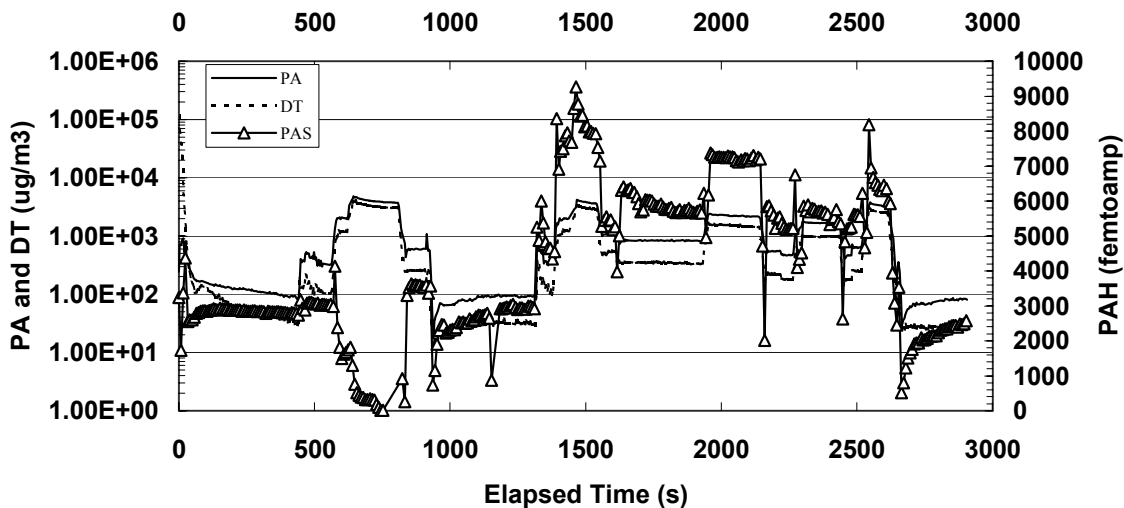


Figure 6-12. AIMD run #6, T-700 engine.

Table 6-7. Engine power settings for AIMD Run #6.

Time (PST)	Elapsed Time, Seconds	Power Setting
08:15	163	idle (approx. 68%)
08:19	403	accelerating
08:21	523	raising to 94%
08:23	643	97%
08:27	883	decreasing to 68%
08:33	1243	raising to 87%
08:34	1363	raising to 98%
08:36	1423	decreasing to 89%
08:44	1903	raising to 96%
08:47	2083	decreasing to 88%
08:49	2203	raising to 94%
08:52	2383	decreasing to 88%
08:54	2503	raising to 96%
08:55	2563	decreasing to 67%

The power setting observations for Run #6 are fairly detailed, but the times recorded in the field notes seem to lag the times of major signal changes by 30 to 60 seconds. Thus power increases noted at elapsed times of 523, 1243, 1363, 1903, 2203, and 2503 seconds seem to result in rising PA and DT data steps at about 560, 1310, 1400, 1960, 2260, and 2560 seconds, respectively. Similar relationships are found between the power setting decreases and the PA and DT decreasing data steps. For example, the decreasing power settings noted at 883, 2083, and 2563 seconds seem to correspond to decreasing data steps at about 920, 2150 and 2620 seconds, respectively.

The PA and DT data in the 2150 to 2460 seconds time interval seem to vary inversely with the power setting. The data traces increase in a distinct step at about 2260 seconds, but the field notes indicate that the engine power was decreased from 94% to 88% in that sequence.

The PAS data trace exhibits a pronounced inverse variation in the elapsed time interval from about 630 seconds to about 840 seconds, during which the field notes indicate power settings of 94% and 97%. The PAS signals decrease to very low values, and then recover at the end of the interval.

Figure 6-13 shows particle size distributions for two power settings for Run #6.

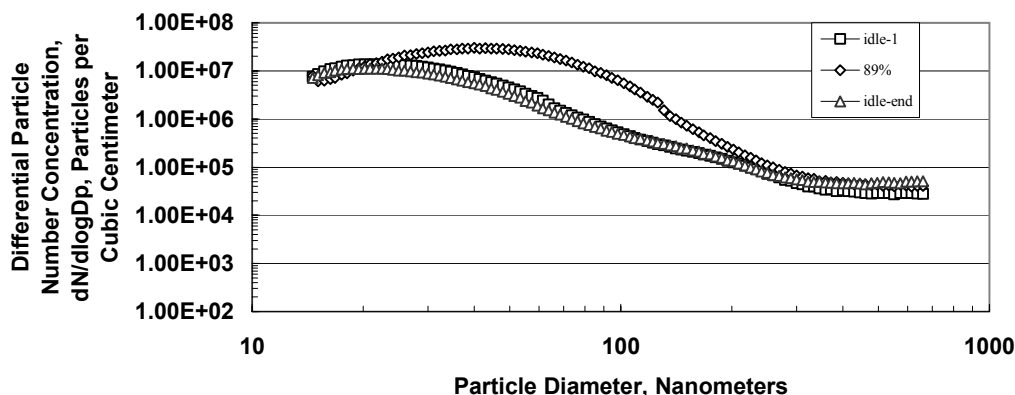


Figure 6-13. Particle size distribution for Run #6, T-700 engine.

The particle size distributions shown in Figure 6-13 for the T-700 engine differ significantly from the T-34 data. Figure 6-13 shows that the T-700 exhaust particles were more numerous than those of the T-34 engine, especially given that the data displayed in Figure 6-13 include a 4.1:1 dilution factor, compared to 3.4:1 for Runs 1-5. The 89% power distribution also peaks at just over 40 nm diameter, which is somewhat larger than all of the T-34 runs except for Run #1. The two idle runs for the T-700 are nearly identical, indicating that similar results were obtained for similar power settings.

6.4.2 Summary of Real-Time Results

- A combined AIMD discharge chamber and instrument dynamic blank resulted in nearly constant PA and PAS output signals of approximately 10 micrograms per cubic meter and 100 femptoamps, respectively. The DT output signal was less constant, ranging from about 5 to 15 micrograms per cubic meter. SMPS data taken during the dynamic blank run indicate that significant amounts of residual aerosol were present in the AIMD augmentor chamber.
- All three real-time instruments seemed to respond to the same events in terms of changes in exhaust particle concentrations.

- All real-time instruments' data outputs sometimes exhibited spikes when engine power settings were changed.
- The PA and DT signals most closely followed each other. The PAS signal sometimes exhibits behavior inverse to the PA and DT, i.e., its signal occasionally falls when the DT and PA signals rise. The investigators have also seen this trend in other studies under increases in power and corresponding increases in PM emissions.
- The PAS readings were not always reproducible as a function of engine power setting. This could be a result of differing PAH concentrations in engine exhaust although the power settings were identical or it could be a result of non-reproducibility in the PAS.
- The PA and DT signals generally but not always rose or fell in proportion to the engine power settings. Typically, as engine settings increased, PA and DT signals increased during the transient, but as the engine condition stabilized the PA and DT signals decreased. Lower PM concentrations at higher engine settings are thought to be due to increased air flow through the turbine.

6.4.3 Evaluation of Photoelectric Aerosol Sensor (Objective #1)

The PAS instrument responds to electrons emitted from irradiated particles that contain surface layers of PAH compounds. Photoelectron emission leaves the particle in a positive charge state, and the sums of the positive charges are measured with an electrometer. Previous work has shown that the response of the PAS is often proportional to the sum of the concentrations of a restricted list of particle-phase PAH compounds known as the "Siegmann" sum after the researcher who first proposed it (e.g., see McDow, et al., 1990).

The fifteen particle-phase PAH compounds used in a modified "Siegmann Sum" for this study were phenanthrene, fluoranthene, pyrene, benzo(b)naphtho(2,1-d)thiophene, benzo(c)phenanthrene, benz(a)anthracene, chrysene, triphenylene, benzo(b+j+k)fluoranthene, benzo(e)pyrene, benzo(a)pyrene, indeno(1,2,3-cd)pyrene, benzo(ghi)perylene, dibenzo(ah+ac)anthracene, and coronene. These compounds, as well as vapor-phase PAH's, are captured in the Gundel denuder sampler (Table 6-1; Zielinska et al., 2003). Aerosol samples entering this sampler first pass through a denuder coated with XAD resin, which effectively traps vapor-phase material. The sample then passes through a filter and into a backup polyurethane foam (PUF) trap. The filter collects particle-phase material, and the PUF trap captures particle-phase compounds that volatilize off the filter. The MOUDI cascade impactor also collects particle-phase, but not vapor-phase PAH compounds.

Figure 6-14 presents a comparison of the run-averaged data from the PAS and the Gundel denuder at the AIMD site.

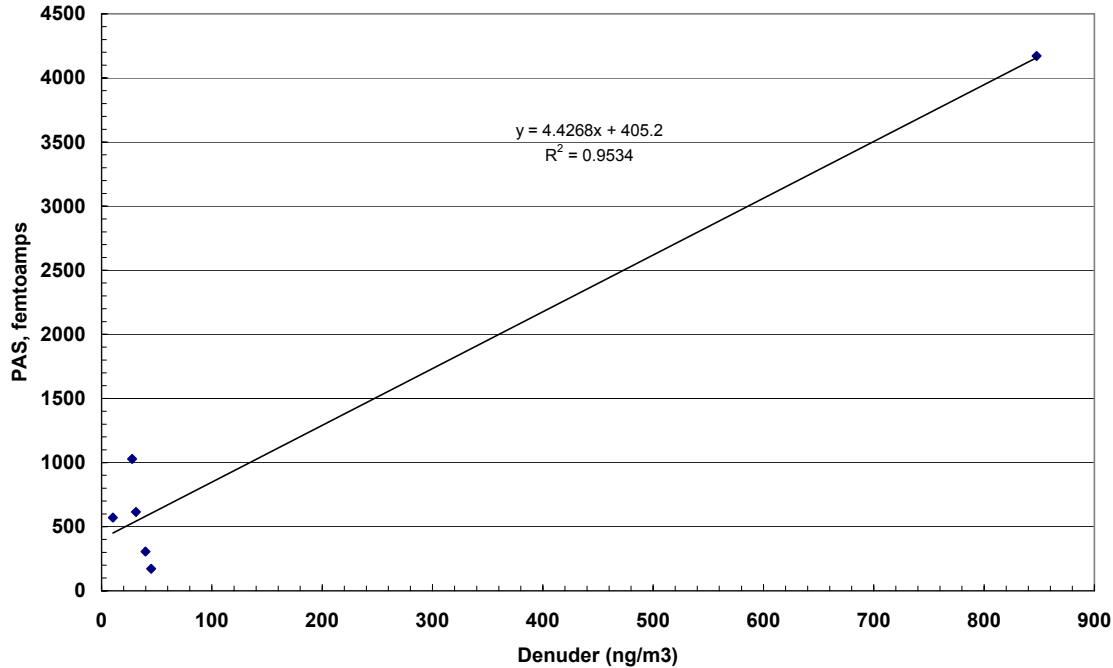


Figure 6-14. PAS signal versus denuder Siegmann sum of particle-bound PAHs.

Figure 6-14 indicates that there is only marginal value to the regression statistics that can be derived from the PAS-Gundel comparison, because most of the available data points cluster at relatively low values, with one data set (from Run #6) at high values. However, the comparison does generally support earlier findings indicating that a PAS signal level of one femptoamp corresponds to roughly one nanogram per cubic meter of net PAH particle-bound material. In the case of this data set, the regression indicates that each ng/m³ of “Siegmann sum” PAH material results in a PAS signal of about 4.4 femptoamps.

The PAS data can also be compared to “Seigmann Sum” measurements conducted by the MOUDI impactor at AIMD. Of the six MOUDI runs, #2, #3, #5, and #6 were analyzed for PAH compound composition. Figure 6-15 shows the plot generated by this comparison. The MOUDI data points include the instrument’s afterfilter data, which correct to some degree for possible volatilization of the MOUDI particulate deposits.

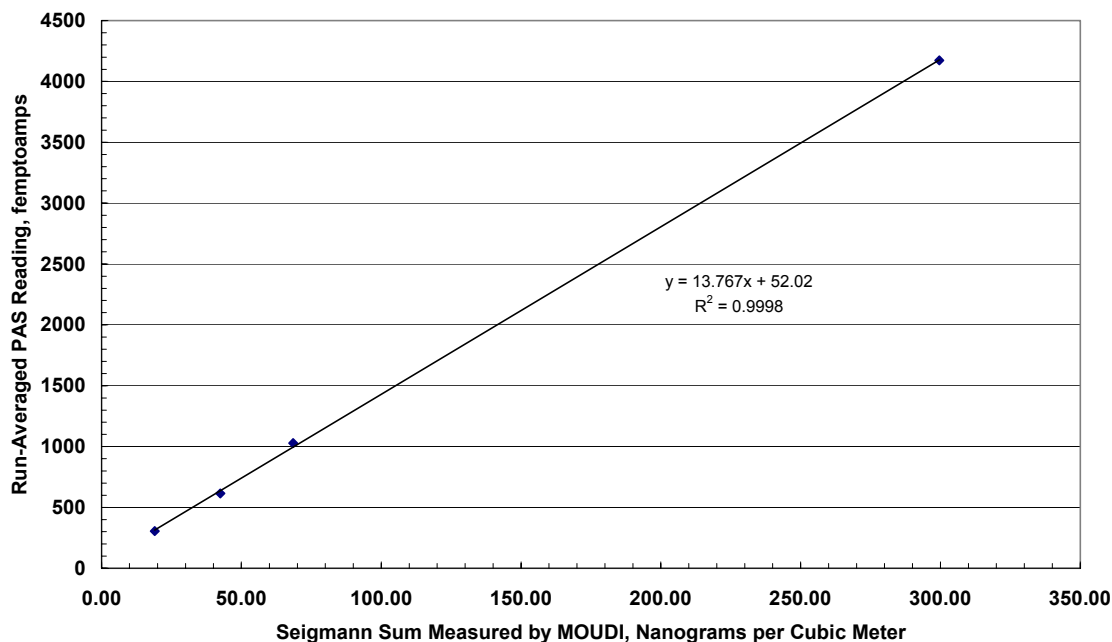


Figure 6-15. PAS signal versus MOUDI Siegmann sum of PAH.

For this comparison, the regression line has a slope of 13.8 femptoamps per ng/m^3 , compared to a value of 4.4 for the PAS-Gundel Denuder sampler comparison. The R^2 value is 0.998, indicating a high degree of correlation. This comparison strongly suggests that, for Runs #2, #3, #5, and #6, the PAS and the MOUDI measured the same averaged quantity with a constant factor relating the two measures. Overall, this comparison lends further credence to the run-averaged performance of the PAS, although the dilution factors for the PAS and the MOUDI were apparently different for Runs #2, #3, and #5. The regression line slope derived by the comparison plotted in Figure 6-14 should be regarded as the most accurate estimate of the PAS-Seigmann Sum relationship for these tests.

Further evaluation of the PAS is given in Appendix 2, which includes comparisons of the PAS and PA data sets.

The Gundel Denuder sampler measurements conducted during these experiments also provide new information regarding the identities and quantities of PAH compounds found in the exhaust from these types of jet engines. The partitioning between the gas- and particle-phases has also been determined. Further description of these findings is given in Appendix 4.

PAS Evaluation at AIMD

- Comparison of run-averaged PAS data to the “Seigmann Sum” of PAH compounds as measured by the Gundel Denuder sampler at AIMD resulted in a regression line slope of 4.4 femptoamps per ng/m^3 . This compares reasonably well with values on the order of approximately 1-3 ng/m^3 femptoamp per cubic meter found in other studies.

- Comparison of the PAS run averages to the MOUDI “Seigmann Sum” for Runs #2, #3, #5, and #6, results in a highly correlated regression line with a slope of 13.8 femptoamps per ng/m^3 . Because of unresolved questions concerning differing dilution factors for the PAS and the MOUDI, this slope value is regarded as less reliable than the one derived from the PAS-Gundel comparison. However, the high degree of correlation between the two data sets lends further credence to the run-averaged PAS data.
- The PAS signal tended to track engine settings at AIMD although in some cases the PAS signal decreased as the signals from the other real-time instruments increased. This erratic behavior was more common at higher emission levels and has also been observed during other studies of the PAS’s performance, which are summarized in Section 3 and Appendix 2 of this report.

6.4.4 Evaluation of Photoacoustic Instrument (Objective #2)

The PA directly measures the absorption of visible light by gases and particles. The absorption due to gases can usually be neglected or corrected for by calibration, so particulate light absorption is measured. For combustion particles, it is usually possible to establish a direct relationship between particulate light absorption and particulate mass concentrations, by means of the specific light absorption parameter. Specific absorption parameters generally vary little for a given source, so it is possible to compare measures of light absorption with measures of particulate mass concentration. For the purposes of the AIMD tests, the PA’s data acquisition system was programmed with a specific absorption coefficient of $5 \text{ m}^2/\text{g}$ at an illumination wavelength of 1047 nm, a wavelength where gaseous absorption is negligible.

In the AIMD tests, four kinds of samplers generated data that quantify particulate mass concentrations. The DustTrak utilizes light scattering and an empirical calibration to provide real-time particulate mass concentration data; the lower size detection limit of the DT is estimated to be about 100 nm. Paradoxically, due to dipole moment effects, black particles scatter more than white particles when they are much smaller than the wavelength, so scattering instruments can detect small black particles better than white ones (see section 6.6.3). The Teflon/quartz and MOUDI samplers expose filters or substrates for the duration of a run and analysis of these provides run-averaged values for particulate mass and carbon species concentrations. The SMPS directly measures particle size distributions, but if particle density is assumed, summed particulate mass concentrations can be estimated from these data for a limited size range. Objective #2 can be addressed by comparing the PA data to real-time data from the DT, and to carbon mass concentrations from the MOUDI and quartz filter samplers.

Comparisons of PA and DT

The PA and DT data were compared for AIMD Runs #1, #3, #5, and #6. Run #4 was a dynamic blank run. Figures 6-16 through 6-19 present PA data plotted against DT data, using all data pairs from each run except for a few outlier pairs that were excluded. Outlier pairs resulted, for example, when a sudden spike occurred in the output of one

instrument but not the other. The number of valid data pairs and the number of excluded outlier pairs are noted on each graph. This kind of comparison does not assume that the DT data are a “standard” to which the PA data are being compared. Rather, the purpose of the comparison is to see whether the PA readings are correlated with the readings of a presumably accurate and precise mass concentration measurement device. Furthermore, the DT responds to all particles, whereas the PA only responds to black carbon.

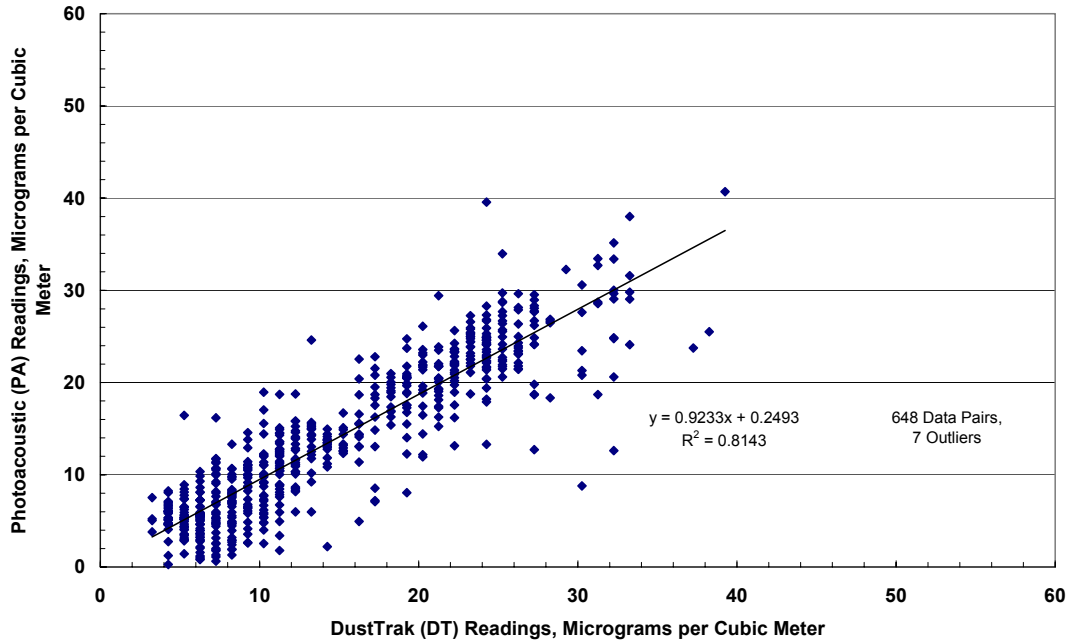


Figure 6-16. Comparison of PA and DT data for AIMD, run #1

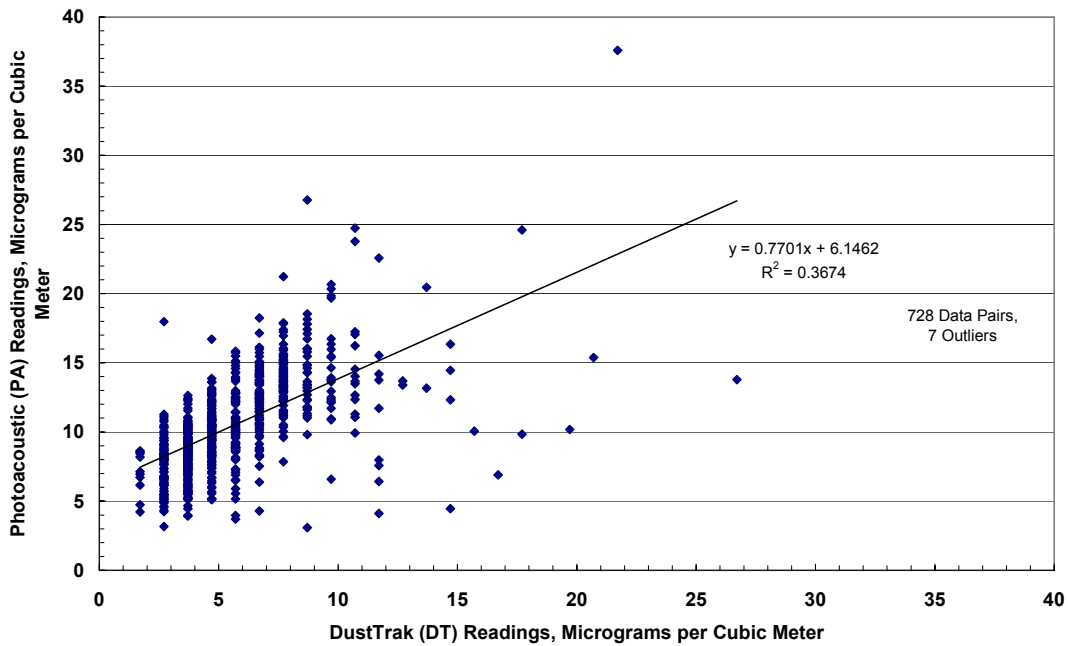


Figure 6-17. Comparison of PA and DT data for AIMD, run #3.

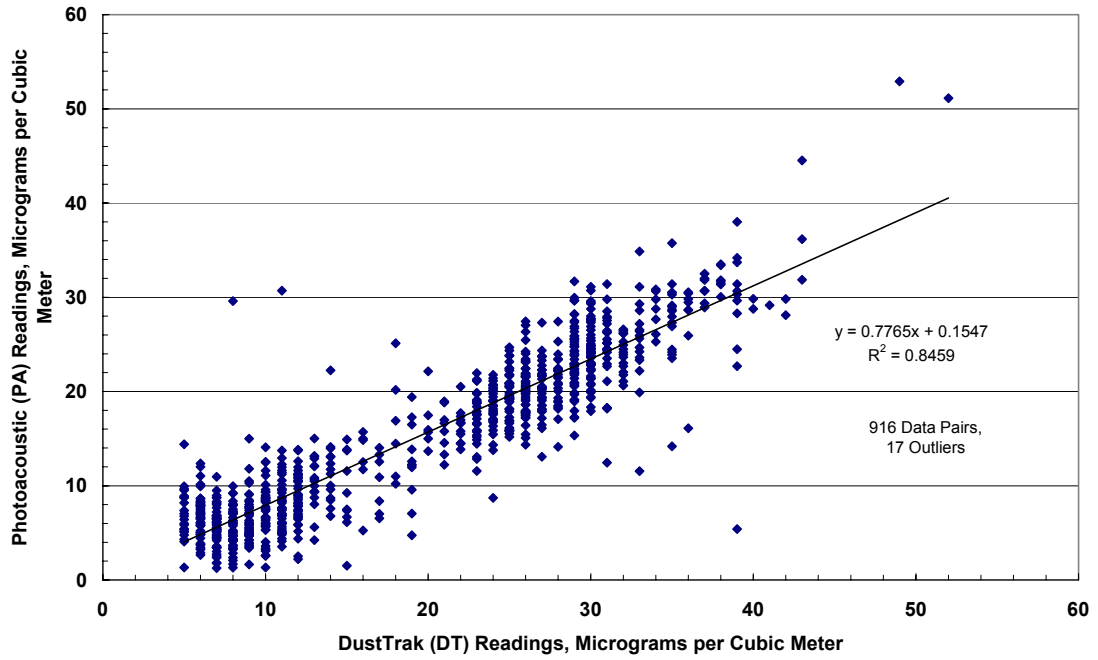


Figure 6-18. Comparison of PA and DT data for AIMD Run #5.

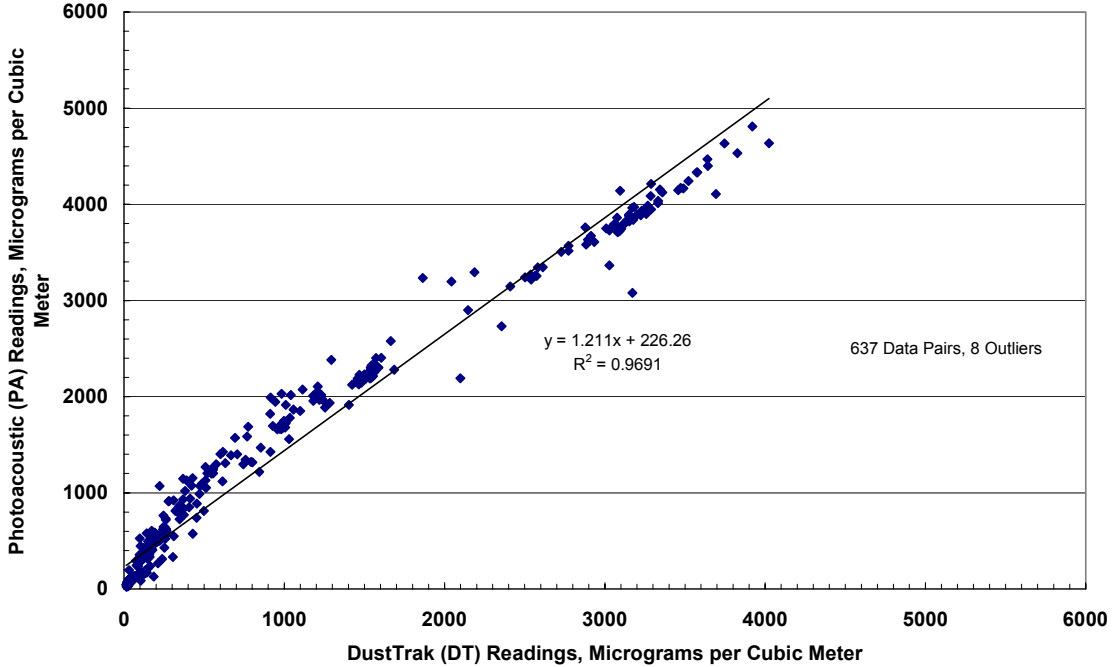


Figure 6-19. Comparison of PA and DT data for AIMD Run #6.

Figures 6-16 through 6-19 show that the PA and DT are usually, but not always, correlated. The R^2 values range from 0.37 for Run #3 to 0.97 for Run #6. The regression slopes vary from 0.8 to 1.2; for the TF-34 runs (#1, #3, #5), the slope ranges from 0.77 to 0.92, and increases to 1.21 for the T-700 helicopter engine. This analysis generally supports the conclusion that the PA and the DT measured closely related exhaust properties during these experiments, both in terms of absolute magnitudes of signals, and in terms of the transient values of signals when changes occurred.

Comparison of PA and Filter/Impactor Data

The run averages of the PA data can be compared with the MOUDI cascade impactor and quartz filter measurements of “elemental”, or refractory carbon collected during an entire run. “Elemental” carbon (EC) is usually associated with the light-absorbing fraction of combustion particles, although in some unusual cases soil dust particles as well as the non-refractory fraction of combustion material may contribute to light absorption. Comparisons of this design of the PA with EC measurements have shown very good agreement in other studies (e.g. Moosmuller et al., 1998).

The MOUDI cascade impactor was operated at its design flow rate, 30 liters per minute. Aluminum foil substrates and quartz afterfilters exposed in the MOUDI were stored in ice chests and shipped back to DRI for gravimetric and carbon analyses. Details of these analysis methods are given in Chow (1995). A separate filter sampler also exposed 47mm diameter quartz and Teflon filters during each AIMD run, using a flow rate of approximately 20 liters per minute. These filters were subjected to carbon and gravimetric analyses, respectively.

Table 6-8 lists the run-averaged PA reading together with the EC measurements from the quartz filter and the MOUDI impactor.

Table 6-8. Comparison of PA and EC data from quartz filter and MOUDI.

Run Number	PA Average, $\mu\text{g}/\text{m}^3$	EC from Quartz filter, $\mu\text{g}/\text{m}^3$	EC from MOUDI, $\mu\text{g}/\text{m}^3$
1	16	30	37
3	11	5	28
4	11	0	50
5	14	79	67
6	1065	1269	938

Figure 6-20 displays the information in Table 6-8 in order to better visualize the run-by-run relationships between these three estimates of light-absorbing particles.

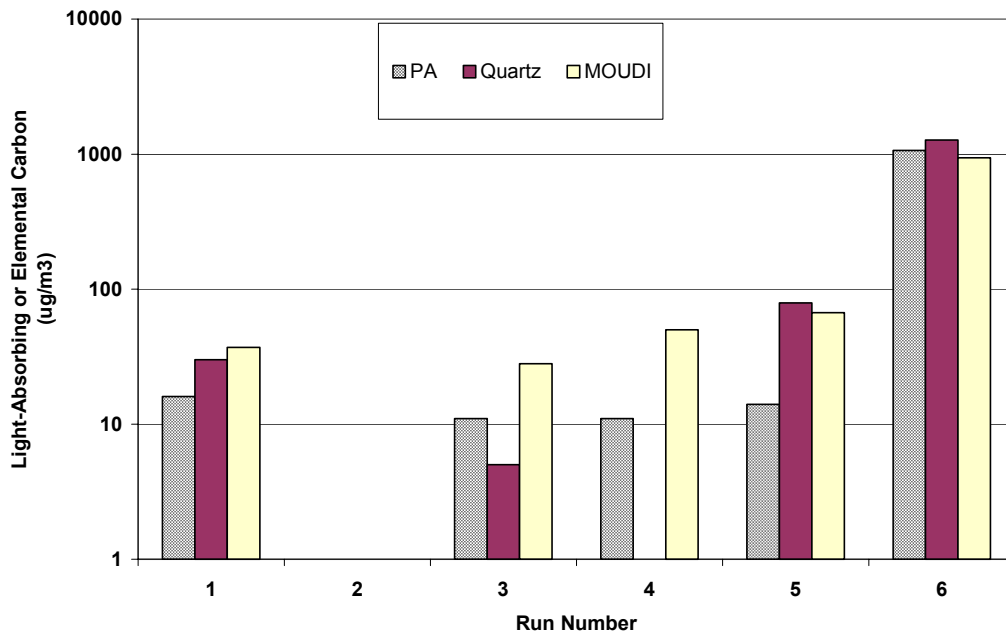


Figure 6-20. Comparison of PA data with quartz filter and MOUDI measurements of EC.

The comparison shown in Figure 6-20 is not favorable for AIMD Runs #3, #4, and #5. The PA measurements reflect the large particle concentration increase shown in Run #6, and all three instruments agree well for this case. Measurements of EC are subject to artifacts, which lead to some uncertainties in the results. However, as will be discussed later in this report, the particulate mass concentration measurements exhibit similar discrepancies for Runs 1-5. We hypothesize that unintended and sample dilution occurred downstream from the MOUDI sample distribution point, so PA malfunction is not suspected in these cases.

Conclusions Regarding Evaluation of PA at AIMD Site

- The PA and the DT apparently measured closely related exhaust properties during these experiments; their real-time data traces closely track each other.
- The PA and two measures of integrated particle elemental carbon concentrations, the quartz filter and the MOUDI, agreed for Run #6 but show disagreement for Runs #1-3, and #5. These discrepancies are hypothesized to be due to a problem with the sample distribution system rather than the PA.

6.4.5 Evaluation of DustTrak Instrument (Objective #3)

Objective #3 called for evaluation of the performance of the DustTrak particle mass monitor in providing real-time measurements of exhaust particle mass concentrations. Table 6-9 presents the run-averaged DT data together with the particle mass concentrations for each run given by the MOUDI impactor and the Teflon filter.

Table 6-9. Mass concentrations from the DustTrak, MOUDI, and the Teflon filter.

Run Number	DT Mass $\mu\text{g}/\text{m}^3$	Teflon Filter Mass $\mu\text{g}/\text{m}^3$	MOUDI Impactor Mass $\mu\text{g}/\text{m}^3$
1	19.9	57	540
2		58	2078
3	5.7	18	654
4	5.3	19	930
5	14.8	124	374
6	693	1735	1738

The data shown in Table 6-9 are plotted in Figure 6-21 in order to allow better visualization of the comparison.

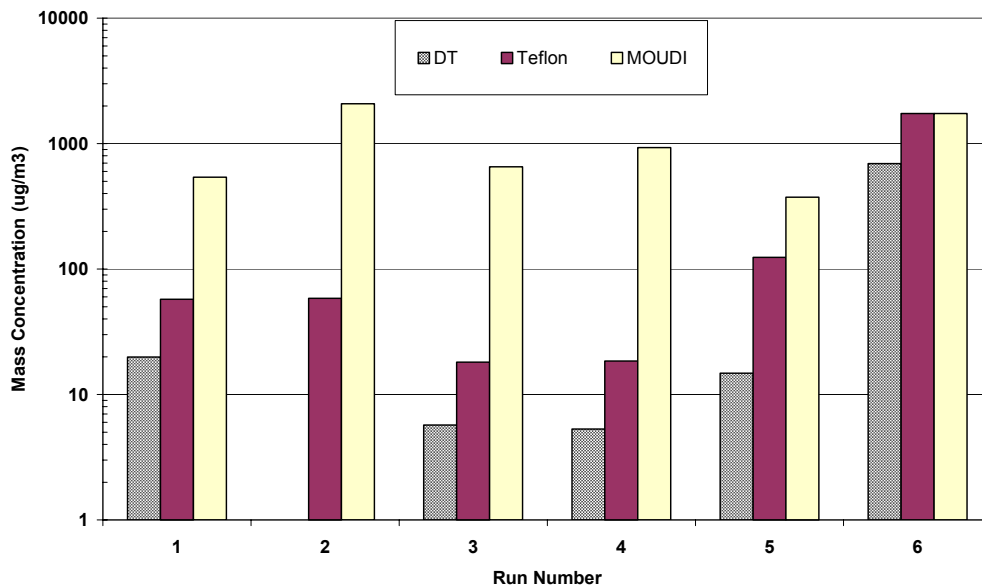


Figure 6-21. Comparison of average DT, filter and MOUDI mass concentrations.

Figure 6-21 shows that the DT and Teflon filter mass concentration measurements track each other for the five runs for which we have data. The DT mass concentration estimate averages about 38% of the Teflon filter value, which may be a reflection of the fact that the DT utilizes an empirical calibration based on mineral test particles in order to convert a light scattering measurement into a particle mass concentration estimate. The comparison between the DT and the Teflon filter could probably be improved by calibrating the DT with particles more similar in size and index of refraction to the actual material of interest, i.e., the jet engine exhaust sampled in these experiments. There is a significant discrepancy between the MOUDI data and the DT and Teflon filter data for Runs #1, #3, #4, and #5. A similar discrepancy was noted earlier for the PA versus quartz filter and MOUDI comparison. We hypothesize that unintentional dilution of the sample occurred downstream from the MOUDI connection for the sample line setup at

the AIMD discharge chamber, and that this unintentional and unknown problem disappeared when the sampling system was moved to the helicopter test pad for Run #6.

AIMD Evaluation of DT (Objective #3)

The AIMD studies provide the following conclusions about the DT:

- The DT's real-time signal seemed well synchronized with that of the PA; it was also generally synchronized with that of the PAS. The variations in the DT signal seemed generally to correspond to changes in engine power settings.
- The DT's run-averaged mass concentration estimates track those of the Teflon filter for the five runs for which we have data. The DT's mass concentration estimates average about 38% of those of the Teflon filter. Recalibration of the DT would probably eliminate much of this discrepancy.
- The DT's run-averaged mass concentration estimate was 40% of the MOUDI measurement for Run #6. We hypothesize that unintended dilution of the sample stream occurred downstream from the MOUDI connection for Runs 1-5.

Comparisons of MOUDI, Teflon Filter, and SMPS Mass Concentration Measurements for AIMD Runs

Particle mass concentrations can be estimated on the basis of SMPS data by assuming the density of the particles. In previous investigations, assuming a density of 1 g/mg^3 led to good agreement between SMPS and MOUDI data obtained in motor vehicle exhaust studies (Rogers et al., 2003). Figure 6-22 presents a comparison of particle mass concentration determinations for all AIMD runs, in which the SMPS estimates are based on the same assumption as Rogers et al. (2003).

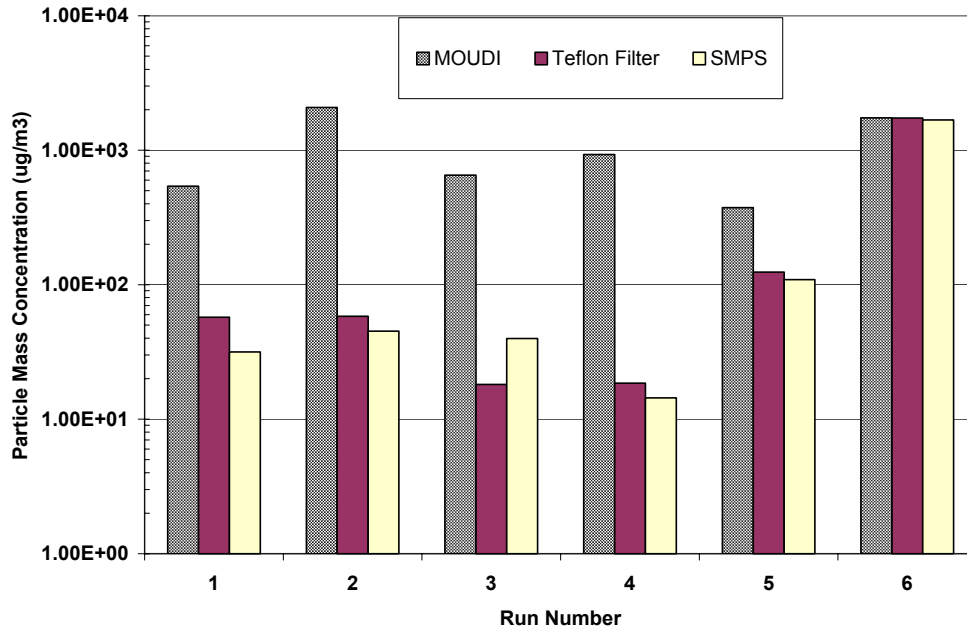


Figure 6-22. MOUDI, Teflon filter, and SMPS mass concentrations for AIMD.

Figure 6-22 shows that there is good agreement between the SMPS and Teflon filter data. However, the MOUDI determinations greatly exceed the Teflon filter and SMPS measurements for all but Run #6. This discrepancy is consistent with the evidence presented earlier in this report and supports the hypothesis that the Teflon filter, DT, PA, and SMPS, but not the MOUDI, were subject to unintended dilution during Runs #1-#5.

The agreement of the SMPS and Teflon filter data for Runs #1-#5, and the agreement of all three methods for Run #6, provides validation of the SMPS particle size distributions shown in Figures 6-3, 6-5, 6-7, 6-9, 6-11, and 6-13. This cross-check would reveal major discrepancies if the SMPS distributions were significantly in error. The particle density assumption probably inserts no more than $\pm 50\%$ uncertainty into the SMPS mass estimations (Rogers et al. 2003).

The agreement between the SMPS and the Teflon filter data indicates that the run-to-run variations in the particle mass concentrations are generally due to variations in the particle size distributions.

6.4.7 Supporting Measurements: Emission Rates

The foregoing discussion has focused on addressing Objectives 1-3 at the AIMD site. The real-time instrument evaluations have sometimes used filter and/or impactor data for comparisons that assist our judgment concerning instrument performance. This approach benefits from comparison of the filter and/or impactor data to comparable data provided by other researchers in similar situations.

The ratios of particulate species concentrations to the mass of fuel consumed are common quantifiers of engine exhaust emissions. These emission factors require estimation of the fuel consumption based on measured carbon concentrations in the exhaust. Here, in accordance with established practice (e.g., Kirchstetter et al. 1999), we assume that the exhaust carbon concentration is represented to a good approximation by the gas-phase carbon in the carbon dioxide and monoxide emissions, which we measured by filling electropolished canisters during each test run. The contents of the canisters were analyzed post-experiment in DRI's laboratories. The Teflon/quartz filter sampler and the canister sampler were subject to the same sample dilutions, even for Runs #1-#5 for which we hypothesize that unintentional dilution occurred downstream from the MOUDI, because their sample inlet lines were connected to the same distribution point. Table 6-10 presents emission factors for particulate mass, elemental carbon (EC), and organic carbon (OC), as measured by the Teflon and quartz filters.

Table 6-10. AIMD PM emission factors derived from Teflon and Quartz filter data.

Run Number	Mass	EC	OC	Total Carbon
1	0.30	0.16	0.25	0.41
2	0.33	0.17	0.77	0.95
3	0.04	0.01	0.11	0.12
5	0.64	0.41	0.65	1.06
6	0.32	0.24	0.07	0.30

Note: all emission factors are given in grams per kilogram of fuel consumed

Table 6-10 indicates that the mass emission factors were similar for Runs #1, #2, and #6, about a factor of two greater for Run #5, and almost an order of magnitude lower for Run #3. The EC emission factors follow a trend similar to the mass factors. The OC emission factors vary considerably. The amount of OC captured by the quartz filter may depend on semi-volatile compounds that transfer from the gas to the condensed phase when they encounter the filter and its deposit layer. The total carbon emission factors sometimes exceed the mass factors, which may be a further sign of the capture of semi-volatile OC compounds.

Run #3 seems anomalous in this analysis, due to the very low emission factors for mass and EC. This observation is consistent with the relatively low run-averaged mass registered by the DT (see Figure 6-21).

For comparison, Petzold and Schroder (1998) performed total carbon and black carbon particulate measurements in the exhaust of a Rolls Royce/SNECMA M45H Mk501 turbofan engine. According to these researchers, this engine represents older technology, with higher carbon emissions than most new engines. The engine was operated at power settings ranging from 11% to 71%, with both high- and low-sulfur content fuel. The carbon determinations were obtained from a thermal filter analysis method that is analogous to, but not identical to, the method used in this SERDP project. Petzold and Schroder (1998) found black carbon factors ranging from 0.1 to 0.6 g/kg fuel and total

carbon emission factors ranging from 0.3 to 0.7 g/kg fuel. Higher power settings produced greater emission factor values.

The total and elemental carbon emission factors found in this study agree quite well with the findings of Petzold and Schroder (1998). The “black” or elemental carbon factors found in the North Island experiments are in the low end of the range given by Petzold and Schroder (1998), as would be expected if the TF-34 and T-700 engines are somewhat newer technology engines compared to the Rolls-Royce unit tested by those investigators. The average of the total carbon factors found in the North Island study is 0.57 grams per kilogram of fuel, which is in the middle of the range cited by Petzold and Schroder (1998). Again, we hypothesize that some of the variation in our OC, hence total carbon factors is due to semi-volatile compounds. Overall, this comparison of one derived measure of exhaust properties, the emission factor, to the findings of an independent research team supports our confidence in the overall validity of our results.

6.4.8 Conclusions Regarding Objectives #1-#3 at AIMD Site

Objective #1: Evaluation of PAS

- The PAS signal sometimes exhibits behavior inverse to the PA and DT, i.e., its signal occasionally falls when the DT and PA signals rise. This is not necessarily proof of malfunction; it could be a reflection of the fact that the PAS, PA, and DT all measure fundamentally different parameters.
- The PAS readings were not always reproducible as a function of engine power setting. This could be a result of differing PAH concentrations in engine exhaust although the power settings were identical, or it could be a result of non-reproducibility in the PAS.
- In the case of this data set, the regression indicates that each nanogram per cubic meter of “Siegmann sum” PAH material results in a PAS signal of about 4.4 femptoamps.

Objective #2: Evaluation of PA

- The PA and DT signals most closely followed each other.
- The PA and DT signals did not always rise or fall in proportion to the engine power settings.
- The PA and the DT apparently measured closely related exhaust properties during these experiments; their real-time data traces closely track each other.
- The PA and two measures of integrated particle elemental carbon concentrations, the quartz filter and the MOUDI, agreed for Run #6 but show disagreement for Runs #1-3, and #5. These discrepancies are hypothesized to be due to a problem with the sample distribution system rather than the PA.

Objective #3: Evaluation of DT

- The DT's real-time signal seemed well synchronized with that of the PA; it was also generally synchronized with that of the PAS. The variations in the DT signal seemed generally to correspond to changes in engine power settings.
- The DT's run-averaged mass concentration estimates track those of the Teflon filter for the five runs for which we have data. The DT's mass concentration estimates average about 38% of those of the Teflon filter. Recalibration of the DT would probably eliminate much of this discrepancy.
- The DT's run-averaged mass concentration estimate was 40% of the MOUDI measurement for Run #6. We hypothesize that unintended dilution of the sample stream occurred downstream from the MOUDI connection for Runs 1-5.

6.4.9 Conclusions for all Real-Time Instruments

- All three real-time instruments seemed to respond to the same events in terms of changes in exhaust particle concentrations.
- All real-time instruments' data outputs sometimes exhibited spikes when engine power settings were changed.
- The agreement between the SMPS and the Teflon filter data indicates that the run-to-run variations in the particle mass concentrations are generally due to variations in the particle size distributions.

6.5 Flightline Measurements

The three main project objectives were addressed at the “Flightline” site at North Island by means of a portable instrument pallet. The PAS, PA, DT, and an SMPS were therefore able to be deployed out onto the tarmac on short notice, and also could be quickly moved away in order to avoid interfering with the Navy’s ongoing operations. Figure 6-23 shows an illustration of the pallet, its instruments, and the dilution system included on board.

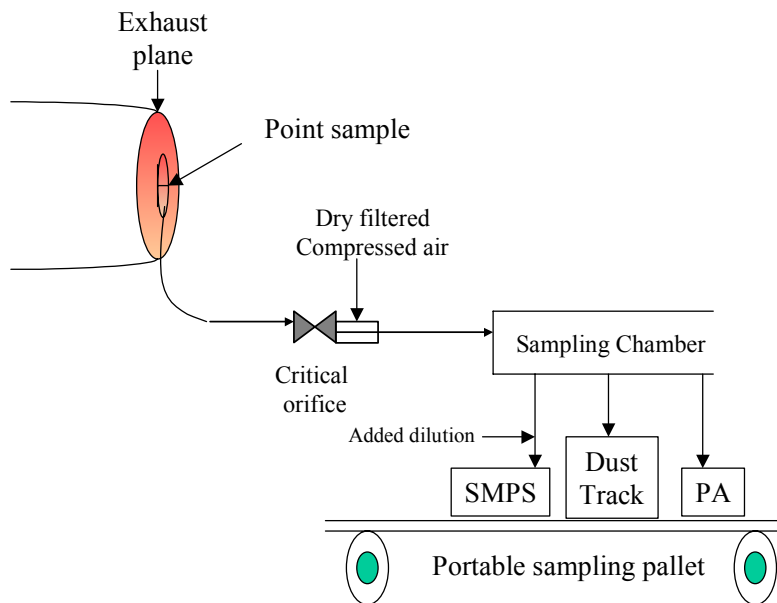


Figure 6-23. Portable sampling pallet.

Table 6-11 lists the five experiment runs that were conducted at the Flightline site. All five runs involved F/A-18C aircraft equipped with F-404-GE-400 engines. Exhaust samples were extracted from engine exhaust using a 1.6 cm diameter, 1-meter long stainless steel line leading to an eductor/dilutor system similar to that used at the AIMD site. It can be assumed that no ambient air dilution occurred at the engine exhaust cone. The eductor dilution ratio for these tests was 2.1:1 (2.1 parts particle-free, dry air to one part exhaust sample).

Table 6-11. SERDP experiments conducted at flightline site.

Flightline Run	Date	TIME (PST)	Aircraft ID and Sampling Side*
1	1/29/02	10:07:05-10:08:08	164037, right
2	1/29/02	13:20:14-13:35:50	164037, right
3	1/30/02	12:44:53-13:15:04	164037, right
4	1/31/02	12:52:05-13:16:04	164257, right
5	2/1/02	09:58:39-10:26:15	164037, left

*Note: Sampling side from pilot’s perspective

The PAS, PA, and DT were deployed on the pallet for all runs. The Aircraft Environmental Support Office (AESO) at North Island deployed an SMPS for Runs #3 through #5.

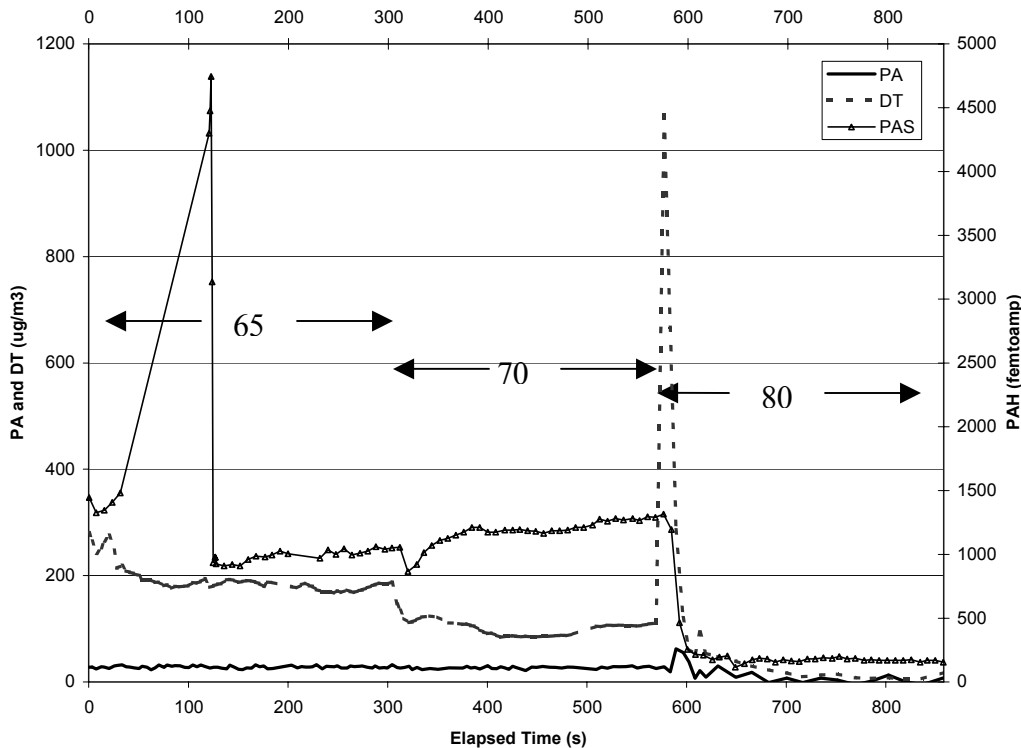


Figure 6-24. Flightline run #1, F-404-GE-400, right engine, plane 164037.

Run #1 consisted of three segments: the engine power setting was 65% from the beginning of the run to 361 seconds elapsed time, then 70% from 361 seconds to 583 seconds, and finally 80% from 583 seconds until the end of the run (Figure 6-24). The DT data in Figure 6-24 show three distinct steps, decreasing in magnitude from about 200 to about $10 \mu\text{g}/\text{m}^3$ as the power setting increased. The DT exhibits a spike at 577 seconds, which corresponds to the transition from 70% to 80% power.

The PA data are at very low levels, starting at less than $30 \mu\text{g}/\text{m}^3$ and falling off to less than $5 \mu\text{g}/\text{m}^3$ by the end of the run. The PA data exhibit a small spike at 583 seconds, corresponding to the spike in the DT data. The PAS data exhibits a spike at 120 seconds; this feature of the data does not correspond to any known physical phenomenon, and may be spurious. Both the DT data and the PAS data exhibit a step at about 320 seconds. The PAS data recover to their former values and slowly increase following this step, while the DT data slowly decrease. Overall, the DT data decrease as the engine power setting increases, while the PAS data increase as the power setting increases from 65% to 70%, then decrease as the setting increases from 70% to 80%.

Run #2, using the same engine as Run #1, included power setting increases from 65% to 70%, and from 70% to 80%, at 260 and 441 seconds elapsed time, respectively (Figure 6-25). The DT data again decreased inversely as the power setting increased, with a spike at the 70%-80% transition, similar to Run #1. The PA data also decreased as the power settings increased, with a small spike at the 70%-80% transition. The PA signal went slightly negative at 461 seconds. Unlike Run #1, the PAS data for Run #2 exhibit regular steps that decreased in magnitude as the power setting increased.

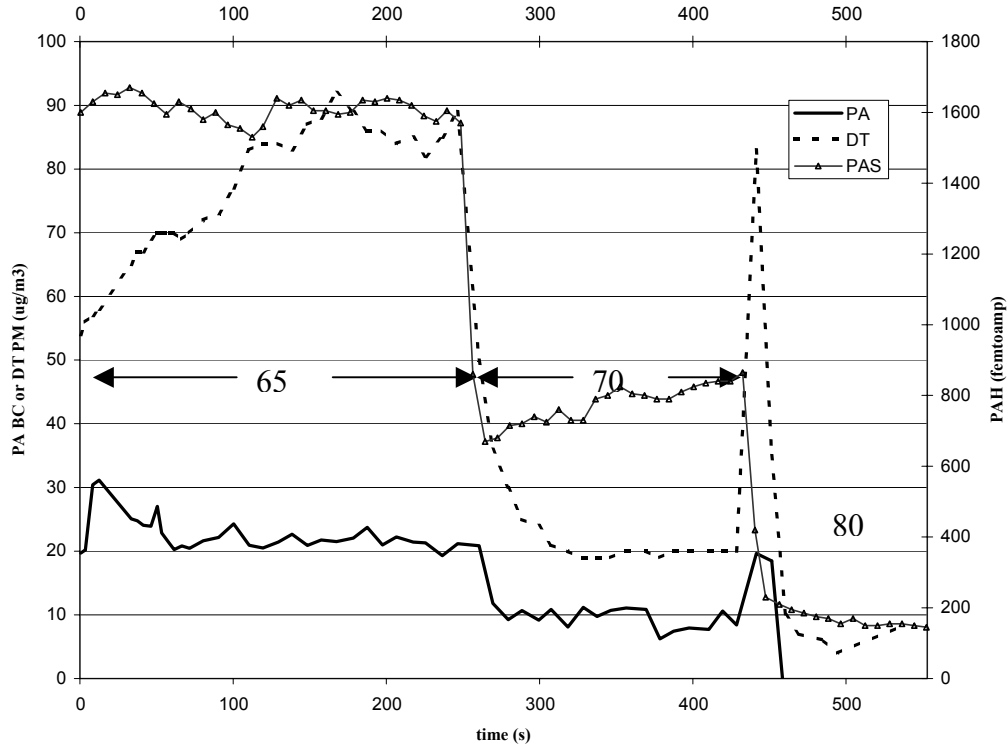


Figure 6-25. Flightline run #2, F-404-GE-400, right engine, plane 164037.

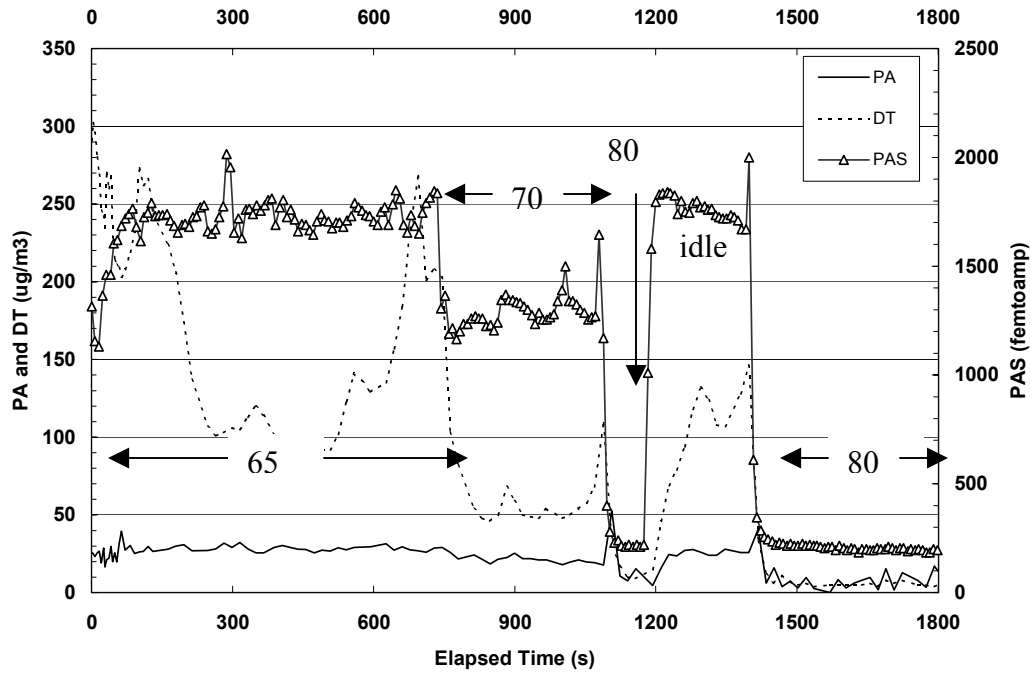


Figure 6-26. Flightline run #3, F-404-GE-400, right engine, plane 164037.

Run #3 consisted of five segments; power settings were changed from 65% to 70%, 70% to 80%, 80% to idle, and idle to 80%, at elapsed times of 729, 1070, 1194, and 1398 seconds, respectively (Figure 6-26). The PAS data exhibit roughly the same magnitudes for the 65% and the idle segments, which is probably a reflection of the fact that those two settings are nearly identical. The PAS output decreased from the 65% to the 70% segment, and more so for the two 80% segments. The PAS signal levels are quite reproducible for the two 80% segments.

The PA data exhibit spikes following the 1070 and 1398 transitions, and signal levels are greatest for the 65% and idle power settings. After the spikes, the PA signal drops as the additional air flowing through the turbine decreases the PM concentrations. Again, however, the PA's readings of light-absorbing particle mass concentrations are well below the mass concentration readings of the DT, indicating that much of the overall particle mass is non-light absorbing. The DT data vary quite widely for this run, but again generally vary inversely with the engine power setting.

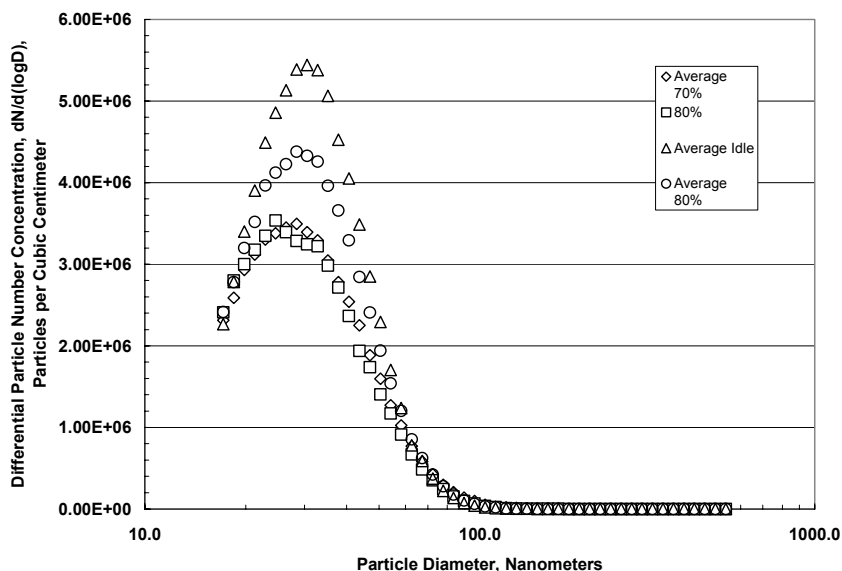


Figure 6-27. Particle size distribution, run #3, right engine, plane 164037. Data provided by North Island AESO.

The distributions in Figure 6-27 all peak at about 30 nanometers with a single mode. The greatest particle number concentrations were observed for the idle period. The lowest concentrations were observed for the 70% period and the brief 80% period that started at 1070 seconds elapsed time. (The 70%, idle, and last 80% power setting intervals resulted in multiple SMPS scans; their results were averaged to create the single curves shown in Figure 6-27.) The longer 80% period that started at 1398 seconds resulted in the distribution falling between the lowest and highest cases in Figure 6-27. Therefore an inconsistency was observed in terms of the different distributions for the two 80% power-setting intervals. Apart from this discrepancy, Figure 6-27 shows that idle conditions again generated relatively high emissions. Summed particle mass concentrations can be estimated from the SMPS distributions by assuming the density of the particles, as was previously discussed for the AIMD data. These estimates will be tabulated and discussed later in this report.

Run #4 consisted of two segments, beginning at 70% power and changing to a 65% power setting at 243 seconds elapsed time. Once again, the PAS and DT data indicate that particulate emission concentrations were greater for near-idle conditions than for the 70% power setting. The PA again recorded only very low levels of light-absorbing particles. Overall, the three instruments' signals were lower for this run than for any of the others.

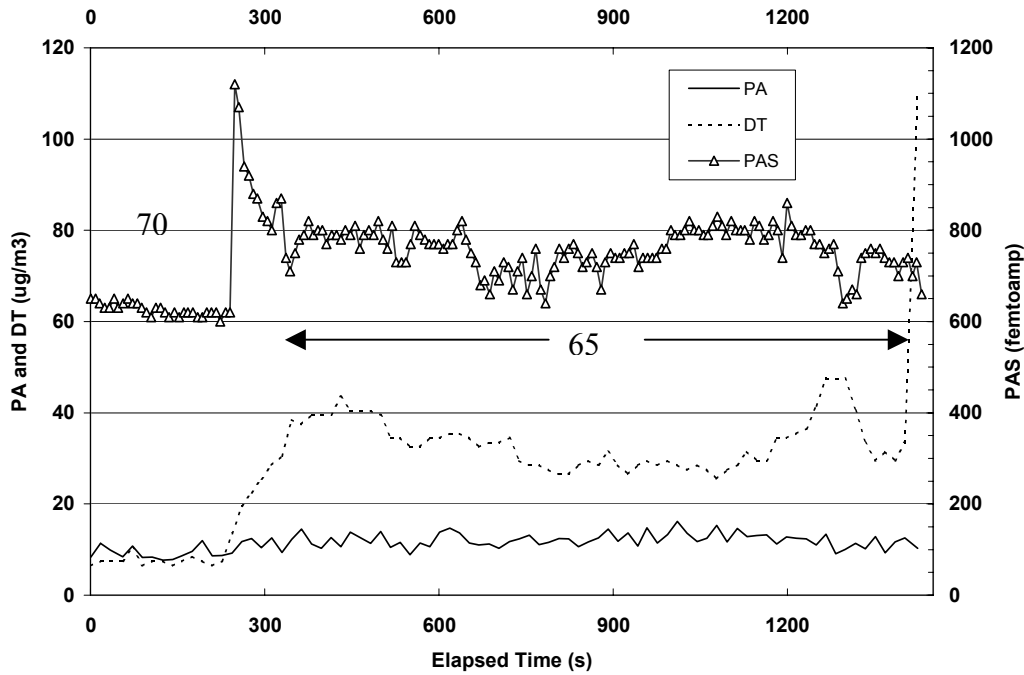


Figure 6-28. Flightline run#4, right engine, plane 164257.

The engine power settings for Run #5 were 65% from zero to 610 seconds, and 70% from 610 to 1207 seconds. For this run the PAS data generally varied directly with the power settings and inversely to the DT readings. The PAS data also show an early and temporary peak from about 100 to 150 seconds.

Both the DT and the PA data again show a brief spike when the power setting was changed; the DT spike was at 630 seconds, and the PA spike was at 626 seconds. The DT data again varied inversely with the power setting, and the PA readings also fell slightly as the power setting increased.

The engine power settings for Run #5 were 65% from zero to 610 seconds, and 70% from 610 to 1207 seconds (Figure 6-29). For this run the PAS data generally varied directly with the power settings and inversely to the DT readings. The PAS data also show an early and temporary peak from about 100 to 150 seconds. Both the DT and the PA data again show a brief spike when the power setting was changed; the DT spike was at 630 seconds, and the PA spike was at 626 seconds. The DT data again varied inversely with the power setting, and the PA readings also fell slightly as the power setting increased.

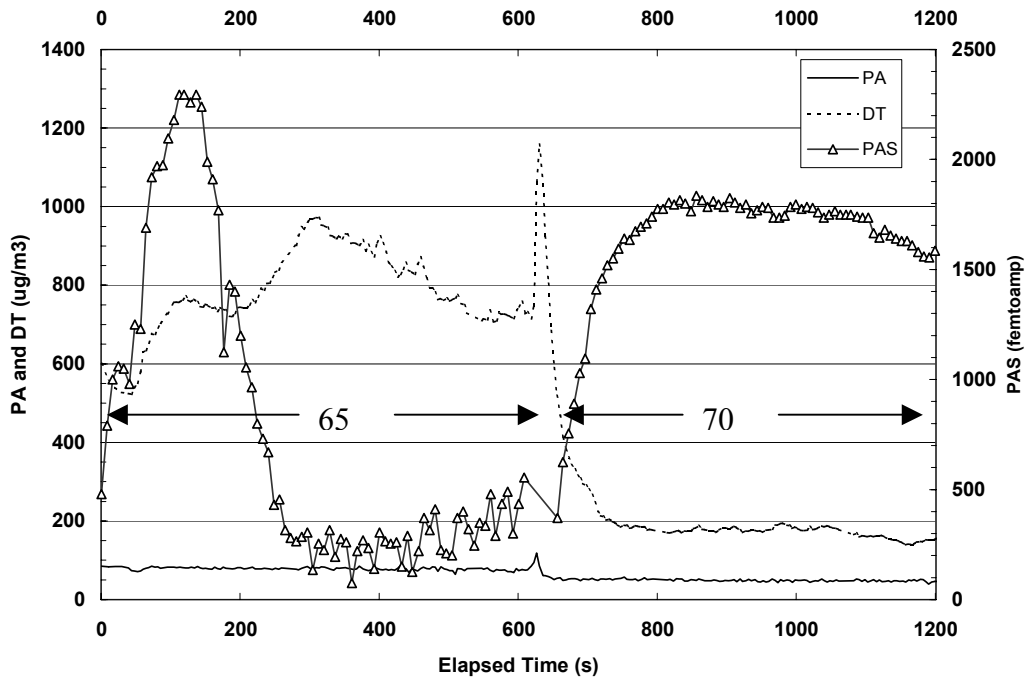


Figure 6-29. Flightline run#5, left engine, plane 164037.

The distribution shown in Figure 6-30 is characterized by a single mode peaking at about 40 nanometers diameter. The relatively high differential particle concentration values suggest that the integrated particle mass concentration estimated on the basis of this distribution will be relatively high.

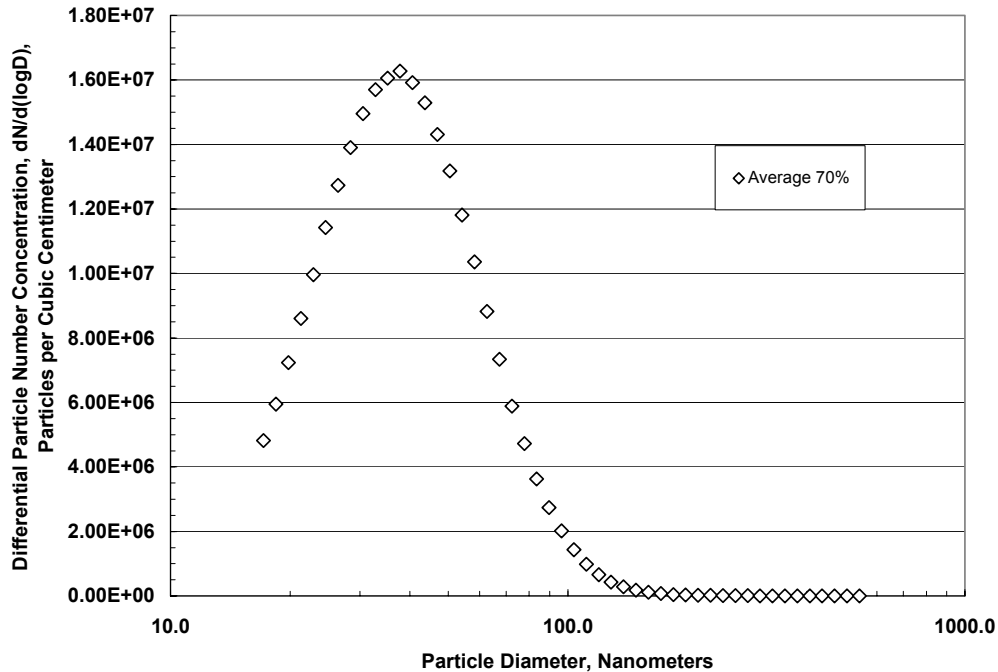


Figure 6-30. Particle size distribution, run#5, left engine, plane 164037. North Island AESO provided these SMPS results.

6.5.1 Summary of Flightline Observations

- The PAS readings often, but not always, varied inversely with the engine power setting. Occasionally the PAS data exhibit variations that do not correspond to any known variation in the particle emission source. Apparently spurious PAS signals were also observed in the AIMD experiments.
- The PA readings were relatively constant, and lower than those of the DT, for all runs. The PA data often exhibited a spike when engine power settings were changed.
- The DT readings were significantly higher than those of the PA, indicating that light-absorbing particles were not the major constituent of the exhaust particle population. The DT signals varied considerably and generally fell when the power setting was increased.
- The SMPS size distributions exhibited single modes peaking at diameters in the 20 to 50 nm range. Peak differential particle concentrations generally, but not always, varied inversely with engine power settings.

6.5.2 Evaluation of the Photoelectric Aerosol Sensor (Objective #1)

In general, the PAS signal followed the aircraft's engine setting in a predictable manner, decreasing as engine setting increased, with the exception of run#5 in which the PAS signal decreased while the engine setting remained constant. This type of erratic behavior has been observed during other SERDP studies, described in Section 3 of this report and Appendix 2. Figure 6-31 shows the correlation between the average PAS and PA measurements for each run and setting pair. The results correlate somewhat although the correlation was not nearly as good as that reported for aircraft ground support vehicles ($R^2 = 0.99$, Appendix 2). Baltensberger et al. (2001) and Matter et al., (1999) report that the PAS signal correlates well with EC concentration for vehicle exhaust. Comparing the PAS and DT results yielded a poor correlation ($R^2 = 0.56$), and one would not expect PM mass to correlate well with PAH content. A more comprehensive evaluation of the PAS was performed at AIMD, where the PAS response was compared with denuder/filter and MOUDI PAH results.

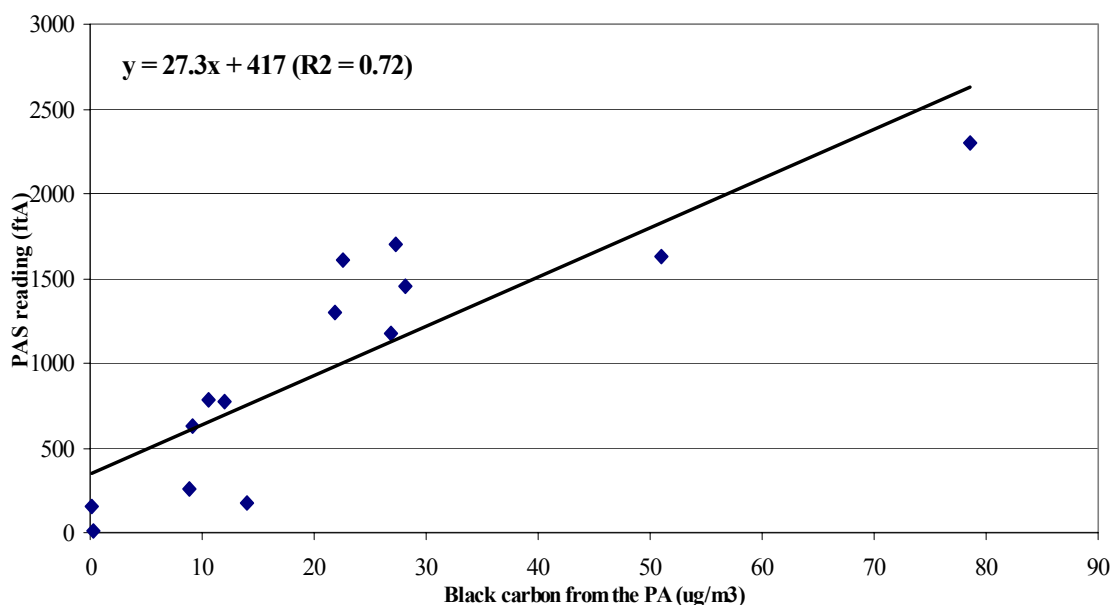


Figure 6-31. Correlation between PA BC results with PAS PAHs results.

Summary of the PAS Data from Flightline Experiments

- The correlation between the average PAS and PA results indicates that the two instruments track related properties.
- The PAS results do not track the total particle mass as expected.

6.5.3 Evaluation of the Photoacoustic Instrument (Objective #2)

Comparison of PA and DT

Figures 6-32 through 6-36 display scatterplots of all PA and DT data pairs, for Flightline Runs #1 through #5, respectively. As was discussed for the AIMD results, comparison of the PA to the DT data allows one kind of evaluation of the PA data, since the DT provides a real-time measure of the particle mass concentration. However, a close relationship between the PA and DT data isn't expected.

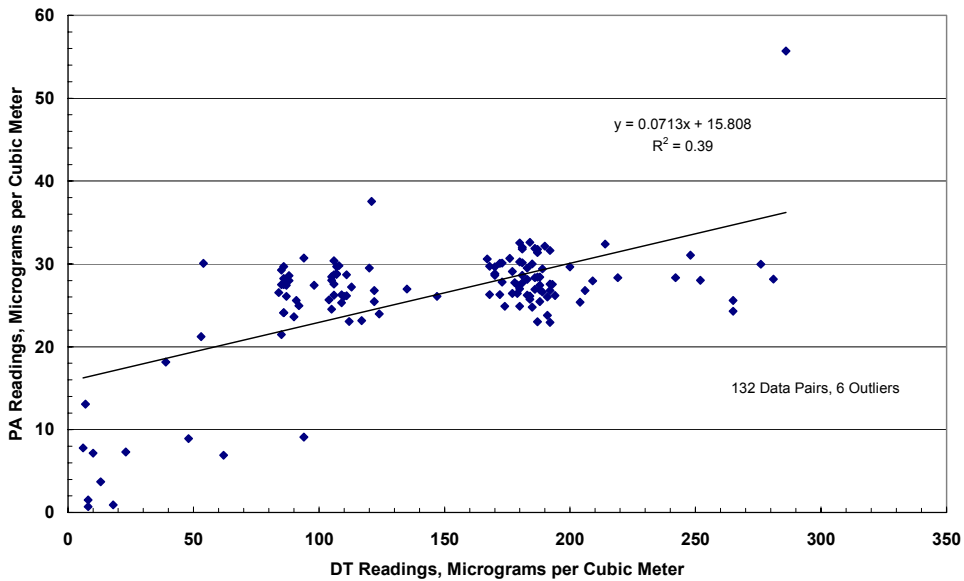


Figure 6-32. Comparison of PA and DT data, run #1.

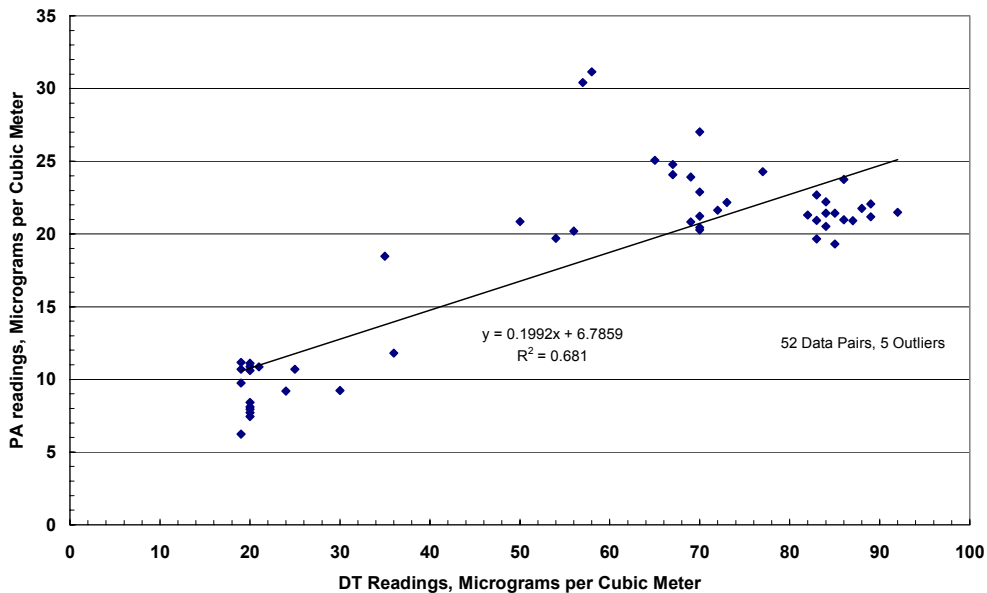


Figure 6-33. Comparison of PA and DT data, run #2.

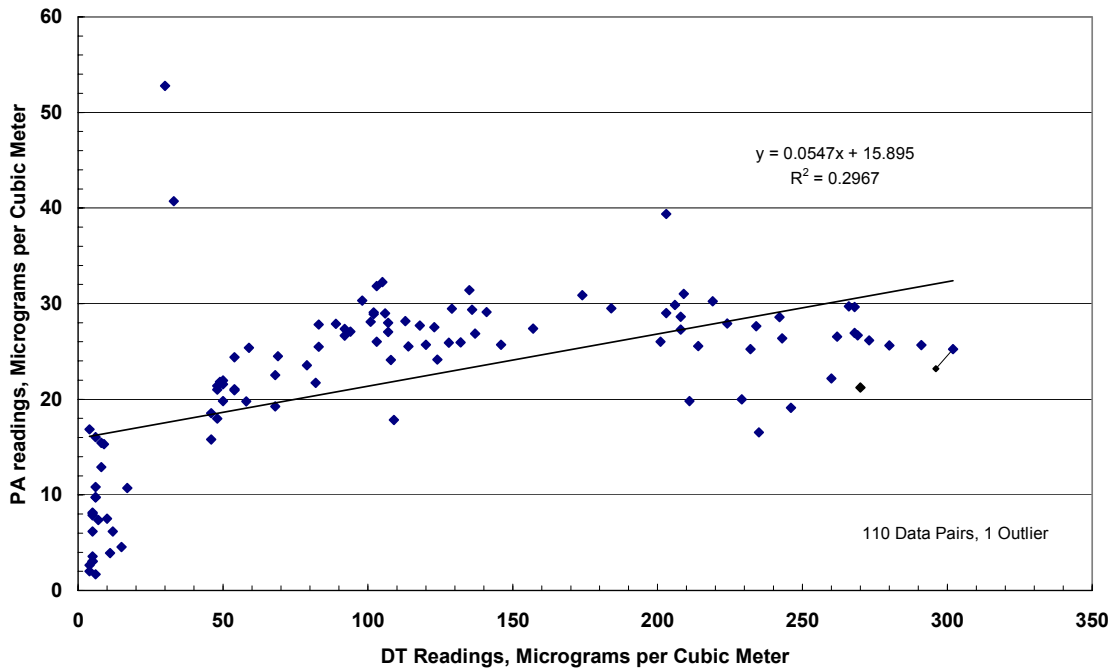


Figure 6-34. Comparison of PA and DT data, run #3.

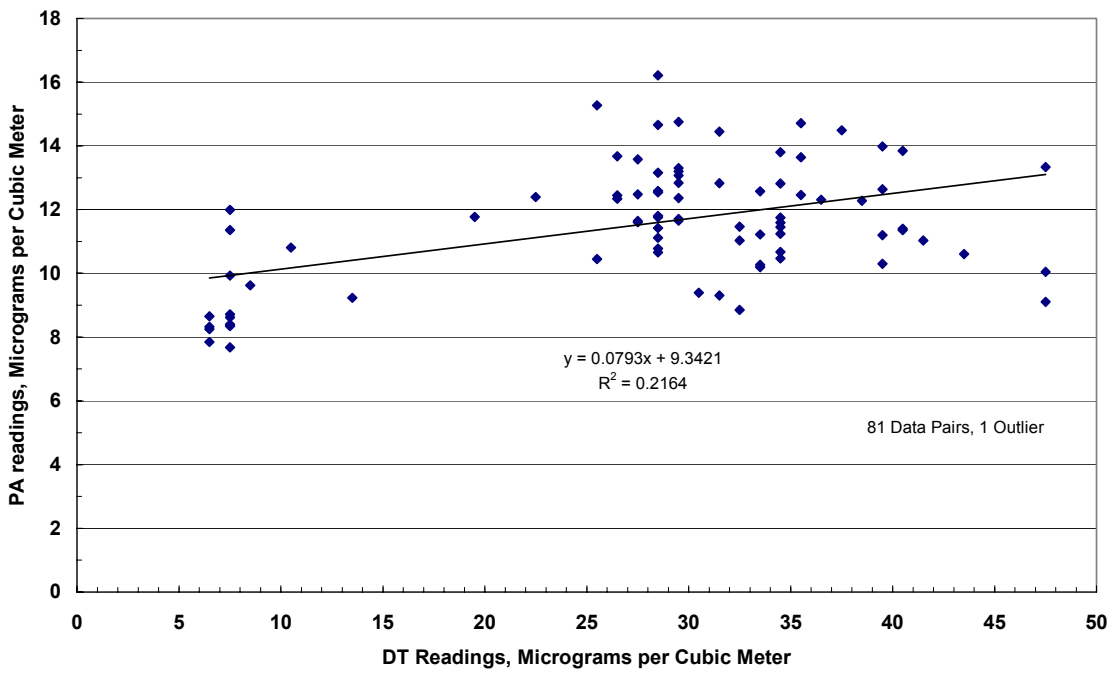


Figure 6-35. Comparison of PA and DT data, run #4.

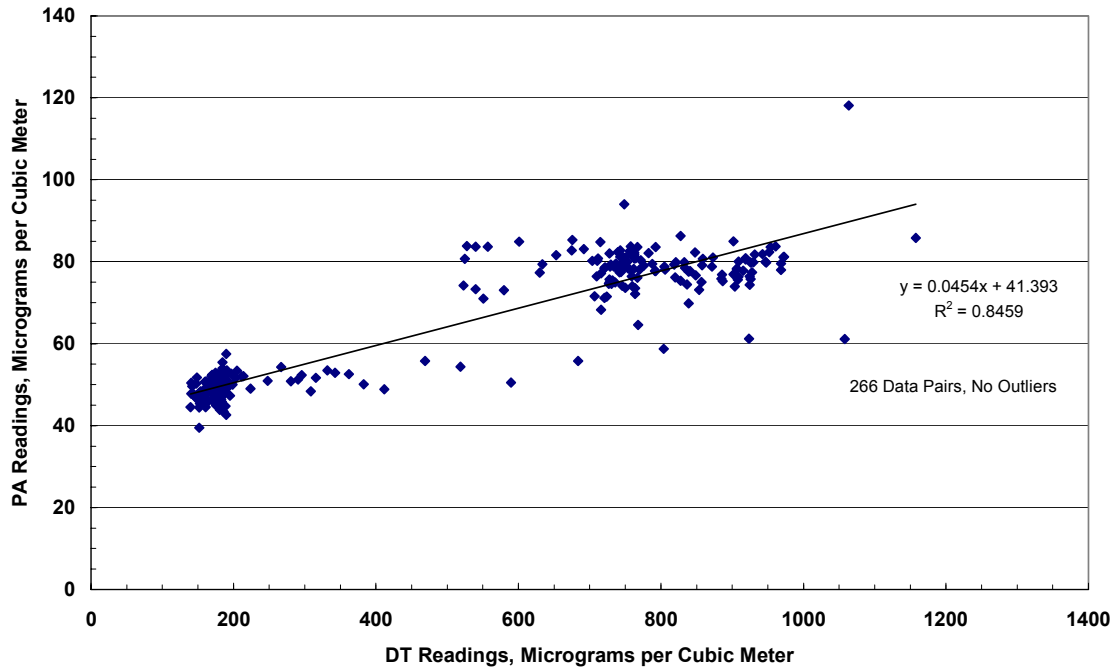


Figure 6-36. Comparison of PA and DT data, run #5.

Unlike the PA-DT comparisons for the AIMD experiments, which gave regression slopes near unity and high r-squared values in all but one case, the comparisons shown in Figures 6-31 to 6-35 indicate slopes in the 0.05 to 0.2 range, and r-squared values from 0.22 to 0.85. With the possible exception of Flightline Run #5, these comparisons show a great deal of scatter and the underlying relationship, if any, between the PA and the DT is not clear. Part of the underlying reason that the relationship between the two data sets is complex is given by Figures 6-24, 6-25, 6-26, 6-28, and 6-29, the time series plots, which show that the PA signal was generally constant in a relative sense, while the DT signal varied considerably even within a time interval corresponding to a constant power setting.

The flightline tests involved one advantage compared to the AIMD cases, namely that the engine power settings and their corresponding time intervals were always quite clear. This allows averaging of the PA and DT data over corresponding power setting intervals, which was not possible for the AIMD data. Averaging in this way attenuates some of the scatter from the data and allows the entire five-run data set to be exhibited on one plot, Figure 6-37.

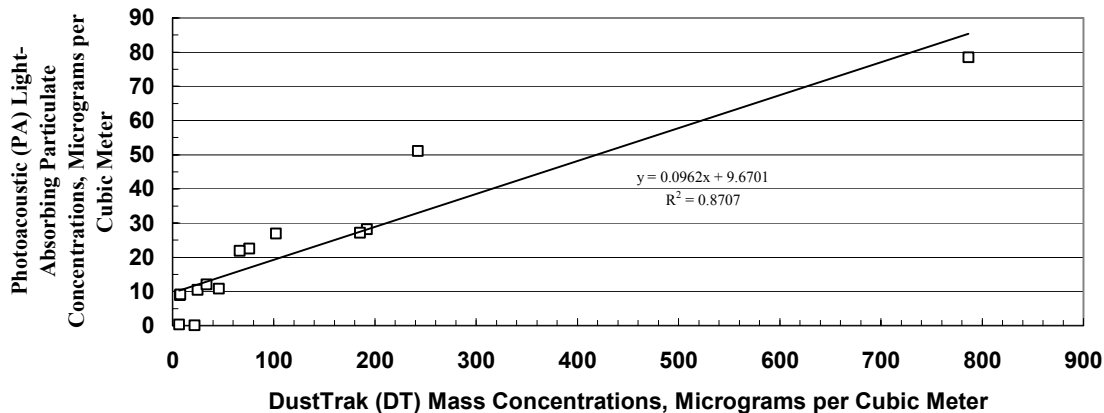


Figure 6-37. Comparison of PA and DT data for all flightline runs.

Figure 6-37 indicates that the averaging approach is successful in revealing a consistent underlying relationship between the two data sets. The r-squared value, 0.87, indicates a significant relationship. The slope, approximately 0.1, indicates that the PA detects about one-tenth of the overall particle population; this is the light-absorbing fraction of the total population for the flightline tests. The y-intercept, approximately $10 \mu\text{g}/\text{m}^3$, may be a reflection of the fact that the lower detection limit of the DT is estimated to be about 0.1 micrometers, while the PA will register light absorption from black particles of all sizes, in proportion to the mass concentration.

Summary of Comparison of PA and DT Data from Flightline Experiments

- The good correlation between the averaged PA and DT data sets indicates that the two instruments tracked and measured closely related properties of the same aerosol particle population.
- The slope of the regression line in Figure 6-38, 0.096, indicates that fewer than 10% by mass of the particles detected by the DT were light absorbing. This upper-limit percentage is conservative, i.e., over-estimated, because the PA can detect particles smaller than the DT.

6.5.4 Conclusions Regarding Objectives #1-#3 at Flightline Site

- An portable instrument pallet was designed to accommodate the PAS, PA, DT, and SMPS. The pallet included an eductor-dilutor sample inlet system, and was effective in allowing exhaust measurements to be obtained from tethered aircraft at the Flightline site. The pallet met its design objectives in terms of safety, reliability, and rapid portability.
- The instruments performed well under the challenging requirements of the flightline: high levels of vibration and noise and rapid deployment.

- The PAS readings often showed the same inverse variation with engine power setting as was shown by the PA and DT. However, in some cases, the PAS signal variations did not correspond to any known variation in the exhaust sources.
- The PA readings, on average, were less than 10% of the DT readings, suggesting that less than 10% of the exhaust particle mass was light-absorbing. The PA data often exhibited a spike when the engine power setting was changed.
- The DT readings generally fell when the power setting was increased. The DT signals sometimes exhibited a spike when engine power settings were changed.
- Comparisons of exhaust particle mass concentration data from the DT and the SMPS raise the possibility that, under some conditions, the SMPS detects “nanoparticle” (i.e., particles smaller than 50 nm) phenomena. Other instruments such as the DT may not detect these phenomena due to the small particle detection limits of the given instrument. However, the evidence for this problem is sparse at this time, and further study would be advisable before altering the other major conclusions of this study for this reason.

6.6 Overall Conclusions from North Island Experiments

The three primary objectives of this report were to evaluate the PAS, the PA, and the DT while sampling jet engine exhaust under field conditions. While characterization of jet exhaust was not a primary objective of the research, the field work led to the following findings concerning its properties:

- For the TF-34, T-700, and F404 engines, low power settings generally produced greater mass concentrations of particulate emissions, and vice-versa. Low power settings have less air flowing through the engine, diluting the particle concentration.
- The TF-34 data were collected at the AIMD augmentor chamber, which involved unquantified amounts of ambient air dilution. For the T-700 and F404 studies for which undiluted exhaust was sampled, the measured mass emissions ranged from about 100 $\mu\text{g}/\text{m}^3$ to about 4 $\mu\text{g}/\text{m}^3$ (corrected for dilutions).
- The TF-34 samples were taken from the AIMD augmentor chamber, which involved possible contamination from vapor-phase material outgassing from the chamber walls as well as residual aerosol left over from previous tests. Residual aerosol is probably flushed out at the onset of each new test. With this caution, the TF34 as well as the T-700 test results indicate that the exhaust particles were mostly composed of light-absorbing carbon. At the Flightline site, measurements of the F404 engine exhaust indicated that only a small fraction (less than 10%) of the particulate mass was light-absorbing carbon.

- For all engines tested, there is evidence that power setting changes cause brief emissions spikes.

6.6.1 Evaluation of PAS (Objective #1)

The PAS instrument was designed for the real-time quantification of particle-phase PAH compounds, which are of critical importance with regard to human health and exposure. PAH compounds are often associated with airborne carbonaceous particulates, as commonly result from combustion processes. Filters and substrates can be exposed and sent to specialized laboratories for analysis and quantification of PAH compounds, but this is expensive and time-consuming. Therefore, a real-time PAH detection instrument is a potentially valuable asset.

Data from the PAS 2000 instruments deployed in this study were compared to data from the Gundel denuder and the MOUDI impactor, two non-real-time but state-of-the-art devices for quantifying PAH compounds. The PAS used in this study were equipped with heated inlets developed for this project (Sarofim and Lighty, 2001). When the PAS data were averaged over a complete experimental run, there seemed to be reasonable agreement with the Gundel and MOUDI data. For TF-34 and T-700 engine exhaust, 1 ng/m^3 of particle-phase PAH compounds (as quantified by the "Seigmann Sum") resulted in a PAS signal level of 4.4 femptoamps. This is in the range of 1-3 ng/m^3 PAH per femptoamp reported by others.

Generally, however, there were repeated indications that the PAS does not always respond in an understandable manner when the particle source undergoes significant changes. The PAS signal sometimes varied inversely to the signals of the other instruments. Furthermore, the PAS signal sometimes displayed a significant change even when the particle source had not undergone any known change. (We cannot rule out errors in the field power setting notes in this regard.)

Overall, for the PAS 2000, the results obtained while sampling rapidly varying jet exhaust (as well as motor vehicle exhaust in previous studies) indicate that further evaluation is needed. This PAS does not yet seem ready for use in routine, as opposed to research, measurements. The goal of a real-time PAH monitor is highly worth pursuing, and various research groups appear to be doing so. A more complete discussion of the PAS evaluation for various military sources can be found in Section 5 of this report.

6.6.2 Evaluation of PA (Objective #2)

The PA signals generally seemed to track the changes in the TF-34 and T-700 exhaust in a quantitative and reproducible manner, although some exceptions were noted (for example, see the elapsed time interval beginning at 1982 seconds, and the 2150 to 2460 elapsed time interval, for AIMD Runs #5 and #6, respectively). Again, errors in the field power setting notes cannot be ruled out. Only a small fraction of the F404 engine exhaust was light absorbing, so the PA signal provided less information for those cases.

The PA and DT data, on average, correlated well. Both instruments' real-time data indicate that they are responding quantitatively to the same variations in the source. Combining the PA and DT seems to be a practical way to capture both the total mass and the light-absorbing carbon ("soot") components of a rapidly varying source. A more complete discussion of the PAS evaluation for various military sources can be found in Section 4 of this report.

6.6.3 Evaluation of DT (Objective #3)

The DT nephelometer is a relatively inexpensive, highly portable instrument that provides an empirical measure of the summed mass concentrations of particles in the approximate diameter range of 0.1 to a few micrometers. During these aircraft measurements, the DT seemed to respond quantitatively to most of the source variations, with a few exceptions as noted in the PA discussion. The conclusion of these tests is that the DT performed surprisingly well, and when calibrated, offers a field-ready option for real-time measurement of particle mass concentrations. When the DT is used in conjunction with the PA, two important measures are obtained, particulate carbon ("soot") and gravimetric mass concentrations.

The DT nephelometer measures particle scattering at a wavelength of 780 nm in a cone of scattering angles near 90 degrees. For the discussion here, the basic behavior of the DT can be understood by considering the theoretical scattering cross section for spherical particles summed over all angles (0 degrees to 180 degrees). Let us suppose that we have calibrated a nephelometer so that it provides an output proportional to the particle scattering coefficient, Sc , in dimensions of inverse distance. The mass scattering efficiency factor is given by the variable MSE (and the vertical axis in [Fig. 1](#)), and as can be seen in [Figure 1](#), is a function of both particle composition, through the refractive index and density, as well as particle size. If we know the particle size and composition, then we can use [Figure 1](#) to compute the mass concentration, M in dimensions of aerosol mass per unit volume, of particles that gave rise to the scattering as

$$M = Sc / MSE \quad (\text{Equation 6-1})$$

Why does the DT give roughly a reasonable value for the mass concentration of exhaust particles even with the relatively large size dependence of MSE? The answer is that it is calibration using weakly absorbing dust particles that have a diameter of around 2 microns. This corresponds to an MSE of a little greater than $1 \text{ m}^2 \text{ g}^{-1}$. If we slide over to the left to smaller particle sizes, we can see that the same MSE applies roughly to 0.1 micron diameter spheres as well, which are roughly the size of combustion particles. So even though the DT is formally calibrated for Arizona road dust, going over the hump, so to speak, shows that the calibration is actually in the ballpark for combustion particles as well. However, there still is a danger. As the particles get ever smaller, the D^3 dependence of scattering in the Rayleigh regime gives rise to decreasing values of MSE, and the need for recalibration based on Equation (6-1).

Incidentally, note that not all particles are created equal. For large diameters, weakly absorbing particles have a mass scattering efficiency about twice that of strongly

absorbing particles, while the opposite is true for small diameters where the ratio is about 5. The dipole moment for small strongly absorbing particles is larger than for small weakly absorbing particles owing to the conductivity implicit in the large imaginary part of the refractive index. Therefore for small jet engine exhaust particles the response from black carbon aerosol will be about a factor of 5 greater than for other particles that absorb weakly.

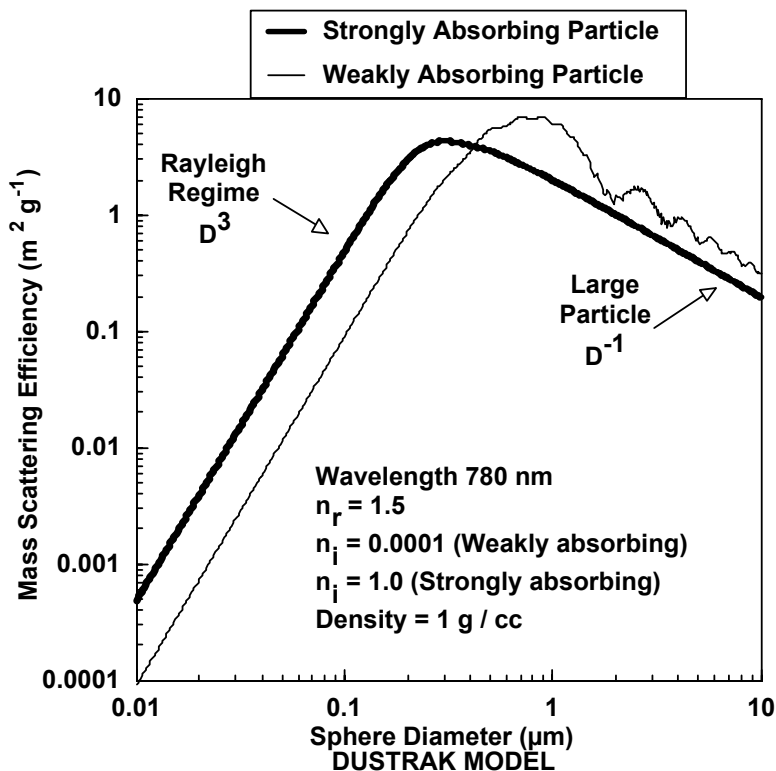


Figure 6-38. Calculated mass scattering efficiency for spherical particles, with sizes and wavelength relevant to the TSI DT calibration.

In summary, the DT is a sensitive instrument for scattering measurements, though one must approach its calibration for mass measurements very cautiously

References

- Arnott, W.P., Moosmuller, H., and Walker, J.W., 2000: Nitrogen Dioxide and Kerosene-Flame Soot Calibration of Photoacoustic Instruments for Measurement of Light Absorption by Aerosols. *Rev. Sci. Instrum.*, **71**, 1-8.
- Burtscher, H., 1992: Measurement and Characteristics of Combustion Aerosols with Special Consideration of Photoelectric Charging and Charging by Flame Ions; *J. Aerosol Sci.*, **23**, 549-595.
- Chow, J.C. 1995: Measurement Methods to Determine Compliance with Ambient Air Quality Standards for Suspended Particles. *J. Air Waste Manage. Assoc.*, **45**, 320-382.
- Gundel, L.A. Lee, V.C., Mahanama, K.R.R., Stevens, R.K., and Daisey, J.M., 1995: Direct Determination of the Phase Distributions of Semi-Volatile Polycyclic Aromatic Hydrocarbons Using Annular Denuders. *Atmos. Environ.*, **29**, 1719.

- Kelly, K. E., Wagner, D.A., Lighty, J.S., Sarofim, A.F., Rogers, C.F., Sagebiel, J., Zielinska, B., Arnott, W.P., and Palmer, G., 2003: Characterization of Exhaust Particles from Military Vehicles Fueled with Diesel, Gasoline, and JP-8. *J. Air Waste Manage. Assoc.*, **53**, 273-282.
- Kirchstetter, T.W., Harley, R.A., Kreisburg, N.M., Stolzenburg, M.R., and Hering, S.V., 1999: On-Road Measurement of Fine Particle and Nitrogen Oxide Emissions From Light- and Heavy-Duty Motor Vehicles. *Atmos. Environ.*, **33**, 2955-2968.
- McDow, S.R., Giger, W., Burtscher, H., et al., 1990: Polycyclic Aromatic Hydrocarbons and Combustion Aerosol Photoemission. *Atmos. Environ. A*, **24**, 2911-2916.
- Marple, V.A., Rubow, K.L., and Behm, S.M., 1991: A Microorifice Uniform Deposit Impactor (MOUDI): Description, Calibration, and Use. *Aerosol Sci. Technol.*, **14**, 434-446.
- Moosmuller, H., Arnott, W.P., Rogers, C.F., Bowen, J.L., Gillies, J.A., Pierson, W.R., Collins, J.F., Durbin, T.D., and Norbeck, J.M., 2001: Time Resolved Characterization of Diesel Particulate Emissions. 1. Instruments for Particle Mass Measurements. *Environ. Sci. Technol.*, **35** 781-787.
- Moosmuller, H., Arnott, W.P., Rogers, C.F., Chow, J.C., Frazier, C.A., Sherman, L.E., and Dietrich, D.L. 1998: Photoacoustic and Filter Measurements Related to Light Absorption During the Northern Front Range Air Quality Study (Colorado 1996/1997). *J. Geophys. Res.*, **103**, 28149-28157.
- Paetow, G., 2003: Personal Communication
- Petzold, A., and Schroder, F.P., 1998: Jet Engine Exhaust Aerosol Characterization. *Aerosol Sci. Technol.*, **28**, 62-76.
- Rogers, C.F., J. Sagebiel, B. Zielinska, W. P. Arnott, J. McDonald, E. Fujita, J. B. Griffin, K. Kelly, D. Overacker, D. Wagner, J. S. Lighty, A. Sarofim, and G. Palmer, 2002: Characterization of Submicron Exhaust Particles from Engines Operating Without Load on Diesel, Gasoline, and JP-8 Fuels. *Aerosol Sci. Technol.*, **37**, 355-368.
- Wang, S.C., and Flagan, R.C., 1990: Scanning Electrical Mobility Spectrometer. *Aerosol Sci. Technol.*, **13**, 230-240.
- Zielinska, B., Sagebiel, J., Arnott, W.P., Rogers, C.F., Kelly, K.E., Wagner, D.A., Lighty, J.S., Sarofim, A.F., and Palmer, G. 2003: Phase and Size Distribution of Polycyclic Aromatic Hydrocarbons in Diesel and Gasoline Vehicle Emissions. Submitted to *Environ. Sci. Technol.*

SECTION 7: EMISSIONS FROM ROCKET FIRINGS

In preparation for the September 2002 rocket firing at Hill Air Force Base in Utah, model rocket engines were tested at UCSD with researchers from Prof. Jamie Schauer's group of the University of Wisconsin at Madison during July 2002. Four different types of rockets were used for the in-lab study, three of which used solid zinc/ammonium perchlorate fuel and the other used black powder. The zinc/ammonium perchlorate rockets were manufactured by Aerotech and the black powder rockets were manufactured by Estes. The types/models of Aerotech rockets used were Blackjack, Blue Thunder and White Lightning. The difference between the types of Aerotech rockets was in the additives that give each rocket a different flame/wake color.

Blue Thunder rockets produced a whitish flame due to the zinc/ammonium perchlorate fuel, but contained no apparent additives. Representative spectra for Blue Thunder model rockets are shown in Figures 7-1a and 7-1b. Both figures show zinc chloride clusters from the fuel while Figure 7-1b shows a particle type that produced mass spectra with ammonium and organics species, which most likely condensed on the particle surface. Elemental carbon was also a common component in the spectra of the Blue Thunder rockets.

White Lightning rockets made a white flame due to the addition of magnesium to the fuel. As with the Blue Thunder rockets, the spectra for the White Lightning rockets (Figures 7-2a and 7-2b) show zinc chloride clusters as well as ammonium-containing particles from the fuel. The White Lightning particles were different from Blue Thunder in that there were few particles that contained elemental carbon and the particles from the White Lightning rockets contained magnesium.

Blackjack rockets produced a black wake, indicating the formation of elemental carbon. Figure 7-3 shows a representative spectrum for the Blackjack model rocket. As with particles from the Blue Thunder and White Lightning rockets, the Blackjack rocket particle spectra contain zinc chloride clusters and ammonium from the fuel. The majority of spectra for the Blackjack rocket consist of this type with elemental carbon ($C_1 - C_5$) in the positive spectra as well as zinc-chloride clusters. Many particles produced by the Blackjack rockets also contained potassium in their spectra. The potassium can be due to impurities, as the ATOFMS is extremely sensitive to this alkali metal.

The Estes black powder engines were tested as well for comparison. As Figure 7-4 shows particles from the Estes engines contained potassium, magnesium, sulfur, and carbon (which is typical of black powder). The major difference in particles from the Estes rockets was the addition of peaks due to sulfates (m/z -64, -80, and -96).

In general, the model rocket tests gave insight into the chemical composition and size distributions of particles expected for the Stage II Minuteman rocket test and were used for comparison.

Blue Thunder Model Rocket

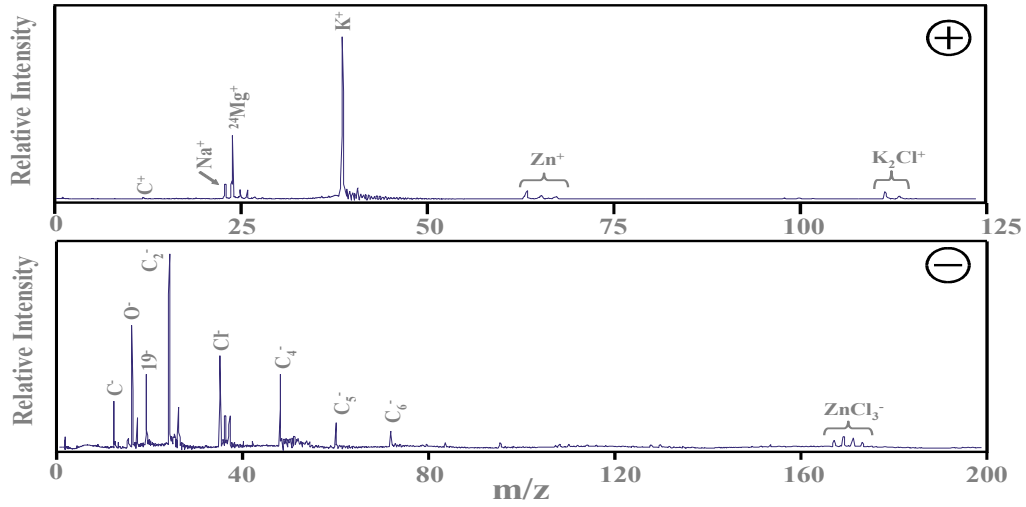


Figure 7-1a. Representative spectra for Aerotech Blue Thunder model rocket.

Blue Thunder Model Rocket

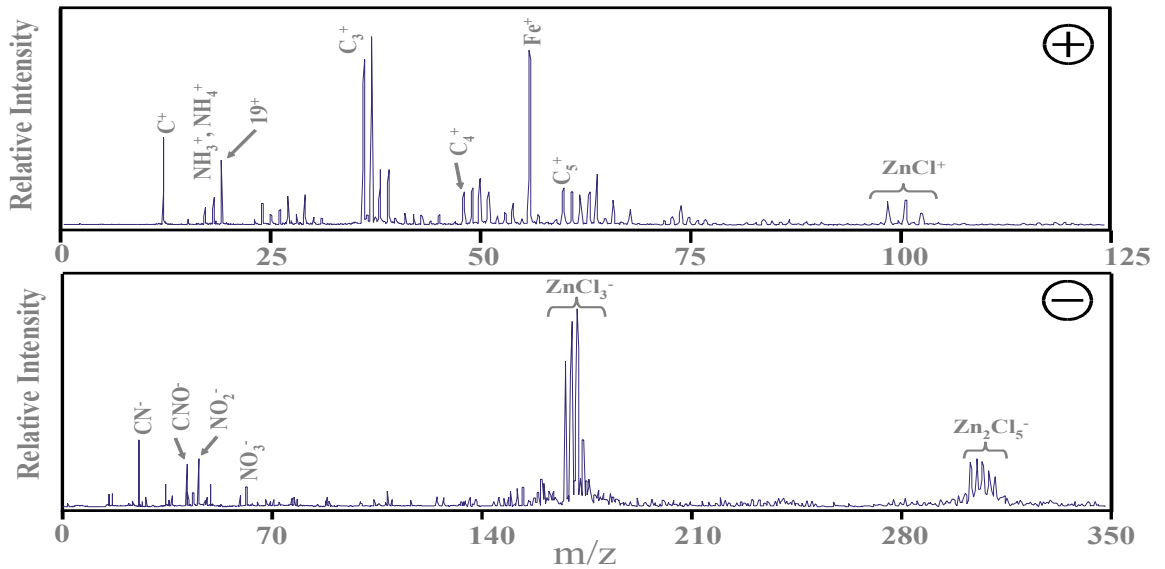


Figure 7-1b. Representative spectra for Aerotech Blue Thunder model rocket.

White Lightning Model Rocket

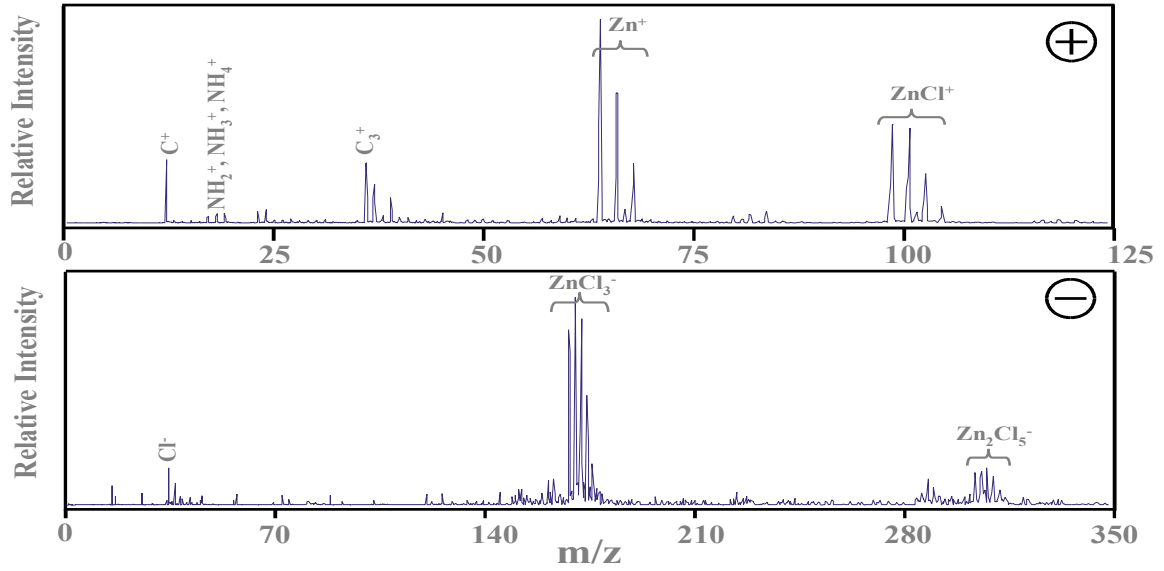


Figure 7-2a. Representative spectra for Aerotech White Lightning model rocket.

White Lightning Model Rocket

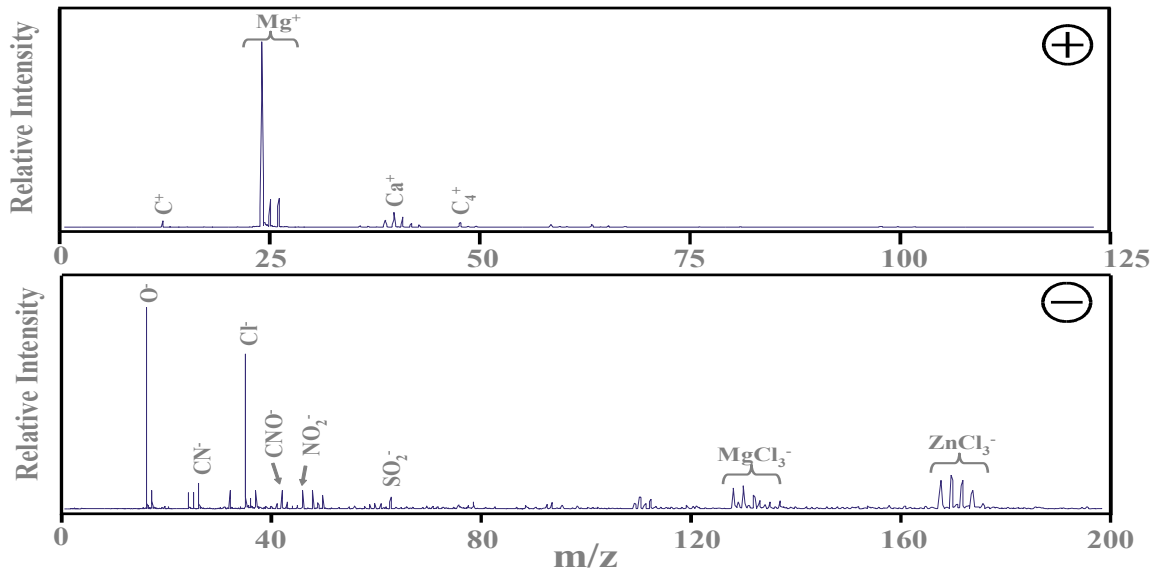


Figure 7-2b. Representative spectra for Aerotech White Lightning model rocket.

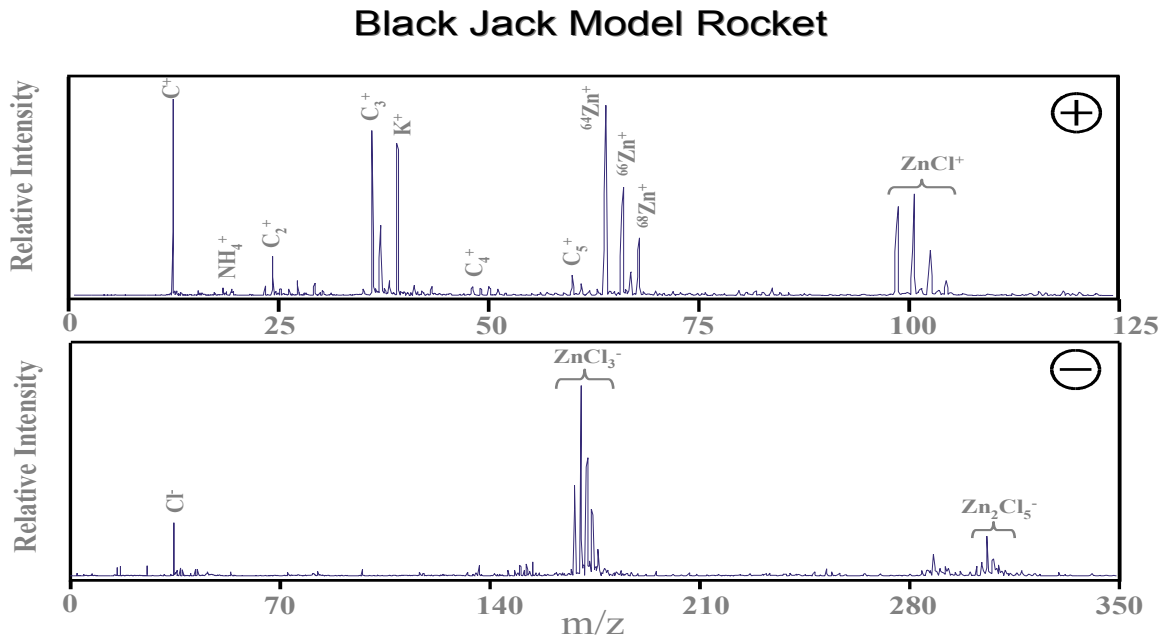


Figure 7-3. Representative spectra for Aerotech Blackjack model rocket.

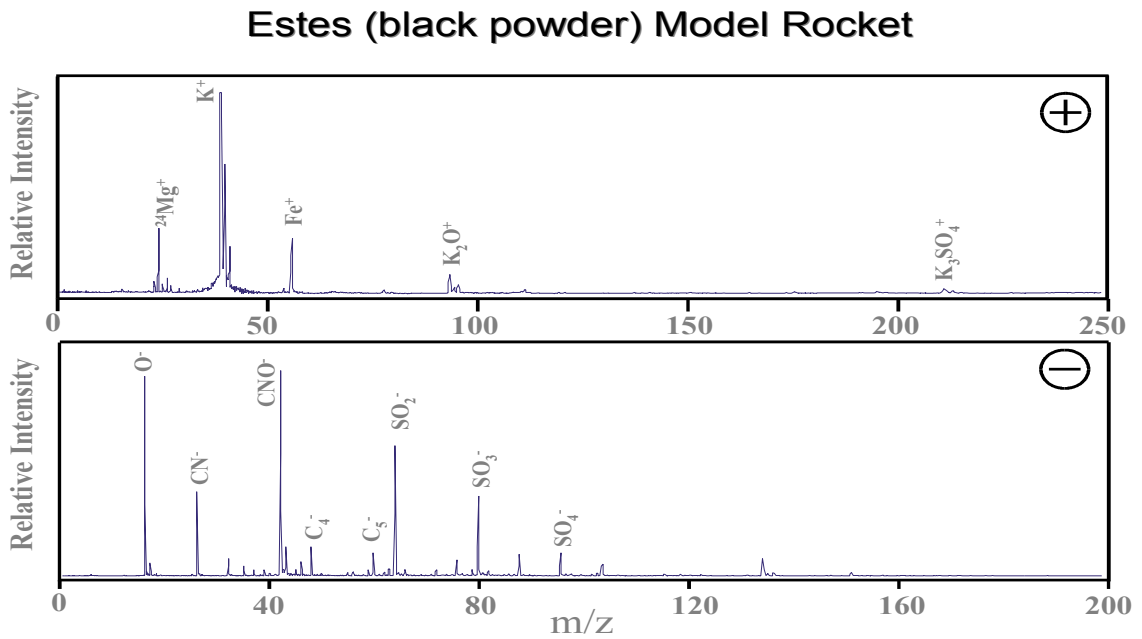


Figure 7-4. Representative spectra for Estes black powder model rocket.

Exhaust emissions from a Minuteman SR19 II rocket motor were collected and analyzed on September 24, 2002 at the Hill AFB testing area. In order to ensure the safety of the ATOFMS instruments, they were not located at the rocket test pad sampling the emissions in real-time. Instead, a 300-L stainless steel vessel with one-inch diameter stainless steel sampling line was used to collect the sample. From the front of the vessel (facing towards the rocket) came the 1-inch diameter stainless steel sampling line that stretched 40-feet along the ground, and then 18-feet into the air secured to a large metal "A"-frame that was staked to the ground. Connected to the back of the vessel were two rotary vane pumps drawing a combined flow of 295-lpm which were controlled by an on/off "threshold" trigger on a DustTrak (TSI) provided by the University of Utah.

When the rocket started firing, particle concentrations in the air instantly increased above a set threshold level on the DustTrak, which in turn triggered a power switch for the pumps on the collection chamber. Once the rocket stopped firing, particle concentrations decreased below the threshold level set on the DustTrak, which shut off the power to the pumps. The sample then sat for 25 minutes to allow the military personnel time to perform a safety check and put out a small fire. Our sampling line had been knocked over during the test by a Hi-Vol sampler setup by a third party consulting group that became airborne from the rocket blast and hit our sampling line. A ball valve for each pump port and the sample port on the chamber were closed and the chamber was taken to the ATOFMS instruments for analysis.

For this study, two ATOFMS instruments were used. The first instrument, with our standard aerosol inlet and interface can reliably size and chemically characterize particles from 170 nm to 3.0 μm . The second instrument is fitted with a newly developed ultrafine interface (aerodynamic lens) that can size and chemically characterize particles between 70 and 250 nm. The ATOFMS instruments along with an SMPS and an APS sampled off the chamber for just over an hour to obtain complete size and composition information from the exhaust plume of the Solid Rocket Motor (SRM).

To distinguish between the soil in the area and rocket emissions, many soil samples were collected before and after the rocket blast. Soil samples were collected in the area where the rocket plume traveled over and areas far away from the blast site. The soil samples were analyzed and the spectra from the rocket emissions were sorted to distinguish particles actually from the rocket from the soil particles suspended by the blast. Due to the fact that the sampling line was knocked down, the ATOFMS data also included local soil/dust that entered the sampling line during the firing event. Therefore, it was important that the soil/dust samples were collected and analyzed for comparison.

A Representative spectrum for the main particle type observed in the wake of the Minuteman SR19 II rocket motor can be seen in Figure 7-5a. Positive spectra attributed to the rocket exhaust consist primarily of aluminum and aluminum oxide from the rocket fuel/combustion catalyst, and trace peaks from other metals (i.e. Li, W). The presence of sodium and potassium in many of the positive spectra may be from an additive or impurity in the rocket fuel. Negative spectra consisted of chlorine and chlorine-metal

cluster ions from the fuel oxidizer, as well as aluminum oxides, ammonium, ammonium nitrate and sulfates.

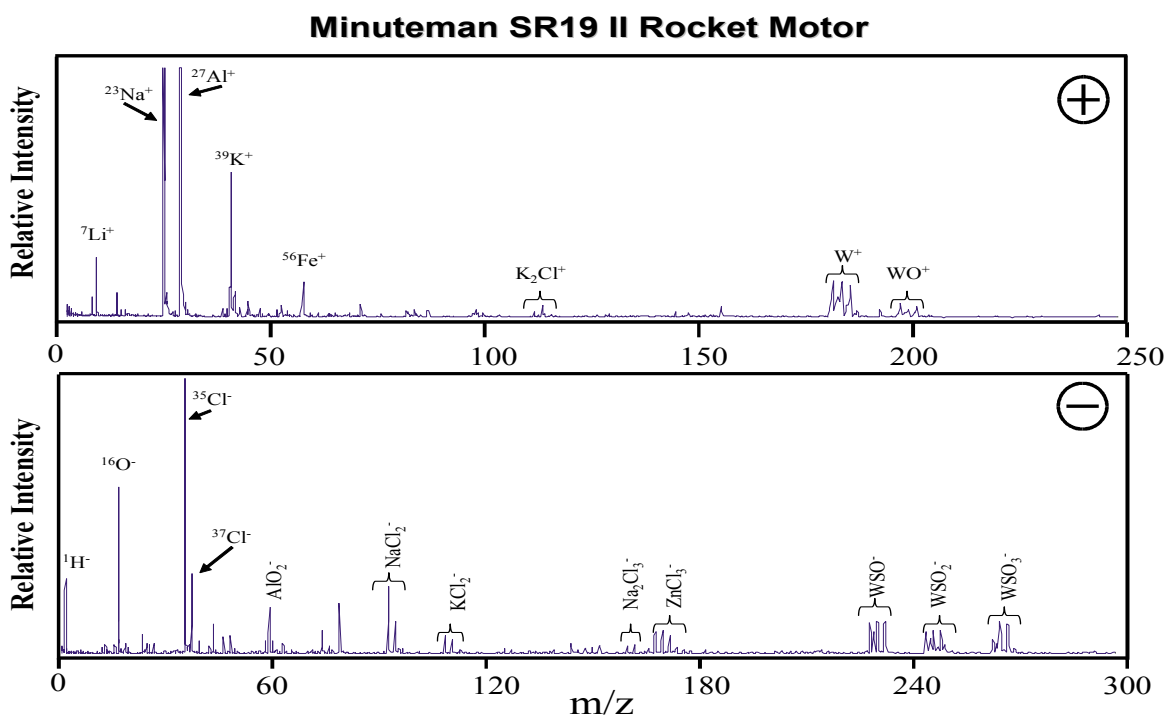


Figure 7-5a. Representative spectra for Minuteman SR19 II rocket motor.

Figure 7-5b shows another major class of particles seen from the rocket wake. The positive spectra of this particle type consisted of peaks attributed to elemental carbon (EC), organic carbon (OC), amines, and lead. Peaks for EC can be seen as +12, +24 and +36 while peaks for OC are at +15, +27 and +37. Peaks attributed to amines are +58, +86 and +118. The negative spectra of this type consist of small peak at -42 from CNO^- , AlO^- at -43, NO_3^- at -62 and -95, -97 (from HSO_4^-) and -106. The presence of this particle type is most likely from the combustion of the carboxyl terminated poly butadiene (CTPB) polymer component in the fuel.

Samples of soil within the rocket exhaust wake zone and outside the zone were analyzed with both ATOFMS instruments to distinguish which spectra obtained during the static rocket firing were from suspended soil. Such spectra were primarily observed with the standard inlet ATOFMS instrument and consisted of particles in the coarse size range. Representative positive and negative ion spectra for the main particle type observed for the soil in the rocket wake zone are shown in Figure 7-6a. Actually, the spectra shown represent the majority of particles seen from all soil samples analyzed (inside and outside the rocket wake zone). The major difference seen from soil samples inside and outside the rocket blast area is the intensity of the Al^+ peak at m/z +27. Positive spectra from the soil samples show that the soil is potassium rich with lithium, sodium, magnesium, and aluminum to a lesser degree. Negative spectra from the soil samples contain O^- , OH^- , CN^- , CNO^- and silicates.

Minuteman SR19 II Rocket Motor

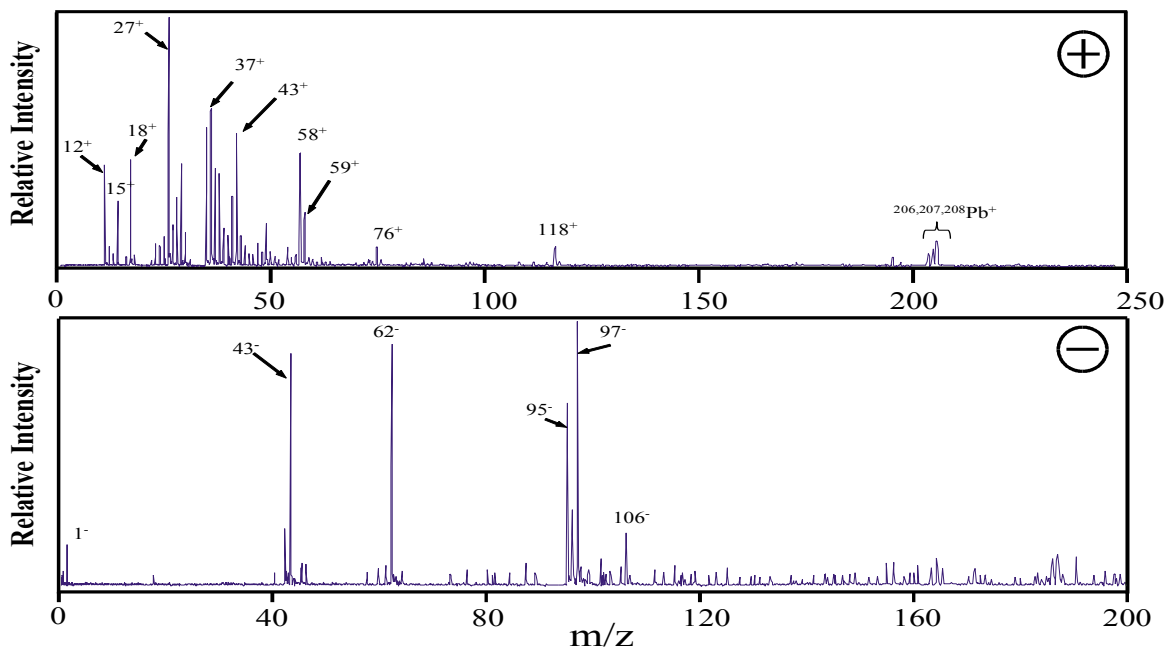


Figure 7-5b. Representative spectra for Minuteman SR19 II rocket motor.

Figure 7-6b shows a representative spectrum of a soil particle that was detected within the rocket blast sample. As shown, this particle type is very similar to that of the soil samples collected prior to and after the rocket firing. The major difference between the two is that the soil particles within the rocket wake have taken up chlorine (m/z -35 and -37) which is abundant within the rocket exhaust. The positive spectra are the same except for the presence of a peak at m/z +74 and 76 which are most likely from the formation of KCl^+ ions.

In general, the major difference between soil particles and rocket exhaust particles is the addition of silicates in the soil-derived particles, as well as the relative abundances of the major metals and the addition of chloride peaks. These tests show ATOFMS is capable of distinguishing between rocket emissions and soil derived particles.

The ATOFMS instrument equipped with an aerodynamic lens inlet for the analysis of ultrafine particles obtained about 2300 spectra with a size peak at 180 nanometers. The other ATOFMS with our standard inlet obtained about 320 spectra and had a size peak at about 1.6 micrometers which could be due to particle agglomeration within the sampling vessel and/or suspended soil from the rocket firing. This study demonstrated that particles in the exhaust emissions of SRMs consist mainly of sub-micron (or fine) particles which are readily distinguishable from local dust or soil sources.

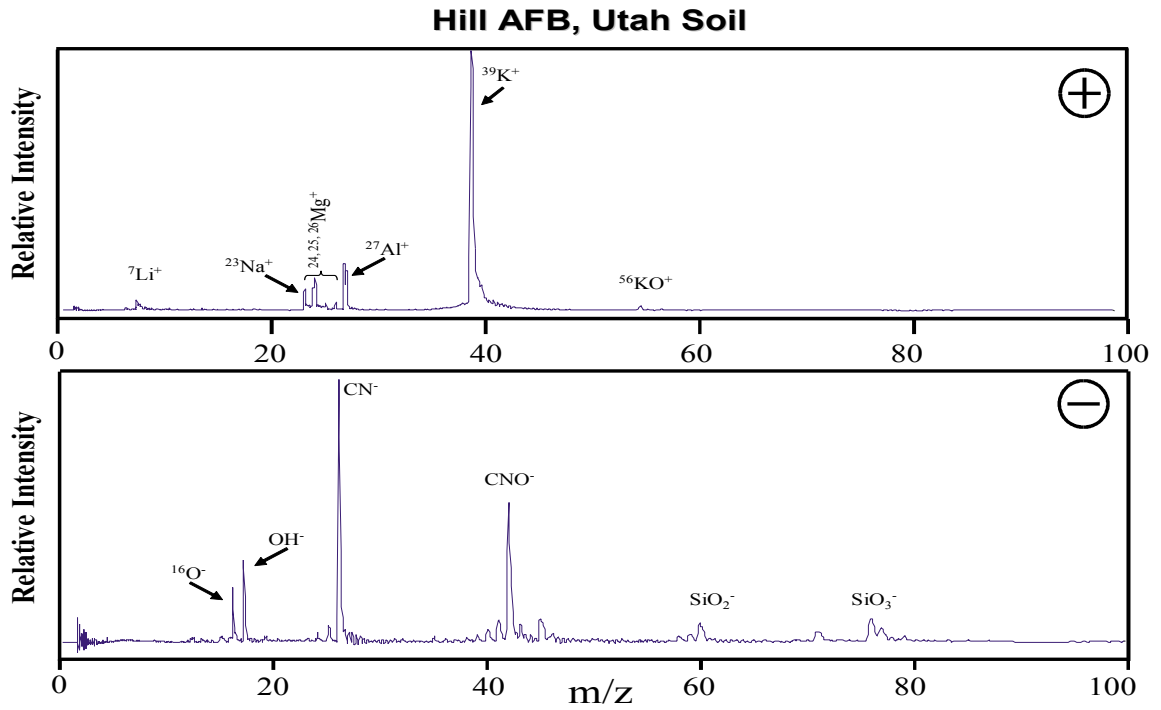


Figure 7-6a. Representative spectra of HAFB soil in rocket wake zone.

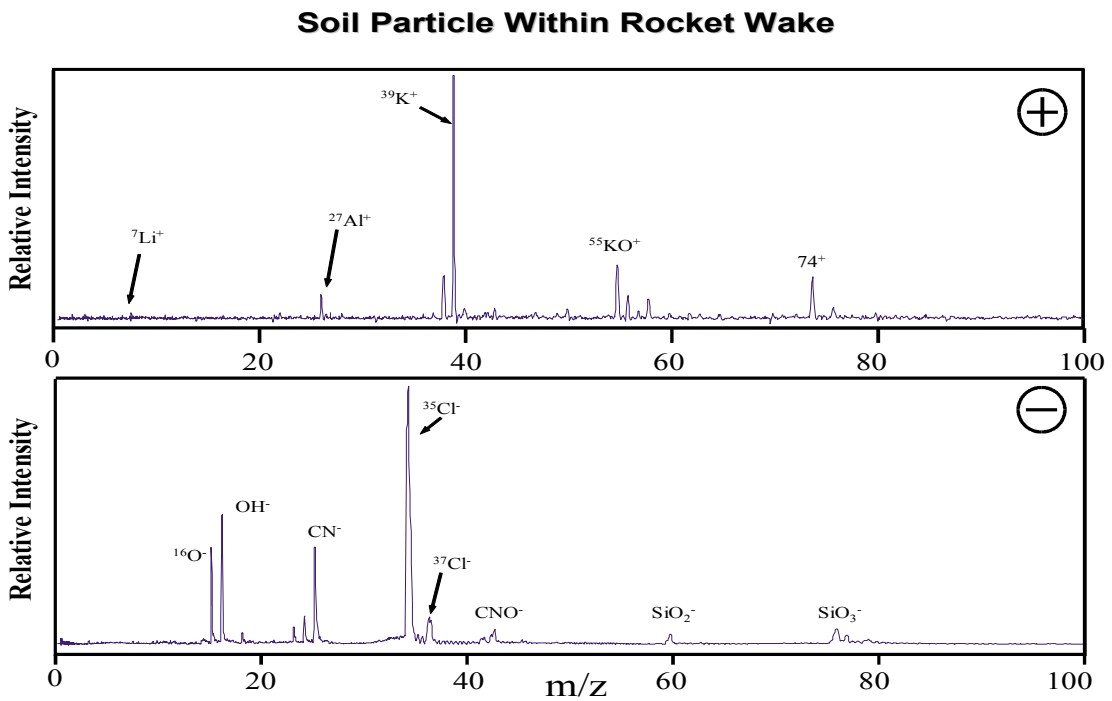


Figure 7-6b. Representative spectra of soil within sampled rocket wake.

SECTION 8: EVALUATION OF DIESEL SOOT FILTERS

The SERDP team collaborated with Dr. Helgeson (NFESC) and his group's ESTCP project to evaluate the effectiveness of diesel soot filters. The complete results have been accepted by the Journal of the Air & Waste management Association and will be published shortly. A draft of the paper can be found in Appendix 5, and a brief summary follows.

In-service diesel engines are a significant source of particulate matter (PM) emissions, and due to their long life and widespread use they have been subjected to increasingly strict emissions standards. Consequently, the wide-scale use of some type of particulate filter is expected. This study evaluated the effect of an Engelhard catalyzed soot filter (CSF) and a Rypos electrically heated soot filter on the emissions from in-service diesel engines in terms of PM, black carbon (soot), particle-bound polycyclic aromatic hydrocarbon concentration, and size distribution. Both filters capture PM. The CSF relies on the engine's exhaust to reach the catalyst regeneration temperature and oxidize soot, whereas the electrically heated filter contains a heating element to oxidize soot. These filters are designed to be durable even when subject to the sulfur content of standard diesel fuel. CSFs were installed on eight in-service military diesel vehicles, and electrical filters were installed on two in-service, JP-8-fueled diesel generators. Particle concentrations and compositions were measured before and after installation of the filter and again after several months of operation. Generally, the CSF removed at least 90% of total PM mass, black carbon, and particle-bound polycyclic aromatic hydrocarbons, and the removal efficiency improved or remained constant after several months of operation. The limited gas-phase pollutant measurements showed that the CSFs also reduced total hydrocarbon and CO emissions. In contrast, the electrical filters removed 44 – 69% of PM mass. In addition to evaluating the soot filters, the sampling team also compared the results of several real-time particle measurement instruments to traditional filter measurements of total mass.

SECTION 9: COMPARISON OF THE EFFECT OF DIESEL AND JP8 FUELS ON PARTICULATE EMISSIONS

9.1 Objectives

The DoD is considering converting many vehicles originally configured for use with diesel fuel to JP8 fuel. Therefore, it is important to understand the potential health effects associated with particulate matter (PM) produced from JP8-fueled engines. The goal of this study was to perform a comprehensive evaluation of the effect of JP8 on PM concentration and composition in engine exhaust. The SERDP team employed real-time particle and gas characterization instrumentation in addition to integrated filter and denuder samples for identification of individual polycyclic aromatic hydrocarbons (PAHs).

Diesel PM has adverse health effects, and it is reasonably anticipated to be carcinogenic (National Toxicology Program 2003; EPA 2002). It contains several PAHs, which are also reasonably anticipated to be carcinogenic, and it contains elemental carbon, which has been linked to adverse cardiac effects (Tolbert et al. 2001). Furthermore, diesel engines are an important source of PM, and studies over the last ten years have linked PM concentration to increased death rates, an increased incidence of asthma, and adverse cardiac effects (EPA 2000, 2002, Dockery et al. 1993, Morawska and Zhang 2002, Peters et al. 2001). More recent evidence indicates that size, surface area, and composition of PM are important factors in determining the health effects associated with PM (Lighty et al. 2000, Maynard and Maynard 2002). For example, fine particles are thought to deposit more deeply in the lungs than larger particles.

9.2 Experimental Methods

The SERDP team measured emissions from a Kubota diesel fueled with diesel and with JP8 under three test conditions. The engine, test conditions, and measurement methods are described in the following sections.

9.2.1 Engine and Test Conditions

The emission tests were performed using the University of Utah's diesel engine test facility, which allows well-controlled engine and sampling conditions. Table 9-1 lists the test and dilution conditions. The test matrix included several duplicate runs to ensure the reproducibility of the results. Hill Air Force Base provided JP8 for the study, and the diesel fuel was Phillips reference diesel fuel, with a cetane number of 46.7 and a sulfur content of 79 ppm.

Table 9-1. Experimental conditions.

Run number	Engine speed (rpm)	Engine load (ft-lb)	Fuel	Dilution ratio*	Temperature (F)	Pressure (mbar)
4	1500	Idle, NA	Diesel	1 in 10.86	86.9	859
3	2200	4	Diesel	1 in 10.86	88.4	862
5	2200	4	Diesel	1 in 10.86	87.3	859
2	2200	8	Diesel	1 in 9.53	84.5	863
9	1500	Idle, NA	JP8	1 in 10.86	87.7	857
8	2200	4	JP8	1 in 10.86	87.2	859
10	2200	4	JP8	1 in 10.86	-	-
7	2200	8	JP8	1 in 10.86	85.5	866
11	2200	8	JP8	1 in 10.86	81.7	870

*raw exhaust in total sample.

The diesel engine is a two-cylinder Kubota model Z482B, with a displacement of 482 cc and a recommended maximum engine loading of 13.8 ft-lb of torque. Fuel consumption varies from 0.8-2.2 l/hr, over a throttle range of 1800-3400 rpm at the shaft. Load simulation is provided by a shaft mounted, direct-drive water-brake dynamometer, manufactured by Land and Sea Corporation. The engine is controlled and monitored with manufacturer-provided software via RS-232 serial connections to an input/output interface module. Engine conditions are controlled through the computer by establishing set points for engine rpm and the dynamometer-induced load. Actuating stepper motors, one cabled to the throttle arm and one on the load valve that regulates the water flow through the dynamometer, are utilized to set rpm and load. These set conditions are maintained with user-defined feedback strategies. Engine data that is monitored and logged include intake airflow rate, fuel consumption, engine oil temperature, exhaust manifold temperature, and engine coolant temperature.

9.2.2 Dilution

In order to keep the PM measurement instruments operating within their ranges and limit water condensation in the sampling systems, the engine exhaust was diluted with dry, particle-free air. The gas-phase measurements of CO, CO₂, NO_x, and O₂ were collected directly from the engine exhaust. Figure 9-1 illustrates the dilution and sampling system, which uses a critical orifice and an eductor to dilute the sample. Briefly, exhaust from the engine's tailpipe flowed into a 1-2 ft long, 3/8" copper sampling probe, located in the exhaust tailpipe. The sample was pulled through a stainless steel critical orifice and into the eductor, where it rapidly mixed with dilution air. Before mixing with the sample, the dilution air passed through a spin-down water filter with a sintered nylon 20-40 µm filter element, a 0.3 µm borosilicate coalescing filter, an activated charcoal filter, and two HEPA filters. Prior to testing, the SMPS performed several scans to ensure that the dilution air was particle free and the sampling system was clean. The diluted sample then passed into a stainless steel sampling chamber where each instrument pulled its sample. The sampling team verified the flows in the dilution system with a Gilibrator flow meter (Gillian Inc.) and an American Meter Corp. dry gas meter.

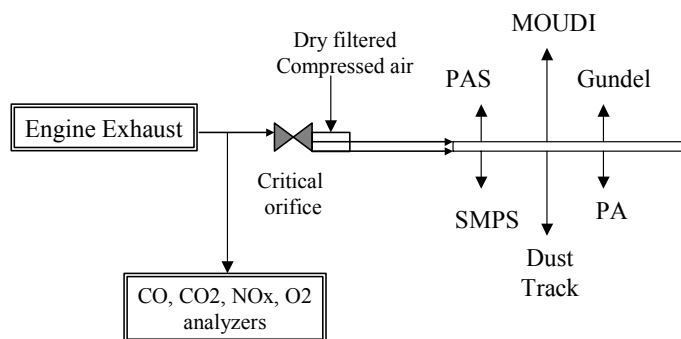


Figure 9-1. Dilution and sampling system.

9.2.3 Emission Measurement Methods

The SERDP team measured particle concentration, particle composition, and gas-phase emissions using a variety of methods (Table 9-2). Briefly, the SERDP team measured PM mass and concentration, black carbon (BC), total particle-bound PAHs, individual gas and particle-phase PAHs, CO, CO₂, NO_x, and O₂.

Table 9-2. Measurement methods.

Instrument	Purpose	Reference
PAS 2000 (PAS)	Real-time PAH detection and quantification	Burtscher, 1992
Photoacoustic analyzer (PA)	Real-time detection and quantification of light-absorbing particles, black carbon	Arnott et al., 2000
DustTrack (DT)	Real-time estimation of particulate mass concentration	Manufacturer's web site, www.tsi.com ; Moosmüller et al., 2001.
Scanning Mobility Particle Sizer (SMPS, TSI, Inc.)	Near-real time measurement of particle size distributions	Wang and Flagan, 1990
Gundel Denuder Sampler	Integrated measurement of PAH compounds in both gas and condensed phases	Gundel et al. 1995
MOUDI (Microorifice Uniform Deposit Impactor, MSP Corp.)	Integrated measurement of particulate mass and carbon	Marple, et al., 1991
California Analytical Inc. ZRH CO/CO ₂ analyzer	Real-time measure of CO and CO ₂	
Thermo Environmental Inc. 42C NO _x analyzer	Real-time measure of NO _x	
Yokogawa Electric Corp. ZA8 O ₂ analyzer	Real-time measure of O ₂	

The PA and PAS are described in Sections 2 and 3 of this report, and the MOUDI and Gundel Denuder sampling and analysis methods are described in Appendix 4. The gas-phase instruments are standard continuous emission monitoring methods.

The SMPS provided particle size distributions for particles ranging from 14.6 - 661 nm (Wang and Flagan, 1990). Integrated mass concentrations from the SMPS were estimated by converting the SMPS differential number data to differential mass data by assuming a particle specific gravity of 1.0 and summing the resulting distributions. Although exhaust particle densities range from 0.5 to 2.0 g/cm³ (Shi et al. 2000), the authors assumed a specific gravity of one in the absence of more accurate data. The SMPS performed between three to ten 135-second size distribution scans at each experimental condition. Thus, the SMPS measurements were averaged, allowing discussion to be based on a single, average size distribution. DustTrack (DT) was selected for the follow-up bus tests and the generator tests. The DT recorded the mass of PM_{2.5} (mg/m³). It operates by measuring 90-degree light scattering at 780 nm and correlating this to mass concentration. Moosmüller et al. 2001 report that the DT measurements correlate well with PM mass from diesel engines.

9.3 Results and Discussion

9.3.1 Real-Time Measurements of PM

Under idle conditions, Table 9-3 shows that JP8 produces lower PM emissions in terms of mass, black carbon, and particle-bound PAHs. This difference is statistically significant at a 95% confidence level (Table 9-4). However, when looking at the higher load conditions, the duplicate runs, and the standard deviations, JP8 does not always produce lower PM emissions. In some cases, Figures 9-2 and 9-3 show that the variations in the results for one fuel are greater than any difference between the diesel and JP8 results. However, JP8 generally produces slightly lower PM emissions. Note that the SMPS could only produce a limited number of scans within the test period, varying from three to ten, whereas the other real-time instruments produced hundreds of data points. Therefore, the differences in the SMPS mass are less likely to be statistically significant due to the limited number of data points.

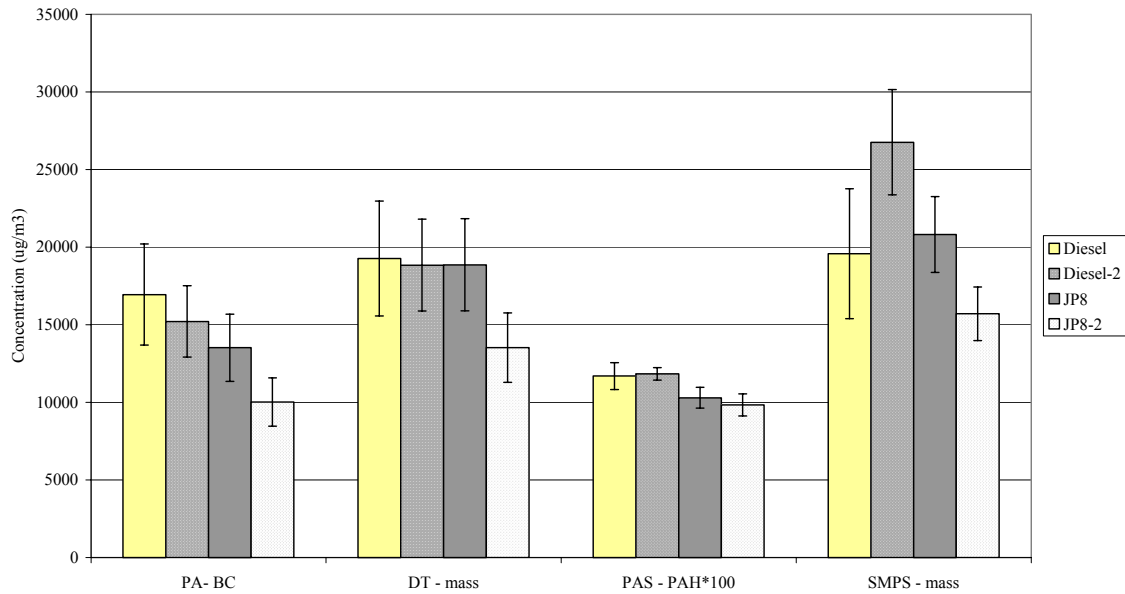


Figure 9-2. Comparison of real-time results for two diesel and two JP8 tests at 2200 rpm and 4 ft-lb. The error bars show the standard deviation.

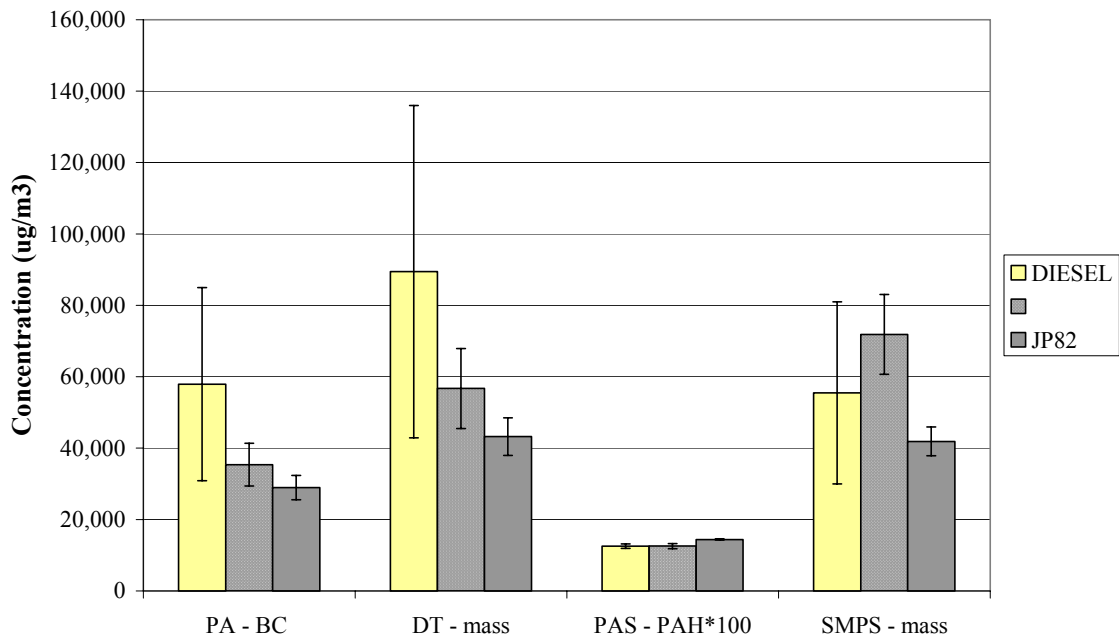


Figure 9-3. Comparison of real-time results for two diesel and two JP8 tests at 2200 rpm and 8 ft-lb. The error bars show the standard deviation.

Table 9-3. Summary of real-time results.

	Diesel				JP8			
	PA (ug/m3)	DT (ug/m3)	PAS (ug/m3)	SMPS (ug/m3)	PA (ug/m3)	DT (ug/m3)	PAS (ug/m3)	SMPS (ug/m3)
Idle								
Average	3070	3395	56.0	4320	1902	1868	47.0	2680
St dev	1240	2110	2.71	215	454	914	2.19	65.5
4 ft-lb (1)								
Average	16,900	19,300	11.7	19600	13,500	18,900	10.3	20,800
St dev	3260	3701	8.66	4180	2171	2970	6.65	2440
4 ft-lb (2)								
Average	15,200	18,800	11.8	26,800	10,020	13,500	9.84	15,700
St dev	2297	2960	4.03	3390	1560	2230	7.14	1730
8 ft-lb (1)								
Average	57,900	89,400	125	55,500	35,400	56,700	126	71,900
St dev	27,030	46,600	6.20	25,500	5960	11,200	7.07	11,200
8 ft-lb (2)								
Average					28,950	43,200	144	41,900
St dev					3380	5280	2.09	4,060

Table 9-4. Conditions where JP8 produced significantly lower emissions, denoted with an x.

Test	BC	PM _{2.5}	Particle-bound PAH	SMPS mass
Idle	x	x	x	x
4 ft-lb	x		x	
4 ft-lb	x		x	x
4 ft-lb	x	x	x	x
4 ft-lb	x	x	x	
8 ft-lb	x	x		
8 ft-lb	x	x		

9.3.2 Gas-Phase Emissions

Table 9-5 summarizes the average gas-phase emissions from at each test condition. Most of the measurements for the duplicate runs agree within 15%, although the JP8 measurements at 8 ft-lb differ significantly. The O₂ readings for the first JP8 run appear to be erroneous, so results for this test should be treated with caution. It is possible that the dynamometer’s load-control was not functioning properly. For a few conditions, some differences are apparent. For example, at the 4 ft-lb condition NO_x emissions for JP8 are slightly higher than those for diesel. Furthermore, JP8 produces higher CO emissions at idle and 4 ft-lb but lower CO emissions at 8 ft-lb. However, these trends reverse at 8 ft-lb. Overall, no consistent trends are evident for the different fuels.

Table 9-5. Average gas-phase emission results.

Measure	Diesel Condition				JP8 Condition				
	Idle	4 ft-lb	4 ft-lb	8 ft-lb	Idle	4 ft-lb	4 ft-lb	8 ft-lb	8 ft-lb
NO _x (ppm)	253	481	501	556	257	581	459	631	401
CO ₂ (%)	2.9	5.9	6.6	9.0	2.94	6.41	5.55	ND	ND
CO (ppm)	416	172	164	219	587	176	238	193	124
O ₂ (%)	16.6	ND	11.4	ND	16.3	11.2	12.4	7.90	12.1

ND: no data.

9.3.3 Particle-Size Distributions

Figures 9-4 to 9-6 compare the average particle size distributions for the diesel and JP8 fuels at each of the three engine settings. For all of the test conditions, a single accumulation mode peak dominates the particle size distributions. At 4 ft-lb, the JP8 did not appear to have a significant effect on the particle size distributions (Table 9-3).

However, it reduced the number concentration at idle and increased the number concentration at 8 ft-lb (Figures 9-3, 9-5). Under all conditions, the JP8 did not change the shape of the particle size distributions significantly. Comparing the idle to the load conditions, increasing engine load caused an increase in particle number and a shift to larger particle sizes, which is consistent with previous results for military vehicles (Kelly et al., 2003).

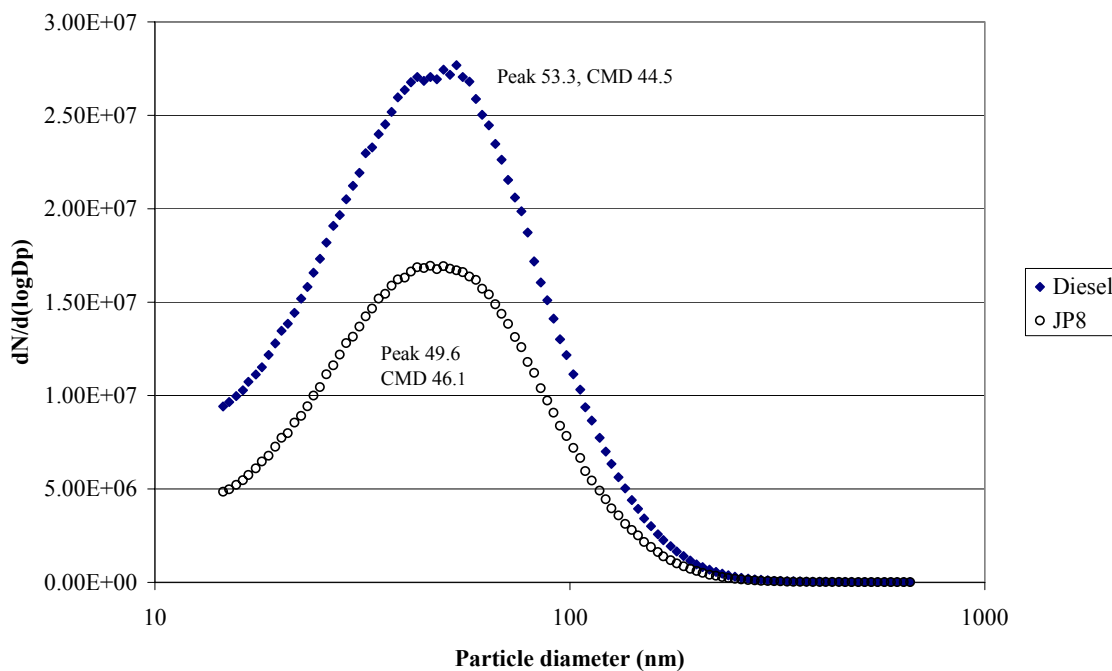


Figure 9-4. Particle size distributions for idle, 1500 rpm.

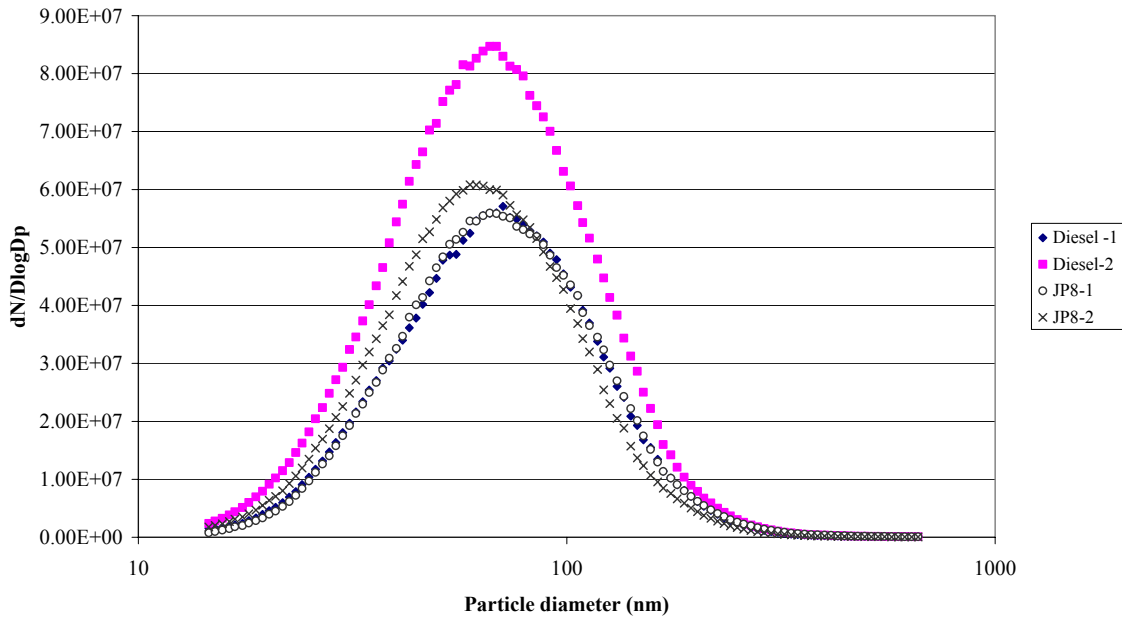


Figure 9-5. Particle size distributions for 4 ft-lb.

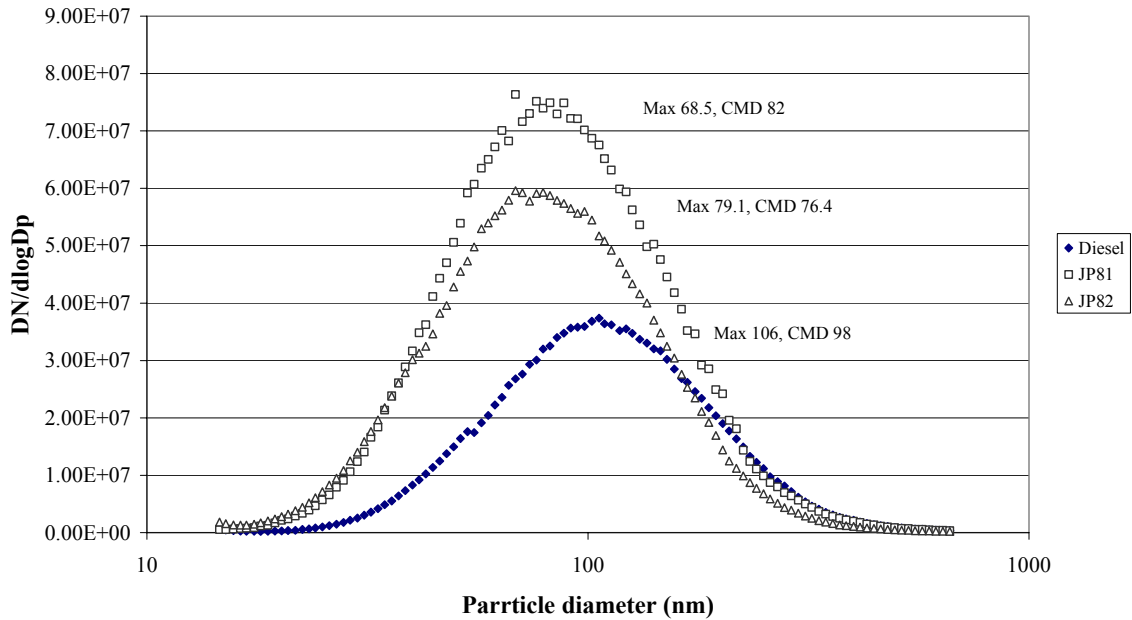


Figure 9-6. Particle size distributions for 8 ft-lb.

9.3.4 Denuder and MOUDI Results for PAHs

Figure 9-7 A, B, C shows the sum of PAHs collected on XAD-coated denuder section, filter and PUF/XAD/PUF section of the annual denuder for all diesel and JP8 fuel runs. Figure 9-7A shows all PAHs analyzed for this study (methylated isomers are summed up for clarity), Figure 1B shows semi-volatile and particle associated PAHs (starting from

phenanthrene up to coronene), and Figure 9-7C - only particle-phase PAHs. As seen in Figure 9-7A, the most volatile gas-phase PAH (naphthalene, methylnaphthalene, dimethylnaphthalene) are the most abundant in both diesel- and JP8-fueled engine exhaust and are emitted roughly in similar amount for corresponding engine cycles. However, the semi-volatile PAHs (Figure 9-7B) are more abundant in the exhaust of the diesel-fueled engine. Especially methyl- and dimethyl-phenanthrenes show higher concentrations in diesel fueled engine exhaust, when comparing corresponding cycles. This is probably due to the higher content of these PAH in the diesel fuel compared to JP8 fuel. In addition, the higher, non-volatile PAH (Figure 9-7C) are also more abundant in the diesel-fueled engine exhaust, although the difference is not as pronounced. These PAHs are believed to be formed during fuel combustion in the engine and are generally not present in the fuel (or present in a very small amount). One can speculate that the methylated semi-volatile PAH are possibly the precursors of higher molecular weight PAHs.

The gas-particle phase distribution of semi-volatile PAH is similar for corresponding engine cycles for both fuels (see Figure 9-8). The percentage of the PAH present in the gas phase is highly dependant on the engine cycle, as shown before (Zielinska et al., 2003).

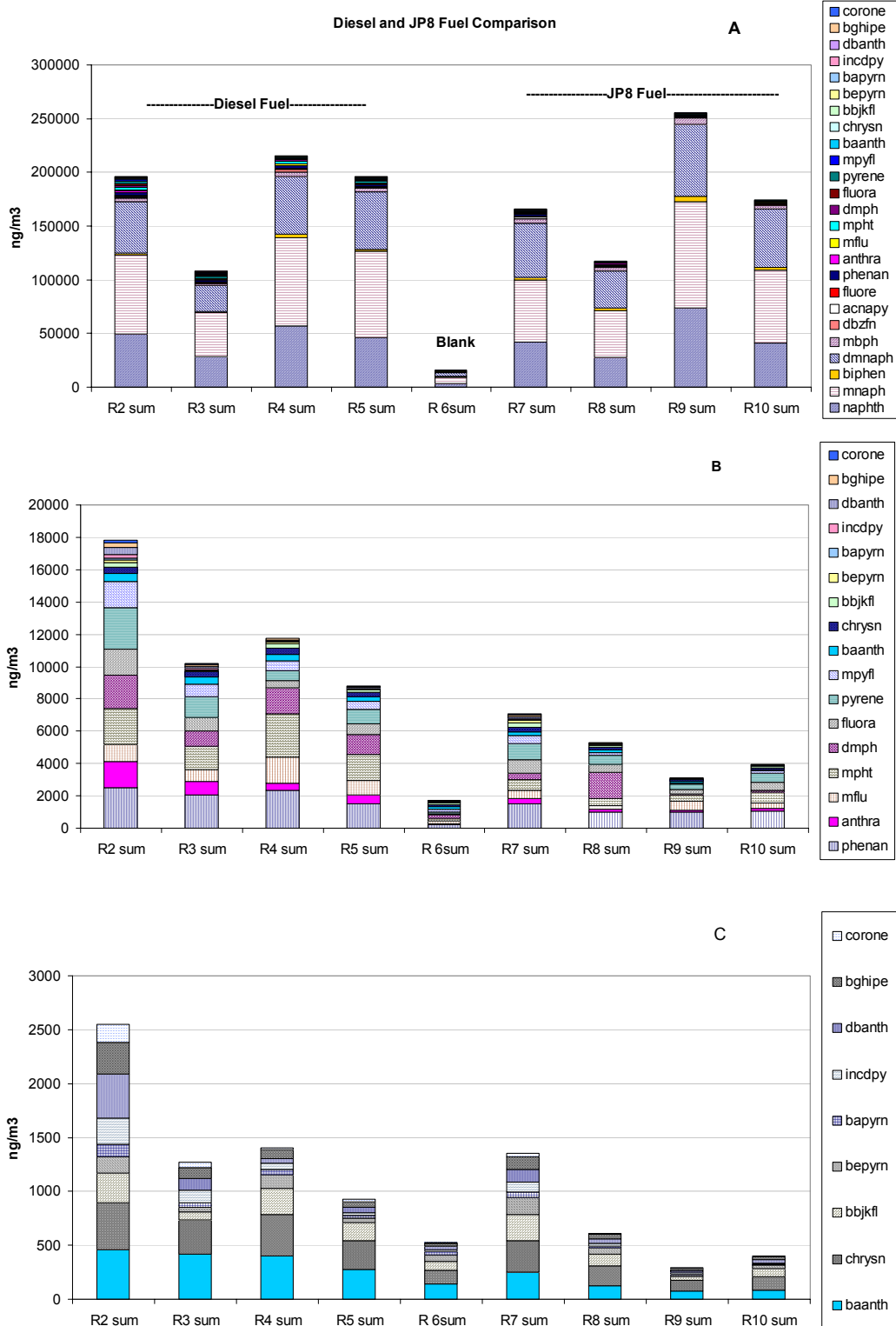


Figure 9-7. The sum of PAH collected on XAD-coated denuder section, filter and PUF/XAD/PUF section of the annual denuder for all diesel and JP8 fuel runs. 1A: all PAH analyzed for this study, 1B: semi-volatile and particle associated PAH, 1C: particle phase PAH;

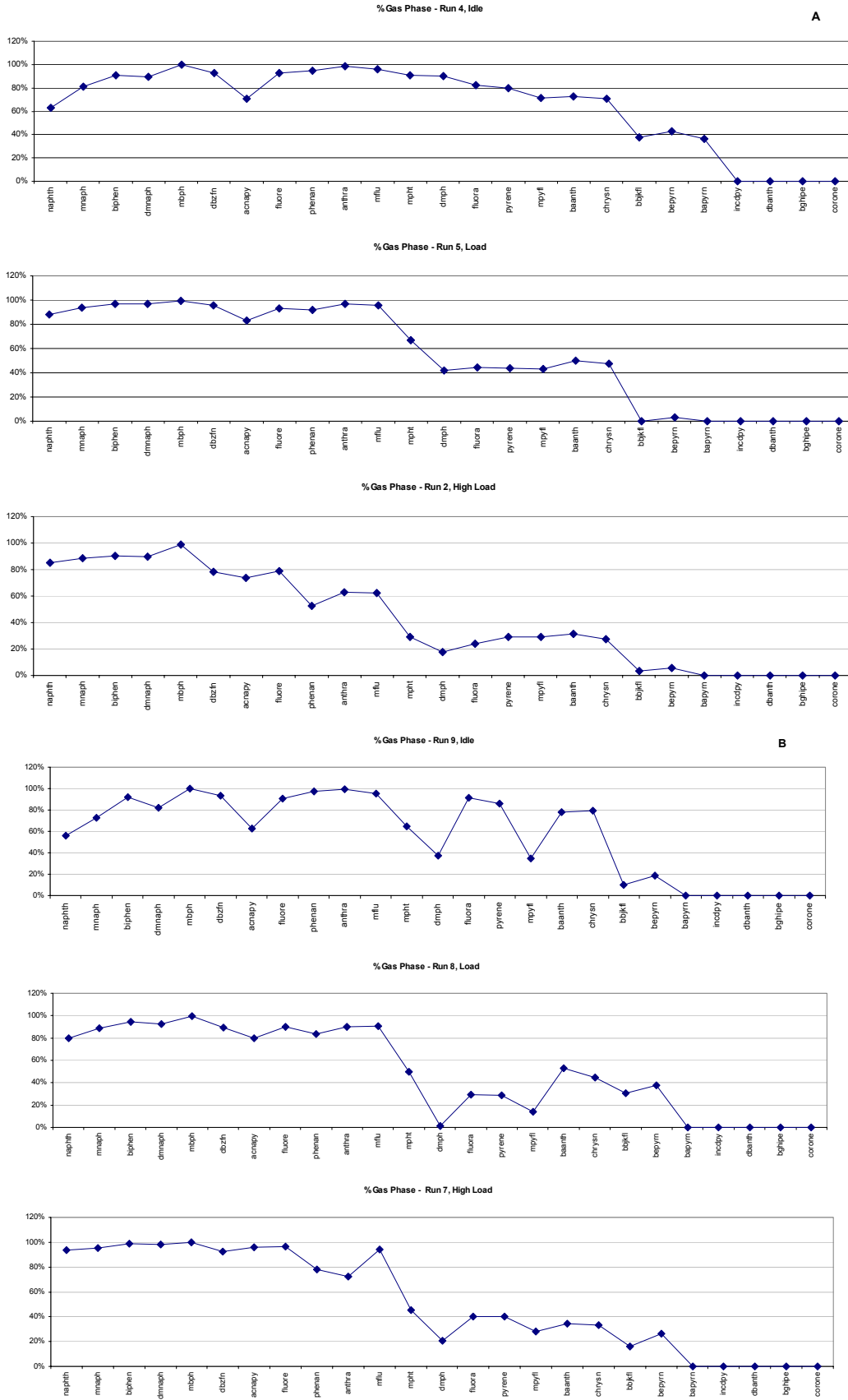


Figure 9-8. The gas-particle phase distribution of semi-volatile PAH.

Figure 9-9 A, B shows the PAH contents on different particle sizes, as measured by MOUDI, for diesel fuel (Figure 9-9A) and JP8 fuel (Figure 9-9B). The gas-phase PAHs (upper panels) are distributed randomly between all stages, which indicates their non-specific adsorption, most likely on the particles collected on the various MOUDI stages (i.e. positive sampling artifact). The particle-associated semi-volatile PAHs (middle panels) and non-volatile 4 through 6-ring PAH (lower panels) are present predominantly on the sub-micron particles collected on MOUDI stages 0.18 μm , 0.096 μm and 0.049 μm . This is consistent with the results reported previously (Zielinska et al., 2003). Semi-volatile PAH are more abundant in diesel exhaust (2200 rpm, 4 ft-lb, run 5), and this is consistent with denuder data. The run of JP8 at 1500 rpm (run 8) shows higher concentrations of particle phase PAH on the after filter, but this might be a positive sampling artifact (i.e. adsorption of gas-phase species on a quartz filter). If the after-filter PAH concentration is disregarded, the total particle-phase PAH concentrations on stages 0.049 - 1.8 μm , is slightly higher for diesel fueled engine exhaust (411 ng/m^3 versus 343 ng/m^3). Again, this is consistent with the denuder data.

Figure 9-10 A and B compares the total of fifteen PAH compounds used in the Siegmann sum (phenanthrene, fluoranthene, pyrene, benzo(b)naphtho(2,1-d)thiophene, benzo(ghi)fluoranthene, benzo(c)phenanthrene, benz(a)anthracene, chrysene/triphenylene, benzo(b+j+k)fluoranthene, benzo(e)pyrene, benzo(a)pyrene, indeno(1,2,3-cd)pyrene, benzo(ghi)perylene, and coronene) collected by MOUDI method and denuder method (only particle phase concentrations, i.e. the sum of denuder filter plus PUF/XAD/PUF solid adsorbent following the filter to account for the blow-off the filter) for run 5 and run 8. It could be seen from this figure that the correlation between denuder and MOUDI was greatly improved for run 8 when the after filter concentrations were omitted. For run 5, this didn't make any difference.

9.3.5 MOUDI Mass and Elemental Carbon Results

The MOUDI mass and elemental carbon results show that JP8 reduces emissions at idle, but the results under load were inconsistent (Table 9-6). The real-time results showed a similar trend at idle but also showed small reductions under load (Table 9-3).

Table 9-6. MOUDI elemental carbon (EC) and total mass concentrations.

Test	Run number	Fuel	Mass ($\mu\text{g}/\text{m}^3$)	EC ($\mu\text{g}/\text{m}^3$)
Idle	4	Diesel	2284	457
4 ft-lb	3	Diesel	3270	1144
4 ft-lb	5	Diesel	3380	1494
8 ft-lb	2	Diesel	8034	4,653
Idle	9	JP8	1833	281
4 ft-lb	8	JP8	3920	1351
4 ft-lb	10	JP8	3420	837
8 ft-lb	7	JP8	8500	3759

9.4 Conclusions

Compared to diesel fuel, JP8 slightly reduced black carbon, PM_{2.5} mass, particle number, and particle-bound PAH emissions at idle. Under load, the results were inconsistent, and under all conditions JP8 had no effect on the shape of the particle size distributions. In terms of denuder and MOUDI results, the JP8 fuel reduced the total concentration (gas and particle phase) of semi-volatile PAHs, particularly methyl- and dimethyl-phenanthrenes, and particle-phase PAHs, but had no effect on the most volatile PAHs. The semi-volatile PAHs and the heaviest PAHs were predominately found in the smallest MOUDI stages. The MOUDI results confirmed the trends seen in the denuder.

References

- Arnott, W.P., Moosmuller, H., and Walker, J.W., Nitrogen Dioxide and Kerosene-Flame Soot Calibration of Photoacoustic Instruments for Measurement of Light Absorption by Aerosols. *Rev. Sci. Instrum.* **2000**, *71*, 1-8.
- Burtscher, H., Measurement and Characteristics of Combustion Aerosols with Special Consideration of Photoelectric Charging and Charging by Flame Ions, *J. Aerosol Sci.*, **1992**, *23*, 549-595.
- EPA *Health Assessment Document for Diesel Exhaust*, **2002**, EPA 600/8-90/057F. National Center for Environmental Assessment, Office of Research and Development, Washington DC.
- Dockery, D.W.; Pope, A.C.; Xiping, X.; Spengler, J.D.; Ware, J.H.; Fay, M.E.; Ferris, B.G.; Speizer, F.E. An Association between Air Pollution and Mortality in Six U.S. Cities; *New Engl. J. Med.* **1993**, *329* (24) 1753-1759.
- Gundel, L.A. Lee, V.C., Mahanama, K.R.R., Stevens, R.K., and Daisey, J.M., Direct Determination of the Phase Distributions of Semi-Volatile Polycyclic Aromatic Hydrocarbons Using Annular Denuders. *Atmos. Environ.* **1995**, *29*, 1719.
- Kelly, K. E., Wagner, D.A., Lighty, J.S., Sarofim, A.F., Rogers, C.F., Sagebiel, J., Zielinska, B., Arnott, W.P., and Palmer, G., 2003: Characterization of Exhaust Particles from Military Vehicles Fueled with Diesel, Gasoline, and JP-8. *J. Air Waste Manage. Assoc.* **2003**, *53*, 273-282.
- Lighty, J.S.; Veranth, J.M.; Sarofim, A.F. Combustion Aerosols: Factors Governing their Size and Composition and Implications to Human Health. Critical Review; *J. Air & Waste Man. Assoc.* **2000**, *50*, 1565-1618.
- Marple, V.A., Rubow, K.L., and Behm, S.M., A Microorifice Uniform Deposit Impactor (MOUDI): Description, Calibration, and Use. *Aerosol Sci. Technol.* **1991**, *14*, 434-446.
- Maynard A.D., R.L. Maynard, A derived association between ambient aerosol surface area and excess mortality using historic time series data, *Atmos. Environ.* *36* **2002**, 5561-5567.
- Moosmuller, H., Arnott, W.P., Rogers, C.F., Bowen, J.L., Gillies, J.A., Pierson, W.R., Collins, J.F., Durbin, T.D., and Norbeck, J.M., 2001: Time Resolved Characterization of Diesel Particulate Emissions. 1. Instruments for Particle Mass Measurements. *Environ. Sci. Technol.* **2001**, *35* 781-787.
- Morawska L., J. Zhang Combustion sources of particles 1. Health relevance and source signatures, *Chemosphere* *49* (2002) 1045-1058.
- National Toxicology Program, *10th Report on Carcinogens*, **2003**, U.S. Department of Health and Human Services, National Toxicology program, <http://ehis.niehs.nih.gov/roc>

Peters A.; Dockery, D.; Muller J.E.; Mittleman M.A. Increased Particulate Air Pollution and the Triggering of Myocardial Infarction; *Circulation*, **2001**, 2810-2815.

Shi, J.P.; Mark, D.; Harrison, R.M. Characterization of Particles from a Current Technology Heavy-Duty Diesel Engine; *Environ. Sci. Technol.* **2000**, *34*, 748-755.

Tolbert P.E., M. Klein, K.B. Metzger, J. Peel, W.D. Flanders, K. Todd, J.A. Mulholland, P.B. Ryan, H. Frumkin Interim Results of the Study of Particulates and Health in Atlanta (SOPHIA), *J. Exposure Analy. and Env. Epid.* **2000**, *10*, 446-460.

Wang, S.C., and Flagan, R.C., 1990: Scanning Electrical Mobility Spectrometer. *Aerosol Sci. Technol.* **1990**, *13*, 230-240.

Zielinska, B., Sagebiel, J., Arnott, W.P., Rogers, C.F., Kelly, K.E., Wagner, D.A., Lighty, J.S., Sarofim, A.F., and Palmer, G. 2003: Phase and Size Distribution of Polycyclic Aromatic Hydrocarbons in Diesel and Gasoline Vehicle Emissions. Submitted to *Environ. Sci. Technol.*

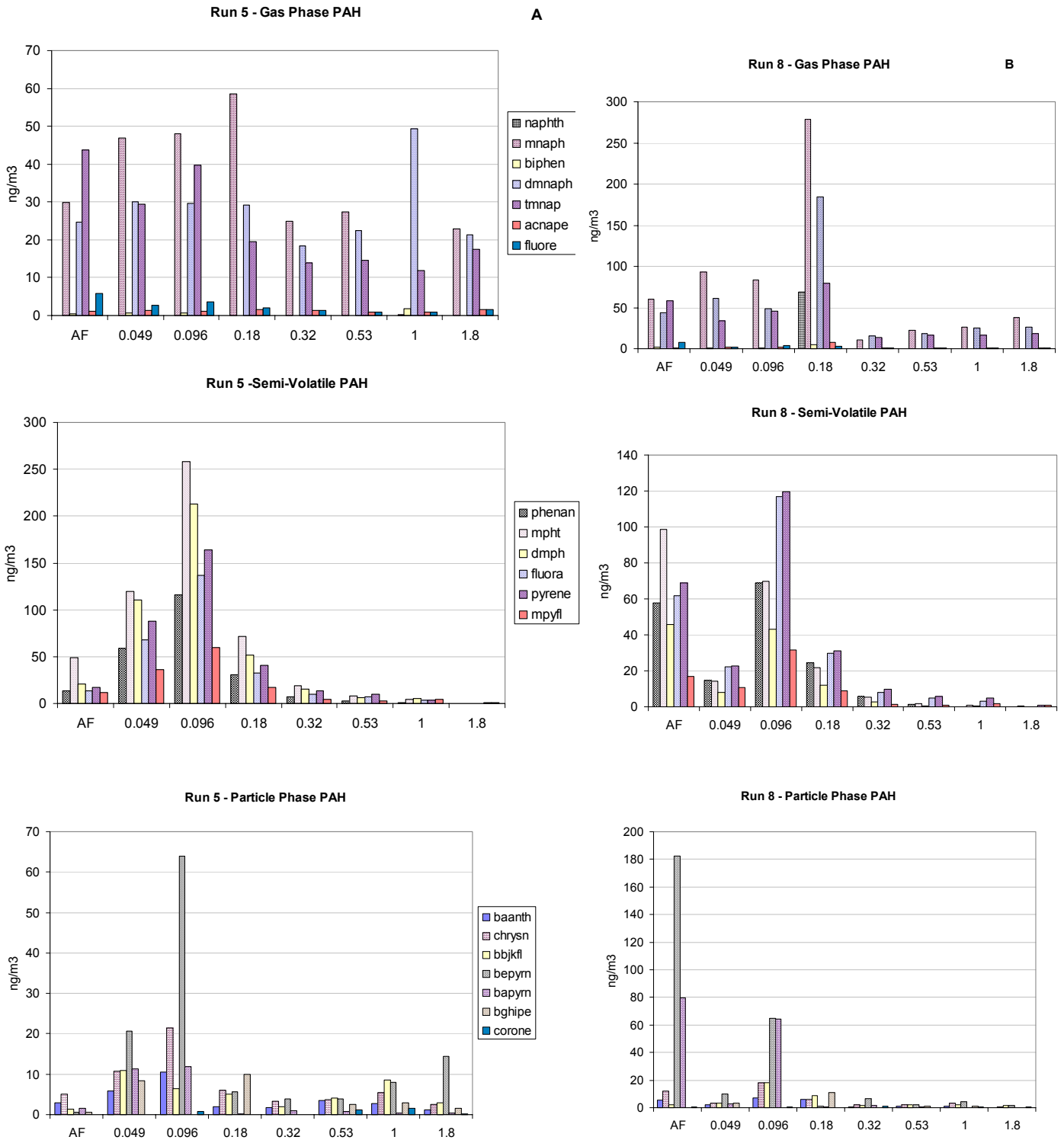


Figure 9-9. PAH contents on different particle sizes, as measured by MOUDI, for diesel fuel (Figure 9-8A) and JP8 fuel (Figure 9-8B).

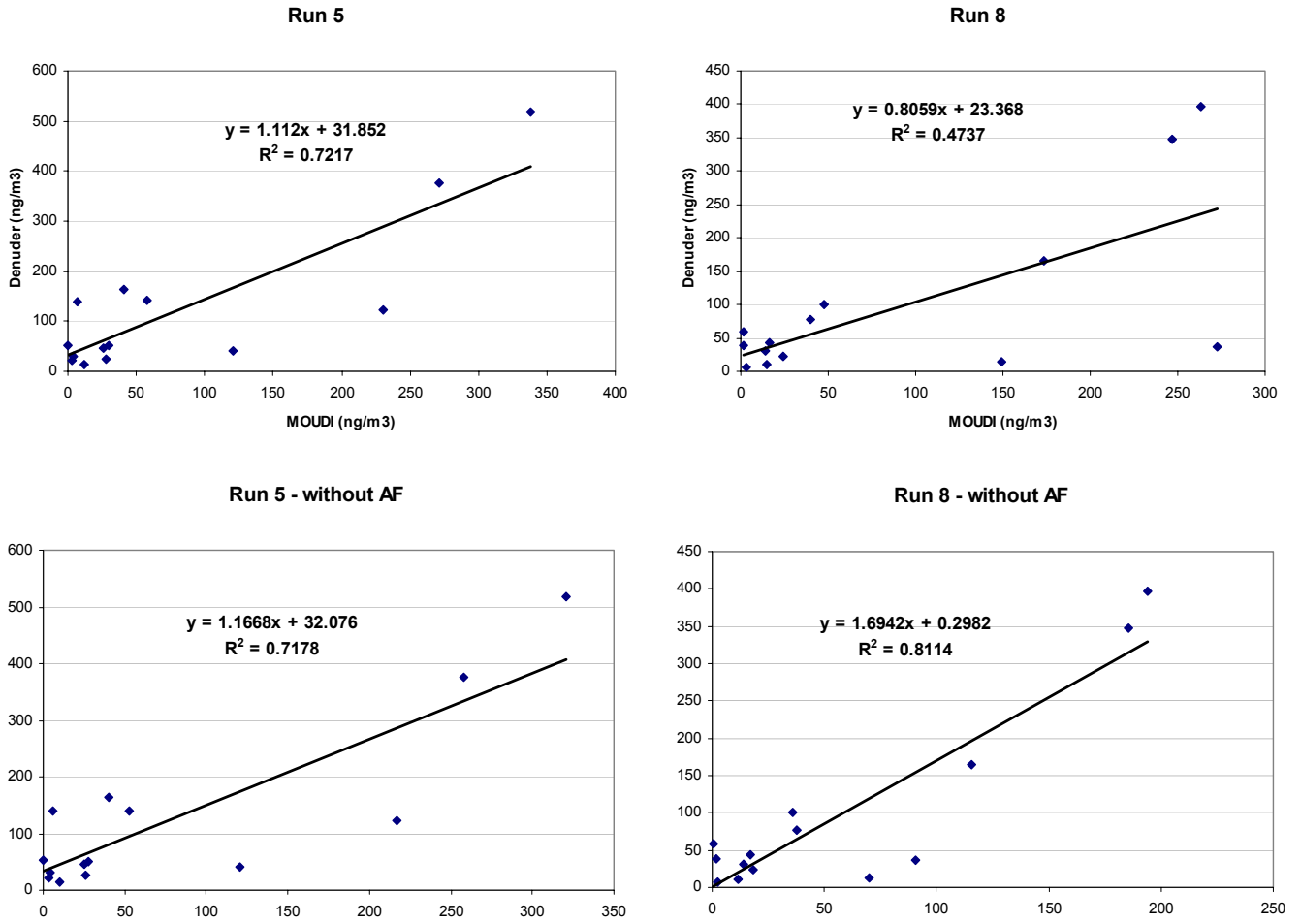


Figure 9-10. Comparison of Siegmansum PAH collected by the MOUDI and denuder.

SECTION 10: SIMULATION OF THE EVOLUTION OF PARTICLE SIZE DISTRIBUTION IN A VEHICLE EXHAUST PLUME

Over the past several years, numerous studies have linked ambient concentrations of particulate matter (PM) to adverse health effects, and more recent studies have identified PM size and surface area as important factors in determining PM's health effects. This study contributes to a better understanding of the evolution of particle size distributions in exhaust plumes. It combines computational fluid dynamics (CFD) with an aerosol dynamics model to examine the effects of: different streamlines in an exhaust plume, ambient particle size distribution, and vehicle and wind speed on the particle size distribution in an exhaust plume. CFD was used to calculate the flow field and gas mixing for unconfined dilution of a vehicle exhaust plume. The calculated dilution ratios were then used in the aerosol dynamics simulation. The results show little difference in particle coagulation along different streamlines. Furthermore, increasing vehicle speed increased the dilution rate and decreased the effects of particle coagulation. Finally, the particle size distribution of ambient air has the greatest impact on the largest and smallest particle sizes in the exhaust plume's particle size distribution.

10.1 Introduction

Particulate matter emissions from internal combustion engines have been studied extensively due to their adverse health effects (Vedal 1997). Studies over the last ten years have linked PM concentration to increased death rates, an increased incidence of asthma, and adverse cardiac effects (EPA 2002, Dockery et al. 1993, Morawska and Zhang 2002, Peters et al. 2001). More recent evidence indicates that the composition, size, and surface area of PM are important factors in determining the health effects associated with PM (Maynard and Maynard 2002, Lighty et al. 2000). Because PM emissions from internal combustion engines are generally smaller than 0.1 μm and finer particles can deposit more efficiently in the lung (Hinds 1999), understanding the evolution of particle size distributions in an exhaust plume could have implications for human health.

The particle size distribution from vehicle exhaust has been measured by using a bag sampler (Kittelson et al. 2000), dilution tunnel (Shi et al. 1999a, 1999b; 2000; Maricq et al. 2001, 2000, 1999; Harris and Maricq 2001; Rogers et al. 2003), and ejector diluter (Abdul-Khalek et al. 1999; Maricq et al. 1999, 2000, 2001; Shi et al. 2000; Harris and Maricq 2001). Accurate measurement of the exhaust particle size distribution at various locations downstream of the exhaust plume is a very difficult task because it involves simultaneous coagulation, nucleation, and dilution by ambient air, which also contains particles. Combining CFD with aerosol dynamics simulation may give us some insight into the particle size distribution downstream of the exhaust plume.

This study couples CFD with aerosol dynamics and focuses on four factors that influence particle size distribution in an exhaust plume: vehicle speed, wind speed, ambient particle size distribution, and the location of particles along an exhaust streamline. The study focused on a diesel fueled Dodge Bobtail.

10.2 Methods

10.2.1 Model Vehicle and Conditions

The vehicle was a 1991 Ford Bobtail-Eagle Model EB-2, and Figure 10-1 shows its geometry. The U.S. Air Force uses Bobtails to tow aircraft and to haul aircraft payloads. Its maximum speed is approximately 25 mph. The air temperature was assumed to be 20°C, and the tailpipe exhaust properties were taken to be those of air at 100°C. The tailpipe was directed to the rear of the vehicle on the left hand side, as viewed from the rear. The diameter of the exhaust pipe was four inches, and the exit velocity was 60 m/s.

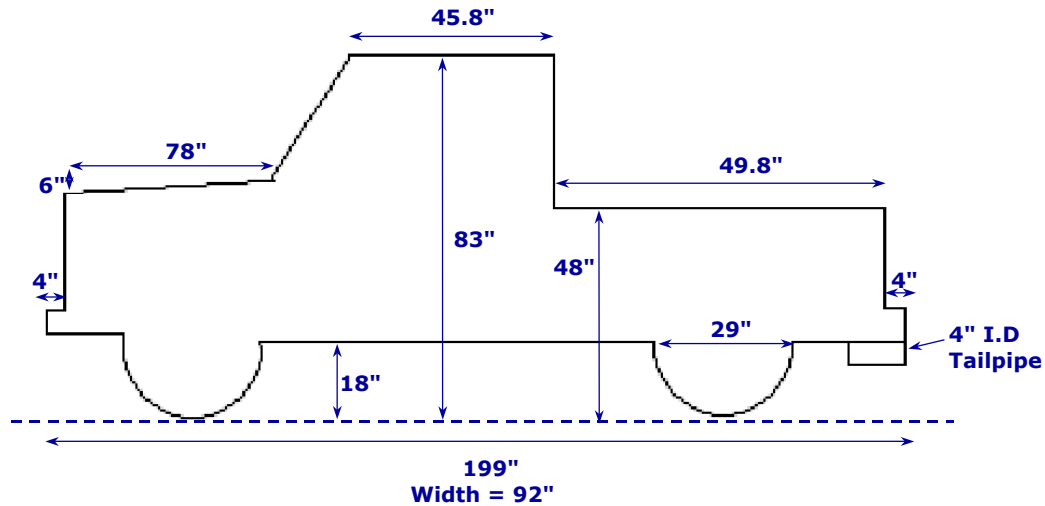


Figure 10-1. Bobtail geometry as modeled.

A measured particle size distribution (Abdul-Khalek et al. 1998) was used. The particle size distribution fit several bimodal, lognormal distributions: an ultrafine mode in the 7 ~ 15 nm diameter range and an accumulation mode in the 30 ~ 40 nm diameter range. Nanoparticles in the ultrafine mode represented only 0.1 ~ 1.5% of particle volume (mass), but 35 ~ 97% of the particle number (Abdul-Khalek et al. 1998; Kittelson 1998). Typical exhaust particulate matter mass concentrations from well-maintained modern diesel engines are 15 ~ 30 mg/m³ (Abdul-Khalek et al. 1998). The older diesel engines emit more particle mass. Compared with older engines, the modern engines emit low particle mass concentrations but may actually emit larger number concentrations than the older designs. The measured particle number concentrations are reported to be on the order of 10¹³ ~ 10¹⁴ particles/m³ (Abdul-Khalek et al. 1998; Kittelson 1998; Morawska et al. 1998). A mid-range PM emission concentration of 20 mg/m³ was used as the initial PM concentration for the aerosol dynamics simulations (Abdul-Khalek et al. 1998; Kelly et al., 2003). The PM emissions for the bobtail contained 1% by mass nucleation-mode particles, with a geometric mean diameter of 7 nm and geometric standard deviation of 1.2, and 99% accumulation-mode particles with geometric mean diameter of 35 nm and geometric standard deviation of 2.0, as shown in Figure 10-2 (Abdul-Khalek et al. 1998).

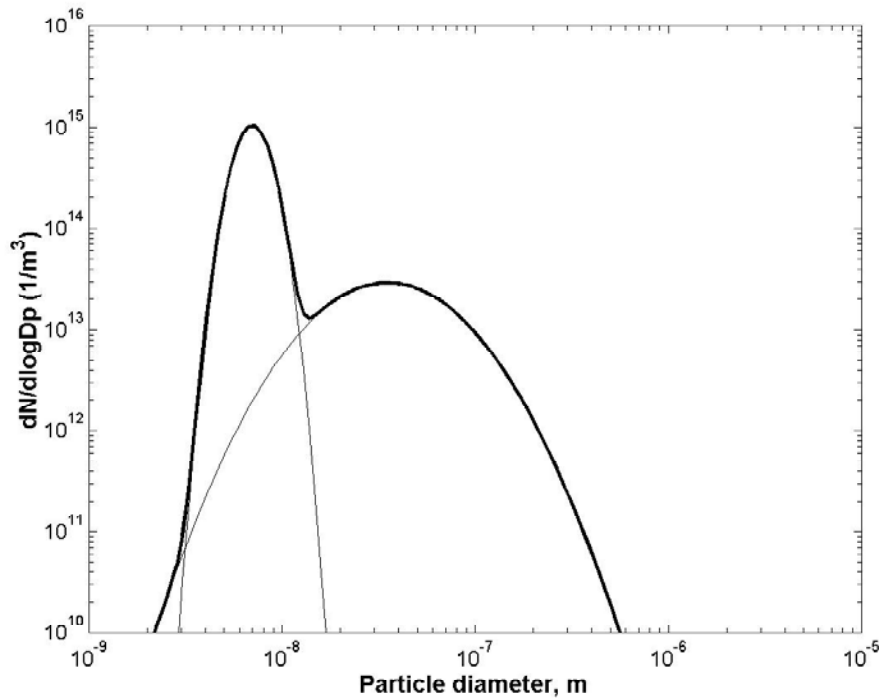


Figure 10-2. Model particle size distribution for the Dodge bobtail.

To determine the effects of ambient particle size distribution on exhaust particle size distribution, three ambient conditions were examined: dilution with particle-free air, dilution with ambient air containing particles, and doubling the concentration of atmospheric particles. The particle size distribution of the atmospheric aerosol (Whitby et al. 1978; Jacobson 1999) is described by three lognormal modes: a nucleation mode (or ultrafine), an accumulation mode, and a coarse mode.

10.2.2 Computational Fluid Dynamics Methods

Computational Fluid Dynamics (CFD) simulations were performed to evaluate the dispersion of tailpipe exhaust under various driving and wind conditions. Simulations were performed using the three-dimensional CFD code Banff (Adams et al., 1995). Banff is a steady-state, structured, orthogonal grid CFD code. The standard $k-\epsilon$ model was used for turbulence. Because mixing downstream of the vehicle is of primary interest in this study, the CFD model is not intended to be a fully detailed aerodynamic vehicle simulation. We do not attempt to fully resolve the vehicle geometry or the fluid boundary layers surrounding the vehicle, since these are expected to have little effect on downstream exhaust mixing. The Bobtail was simulated by creating a rectangular computational grid 12 m high by 65.5 m long by 11.7 m wide – essentially a computational wind tunnel (Figure 10-3). The size of the computational grid was 1.3 million cells. This large size was required because of the large length scale disparity in the system. The tailpipe is four inches in diameter, and the maximum system dimension is 65.5 m – roughly a factor of 650. The relatively large grid size was a result of the tradeoff between resolution and grid quality. The back of the truck is 50 meters from the

exit of this grid. For all calculations it is assumed that the vehicle is either moving in ambient air or that the vehicle is stationary, with a specified head wind.

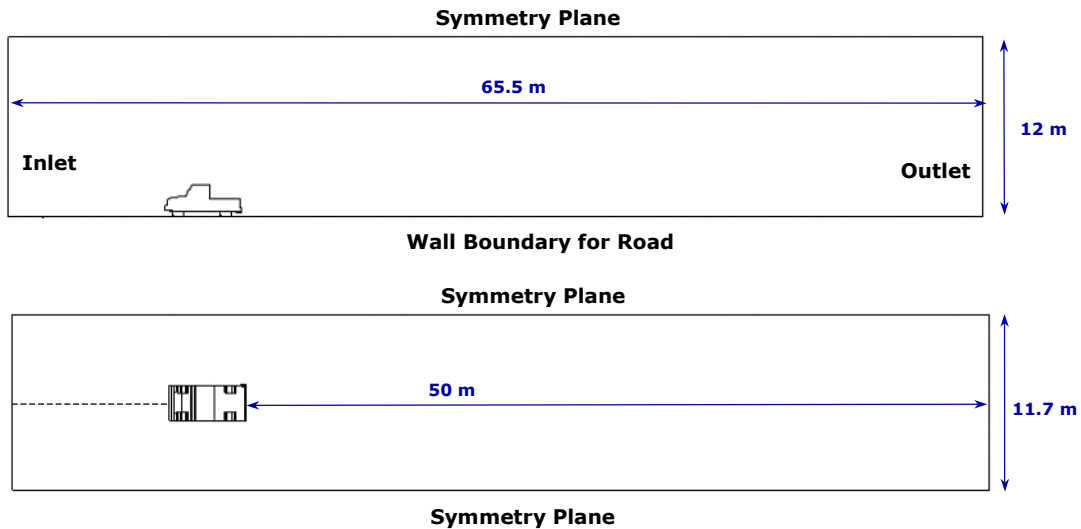


Figure 10-3. Computational domain for the CFD simulations. The upper figure is a side view; the lower figure is a plan view. Boundary condition types are indicated. The number of computational cells was 1.3 million.

Free-stream conditions were approximated at the top, and left and right sides of the computational box by making the computational grid large compared to the truck and by applying symmetry boundary conditions. For the stationary vehicle cases a no-slip wall boundary condition was used on the bottom boundary. For the moving vehicle cases, the velocity component in the streamwise direction is fixed at the wind velocity in the cell nearest to the wall.

Ten CFD simulations were run. The first group models the vehicle moving at 5, 10, 15, 20, and 25 mph. In the second group, the vehicle is stationary and the above wind speeds were blowing toward the front of the vehicle (i.e., a headwind). The exhaust dilution results for the two sets of cases are nearly identical for the same wind speed. Only near the road do the two cases differ. As expected, the degree of dilution was higher when the air velocity was higher relative to the truck. The vertical position of the maximum exhaust concentration was higher in the lower velocity cases than in the higher velocity cases, although the magnitude of the maximum concentration at these positions was lower for the high velocity cases.

To evaluate conditions further downstream of the vehicle, three additional simulations were performed for vehicle speeds of 5, 15, and 25 mph. A separate computational grid was created with identical dimensions and cell spacing in the cross-stream directions. This grid extended from the exit of the original grid 40 meters downstream. A separate grid was required because of the large number of computational cells in the original grid. Simply extending the original grid would not have allowed both reasonable grid resolution/cell quality, and simulation times. The size of the grid extension was 725,000 cells. All exit gas, flow, and turbulence model properties from the original grid were used as inlet properties to the grid extension on a direct cell-by-cell basis. By using the same grid dimensions in the plane of the exit no interpolation of flow properties was

required, resulting in improved accuracy, and matching at the interface between the original and extended simulations.

The results of the two simulations were combined to give results at up to 90 meters downstream of the tailpipe. The contours of mixture fraction (or inverse dilution ratio) matched well for the 15 and 25 mph cases. For the 5 mph case, while the values at the interface matched, the slope of the contour lines at the interface was not continuous. This discontinuity was a result of the outflow boundary condition at the exit of the original grid, and the dependence of the flow field on the surrounding conditions, which are only one-sided at the grid interface. For the 5 mph case, the contour lines were smoothed slightly at the grid interface, 50 meters downstream of the tailpipe.

10.2.3 Aerosol Dynamics Modeling

The calculated dilution ratios from CFD results were used in the aerosol dynamics simulation. Five streamlines were calculated for each case. Figure 10-4 shows the starting positions of the five streamlines in the tailpipe exit plane.

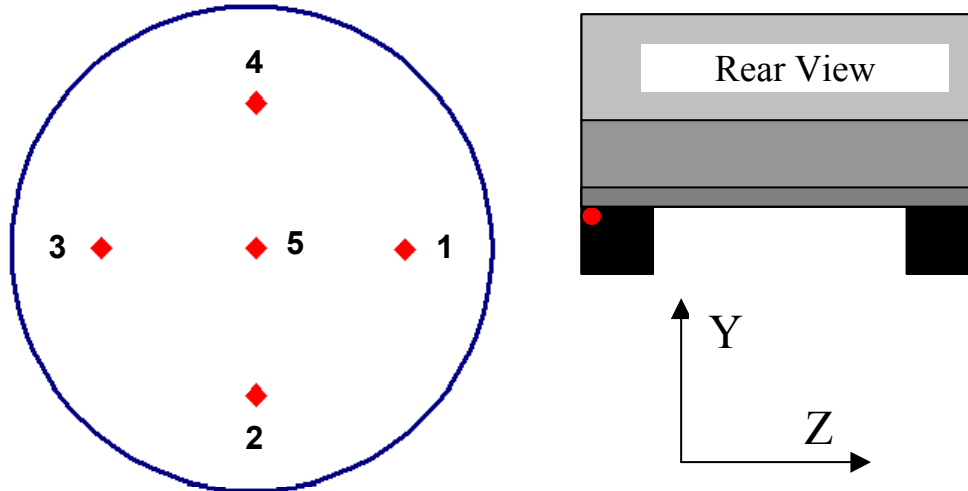


Figure 10-4. Diagram showing the starting positions of the various points in the tailpipe for streamline calculations.

The aerosol dynamics code solves coagulation equations with allowance for simultaneous dilution. In this system, the particles are being diluted continuously by ambient air containing particles with number concentration, na . First, the exhaust mass fraction was converted to dilution ratio, using the temperature and density from the CFD solutions. The equation describing the time-dependent dilution is (Jiang 2003):

$$\frac{dn}{dt} = -\frac{na - n}{D} \frac{dD}{dt} \quad (1)$$

In an aerosol system consisting of m particle size classes, the particle coagulation process can be described by following ordinary differential equations representing the change in particle number due to particle collisions (Jiang et al. in press)

$$\left. \frac{dn(v_i, t)}{dt} \right|_{v_j} = -\beta(v_i, v_j)n(v_i, t)n(v_j, t) \quad (2)$$

$$\left. \frac{dn(v_j, t)}{dt} \right|_{v_i} = -\beta(v_i, v_j)n(v_i, t)n(v_j, t) \quad (3)$$

$$\left. \frac{dn(v_k, t)}{dt} \right|_{v_i, v_j} = \beta(v_i, v_j)n(v_i, t)n(v_j, t) \quad (4)$$

where, $1 \leq i \leq m, i \leq j \leq m,$

$v_k = v_i + v_j,$

$v_i =$ the particle volume of size class $i,$

$n(v_i, t) =$ the particle number concentration for size class i at time $t,$

$\beta =$ collision frequency

Combining the dilution equation into the coagulation equation, we have:

$$\frac{dn(v_i, t)}{dt} = -\frac{na(v_i) - n(v_i, t)}{D(t)} \frac{dD(t)}{dt} - \beta(v_i, v_j)n(v_i, t)n(v_j, t) \quad (5)$$

Solving equation sets (3), (4), and (5) simultaneously, we obtain the particle coagulation results incorporating time-dependent dilution ratio.

The aerosol dynamics model used in this study does not predict nucleation and can only deal with nucleation by including a particle source term with specified initial diameter and number generation rate. Predicting the details of nucleation is difficult due to uncertainty in the thermodynamic properties of the related vapor mixtures from the plume.

10.3 Results and Discussion

10.3.1 CFD Results

The dilution ratio is defined as $R_{dil} = V_t / V_p,$ where V_t is the mixture volume of plume and ambient air, and V_p is the volume of plume.

Figures 10-5 and 10-6 show contours of $\ln(R_{dil})$ near the rear of the vehicle for the cases in which the vehicle is moving at 5 and 25 mph, respectively. The contours are shown in

the vertical plane passing through the tailpipe axis. Differences in exhaust dilution among the cases are minimal in the region shown, indicating that mixing of exhaust and ambient air is dominated by effects of the exhaust momentum, which is the same for all the cases. This is at least partly due to the fact that the exhaust stream immediately behind the vehicle is shielded from the ambient airstream by the vehicle body.

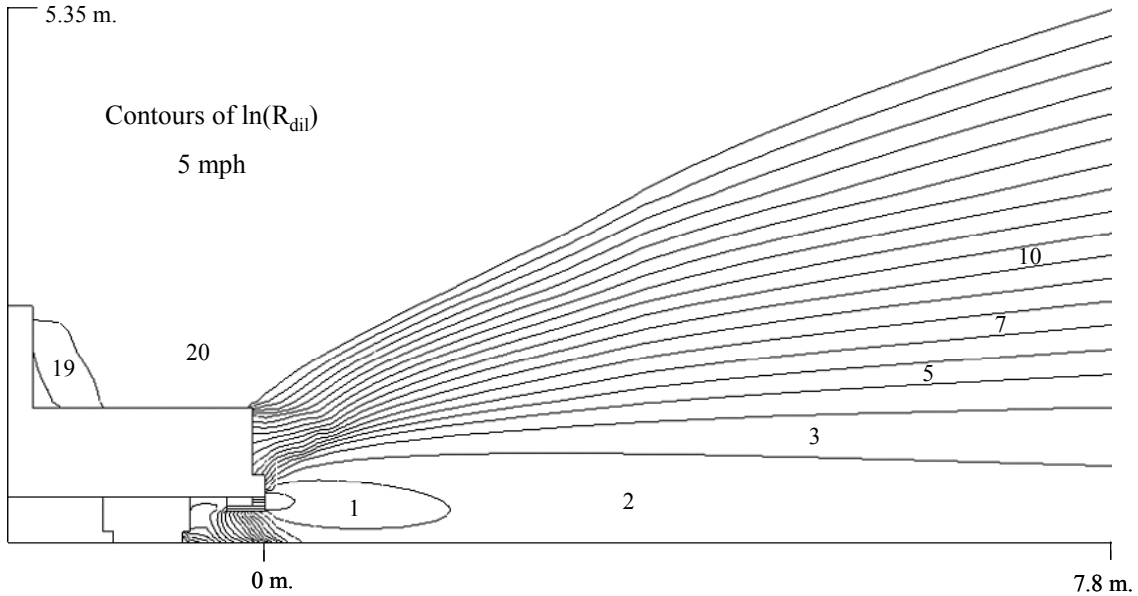


Figure 10-5. Contours of the natural log of dilution ratio for the vehicle moving at 5 mph. Labeled regions range in value from the number shown to the next higher value.

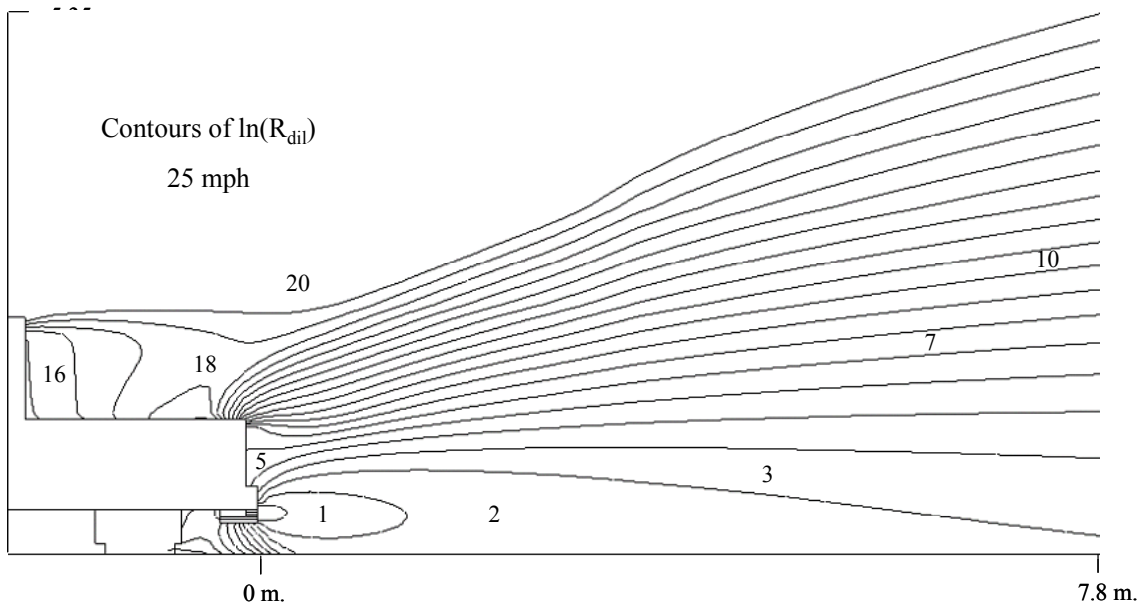


Figure 10-6. Contours of the natural log of dilution ratio for the vehicle moving at 25 mph. Labeled regions range in value from the number shown to the next higher value.

Figure 10-7 shows the same contours as Figures 10-5 and 10-6 over the entire computational domain. Significant differences in dilution can be seen beyond about a

vehicle length downstream of the tailpipe exit. As expected, faster dilution occurs for faster wind speeds relative to the vehicle. Faster air speed relative to the vehicle results in increased turbulent kinetic energy, leading to faster mixing. The results for the fixed vehicle cases (not shown) were similar.

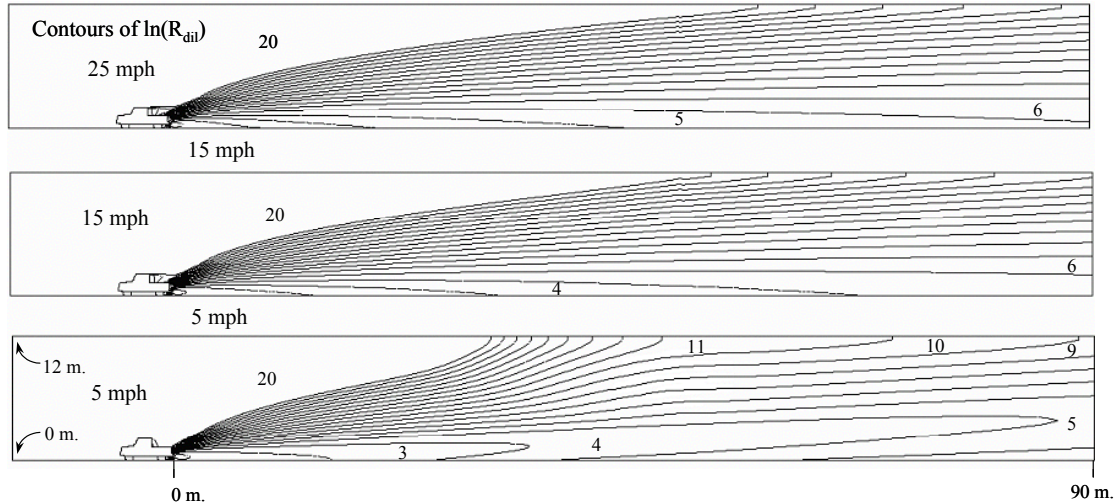


Figure 10-7. Contours of the natural log of dilution ratio for the vehicle moving at 5, 15, and 25 mph. Labeled regions range in value from the number shown to the next higher value. The computational grid was extended by 40 meters downstream for these cases.

Figures 10-8 and 10-9 show $\ln(R_{dil})$ for the same cases. The quantity $\ln(R_{dil})$ is plotted as a function of downstream distance from the tailpipe exit along three horizontal lines. These lines are in the vertical plane passing through the tailpipe axis at heights measured from the ground corresponding to the tailpipe center (16 in.), an elevation near the middle of the vehicle (50 in.) and the top of the vehicle (83 in.). In all cases the tailpipe $\ln(R_{dil})$ is zero at $x = 0$, indicating pure exhaust. The value increases as the exhaust mixes with ambient air. Along the 50 in. and 83 in. elevations $\ln(R_{dil})$ is large at $x = 0$, indicating pure ambient air, then decreases as exhaust fluid is mixed in. A minimum is reached and $\ln(R_{dil})$ begins increasing again as additional ambient air is mixed in.

Figures 10-8 and 10-9 also show that mixing is nearly independent of velocity near the rear of the vehicle. All cases and locations show the trend of faster mixing of ambient air with exhaust for faster vehicle speeds resulting in more dilution (higher $\ln(R_{dil})$) at all locations.

In the 5 mph case, Figure 10-8 shows that the line at the tailpipe level becomes more dilute than the higher elevations beyond about 35 m downstream. This is due to buoyancy of the exhaust stream, which is hotter than the ambient air (100 °C vs. 20 °C). As the exhaust stream rises due to buoyancy, exhaust gas is carried away from the tailpipe elevation into the higher elevations. Exhaust buoyancy is overcome by the ambient airstream momentum in the faster cases. The buoyant lifting of the exhaust stream is evident in Figure 10-10 .

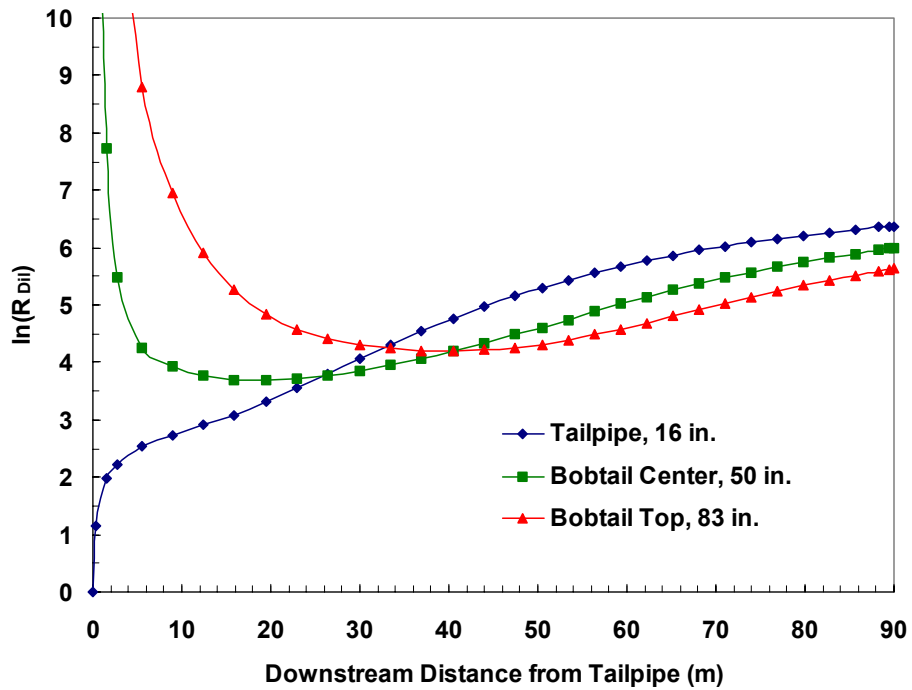


Figure 10-8. Natural log of dilution ratio for the vehicle moving at 5 mph for three elevations. All curves are in the vertical plane passing through the tailpipe axis.

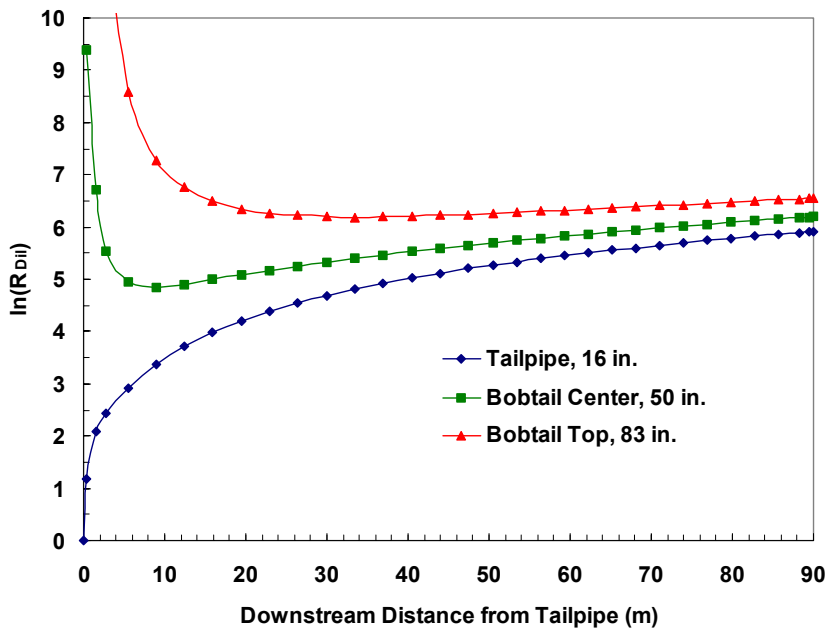


Figure 10-9. Natural log of dilution ratio for the vehicle moving at 25 mph for three elevations. All curves are in the vertical plane passing through the tailpipe axis.

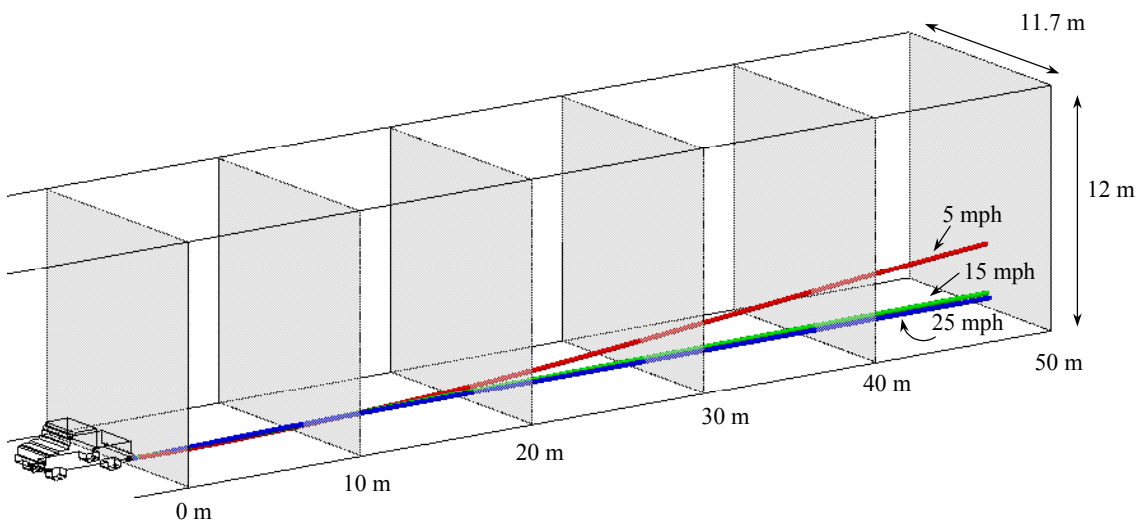


Figure 10-10. Flow streamlines beginning in the center of the tailpipe for three vehicle speeds. The 15 and 25 mph streamlines nearly overlap.

10.3.2 Aerosol Dynamics Simulation Results

The aerosol dynamics simulations were completed for four vehicle/wind conditions along the plume streamlines starting at the tailpipe exit and continuing to 50 m downstream (Table 10-1). Figure 10-11 shows how dilution ratios vary with time in the exhaust plumes for case 1 and 2, the slowest and most rapid dilution conditions. Comparing the dilution ratios for all four vehicle/wind conditions shows that little difference exists between a vehicle moving at 25 mph and a stationary vehicle with a headwind of 25 mph. For example, the slope of the line in Figure 10-12 (case 2) is 32 s^{-1} , whereas the slope of a similar line for the stationary vehicle with a 25 mph headwind is 31 s^{-1} (Table 10-1). The slower wind/vehicle speeds exhibit similar results. Figure 10-11 also illustrates the effect of the five different streamlines on dilution ratio for case 1 and case 2. Basically, the dilution ratios for the various streamlines all collapse into one curve and can be approximated by a single linear function, which greatly simplifies the simulations.

Table 10-1. Vehicle/wind conditions for the aerosol dynamics simulations.

Case	Vehicle speed (mph)	Wind speed (mph)*	Slope of dilution ratio curve (s^{-1})
1	0	5	3.75
2	25	0	32
3	5	0	4.4
4	0	25	31

*headwind

The results of the aerosol dynamics simulation are shown in Figures 10-12 – 10-14. All cases show that more coagulation occurs in the slow diluting case (case 1) than in the rapid diluting case (case 2), and coagulation reduces the number of particles in the nucleation peak and shifts the distribution to larger sized particles (Figures 10-12 – 10-14). This agrees with the experimental results of Maricq et al. (2001). The scavenging of

small particles by coagulation is most evident in case 1 for slow dilution with clean air (Figure 10-12). The scavenging effect is much less significant for the rapid dilution case because rapid dilution curtails coagulation.

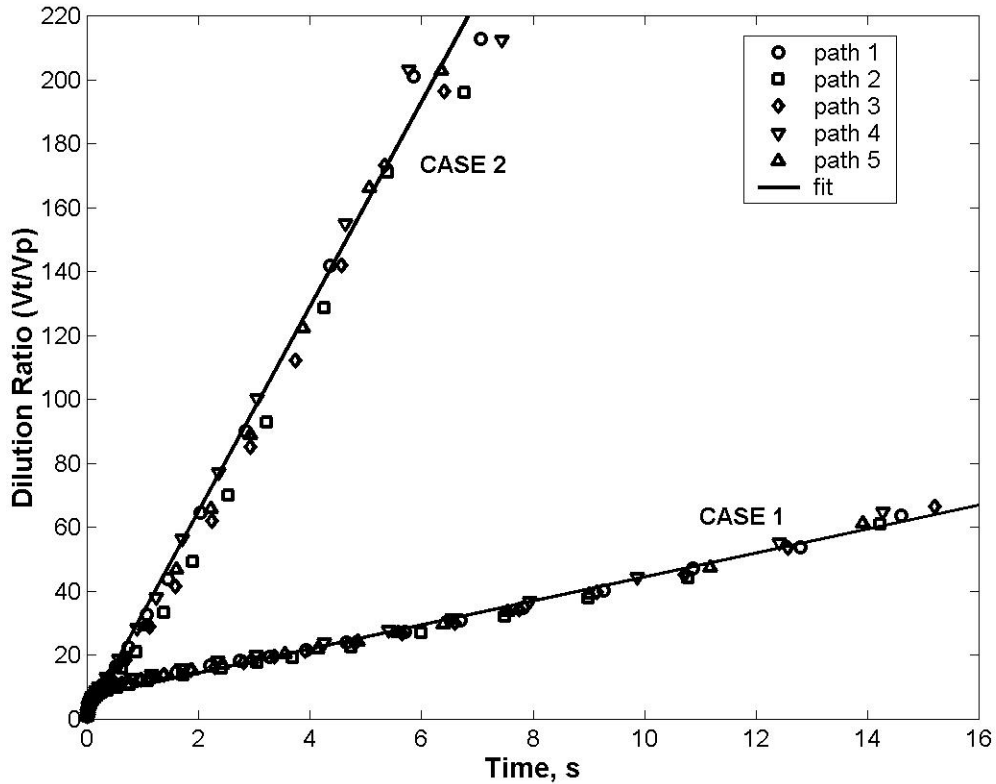


Figure 10-11. Comparison of the five streamlines for case 1 and case 2, slow and rapid dilution, respectively.

Figures 10-15 and 10-16 show the effect of ambient particles on the particle size distributions in exhaust plumes. The Figures compare the initial particle size distribution with predicted particle size distributions from 50 m downwind, corrected for dilution. The figures also illustrate that ambient particles only affect the upper and lower ends of the particle size distributions of the exhaust plume. One implication of the results is that when measuring the particle size distribution from emissions, fast dilution is very important for curtailing the coagulation. However, nucleation effects, not included in the aerosol dynamics model, may also be important.

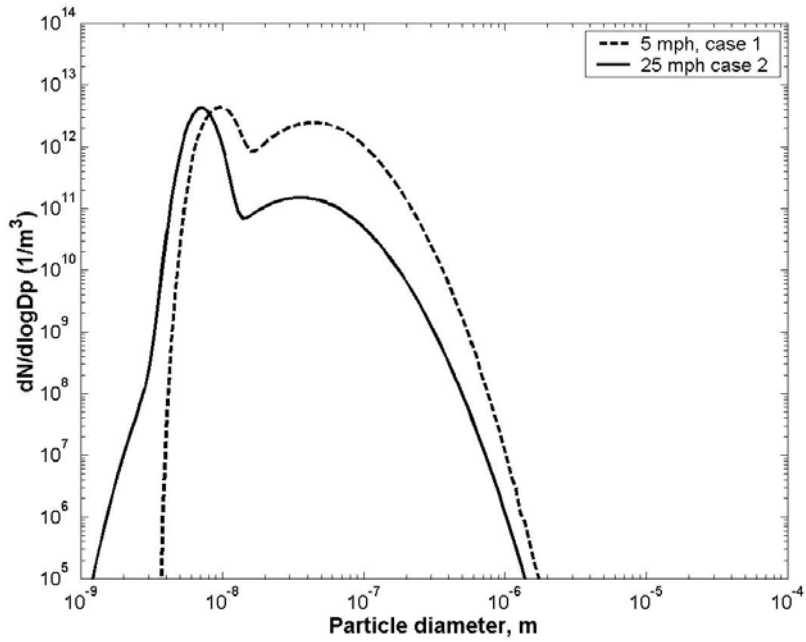


Figure 10-12. Bobtail particle size distributions at 50 m downwind, dilution with particle-free air.

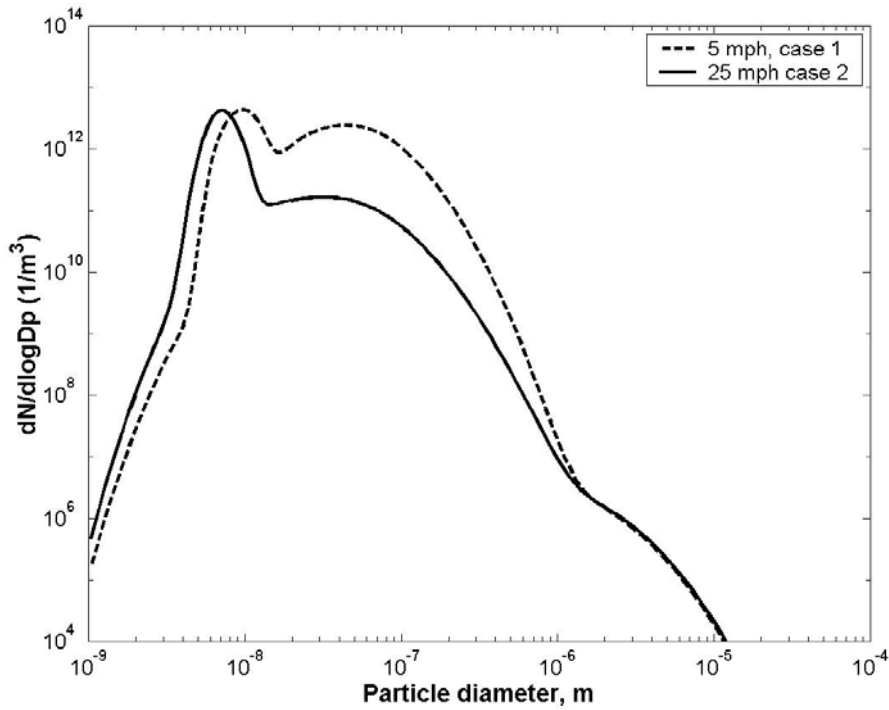


Figure 10-13. Bobtail particle size distributions at 50 m downwind, dilution with ambient air.

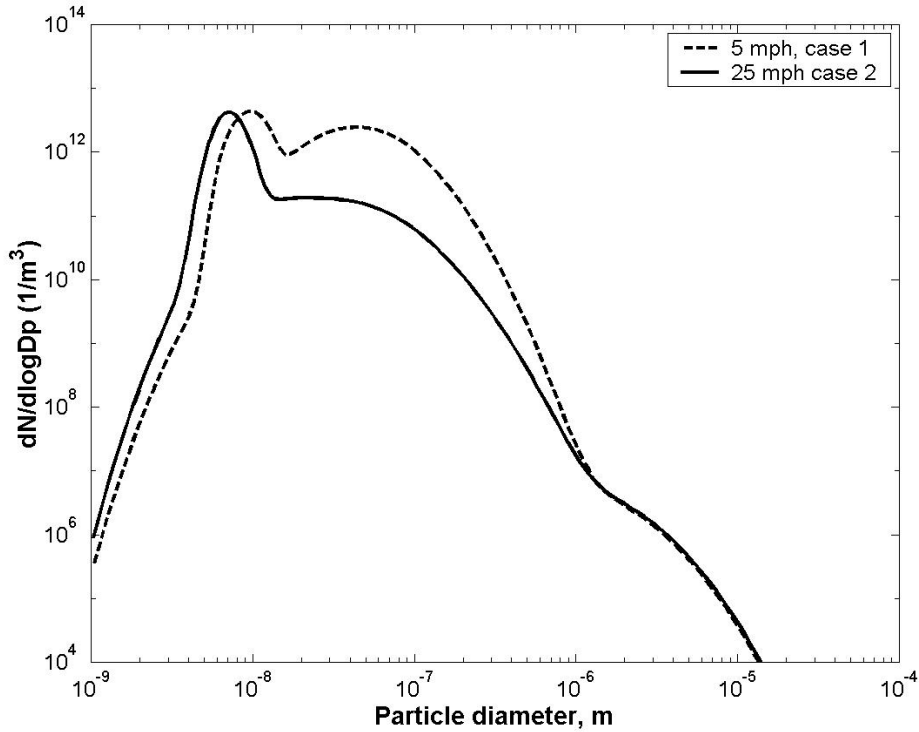


Figure 10-14. Bobtail particle size distributions at 50 m downwind, dilution with double-concentration ambient air.

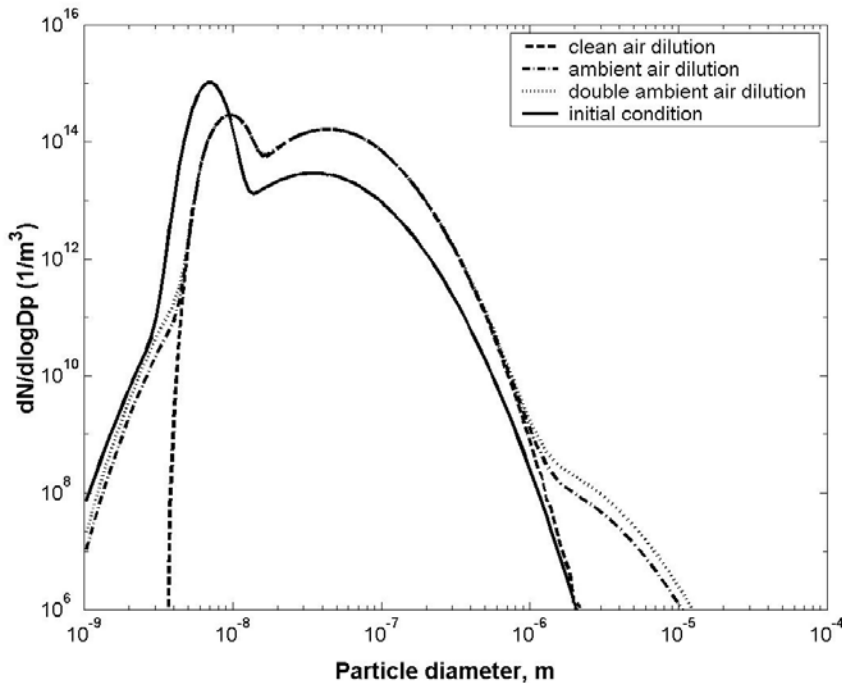


Figure 10-15. Simulation results for case 1 showing the effects of dilution with particle-free and ambient air. The particle size distributions from 50 m downwind are corrected for dilution to the tailpipe particle size distribution.

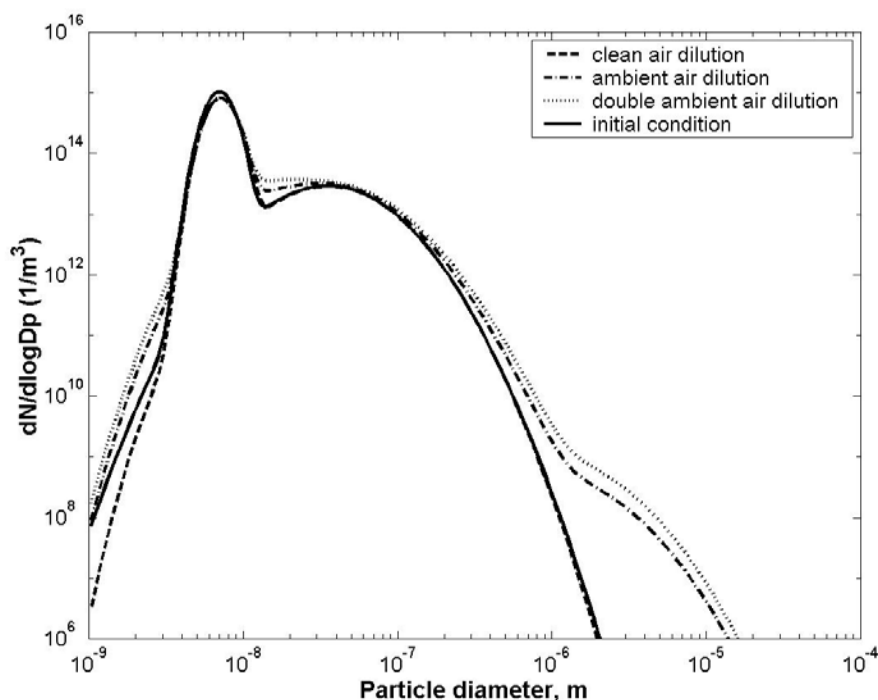


Figure 10-16. Simulation results for case 2 showing the effects of dilution with particle-free and ambient air. The particle size distributions from 50 m downwind are corrected for dilution to the tailpipe particle size distribution.

10.4 Conclusions

CFD was used to calculate the flow field and gas mixing for unconfined dilution of a vehicle exhaust plume with ambient air containing atmospheric aerosols. The calculated dilution ratios were used in the aerosol dynamics simulation. The simulations focused on four factors that influence particle size distribution in an exhaust plume: vehicle speed, wind speed, ambient particle size distribution, and the location of particles along an exhaust streamline. The results show little difference in particle coagulation along different streamlines, and the dilution ratios for various streamlines all collapse into one curve and can be approximated by a linear function. Further, ambient aerosol only affects the upper and lower ends of the particle size distribution of exhaust plume. In addition, rapid dilution (rapid speed) can effectively quench the particle coagulation, while coagulation resulted the reduction in the nucleation peak of the particle size distribution in slower dilution case. Finally, vehicle speed and wind speed essentially produce the same effect. One implication of the results is that when measuring the particle size distribution from emissions, fast dilution is very important for curtailing the coagulation provided that coagulation and surface growth are the dominant mechanisms.

Acknowledgements

This research was supported by Strategic Environmental Research and Development Program (SERDP) Project CP-1106, Characterization of Particulate Emission: Size

Characterization and Chemical Speciation and by the Center for the Simulation of Accidental Fires and Explosions (C-SAFE).

References

- Abdul-Khalek, I.S.; Kittelson, D.B.; Graskow, B.R.; Wei, Q.; Brear, F. Diesel Exhaust Particle Size: Measurement Issues and Trends. 980525, Society of Automotive Engineers, Warrendale, PA, 1998
- Abdul-Khalek, I. S.; Kittelson, D. B.; Brear, F. The Influence of Dilution Conditions on Diesel Exhaust Particle Size Distribution Measurements. 1999-01-1142, SAE Technical Paper Series
- Adams, B. R., et al, eds. *Technical Overview of Reaction Engineering International Combustion Simulation Software*, Reaction Engineering International, SLC, UT, 1995.
- EPA *Health Assessment Document for Diesel Exhaust*, 2002, EPA 600/8-90/057F. National Center for Environmental Assessment, Office of Research and Development, Washington DC.
- Dockery, D.W.; Pope, A.C.; Xiping, X.; Spengler, J.D.; Ware, J.H.; Fay, M.E.; Ferris, B.G.; Speizer, F.E. An Association between Air Pollution and Mortality in Six U.S. Cities; *New Engl. J. Med.* **1993**, 329 (24) 1753-1759.
- Harris, S. J.; Maricq, M. M. Signature Size Distributions for Diesel and Gasoline Engine Exhaust Particulate Matter. *Aerosol Science* 2001, 32:749-764
- Hinds, W. C. *Aerosol Technology: properties, behaviors, and measurement of airborne particles*. 1999, John Wiley & Sons, New York
- Jacobson, M.Z. *Fundamentals of Atmospheric Modeling*. Cambridge University Press: New York 1999
- Jiang, P. *Aerosol Dynamics: Model Development and Applications*. PhD Thesis, The University of Utah December 2003
- Jiang, P.; Lighty, J.S.; Sarofim, A.F.; Eddings, E.G. Coagulation Simulation and Inference of Initial Particle Size Distributions. *Aerosol Science and Technology* (submitted)
- Kittelson, D.B. Engines and Nanoparticles: A Review. *J. Aerosol Sci.* 1998, 29(5/6):575-588.
- Kittelson, D. B.; Johnson, J.; Watts, W.; Wei, Q.; Drayton, M.; Paulsen, D.; Bukowiecki, N. Diesel Aerosol Sampling in the Atmosphere. 2000-01-2212, SAE Technical Paper Series
- K.E. Kelly, D.A. Wagner, J. S. Lighty, A.F. Sarofim, C.F. Rogers, J. Sagebiel, B. Zielinska, W. P. Arnott, and G. Palmer (2003) Characterization of Exhaust Particles from Military Vehicles Fueled with Diesel, Gasoline, and JP-8, *J. Air & Waste Management Assoc.* 53: 273-282.
- Lighty, J.S.; Veranth, J.M.; Sarofim, A.F. Combustion Aerosols: Factors Governing their Size and Composition and Implications to Human Health. Critical Review; *J. Air & Waste Man. Assoc.* **2000**, 50, 1565-1618.
- Maricq, M. M.; Chase, R. E.; Podsiadlik, D. H.; Vogt, R. Vehicle Exhaust Particle Size Distributions: A Comparison of Tailpipe and Dilution Tunnel Measurements. 1999-01-1461, SAE Technical Paper Series
- Maricq, M. M.; Podsiadlik, D. H.; Chase, R. E. Size Distributions of Motor Vehicle Exhaust PM: A Comparison Between ELPI and SMPS Measurements. *Aerosol Science and Technology* 2000, 33:239-260
- Maricq M.M.; Chase, R.E.; Xu, N. A Comparison of Tailpipe Dilution Tunnel, and Wind Tunnel Data in Measuring Motor Vehicle PM. *J. Air & Waste Manag. Assoc.* 2001 51:1529-1537.
- Maynard A.D., R.L. Maynard, A derived association between ambient aerosol surface area and excess mortality using historic time series data, *Atmos. Environ.* 36 **2002**, 5561-5567.
- Morawska, L.; Bofinger, N.D.; Kocis, L.; Nwankwoala, A. Submicrometer and Supermicrometer Particles From Diesel Vehicle Emissions. *Environ. Sci. Technol.* 1998, 32(14):2033-2042

- Morawska L., J. Zhang Combustion sources of particles 1. Health relevance and source signatures, *Chemosphere* 49 (2002) 1045-1058.
- Peters A.; Dockery, D.; Muller J.E.; Mittleman M.A. Increased Particulate Air Pollution and the Triggering of Myocardial Infarction; *Circulation*, **2001**, 2810-2815.
- Rogers, C. F.; Sagebiel, J. C.; Zielinska, B.; Arnott, W. P.; Fujita, E. M.; McDonald, J. D.; Griffin, J. B.; Kelly, K.; Overacker, D.; Wagner, D.; Lighty, J. S.; Sarofim, A. F.; Palmer, G. Characterization of Submicron Exhaust Particles from Engines Operating Without Load on Diesel and JP-8 Fuels. *Aerosol Science and Technology*, 2003, 37:355-368
- Shi, J. P.; Harrison, R. M. Investigation of Ultrafine Particle Formation During Diesel Exhaust Dilution. *Environmental Science and Technology* 1999a, 33:3730-3736
- Shi, J. P.; Harrison, R. M.; Brear, F. Particle Size Distribution from a Modern Heavy Duty Diesel Engine. *The Science of the Total Environment* 1999b, 235:305-317
- Shi, J. P.; Mark, D.; Harrison, R. M. Characterization of Particles from a Current Technology Heavy-Duty Diesel Engine. *Environmental Science and Technology* 2000, 34:748-755
- Vedal, S. Ambient Particles and Health: Lines that Divide. *J. Air and Waste Management Assoc.* 1997, 47:551-581
- Whitby, K.T. The Physical Characteristics of Sulfur Aerosols. *Atmos. Environ.* 1978, 12:135-159

APPENDIX 1:

USER GUIDE FOR CHARACTERIZING

PARTICULATE MATTER



User Guide for Characterizing Particulate Matter

Evaluation of Several Real-Time Methods

University of Utah

K.E. Kelly, A.F. Sarofim, J.S. Lighty, D.A. Wagner

Desert Research Institute

W.P. Arnott, C.F. Rogers, B. Zielinska

University of California San Diego

K.A. Prather

This project was sponsored by the Strategic Environmental Research and Development Partnership, CP-1106 characterization of particulate emissions: size fractionation and chemical composition.

Table of Contents

Introduction	1-1
What is particulate matter?	1-1
Why is particulate matter important?	1-2
Why characterize PM?	1-3
How can newly developed instruments help characterize PM?	1-3
How do you collect PM samples?	1-4
Resources	1-4
References	1-4
Photoacoustic Analyzer	2-1
What is soot?	2-1
How does it work?	2-2
When can you use the photoacoustic analyzer?	2-2
Cost comparison	2-4
Comparison of the PA with other methods	2-5
Vision for use	2-6
Resources	2-7
References	2-7
Photoelectric Aerosol Sensor	3-1
What are PAHs?	3-1
How does it work?	3-2
When can you use the photoelectric aerosol sensor?	3-4
Cost comparison	3-5
Comparison of the PAS with other methods	3-5
Vision for use	3-7
Resources	3-7
References	3-7
Aerosol Time-of-Flight Mass Spectrometer	4-1
Why is understanding the size and composition of individual particles useful?	4-1
How does it work?	4-1
When can you use the ATOFMS?	4-5
Cost comparison	4-6
Comparison of the ATOFMS with other methods	4-6
Vision for use	4-8
Resources	4-8
References	4-9

Table of Contents (continued)

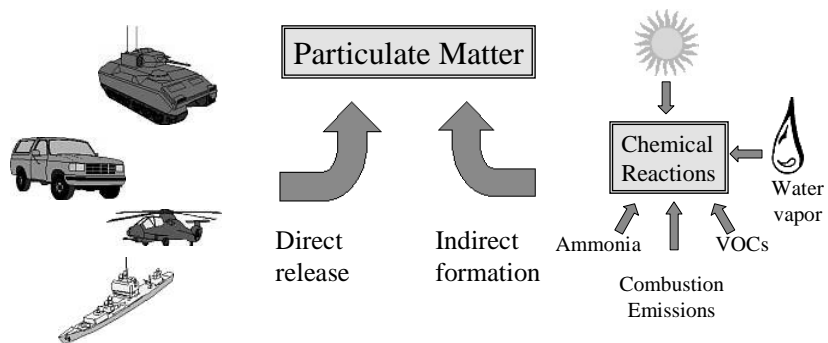
Dilution and Sampling	5-1
Sample types	5-1
Types of measurements	5-2
Effects of dilution systems	5-2
Dilution gas	5-4
General ecommendations for dilution/sampling systems	5-4
Common systems	5-5
Rules of thumb for selecting a dilution/sampling system	5-10
Resources	5-11
References	5-11

Introduction

This User's Guide is intended to assist environmental or military personnel who work with air quality measurements, regulations, and planning for the Department of Defense. Specifically, it focuses on an evaluation of three newly developed instruments for characterizing particulate matter (PM), general PM sampling recommendations, and background on PM.

What is particulate matter?

PM is material suspended in the air, and it can include soil, road dust, soot, smoke, and liquid droplets. PM can come directly from sources like vehicles, ships, aircraft, unpaved roads, and wood burning. Larger particles, those with a diameter larger than $2.5\ \mu\text{m}$ ($\text{PM}_{2.5}$), typically come



VOCs: volatile organic compounds

from unpaved roads and wind-blown dust, but finer particles, those smaller than $\text{PM}_{2.5}$, typically come from combustion sources: vehicles, ships, etc. PM is also formed in the air when gases from burning fuels react with sunlight and water vapor (Figure 1-1).

Figure 1-1. Example of the direct release and indirect formation of particulate matter.

PM found in the atmosphere is made up of many compounds including soil, nitrate, sulfate, soot and organic carbon (Figure 1-2). Organic carbon includes products of incomplete combustion, such as polycyclic aromatic hydrocarbons (PAHs) and unburned fuel. The composition of PM can vary dramatically depending on the source or process condition. For example, PM from a gasoline vehicle, diesel vehicle, woodstove, or a coal-fired boiler would have dramatically different composition.

Why is particulate matter important?

Particulate matter can cause serious health effects and impair visibility. Studies over the last ten years have linked PM concentration to increased death rates, an increased incidence of asthma, and adverse cardiac effects (EPA 2000, 2002; Dockery et al. 1993; Morawska and Zhang 2002; Peters et al. 2001). More recent evidence indicates that size, surface area, and composition of PM are important factors in determining the health effects associated with PM. For example, fine particles are thought to deposit more deeply in the lungs than larger particles (Lighty et al. 2001, Maynard and Maynard 2002). In addition PM, especially PM from combustion sources, contains polycyclic aromatic hydrocarbons (PAHs), which are reasonably anticipated to be carcinogens (NTP 2003), and elemental carbon, which is linked to adverse cardiac effects (Tolbert et al. 2001).

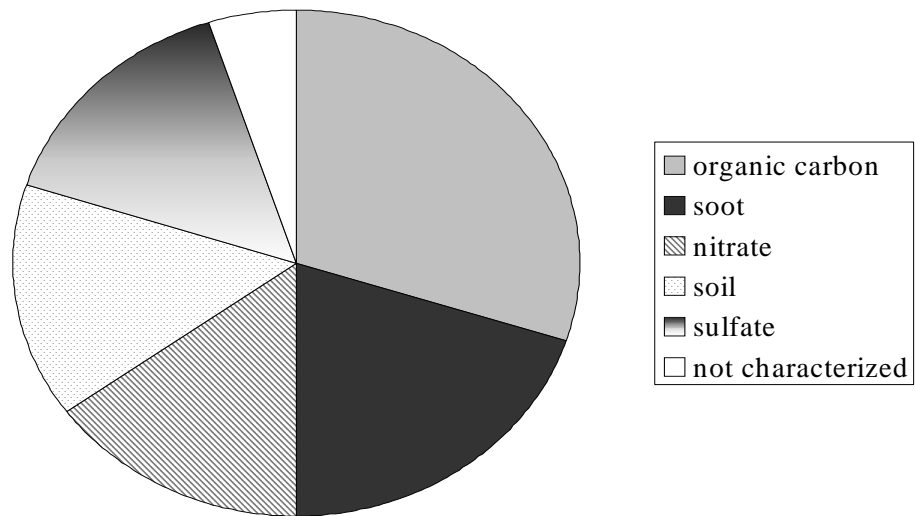


Figure 1-2. Composition of an example atmospheric particle.

PM causes adverse health effects

The EPA directly regulates atmospheric levels of PM₁₀, and it indirectly regulates PM through its visibility programs. New regulations to control PM_{2.5} concentrations have recently been developed. In addition to regulations on the atmospheric PM levels, the EPA, the states, and other agencies also regulate PM emissions from a variety of sources, such as vehicles, power plants, aircraft, and various industries. Finally, the Occupational Safety and Health Administration regulates PM levels in workplaces.

Size and composition of PM are important factors in determining their health effects

Why characterize PM?

Information about the size and composition of PM in the atmosphere can provide clues about its source. For example, larger particles that contain distinctive compounds, such as iron, silica, potassium, sodium, magnesium and chloride, are likely from wind-blown soil and ocean spray, but smaller particles that contain elemental and organic carbon are likely from a combustion sources. As another sample, PM from a Minuteman rocket motor contains large quantities of aluminum compared to soil particles (Sarofim and Lighty 2003).

PM composition can provide information about its source and its health effects

The size and composition of PM can also provide clues about process performance. For example, an engine operating at idle tends to emit smaller particles than the same engine under load. Engine operating condition also effects the portion of the particle made of organic and elemental carbon. Characterizing PM can also help understand its potential health effects (EPA 2002, HEI 2002). Research in this area is still ongoing (NRC 1988-2001), and the Health Effects Institute is a good resource for health effects information (See the resource list at the end of this section).

How can newly developed instruments help characterize PM?

Traditionally, determining the composition of PM was a time-consuming process. It required collecting and analyzing filters or sets of impactor substrates for composition. Although filter samples can provide detailed information about PM composition and some information about PM size, their analysis can be expensive and time consuming. The analysis methods also require a minimum amount of material, so collecting samples from the atmosphere can take many hours or even days. It is also challenging to collect sufficient PM from clean sources, such as a new gasoline vehicle. In addition, filter samples cannot provide information about process transients, when high PM emissions typically occur.

This guide reviews three newly developed instruments for use in determining PM composition.

- The photoacoustic analyzer measures black carbon, also called elemental carbon, or soot (Section 2).
- The photoelectric aerosol sensor measures particle-bound polycyclic aromatic hydrocarbons (Section 3).
- The aerosol time-of-flight mass spectrometer measures the size and composition of individual particles (Section 4).

These instruments offer several potential benefits over traditional measurements including near real-time results, cost savings, and information about transient conditions.

How do you collect PM samples?

Designing or selecting a system for collecting PM samples can be challenging, and it is important to consider the PM source, the type of measurements you need, and the potential errors associated with the system. Section 5 of this guide discusses several common systems and offers some general guidelines.

Resources

General information about airborne particles:

EPA's PM information page <http://www.epa.gov/oar/oaqps/regusmog/infpart.html>

Hinds W.C. *Aerosol Technology*, 2nd edition, John Wiley & Sons: New York, **1999**.

Kouimtzis T. (ed.) *Airborne Particulate Matter*, Springer Verlag: Heidelberg **1995**.

Maynard R.L., C.V. Howard, *Particulate Matter: Properties and Effects Upon Health*, Oxford: Bios Scientific, **1999**.

Wilson R., D. Spengler (eds). *Particles in Our Air: Concentrations and Health Effects*, Harvard University Press: Cambridge MA, **1996**.

Health effects of particles: Health Effects Institute <http://www.healtheffects.org>

Information about the User's Guide: Kerry Kelly kelly@eng.utah.edu

References

EPA, *PM-How Particulate Matter Affects the Way We Live & Breathe*, Office of Air Quality Planning & Standards, Washington DC, **2000**.

EPA, *Health Assessment Document for Diesel Exhaust*, EPA 600/8-90/057F. National Center for Environmental Assessment, Office of Research and Development, Washington DC, **2002**.

Dockery, D.W., A.C. Pope, X. Xiping, J.D. Spengler, J.H. Ware, M.E. Fay, B.G. Ferris, F.E. Speizer, An Association between Air Pollution and Mortality in Six U.S. Cities; *New Engl. J. Med.* **1993**, 329 (24) 1753-1759.

HEI (Health Effects Institute) Understanding the Health Effects of Components of the Particulate Matter Mix: Progress and Next Steps, *HEI Perspectives*, April **2002**.

Lighty, J.S., J.M. Veranth, A.F. Sarofim, Combustion Aerosols: Factors Governing their Size and Composition and Implications to Human Health. Critical Review; *J. Air & Waste Man. Assoc.* **50** **2000**, 50, 1565-1618.

Maynard A.D., R.L. Maynard, A Derived Association between Ambient Aerosol Surface Area and Excess Mortality using Historic Time Series Data, *Atmos. Environ.* 36 **2002**, 5561-5567.

Morawska L., J. Zhang Combustion Sources of Particles 1. Health Relevance and Source Signatures, *Chemosphere* 49 (2002) 1045-1058.

National Research Council (NRC), *Research Priorities for Airborne Particulate Matter*, volumes I – III, **1998, 1999, 2001** Washington D.C.: National Academy Press, <http://www.nas.edu/nrc/>

National Toxicology Program, *10th Report on Carcinogens*, U.S. Department of Health and Human Services, National Toxicology program, **2003**, <http://ehis.niehs.nih.gov/roc>

Peters A.; D. Dockery, J.E. Muller, M.A. Mittleman M.A. Increased Particulate Air Pollution and the Triggering of Myocardial Infarction; *Circulation*, **2001**, 2810-2815.

Sarofim A.F., J.S. Lighty; Characterization of Particulate Emissions: Size Fractionation and Chemical Speciation, Final Report, Strategic Environmental Research and Development Program, **2003**.

Tolbert P.E., M. Klein, K.B. Metzger, J. Peel, W.D. Flanders, K. Todd, J.A. Mulholland, P.B. Ryan, H. Frumkin Interim Results of the Study of Particulates and Health in Atlanta (SOPHIA), *J. Exposure Analy. and Env. Epid.* 10 **2000**, 446-460.

Photoacoustic Analyzer

for the measurement of soot

The photoacoustic analyzer (PA) measures soot concentration, also called black carbon or elemental carbon, in real time. The PA actually measures light absorption, which is closely correlated to soot concentration. It offers several advantages over traditional filter measurements of soot including rapid turnaround of results, study of transient conditions, large dynamic range, and

The PA measures soot concentration in real time

What is soot?

Soot comes from the combustion of jet fuel, gasoline, diesel and other fuels, and it makes up a large fraction of particulate matter in the atmosphere. Soot has been linked to adverse health effects including dysrhythmia and cardiovascular disease (Tolbert et al. 2000), and it is a significant component of diesel exhaust particulates, which are reasonably anticipated to be carcinogenic (National Toxicology Program 2003). Soot also contributes to global warming and impaired visibility (haze).

Soot is linked to health effects

When discussing soot, it is useful to understand the terms elemental carbon (EC), soot, and black carbon (BC). If you collect particulate matter on a filter, elemental carbon is the material that remains after heating the filter to 700°C, and soot is the material remaining on a filter after extracting it with a solvent. Black carbon is the part of particulate matter that absorbs light. The PA actually measures black carbon, but it is closely correlated to elemental carbon and soot concentration. For simplicity, we've used the term soot throughout the guide.

In general, soot isn't regulated directly, but it is a significant component of particulate matter, especially particulate matter smaller than 2.5 µm in diameter (PM_{2.5}). However, soot is regulated indirectly through standards for particulate matter, opacity, smoke, and visibility. As evidence for the health effects of particulate matter grows, regulations on particulate matter are becoming increasingly stringent. In addition, increasing emphasis is being placed on fine particulate matter. This will likely result in requirements for reduced soot emissions from diesel and aircraft engines.

Soot is a major component of PM_{2.5}

How does it work?

The PA rapidly measures light absorption as particles flow through the instrument, without the need to collect particles on a filter. The light absorption correlates to soot concentration. The PA also has a large dynamic range (130 dB), making it suitable for use on a wide range of exhaust and ambient samples. Specifically, the instrument measures light absorption at a laser wavelength of 1047 nm. Soot absorbs very strongly at this wavelength, in contrast to other types of particles and gases. Sample air is pulled continuously through an acoustical waveguide, and the laser also passes through the waveguide (Figure 2-1). The laser power is modulated at the resonance frequency of the waveguide. Now when soot absorbs light, it is heated. This heat transfers very rapidly to the surrounding air, in a time that is much shorter than the period of the laser-beam modulation, so all of the heat from light absorption comes out of the particles during each acoustic cycle. Upon receiving heat, the surrounding air expands, generating a pressure disturbance (i.e. an acoustical signal) that is measured with a microphone attached to the waveguide. Since soot absorbs light throughout the entire particle volume, the light absorption measurement is also a measure of soot mass concentration. This is the reason that light absorption can be used as a measure of black carbon mass concentration.

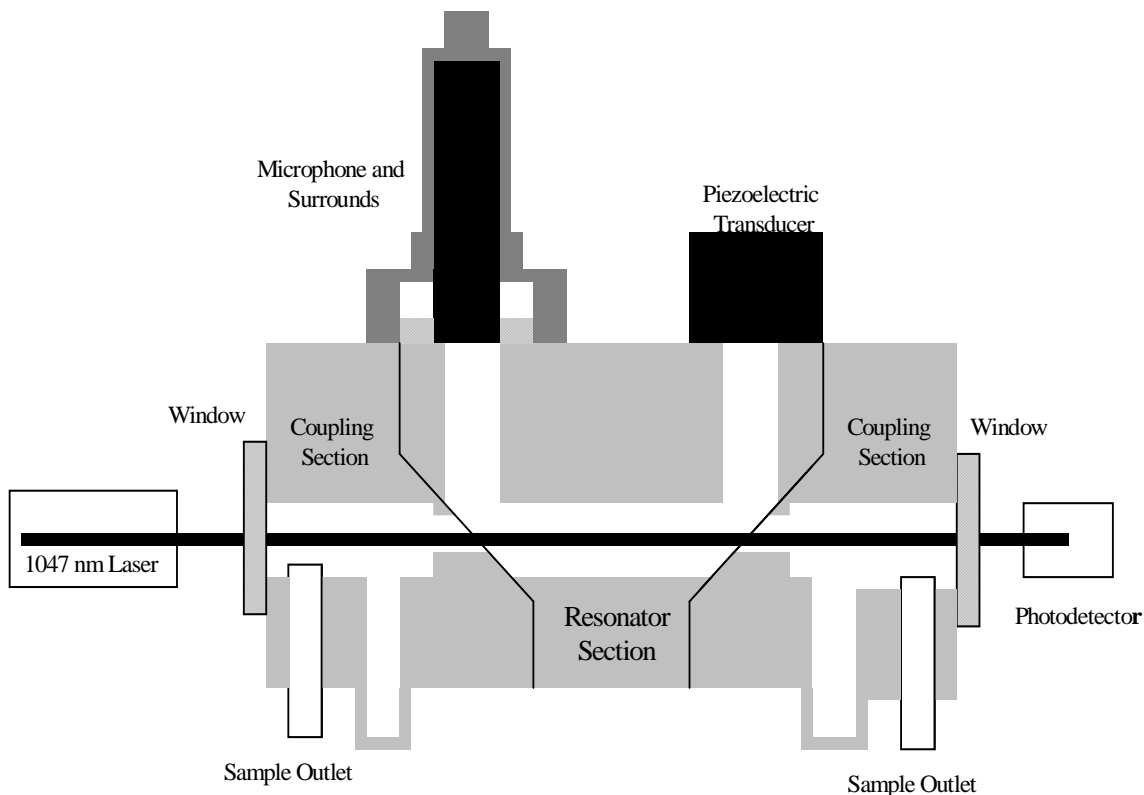


Figure 2-1. Schematic of the photoacoustic analyzer.

When can you use the photoacoustic analyzer?

The PA can measure soot from a variety of emission sources and ambient air. It is portable and suitable for field testing. However, there are a few practical considerations for using the PA:

- The PA operates best between temperature ranges of 40°F to 100°F.
- Particle concentrations should range from 50 ng/m³ to 100 mg/m³.
- The relative humidity of a sample should not exceed 80%.
- The PA must remain dry and protected from the elements.

The PA has been successfully demonstrated on emissions from gasoline and diesel vehicles, jet aircraft, brick kilns, and domestic trash burning. Figure 2-2 shows an example of how well the results from the PA correspond to filter measurements of elemental carbon (not organic carbon) for a variety of aircraft ground support equipment. Organic carbon is the portion of particulate matter that volatilizes when heating a filter from 300°C to 700°C.

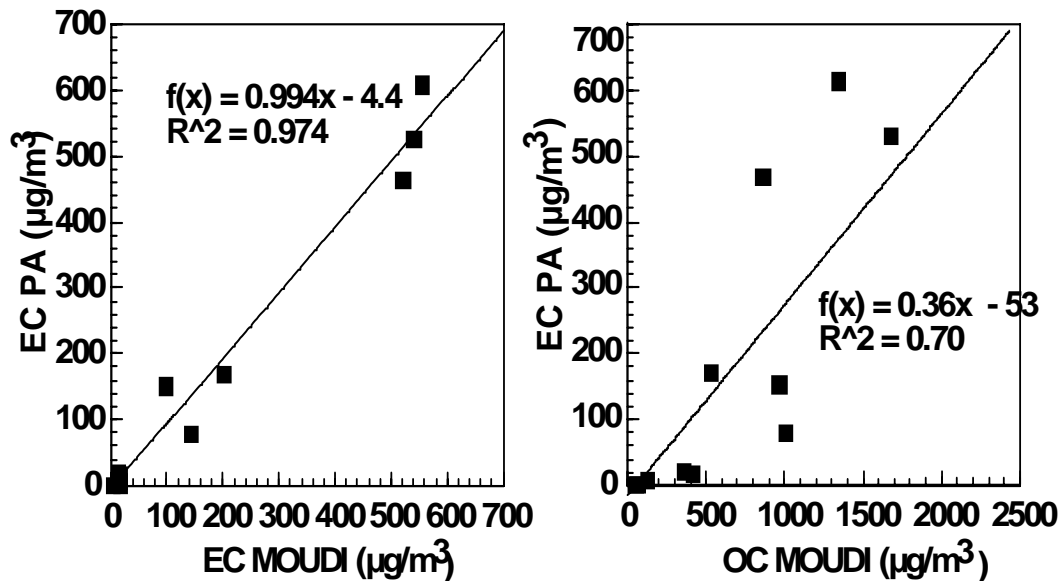


Figure 2-2. Comparison of PA results with filter measurements of EC and organic carbon OC.

One of the main benefits of the PA is its ability to provide information on transient conditions, as in Figure 2-3. It shows how soot concentration varies with engine condition for a diesel Dodge Bobtail (Hill Air Force Base, 2000).

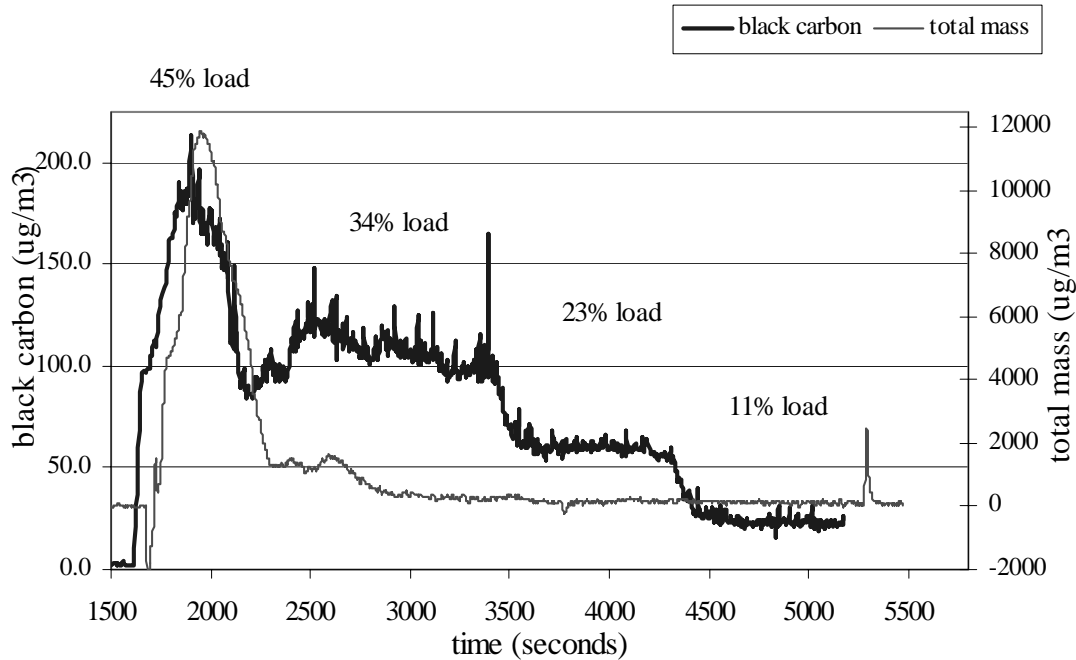


Figure 2-3. PA signal versus engine load.

Cost comparison

Currently, the purchase price of PA assembled from premium components is approximately \$36,000, including a computer. However, it is expected to decrease in the future. Analyzing filters for elemental carbon is relatively inexpensive. If you collected a set of cascade impactor filters, it would cost approximately \$550 to analyze a set of nine filters. One common system for collecting filter samples is a Micro Orifice Uniform Deposit Impactor (MOUDI), and it costs approximately \$12,000. The MOUDI contains eight or ten stages, with cut points ranging from 10 μm to 56 nm. Other impactors are available, but when measuring soot remember that much of it is associated with particles less than 1 μm in diameter. So, care must be taken to ensure that particulate matter is collected in the correct size range. A qualified technician could operate the photoacoustic analyzer or a system to collect filter samples. Because the PA can produce measurements more rapidly, it offers the potential for some labor savings.



As a rule of thumb, if you are interested in collecting a few samples, filter samples are likely to be more cost effective. However, if you need to make numerous measurements or require information on transient conditions, the PA would be more cost effective and relevant.

Comarison of the PA with other methods

There are some differences in how soot, elemental carbon, and black carbon are measured. Elemental carbon is measured as the mass of carbon that evolves on ramping an exposed quartz filter sample from a lower to upper temperature range, typically 500°C to 700°C. In practice, the most reproducible elemental carbon concentration is when 47-mm filters are loaded with 1 mg of material. Filters are exposed, shipped to the laboratory, put in the analysis queue, and eventually analyzed, perhaps months after they were exposed, so the data acquisition rate is often slow. The dynamic range is limited by the need to obtain a loading of about 1 mg/sample on the filter. On the other hand, if you are interested in the size-segregated distribution of elemental carbon, cascade impactors, such as a MOUDI, are more appropriate.

The PA provides results more rapidly than filters

Black carbon is measured by light absorption, and this correlates to soot concentration. The absorption efficiency of soot is much larger than the efficiency of other atmospheric aerosols. Soot aerosols are small enough that the light is absorbed throughout the aerosol volume, so that aerosol light absorption is proportional to the mass concentration of light-absorbing aerosols. The proportionality between aerosol light absorption and soot mass concentration is typically obtained from the linear regression coefficient against elemental carbon. In this sense, soot should be equivalent to elemental carbon in source-profile measurements.

Light absorption measurements are commonly made by filter-based methods in instruments such as aethalometers (Hansen et al. 1984) and particle soot absorption photometers (PSAP). In these methods, a quartz filter is exposed to aerosol, and the attenuation of light through the filter is monitored over time. The filter is a multiple scattering substrate so that the reduction in the transmitted light is proportional to the aerosol absorption cross section. The PSAP calibration requires simultaneous measurement of aerosol scattering coefficient with a nephelometer because a fraction of scattering is subtracted from the apparent light absorption from the filter attenuation (Bond et al. 1999). For very black aerosols, such as those from diesel engines or coal combustors, the multiple scattering character of the filter reduces with aerosol load. Consequently, the reported black carbon concentration can be incorrect by a factor of two, depending on the time history of filter loading. These filter-based methods suffer from low dynamic range because the black carbon concentration is proportional to filter attenuation only

for light filter loads. This limitation reduces the effectiveness of the filter method for source profile measurements of high emitters, as filter changes are needed often. Secondary dilution can extend the upper limit, although quantification of the dilution ratio increases measurement errors. Filter-based measurements perform best with low concentrations of black carbon, such as in ambient applications. The practical flow rates for these instruments range from 1 to 6 l/min, and the flow rate must be accurately determined to quantify filter exposure during a particular time interval. Rapid changes in the relative humidity (over seconds to many minutes) can cause unsatisfactory measurements by these methods.

Filter-based instruments work best for low soot concentrations

The PA also measures aerosol light absorption and can be calibrated to read soot concentration (Arnott et al. 1999, 2000). The aerosol light absorption measurement can be verified independently with measurements of light-absorbing gases, such as NO₂ at known concentrations and for visible wavelengths. Aerosol light absorption is measured in situ, no filters are needed, and flow rates are only important to ensure that aerosols are not deposited in the instrument or sample lines before they are measured. Since the PA's microphones have such a wide dynamic range, the black carbon measurements have the same dynamic range, e.g. a factor of 10⁶. The PA can equally be used in pristine ambient locations or in source profile measurements for high emitters. There are no filter artifacts. Relative humidity influence is likely not important when it is below 80%.

The PA can quantify a large range of soot concentrations and is less sensitive to humidity

Vision for use

DoD users should look to the PA for all of their black carbon mass concentration needs. It is useful in doing ambient measurements at fixed locations such as in air quality measurements at military bases. It is useful in profiling sources at these bases, particularly when dynamometers and constant-volume samplers are used. It is also useful in instrumented vehicles to measure black carbon issuing from the vehicle it is on, or as a function of time and space.

Resources

Website for the photoacoustic analyzer: <http://photoacoustic.dri.edu>

For more information about the photoacoustic analyzer, Dr. Pat Arnott: pat@dri.edu

For general information or information about this User's Guide, Kerry Kelly: kelly@eng.utah.edu

References

Arnott W.P., H. Moosmuller, J.W. Walker, Nitrogen-Dioxide and Kerosene-Flame Soot Calibration of Photoacoustic Instruments for Measurement of Light Absorption by Aerosols. *Rev. Sci. Instrum.* 71 **2000** 4545-4552.

Arnott W. P., H. Moosmüller, C. F. Rogers, T. Jin, R. Bruch, Photoacoustic spectrometer for measuring light absorption by aerosols: Instrument description. *Atmospheric Environment* 33 **1999** 2845-2852.

Bond T.C., T L. Anderson, D. Campbell, Calibration and Intercomparison of Filter-Based Measurements of Visible Light Absorption by Aerosols. *Aerosol Science and Technology* 30(6) **1999** 582-600.

Hansen, A.D.A., H. Rosen, T. Novakov (1984). The Aethalometer - An Instrument for the Real-Time Measurement of Optical Absorption by Aerosol Particles. *Science of the Total Environment* 36 **1999** 191-196.

NTP (National Toxicology Program 10th Report on Carcinogens, U.S. Department of Health and Human Services, National Toxicology Program, **2003**, <http://ehis.niehs.nih.gov/roc/>

Tolbert P.E., M. Klein, K.B. Metzger, J. Peel, W.D. Flanders, K. Todd, J.A. Mulholland, P.B. Ryan, H. Frumkin Interim Results of the Study of Particulates and Health in Atlanta (SOPHIA), *J. Exposure Analy. and Env. Epid.* 10 **2000** 446-460.

Photoelectric Aerosol Sensor

for measuring particle-bound polycyclic aromatic hydrocarbon concentration

The photoelectric aerosol sensor (PAS) qualitatively measures the concentration of particle-bound polycyclic aromatic hydrocarbons (PAHs). It gives a relative measure of particle-bound PAH concentration or, with appropriate calibration, a more accurate measure of PAHs. The PAS may provide a qualitative measure of total PAH concentrations more rapidly and cost effectively than traditional measurements, such as filter extraction and subsequent GC/MS analysis. However, the PAS cannot provide concentrations of individual PAHs, and developing a calibration curve for each instrument and source can be expensive and time consuming.

PAS measures
particle-bound
PAHs

What are PAHs?

PAHs have
negative health
effects

PAHs are a complex group of hundreds of chemicals that are formed during the incomplete burning of fuels, such as oil, wood, gasoline, diesel and jet fuel, and garbage. They are commonly found in vehicle exhaust and cigarette and wood smoke. Figure 3-1 gives the structure of some PAHs. PAHs as a group are reasonably anticipated to be carcinogenic (NTP 2003), and a few individual PAHs, such as benz[a]anthracene and benzo[a]pyrene, are probably carcinogenic (IARC 2003).

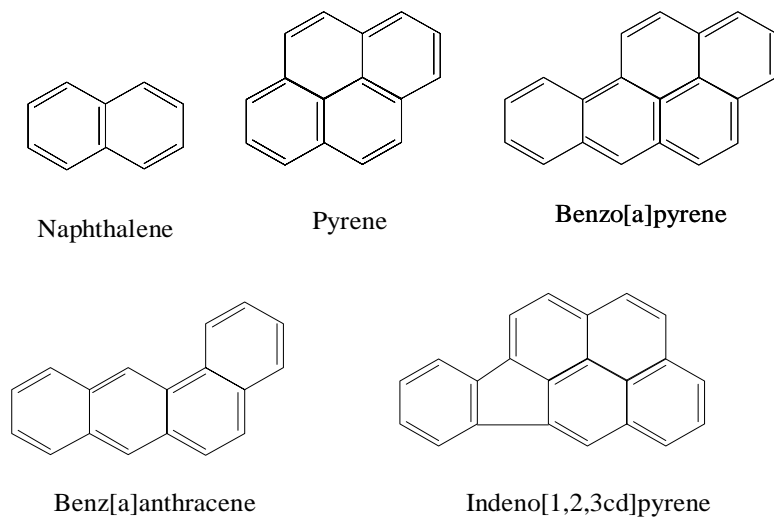


Figure 3-1. Example structure of a few PAHs.

In the atmosphere or in exhaust from a combustion source, PAHs can be found on particles or as a vapor. Heavier molecular weight (MW) PAHs tend to be found on particles, whereas lighter MW PAHs are more typically found as vapors. The phase of the PAHs will also depend on their source and its operating condition. For example, diesel exhaust tends to contain more particle-bound PAHs at higher engine load than at idle conditions.

A few PAHs are regulated directly in the United States, and other countries regulate individual PAHs or classes of PAHs. The EPA regulates emissions of one PAH, naphthalene, as a hazardous air pollutant, and seven PAHs are included on EPA's list of urban air toxics, which may be regulated in the future. Particle-bound PAHs are regulated indirectly through standards for particulate matter, opacity, smoke, and visibility. Typically, PAHs make up a small fraction of particle mass.

PAHs can be found in vapor or on particles

How does it work?

Figure 3-2 shows a schematic of the PAS, and additional instrument details can be found in EPA (1997) and Burtscher (1992). Briefly, samples flow continuously into the PAS and through the eximer-lamp ionization region, where particle-bound PAH molecules are ionized and loose an electron. The photon energy of the lamp is chosen so that gas-phase molecules are not ionized. The negatively charged particles collect on a filter where charge is measured with an electrometer. The charge is integrated over time to give the photoelectric current (in femto- or picoamps). This current should be proportional to the PAH loading on a particle. Three versions of the PAS are available commercially, but they all have similar operating principles.

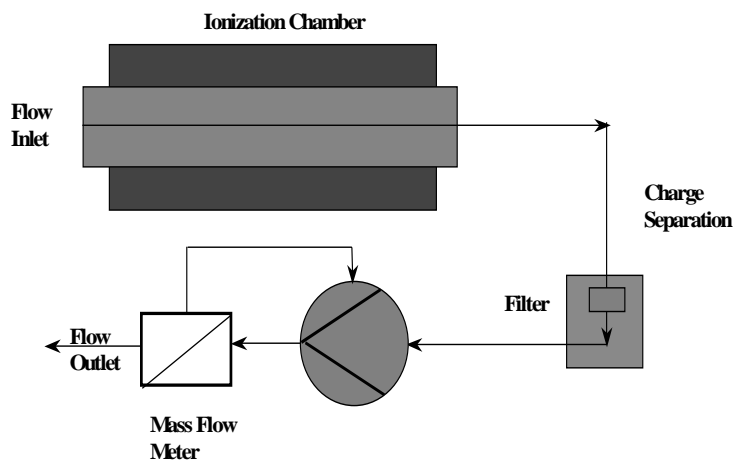


Figure 3-2. Schematic of the PAS.

The PAS was originally calibrated to fifteen individual PAHs (called the Siegmann sum) from several sources, with a universal conversion factor of 1-3 $\mu\text{g}/\text{m}^3$ picoamp⁻¹ (Wilson and Barbour 1994, Wilson et al. 1991, EPA 1999). Because PAHs are such a complex mix of vapor and particle-phase compounds, the PAS responds differently to each type of source, and calibration factors can vary widely (Figures 3-3 and 3-4).

For a more accurate measure of PAHs, calibrate each PAS for each source type

Without an appropriate calibration curve, the PAS will only give you a relative measure of particle-bound PAH levels. Independent comparisons of the PAS and filter measurements are limited (Chuang et al. 1999, Chetwittayachan et al. 2002, Tang et al. 2001, Arnott et al. in progress), and the results are contradictory. Figures 3-3 and 3-4 compare PAS results with filter measurements for military vehicles and aircraft, and they show how the PAS response varies for different sources. The PAS results correlate reasonably well with filter measurements for military vehicles ($R^2 = 0.762$) and better for military aircraft ($R^2=0.99$), but the aircraft correlation is heavily weighted by one data point. The response of each PAS instrument varies for each source type, so a calibration curve for each instrument should be developed for each source. For vehicle and aircraft emissions, it is also interesting to note that the PAS correlates well with soot concentration (Baltensperger et al. 2001, Matter et al. 1999, Arnott et al. in progress).

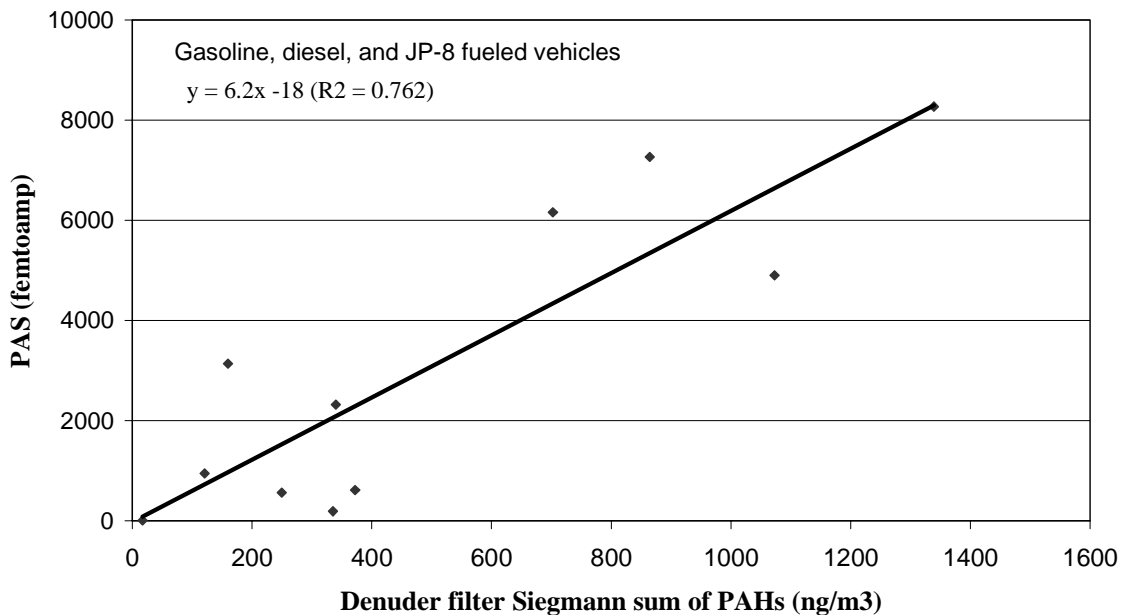


Figure 3-3. Correlation of PAS readings with denuder filter measurements of particle-bound PAHs for several vehicles.

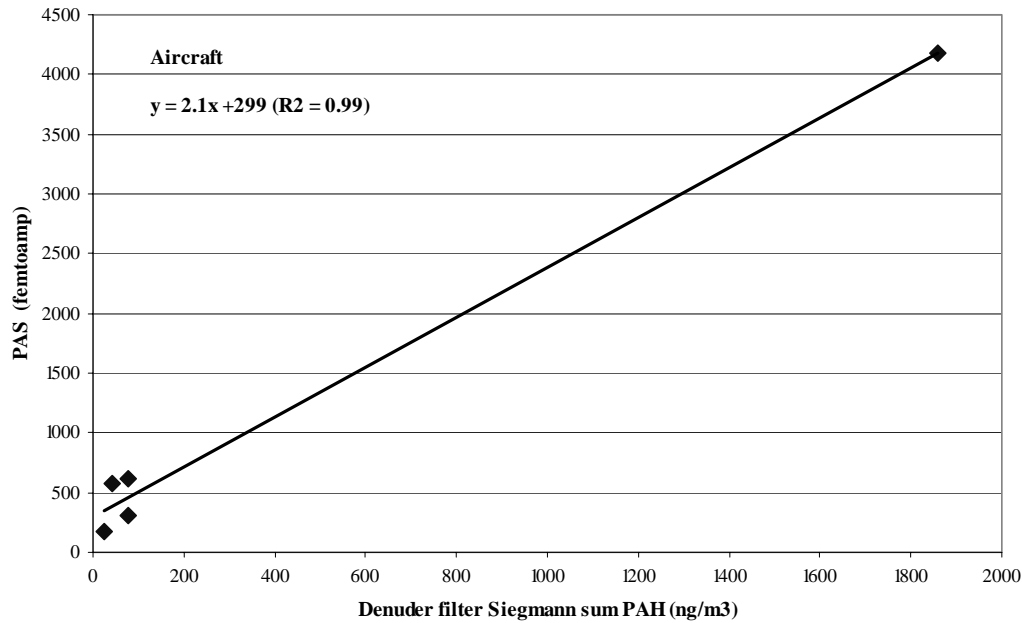


Figure 3-4. Correlation of PAS readings with denuder filter measurements of particle-bound PAHs for aircraft.

When can you use the photoelectric aerosol sensor?

The PAS can qualitatively measure PAH emissions from a variety of emission sources and ambient air. For source sampling, there are a few practical considerations:

PAS results correlate somewhat with filter measurements

- Maintain PAS readings below 50 picoamps. Exposing the PAS to high levels of water vapor or source emissions, such as diesel exhaust, will cause erratic results. Measurements of anything other than ambient air requires dilution with dry, particle free air.
- Keep the PAS inlet temperature constant because PAS results vary with inlet temperature. Studies at the University of Utah found a temperature of approximately 250-300°F to be reduce erratic negative signals. The PAS manufacturers sell a dilution/heated inlet system. Alternatively, you can wrap the inlet line with heating tape.

- The instrument itself should operate at temperatures between 0°F and 105°F.
- Depending on the source, the PAS can detect a minimum PAH concentration of 10 ng/m³.
- The PAS must remain dry and protected from the elements.

Cost comparison

Chemical analysis of PAHs from filter samples is expensive. For example, analyzing nine stages of a cascade impactor for PAHs costs approximately \$4,700 and analyzing a denuder/filter system costs approximately \$1,500 (if the three components are analyzed separately). These costs do not include the labor costs associated with collecting the samples or the costs of the sampling devices. One type of cascade impactor, a micro-orifice uniform deposit impactor (MOUDI), costs approximately \$12,000 for the entire complete setup and a denuder/filter system costs approximately \$2,000 – 4,000 (depending on configuration). Furthermore, chemical analyses for PAHs are time consuming; it typically takes several months to receive the analytical results. Alternatively, the PAS collects data in real time, and the data can be downloaded and analyzed in the matter of days. The PAS 2000 costs approximately \$15,000 (2003 price).

Comparison of the PAS with other methods

There are two basic methods for measuring particle-bound PAHs. The first involves collecting samples on a filter followed by chemical analysis, and the other is the PAS. Filter samples are commonly collected on cascade impactors, such as MOUDIs, or on a denuder/filter system. The MOUDI contains eight to ten stages plus an after filter, and each stage contains a filter. A denuder/filter system contains three parts, a resin-coated denuder that absorbs vapor-phase PAHs, a filter that collects particles, and a cartridge to collect excess particles and vapor from the filter and denuder. The next step in chemical analysis is extracting the filters or denuder/filter components with a solvent, such as hexane. The extract may be concentrated to improve the detection of low-concentration PAHs, and impurities may be removed. Next, the extract is analyzed by an advanced analytical method, such as gas chromatography/mass spectrometry. The entire process of PAH analysis is challenging because of the low concentrations of PAHs, the potential interference from the complex mixtures of chemicals in which PAHs are found, and the reaction of compounds during sampling and storage.

PAH analysis
is challenging

Traditional filter measurements and denuder/filter systems provide some information that cannot be obtained with the PAS. For example, the traditional analyses measure concentrations of individual PAHs, instead of the total particle-bound PAH content as measured by the PAS. In addition, the denuder/filter system provides information on vapor- and particle-

phase concentrations of individual PAHs. Finally, substrates collected on a MOUDI or other cascade impactor can give information on the size of particles on which PAHs are found.

A filter or denuder/filter system requires a minimum amount of material for analysis, but excessive amounts of sample may cause artifacts. If a filter is properly prepared, a trained graduate student or technician can collect a filter or impactor sample. However, it is difficult to determine if there is sufficient sample for PAH analysis before the sampling is complete. After sampling is complete, a small section of the filter can be analyzed for organic carbon content, which provides an indication of the PAH loading. A further complication for cascade impactors, such as a MOUDI, is that mass loading will vary by impactor stage. Operation of the denuder/filter system is delicate and requires an experienced scientist. For example, an individual must ensure that the flow is sufficiently high to prevent very small particles from depositing on the denuder portion. However, if one overloads the denuder, the flow will drop, causing particle deposition and erroneous results. For ambient samples, collecting sufficient material may require several days of sampling, and for source samples it may require from tens of minutes to hours.

Chemical analysis provides more information

The PAS is relatively easy to operate, and it provides results rapidly. However, it is not as accurate as the chemical analysis methods, and it provides less detailed information. A technician or student could operate the PAS. The PAS can measure a large range of PAH concentrations, and it is sensitive enough to detect ambient levels of PAHs down to 10 ng/m³. With dilution the PAS can measure emissions from combustion sources, such as diesel engines. However, care must be taken not to expose the PAS directly to undiluted exhaust from a source like a diesel engine, which will cause erratic signals. Because the PAS records PAH concentrations rapidly (at intervals less than 10 seconds), it is particularly useful for studying transient conditions, such as process start up or engine acceleration. On the other hand, filter analyses require sufficient time for material to deposit on the substrates, and these analyses are not sensitive enough to provide information on transient conditions. The PAS does have a few disadvantages: is not as accurate as the chemical analysis methods, and each instrument should be calibrated for each source type, which is expensive and time consuming. Furthermore, the PAS provides the total concentration of particle-bound PAHs; it cannot provide the concentrations of individual PAHs or information about vapor-phase PAHs.

The PAS provides rapid results

PAH detection and analysis is challenging, and there are significant tradeoffs between chemical analysis methods and the PAS. Chemical analysis provides accurate concentrations of individual PAHs. They can provide the size of particles on which PAHs are associated and which PAHs are found in vapor and particle phases. However, chemical analysis methods are expensive, time consuming, and subject to artifacts. The PAS rapidly provides a relative measure of total PAH concentrations and can provide information on transient conditions. However, more accurate results could be obtained by calibrating each PAS for each source.

Chemical analysis is more accurate and provides more data but is more expensive and time consuming

Vision for use

The PAS is a good choice when a relative measure of particle-bound PAHs is desired or when transient conditions are studied. For example, it would be useful for the preliminary evaluation of a control device, for screening sources for further analysis, or for studying transient conditions. The PAS is a relatively new instrument, and with additional study and independent calibration it may produce more valuable results. Chemical analysis methods are a good choice if you want quantitative PAH concentrations, accurate concentrations of individual PAHs, or information about the phase distribution of PAHs.

Resources

Website for the photoelectric aerosol sensor:

<http://www.ecochem.biz/PAH/PAS2000.htm>

For general information or information about this User's Guide, Kerry Kelly:

kelly@eng.utah.edu

References

Arnott et al., Evaluation of 1047 nm Photoacoustic Instruments and Photoelectric Aerosol Sensors in Source-Sampling of Black Carbon Aerosol and Particle-Bound PAH's from Gasoline and Diesel Powered Vehicles, *in progress*.

Baltensperger, U. E. Weingartner, H. Burtscher, J. Keskiö, Dynamic Mass and Surface Area Measurements. In: P.A. Baron and K. Willeke (eds.) *Aerosol Measurement 2001* New York:Wiley, pp. 387-418.

Burtscher, H. Measurement and Characteristics of Combustion Aerosols with Special Consideration of Photoelectric Charging and Charging by Flame Ions; *J. Aerosol Sci.* **1992**, 23 (6) 549-595.

Chetwittayachan T., D. Shimazaki, K. Yamamoto, A comparison of temporal variation of particle-bound polycyclic aromatic hydrocarbons (pPAHs) concentration in different urban environments: Tokyo, Japan, and Bangkok, Thailand, *Atmos. Environ.* 36 **2002** 2027-2037.

Chuang, J.C, P.J. Callahan, C.W. Lyu, N.K. Wilson, Polycyclic aromatic hydrocarbon exposures of children in low-income families, *J. Exposure Analysis and Environ. Epid.* 2 **1999** 85-98.

EPA. *Field and Laboratory Analyses of a Real-Time PAH Analyzer*, EPA/600/R-97/034; EPA Office of Research and Development, **1997**.

International Agency for Research on Cancer, *IARC Monographs*, **2003**, vol. 1-82 <http://monographs.iarc.fr/monoeval/crthall.html>

Matter U., H.C. Siegmann, H. Burtscher, Dynamic Field Measurements of Submicron Particles from Diesel Engines, *Environ. Sci. Technol.* 33 **1999** 1946-1952.

National Toxicology Program, *10th Report on Carcinogens*, U.S. Department of Health and Human Services, National Toxicology program **2003**, <http://ehis.niehs.nih.gov/roc>

Tang, S., R. Johnson, T. Lanni, W. Webster, T. Tagliaferro, H. Munn, C. Barnes, D. Barnes, K. Newkirck, D. Rivenburgh, D. Guerrieri, *Monitoring of PM-bound polycyclic aromatic hydrocarbons from diesel vehicles by photoelectric aerosol sensor (PAS)*, Automotive Emissions Laboratory, New York Department of Environmental Conservation, March 22, **2001**.

Wilson N.K., Barbour, R.K., Evaluation of a real-time monitor for fine particle-bound PAH in air, *Polycyclic Aromatic Compounds* 5 **1994** 167-174.

Wilson N.K., Chuang, J.C., MR. Sampling polycyclic aromatic hydrocarbons and related semivolatile organic compounds in indoor air. *Indoor Air* 4 **1991** 513-512.

Aerosol Time-of-Flight Mass Spectrometer

for measuring individual particle size and composition

The aerosol time-of-flight mass spectrometer (ATOFMS) determines size and composition of single particles in near real-time. It is available commercially from TSI Inc. (Model 3800). The ATOFMS is a powerful tool because it provides associations between compounds within single particles, and this information can be used to identify a particle's source. The ATOFMS also provides PM composition for transient conditions, when bulk techniques, such as filters, cannot.

The ATOFMS determines a particle's size and composition

Why is understanding the size and composition of individual particles useful?

Studies over the last ten years have linked particulate matter (PM) concentration to adverse health effects, and more recent evidence indicates that size, surface area, and composition of PM are important factors in determining the health effects associated with PM. For example, certain metals found in PM, such as iron, nickel and vanadium have been linked to adverse effects on the lung. The composition of individual particles can also provide insight into particle formation and chemistry, and it can help identify the source of a particle by its chemical composition, i.e., fingerprint. For example, it can provide fingerprints for specific sources, such as explosives, diesel engines, and biological aerosols.

A particle's size and composition can provide clues about its source and health effects

How does it work?

Figure 4-1 shows a schematic of the ATOFMS. The ATOFMS consists of three regions:

- Particle sampling region
- Particle sizing region
- Mass spectrometry region

In the commercially available ATOFMS, particles are introduced into the particle-sampling region under atmospheric pressure through a converging nozzle where they are accelerated according to their aerodynamic size. Smaller particles reach a higher terminal velocity than larger particles. The accelerated particle next enters the particle sizing region, where particle velocity is measured by recording the transit time for the particle to pass between two continuous-wave laser beams

positioned a fix distance apart. Particle size is then determined by comparing the velocity of the particle to a calibration curve, which is obtained using particles of known size. Finally, the particle reaches the mass spectrometry region. Using the known speed of the particle, a Nd:YAG laser at 266 nm is fired at the exact time the particle reaches the center of the ion source in the mass spectrometer. This laser pulse desorbs and ionizes the compounds making up the particle. The ions formed in this process are analyzed by a bipolar time-of-flight mass spectrometer. The resulting mass spectra are then used to determine the chemical composition of the particle.

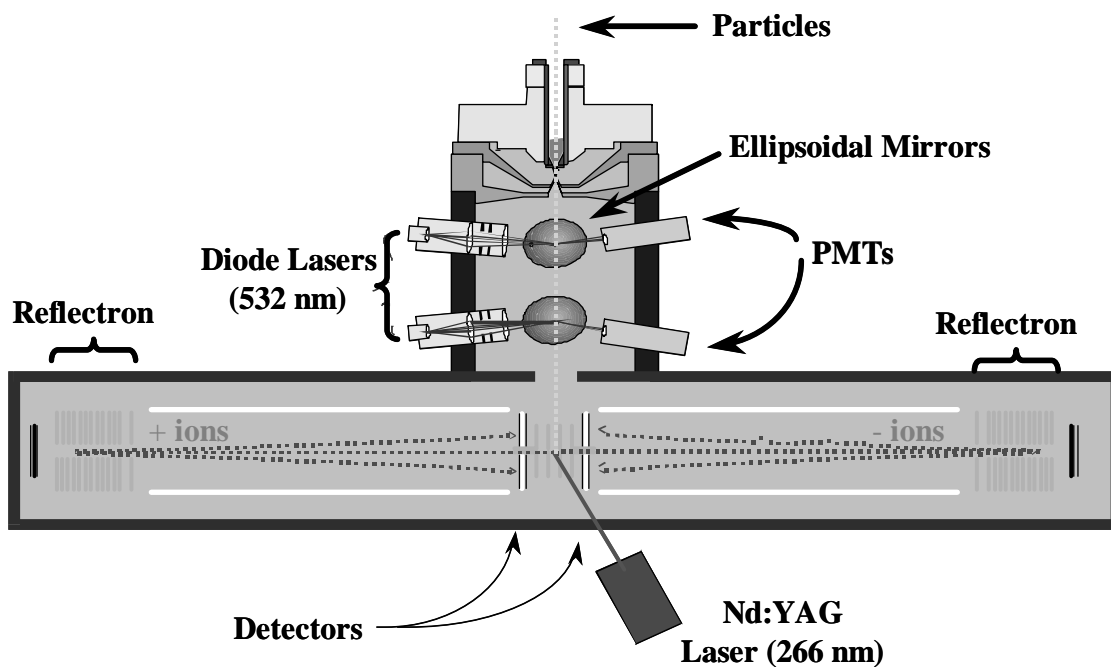


Figure 4-1. Schematic of the ATOFMS.

The operation of the ATOFMS is based on two established methods:

- Aerodynamic particle sizing
- Time-of-Flight Mass Spectrometry (TOFMS)

What is aerodynamic sizing?

Aerodynamic particle sizing is based on the inertia of particles. When a gas expands, it is accelerated. Particles suspended in the gas are also accelerated, but the extent of the acceleration depends on their aerodynamic diameter. The aerodynamic diameter is defined as the diameter of a unit density (density = 1 g/cm³) sphere that has the same settling velocity as the particle (TSI, 2002). Not only the physical diameter but also the shape and density of the particle are taken into account. The smaller a particle, the higher the acceleration and therefore the terminal velocity it reaches. This velocity can be determined by measuring the time it takes the particle to travel a known distance. Usually this transit time is measured using a split laser beam or with beams from two lasers (which is used in the 3800 ATOFMS). The scattered light is collected with a detector and the signals are used to start and stop a clock registering the transit time. Transforming the transit time into size is done by calibrating the instrument with a number of particles of known size to create a calibration curve. This calibration curve is then used to determine the size of the unknown sample (TSI, 2002).

What is time-of-flight mass spectrometry?

There are many types of mass spectrometry (MS). A common component of all MS systems is that ions are separated based on their mass-to-charge ratio (m/z). The first mass spectrometry instruments used a magnetic field to separate ions. Later instruments used magnetic and electric fields. Other common methods include those that use quadrupole mass filter, quadrupole ion traps, ion traps in static magnetic fields (Fourier transform mass spectrometry), and time-of-flight (TOF-MS) measurements. Each method has its advantages and disadvantages depending on the application. FTMS, for example, can provide extremely high mass resolution. Quadrupole and quadrupole ion trap instruments can be very small. TOF instruments offer the advantage of not being a scanning method, that is, you get a complete spectrum for each ionization event. As the name suggests, TOFMS accelerates ions to a specific kinetic energy and measures the ions' time-of-flight between a distinct starting point (often the ionization event) and the arrival at the detector. The ions arrival times are correlated with their mass-to-charge ratios, with smaller m/z ions arriving before larger m/z ions. Upon calibration of the mass spectrometer, the measured ion transit times can be converted to the corresponding mass-to-charge ratios, which are related to the chemical components in the original particles. The most common start event is the pulse of the desorption/ionization (D/I) laser. This event starts the data logging; the ion current from the detector is recorded over time and creates the mass spectrum. Ions created in the ion source are accelerated into the flight tube by a potential that is usually created by two source plates. As all ions have the same energy, the potential where they were formed, the acceleration (and therefore the velocity they reach at the end of the ion source) depends only on their mass-to-charge ratio:

$$eV = \frac{mv^2}{2z}$$

$$v = \sqrt{\frac{2zeV}{m}}$$

where: eV is the potential energy of the ion,
 m/z is the mass-to-charge ratio,
 and v is velocity.

This equation shows that ions with a small m/z are accelerated to a higher terminal velocity than ions with a large m/z . After the initial acceleration step, the ions enter the flight tube, also known as the field free region or drift region. This part of the mass spectrometer is held at a constant potential (hence the name *field free region*) and the ions drift at the velocity they achieved from their acceleration in the ion source (*drift region*). During this time, ions separate based on their velocity and therefore their m/z . At the end of the flight tube, they hit a detector and create an ion current that is measured and recorded to create the mass spectrum.

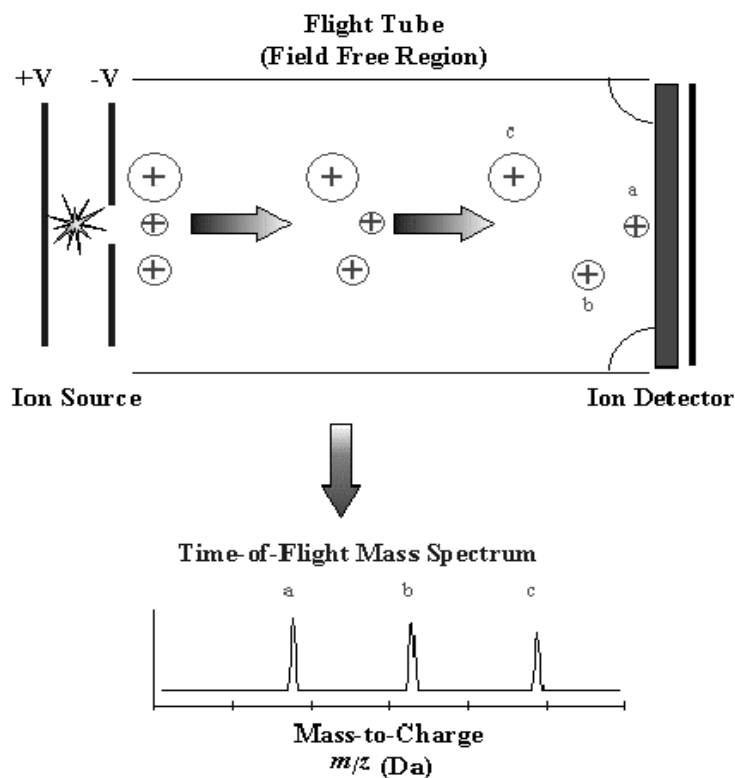


Figure 4-2. Time-of-flight mass spectrometry principles.

During the desorption/ionization event, ions can obtain additional kinetic energy from the explosion during desorption. Some ions travel in the direction they are accelerated in, while other ions travel in the opposite direction. This leads to a spread in energy for ions with the same m/z . As a result of this, ions with the same m/z end up with different velocities, which results in peak broadening due to different arrival times at the detector (low mass resolution). One way to correct this resolution issue is to use a reflectron or ion-mirror. The reflectron consists of a number of parallel, concentric electrodes to which a potential ramp is applied. The most common type of reflectron is the linear reflectron, which shows a linear potential increase. As the ions enter the reflectron, they slow down, stop, turn around, and are accelerated out of the reflectron again. Ions with higher energies penetrate the reflectron more deeply than ions with a smaller energies. Faster ions (high energy ions) therefore travel deeper into the reflectron than slower ions *of the same m/z* and spend more time in the reflectron. With the voltages set correctly, all ions of the same m/z are focused at the same arrival time on the detector surface (see Figure 4-3).

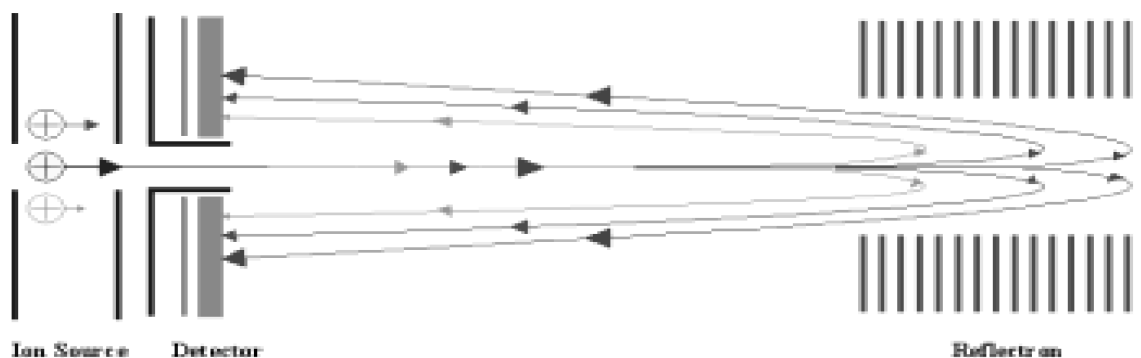


Figure 4-3. The reflectron focuses ions with different velocities/energies in time onto the detector.

When can you use the ATOFMS?

The ATOFMS has a few practical considerations:

- The commercially available version of the ATOFMS detects PM in the size ranging from 300 nm to 3 μm . It is possible to modify the ATOFMS with an aerodynamic lens to detect smaller sized particles, as small as 50 nm.
- The ATOFMS is mobile and frequently operates in the field. However after moving, the instrument's lasers may need alignment. In addition, it weighs approximately 800 lbs.
- For power, the ATOFMS requires 20 A of 220-240 VAC and 20 A of 110-120 VAC.
- The instrument itself should operate at temperatures between 50°F and 95°F.
- The ATOFMS must remain dry and protected from the elements.

Cost comparison

The ATOFMS is relatively expensive compared to an individual bulk sample. It currently costs \$360,000. However, it can provide information that is not available through any other methods. Costs for the analysis of bulk samples (i.e., filters) range from a few dollars to a few thousand dollars per filter. If you are collecting and analyzing many bulk samples, the analysis costs can quickly run into the range of the ATOFMS's price. For the ATOFMS, a trained scientist must collect the samples and interpret the results. By comparison, bulk samples can be collected by a technician and sent away for analysis.

The ATOFMS is more expensive than bulk samples, but it can provide more data

Comparison of the ATOFMS with other methods

There are two basic methods for measuring particle size and concentration. The first involves single-particle mass spectrometry and the other involves collecting bulk samples on a set of cascade impactors or filters followed by chemical analysis.

Single-particle mass spectrometry

A number of mass spectrometer designs have been developed for aerosol analysis in the past decade. The other alternative single-particle methods (i.e. PALMS, RSMS) either provide limited size information or must step through discrete particle sizes. The ATOFMS is the only commercially available single particle MS and the system offers the highest size resolution and real-time analysis of particle size and composition across a range of sizes from 50 nm up to 7-8 μm . A complementary alternative to single particle mass spectrometry is aerosol mass spectrometry (AMS), a system developed by Aerodyne, which collects the average composition of an ensemble of many particles. This technique can be more quantitative than single-particle instruments but does not provide any information on the chemical associations within individual particles (or mixing state).

Single-particle mass spectrometry is the only method to provide the composition of single particles, and the ATOFMS was the first commercially available instrument. When comparing ATOFMS to bulk methods, the advantages and disadvantages are similar to other single-particle mass spectrometry methods.

The key advantage is that ATOFMS can be used to determine associations between species within individual particles. These associations can be linked with sources, making source apportionment much more straightforward than bulk measurements, which scramble the chemical information from multiple sources collected over some long sampling interval.

Also, the associations are key to understanding the health effects of these particles, as well as their optical properties, which are important in climate change issues. It is impossible to get these associations with bulk techniques, which mix the chemical signatures of thousands of particles together. Furthermore, the ATOFMS can acquire information on much shorter timescales than bulk measurements, which must sample for many hours in order to collect enough material for analysis, precluding the observation of short-term changes in PM composition.

The key disadvantage of the ATOFMS is its cost and the learning curve required to interpret the spectra. However, the commercial system is now being successfully used by a broader set of users, and more information is becoming available on particle types and analysis methods. The commercial ATOFMS is the only available method that can continuously measure single particle size and composition. New ATOFMS systems are currently being designed which will reduce the size, weight, and power requirements and the overall cost of the system. This will make them more widely available.

Experience is needed to operate the ATOFMS and interpret its results

Bulk samples

Bulk PM samples are commonly collected on cascade impactors, such as a micro-orifice uniform deposit impactors (MOUDIs) or Andersen impactors. The impactors contain eight to ten stages plus an after filter, and each stage contains a filter. Depending on the analysis method, the next step may be extracting the filters a solvent, such as hexane. The extract can be concentrated to improve the detection of low-concentration compounds, and impurities may be removed. Next, the extract or the filter is analyzed by an advanced analytical method, such as gas chromatography, mass spectrometry, x-ray fluorescence, or instrumental neutron activation analysis. Some compounds are present in low concentrations, so analysis can be challenging.

Furthermore, evaporation, condensation, and reaction of compounds during sampling, extraction, and storage can also cause artifacts.

Chemical analysis of filter samples for some compounds is challenging

Cascade impactor samples provide PM within a certain size range, such as 0.05 μm to 0.1 μm , so the PM sizing is not as precise as the ATOFMS. Furthermore, a filter requires a minimum amount of material for analysis; depending on the source, sample collection may take hours or even days, so any transient differences in PM composition will be lost in the bulk sample. It is also difficult to

determine if there is sufficient sample for analysis before the sampling is complete. A further complication for cascade impactors is that material loading will vary by impactor stage.

The key advantage of a filter/impactor samples is that they are less expensive than ATOFMS measurements or other single-particle mass spectrometry methods. Furthermore, a trained technician can collect samples instead of an experienced scientist. However, these bulk measurements lack the ability to provide rapid results, information about transient conditions, and associations between species in individual particles.

Bulk samples cannot provide data on transient conditions

Vision for Use

The most obvious applications for DoD users would be source apportionment (as demonstrated in SERDP project CP1106) and detection of signature compounds, including biowarfare detection. Biological particles can easily be discriminated from other atmospheric particles on a continuous basis. These instruments conceivably could detect individual bacteria and discriminate between them and particles from other sources. ATOFMS could acquire this information continuously so the particles of concern could be detected instantaneously for early warning. This has serious defense ramifications.

Resources

For more information about time-of-flight mass spectrometry:

Cotter, R.J. The new time-of-flight mass spectrometry. *Analy. Chem.* 71(13) **1999** 445A-451A.

Cotter, R. J. Time-of-flight mass spectrometry, instrumentation and applications in biological research. *J. Liq. Chrom. & Rel. Technol.* 21(6) **1998** 903-914.

Mamyrin, B.A., V.I. Karataev, D.V. Shmikk, V.A. Zagulin, *Sov. Phys. JETP* **1973** pp. 37, 45.

For additional information about the ATOFMS:

ATOFMS Web site <http://www.tsi.com/particle/products/massspec/3800.shtml>

Galli, M., S.A. Guazzotti, K.A. Prather, Improved Lower Particle Size Limit for Aerosol Time-of-Flight Mass Spectrometry. *Aerosol Sci. & Technol.* 34(4) **2001** 381-385.

Gross, D.S., M.E. Galli, P.J. Silva, S.H. Wood, D.Y. Liu, K.A. Prather, Single Particle Characterization of Automobile and Diesel Truck Emissions in the Caldecott Tunnel. *Aerosol Sci. & Technol.* 32(2) **2000** 152-163.

Middlebrook, A.M.; D.M. Murphy, S.H. Lee, et al. A Comparison of Particle Mass Spectrometers during the 1999 Atlanta Supersite Project. *J. Geophys. Res. [Atmospheres]* **2003** 108(D7).

Noble, C.A., K.A. Prather, Real-Time Single Particle Mass spectrometry: A Historical Review of a Quarter Century of the Chemical Analysis of Aerosols. *Mass Spec. Rev.* 19(4) **2000** 248-274.

Noble, C.A., K.A. Prather, Aerosol Time-of-Flight Mass Spectrometry. *Analy. Chem. Aerosols* **1999** 353-376.

Suess D.T., K.A. Prather, Mass Spectrometry of Aerosols, *Chem. Rev.* 99 **1999** 3007-3035.

Wexler, A., K.A. Prather, Introduction: Online Single Particle Analysis. *Aerosol Sci. & Technol.* **2000** 33(1-2) 1-2.

ATOFMS Applications:

Guazzotti, S. A., J.R. Whiteaker, D. Suess, K.R. Coffee, K.A. Prather, Real-Time Measurements of the Chemical Composition of Size-Resolved Particles during a Santa Ana Wind Episode, California USA. *Atmos. Environ.* 35(19) **2001** 3229-3240.

Liu, D.Y., D. Rutherford, M. Kinsey, K.A. Prather, Real-Time Monitoring of Pyrotechnically Derived Aerosol Particles in the Troposphere. *Analy. Chem.* **1997** 69(10), 1808-1814.

Liu, D.Y., R.J. Wenzel, K.A. Prather, Aerosol Time-of-Flight Mass Spectrometry during the Atlanta Supersite Experiment: 1. Measurements. *J. Geophys. Res. [Atmospheres]* **2003** 108(D7).

Prather, K., C. Noble, D. Liu, P.J. Silva, Single Particle Analysis of Transient Variations occurring in Atmospheric Aerosols. *J. Aerosol Sci.* **1998** 29(Suppl. 1, Pt. 2), S1185-S1186.

Silva, P.J, R.A. Carlin, K.A. Prather, Single Particle Analysis of Suspended Soil Dust from Southern California. *Atmos. Environ.* 34(11) **2000** 1811-1820.

Suess, D.T., K.A. Prather, Reproducibility of Single Particle Chemical Composition during a Heavy Duty Diesel Truck Dynamometer Study. *Aerosol Sci. & Technol.* 36(12) **2002** 1139-1141.

Wenzel, R.J., D.Y. Liu, E.S. Edgerton, K.A. Prather, Aerosol Time-of-Flight Mass Spectrometry during the Atlanta Supersite Experiment: 2. Scaling Procedures. *J. Geophys. Res. [Atmospheres]* **2003** 108(D7).

Whiteaker, J.R., K.A. Prather, K.A. Detection of Pesticide Residues on Individual Particles. *Analy. Chem.* 75(1) **2003** 49-56.

For general information or information about this User's Guide, Kerry Kelly:

kelly@eng.utah.edu

References

Hinds, W.C. *Aerosol Technology*, 1 ed.; John Wiley & Sons: New York **1982**.

TSI, *Model 3800 Aerosol Time-of-Flight Mass Spectrometer Instruction Manual*, P/N 1930036. TSI Incorporated **2002**.

Dilution and Sampling

Design and selection of a dilution/sampling system is one of the most challenging problems associated with characterizing particulate matter (PM). This section highlights some important things to consider when selecting a dilution/sampling system, and it is divided into:

- Sample types
- Types of measurements
- Effects of dilution systems
- Dilution gas
- General recommendations for dilution/sampling systems
- Common systems
- Rules of thumb

What type of samples will you be collecting, ambient or source?

Sample types

If you are collecting a PM sample, the first question to ask is whether you'll be collecting a source sample or an ambient sample. For sources, your sample intake will be located directly in the exhaust, i.e., in the tailpipe of a vehicle. For ambient samples, your intake is located out of the direct exhaust of any sources. Typically, ambient samples experience much lower levels of PM than source sampling. This guide focuses on source sampling. For guidance on ambient sampling see the list of resources at the end of this section.

For source sampling, the instruments discussed in this guide (and most particle instruments) require dilution in order to operate within their required ranges. Dilution with dry gas also may approximate the processes that occur naturally after exhaust particles and gases mix with ambient air. It also reduces the humidity of the sample gas and water condensation in the sample lines.

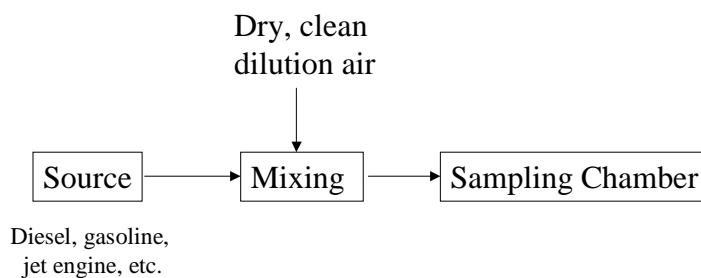


Figure 5-1 illustrates a generic dilution system. In most systems, exhaust from a source is pulled into a chamber, where it mixes with dry, clean dilution air; this mixture then flows into a sampling chamber, where particle instruments are located.

Figure 5-1. Generic dilution and sampling system.

Types of measurements

Currently, particle mass is a regulated pollutant, but interest is growing in particle number and composition. Your design and selection of a dilution/sampling system will depend on what you'd like to measure.

Extensive research on the effects of dilution systems on PM shows that dilution/sampling systems typically affect particle counts for particles less than 50 nm in diameter (Maricq et al. 2001; Abdul-Khalek et al. 1999; Kittelson et al. 1999, 2000, 2002; Shi and Harrison 1999). There are two main effects. Rapid cooling can cause nucleation of droplets of sulfuric acid or hydrocarbons. These are usually in the size range of 1 nm and produce an artificially large number count. Alternatively if large numbers of particles exist in the nucleation size range, they will agglomerate with larger particles if the

Do you want to measure PM mass, number, or composition?

Dilution systems have the biggest effect on

dilution rate is not fast enough and the number count will be artificially low. If the systems are clean and operated properly, they have little effect on particle mass or bulk composition. In other words, if you are only concerned about particle mass, selection of the dilution system is not as important as if you were concerned about particle number.

Effects of the dilution systems

Recent studies have shown how dilution conditions can affect particle number concentrations, particularly for very small particles (Maricq et al. 2001; Shi and Harrison 1999; Kittelson et al. 1999, 2000; Abdul-Kahlek et al. 1999). Specifically, dilution ratio, temperature, humidity, residence time, and system configuration can dramatically affect the formation of nanoparticles, particles less than 50 nm in diameter (definition from Baumgard and Johnson 1996). However, these factors tend to have little effect on particle mass.

Humidity

As humidity of dilution air increases, the number of nanoparticles increases (Abdul-Khalek et al. 1999). Dilution air should be dry to limit this effect.

Temperature

As temperature increases, the number of nanoparticles decreases (Abdul-Khalek et al. 1999; Kittelson 2000). Ensure that the temperature is recorded.

Residence time in the dilution/sampling chamber

The effects of residence time depend upon other factors such as dilution temperature, dilution ratio, and relative humidity. If these factors are held constant, as residence time increases particle counts increase (Abdul-Khalek et al. 1999). It is possible that additional residence time allows particles that are too small to detect to grow to a detectable size (Brockhorn 1994; Gulder, 2000). Another important process in particle growth is coagulation – small particles collide and stick to each other or stick to larger particles. This causes the number of smaller particles to decrease and the number of larger particles to increase. Figure 5-2 illustrates the effect of coagulation on a particle size distribution in a bag sample. For both processes, growth of nanoparticles to a detectable size and the loss of nanoparticles through coagulation, could affect the particle number. These factors would not affect particle mass, only particle count. The Hildemann dilution system and the constant-volume dilution system have a greater residence time than eductor systems, and the bag sampling system has the longest residence time.

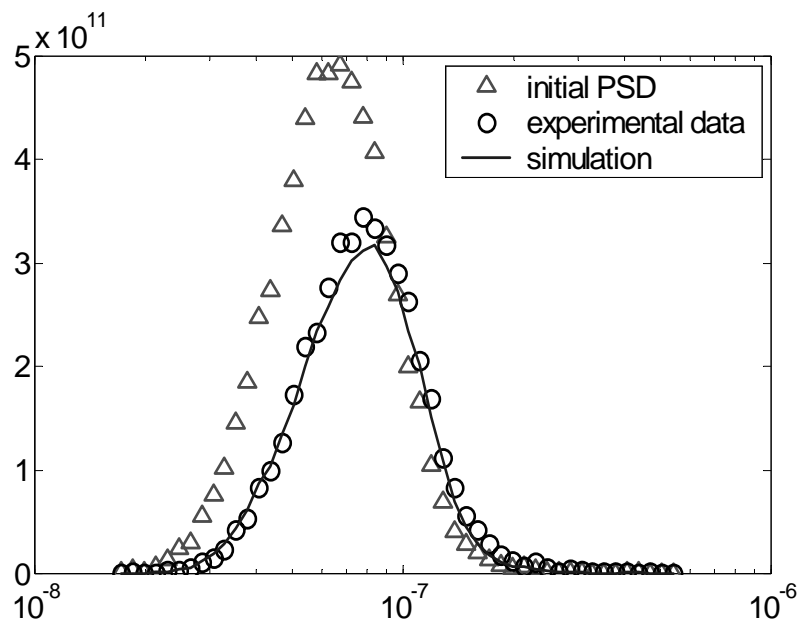


Figure 5-2. Particle size distributions in a Tedlar bag at 0.44hr and 1.24 hr, demonstrating the effect of coagulation (Jiang et al., 2002).

Dilution system configuration

PM can adhere to sampling lines, sampling chambers, and sampling bags. Maricq et al. (2001) found that transfer hoses can act as storage reservoirs for particles. This is because particles in warm exhaust gas are attracted to cold sample lines, where they can outgas at a later time. Therefore, sample lines should be as warm as or slightly warmer than the exhaust sample to prevent particles from sticking to the sample lines. In addition, sample lines should be as short as possible and replaced or cleaned often. The surface area in a sampling system should also be limited to reduce PM wall losses.

Dilution gas

Typically dilution is performed using compressed air. The compressed air or other dilution gas should be dry, particle free, and free of other contaminants, such as oil. This is accomplished by a series of traps and filters. A common compressed air clean up system includes: a spin-down water filter with a sintered nylon 20-40 μm filter element, a 0.3 μm borosilicate coalescing filter, an activated charcoal filter, and two HEPA filters. Prior to testing, it's a good idea to test the dilution air to ensure that it is clean and particle free with an optical particle counter, a scanning mobility particle sizer, or another particle measurement instrument.

General recommendations for dilution/sampling systems

Design your dilution/sampling system to limit particle deposition and re-entrainment by:

- Diluting your sample as close to the source as possible.
- Making your sample lines as short as possible and avoiding bends and sharp turns in the lines.
- Matching the temperature in your sample line to the exhaust temperature and matching your diluted exhaust temperature closely to the sampling chamber temperature.
- Replacing or cleaning your sample inlet line often.
- Frequently cleaning your sampling chamber.
- Avoiding plastic or rubber components that could collect or outgas material into the sampling system.

Control and understand your sampling conditions by:

- Carefully measuring and recording your sample and dilution flows.
- Measuring and recording the temperature of your undiluted sample, and the temperature and relative humidity of the diluted sample.
- Using clean, dry, particle free air to dilute samples.

If you want to compare your results to previous studies:

- Ensure that you use the same sampling/dilution conditions, or duplicate the sampling/dilution conditions as close as possible.

Common systems

We'll discuss four common types of dilution systems: an eductor system, a Hildemann system with an aging chamber, a constant-volume dilution sampler, and a bag sampling system. Other types of dilution/sampling systems exist, but these four systems are the most common. They also contain important aspects of most dilution systems.

Eductor sampling system

The eductor dilution/sampling system provides rapid mixing of the exhaust sample and dilution air (Figure 5-3). An eductor sampling system consists of an eductor, with a critical orifice located on the suction inlet, and an expansion/sampling chamber where individual instrument pull samples at atmospheric pressure. The eductor (also known as an ejector) operates by introducing pressurized (motive) air into a diverging nozzle system, where the motive air rapidly expands, creating a local region of low pressure that draws the sample into the eductor. The critical orifice is a precisely machined hole, located on the suction side of the eductor, through which the sample flow is regulated. The sample flow rate through the critical orifice increases with increasing motive airflow up to the point at which the pressure upstream of the critical orifice is twice that of the pressure downstream. At this point, the velocity of the sample through the critical orifice is choked and will not increase, regardless of any further increase in the motive airflow. In this system the particulate matter spends a short time between dilution and sampling, typically on the order of seconds.

Eductor systems
rapidly dilute a
sample

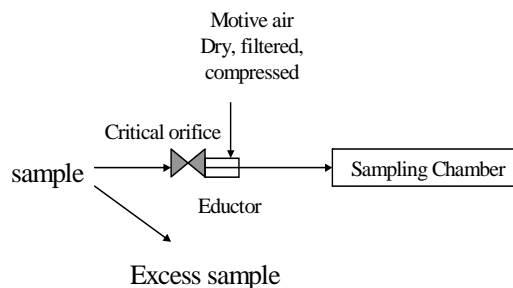


Figure 5-3. Eductor dilution system.

Advantages

1. Small, transportable, and relatively easy to set up.
2. Number counts from this type of system agree well with wind tunnel results (Maricq et al., 2001).
3. It is simpler to operate than some other systems.
4. It is relatively inexpensive to construct.

Disadvantages

1. Flows must be measured accurately.
2. The critical orifice can get clogged, so the pressure drop must be monitored continually.

Hildemann Dilution Sampler

The dilution tunnel/residence chamber was originally developed by Hildemann et al. (1991) to characterize the organic components of particles at very low concentrations. The key property of this system is that particles spend a relatively long time between dilution and sampling, typically from tens of seconds to minutes, and this was designed to approximate atmospheric processes (Figure 5-4). In this sampling system, a portion of the exhaust from the source flows into a heated line and venturi flow meter. It then mixes with dilution air and flows into a residence chamber. Typical residence times range from tens of seconds to several minutes.

The Hildemann system has a residence chamber

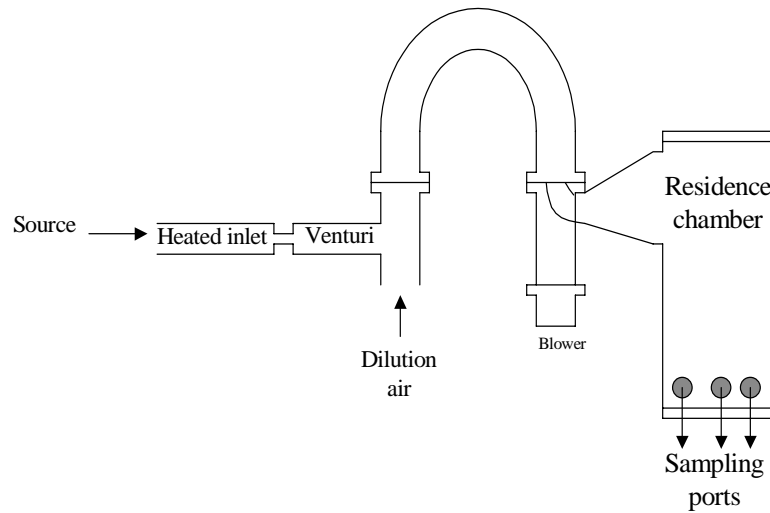


Figure 5-4. Hildemann dilution system.

Advantages

1. It provides a large volumetric flow, which is necessary for some analyses.
2. It permits complete mixing and cooling of the sample to ambient temperature.
3. The residence chamber allows particles, exhaust gas, and dilution air to reach equilibrium.

Disadvantages

1. It is large and not very portable.
2. It is time consuming to clean.
3. The long residence time can lead to the loss of nanoparticles, which coagulate to form larger particles. This would not affect particle mass but could affect particle number count.
4. The long residence time can also cause particles that are too small to detect to grow to a detectible size.
5. The system is moderately complex and must be monitored to ensure constant flows and prevent leaks.
6. It is moderately expensive to construct.

Constant-volume sampler

Constant-volume samplers are typically found in vehicle certification laboratories, and this type of sampler is required to certify vehicle emissions according to EPA regulations. These samplers provide a constant total volume of sample plus diluted air (Figure 5-5). All of the exhaust flows into the sampler. Because the quantity of exhaust emitted by a source, such as a vehicle, changes with setting (i.e., engine speed or load), the dilution rate also changes to provided a constant volume. If you need certification testing, it is best to go to an established vehicle certification laboratory.

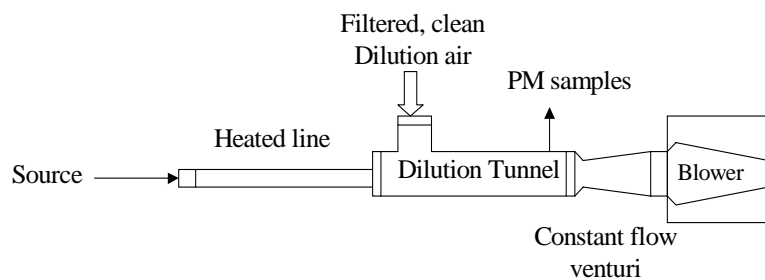


Figure 5-5. Constant-volume dilution sampler.

Advantages

1. The total exhaust flow rate does not need to be measured.
2. This is the EPA certification method.
3. It easily generates emission rates for vehicles in terms of particulate matter per mile.

A constant-volume sampler is used for vehicle certification

Disadvantages

1. This system is not very portable.
2. A different sized system is required for dramatically different sources (i.e., a passenger vehicle versus a heavy-duty diesel truck).
3. It must be operated by experienced personnel.
4. The heated line can act as a reservoir for particles.

Bag sampling system

A bag sampling system can be used to capture a known volume of sample, and the contents of the bag can then be analyzed at another time and location. This type of system is particularly useful when it is not possible to place instruments close to a source or when a source produces erratic emissions. However, a bag sampling system can cause static losses of PM to the bag's walls and changes in the particle size distribution due to coagulation. Coagulation leads to the loss of smaller particles and the growth of larger particles. Analyzing samples as rapidly as possible can reduce artifacts associated with bag sampling.

Figure 5-6 illustrates an example bag-sampling system, and these systems can be purchased commercially. A stainless steel, airtight container is fitted with a sampling bag through a clamp-down lid. A twist valve is affixed to the inlet of the sampling bag, and an actuated ball valve is placed in line with the sample inlet. A vacuum pump evacuates the space between the stainless steel container and the sampling bag. Upon opening the ball valve on the sample inlet, sample is drawn into the bag until the pressure in the bag is the same as that between the stainless steel container and the sampling bag. Once the bag is filled, the sample ball valve and twist valve are closed. After detaching the sample bag from the stainless steel container, the twist valve inlet can be connected directly to an analyzer sample inlet or to a dilution system for further analysis.

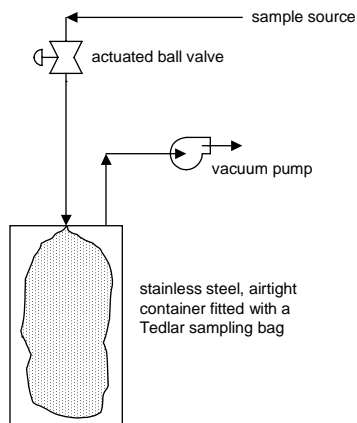


Figure 5-6. Bag sampling system.

Advantages

1. The system is small, robust, transportable, and relatively easy to set up.
2. It is relatively inexpensive to construct or purchase.
3. It provides an uniform sample, which may be necessary for some instruments.

A bag-sampler is good when instruments cannot be placed near a source

Disadvantages

1. This system can cause changes in the particle mass and size distribution. These changes are not well quantified and can include static particle losses and changes to the particle size distributions. Bags should be analyzed as rapidly as possible.
2. The dilution ratio may be difficult to determine. If you collect emissions downwind from a source, the sample will be diluted by ambient air. For combustion sources, the dilution ratio can be estimated with CO and CO₂ concentrations, but for other sources, i.e., sand blasting, the dilution ratio may be difficult to determine.
3. It will provide an aggregate sample, so variations in PM concentration or composition that occurred during the sampling interval will be lost.

A bag sampling system can cause particle loss and changes in the particle size distribution

Rules of thumb for selecting a dilution/sampling system

To summarize, we've provided some general guidelines for selecting a dilution/sampling system:

If you only want to measure particle mass from a source:

- For general use, select an eductor system.
- For vehicle certification, select a laboratory with a constant-volume sampling system.

If you want to measure particle number concentration:

- Select an eductor system.

If you want to measure particle composition:

- Select an eductor system or a Hildemann system, depending on the volume of sample required.

If you want the least expensive system:

- Select an eductor system.

If you cannot place instruments or a sampling/dilution system near a source:

- Select a bag sampling system and analyze the samples as quickly as possible.

Resources

For general information or information about this User's Guide, Kerry Kelly:

kelly@eng.utah.edu

EPA's PM_{2.5} Monitoring Information: <http://www.epa.gov/ttn/amtic/amticpm.html>

EPA's Supersite Program: <http://www.epa.gov/ttn/amtic/supersites.html>

EPA's PM Method: <http://www.epa.gov/ttn/amtic/pm.html>

References

Abdul-Khalek, I.S.; D.B. Kittelson, F. Brear, The Influence of Dilution Conditions on Diesel Exhaust Particle Size Distribution Measurements, Paper 9801142, Society of Automotive Engineers, Warrendale, PA, **1999**.

Baumgard, K.J., J.H. Johnson, The Effect of Fuel and Engine Design on Diesel Exhaust Particle Size Distributions, Paper 960131, SAE International, Warrendale, PA, **1996**.

Brockhorn, H. Soot Formation in Combustion, Mechanisms, and Models, Springer Series in Chemical Physics, Springer-Verlag: Berlin **1994**, vol. 59.

Gulder, O.L. Soot Particulate Formation in Combustion, *Trans. Can. Soc. Mech. Eng.* 1999, 23, 225-240.

Hildemann, L.M., G.R. Markowski, G. Cass, Chemical Composition of Emissions from Urban Sources of Fine Organic Aerosol, *Environ. Sci. Technol.* 25 **1991**744-759.

Jiang, P., J.S. Lighty, A.F. Sarofim, E.G. Eddings, 2002, Coagulation Simulation and Inference of Initial Particle Size Distributions, *Annual Meeting, American Association for Aerosol Research*.

Kittelson, D, Watts, W., Johnson, J. *Diesel Aerosol Sampling Methodology – CRC E-43*, 8/19/2002, Coordinating Research Council, <http://www.crcao.com/reports/recentstudies00-02/UMN%20Final%20E-43%20Report.pdf>

Kittelson, D.B., J. Johnson, W. Watts, Q. Wei, M. Drayton, D. Paulsen, Diesel Aerosol Sampling in the Atmosphere, Paper 2212, Society of Automotive Engineers, Warrendale, PA, **2000**.

Kittelson, D.B., M. Arnold, W.F. Watts, *Review of Diesel Particulate Matter Sampling Methods*, Final Report, University of Minnesota, Department of Mechanical Engineering, Center for Diesel Research, Minneapolis, MN, **1999**.

Maricq, M.M.; Chase, R.E.; Xu, N. A Comparison of Tailpipe, Dilution Tunnel, and Wind Tunnel Data in Measuring Motor Vehicle PM, *J. Air Waste & Man. Assoc.* 51 **2001** 1529-1537.

Shi, J.P.; Harrison, R.M. Investigation of Ultrafine Particle Formation during Diesel Exhaust Dilution. *Environ. Sci. Technol.* 33 **1999** 3730-3736.

APPENDIX 2:

EVALUATION OF 1047 NM PHOTOACOUSTIC INSTRUMENTS AND PHOTOELECTRIC AEROSOL SENSORS IN SOURCE-SAMPLING OF BLACK CARBON AEROSOL AND PARTICLE BOUND PAH'S FROM GASOLINE AND DIESEL POWERED VEHICLES

Evaluation of 1047 nm photoacoustic instruments and photoelectric aerosol sensors in source-sampling of black carbon aerosol and particle bound PAH's from gasoline and diesel powered vehicles.

by

W. P. Arnott, B. Zielinska, C. F. Rogers, and J. Sagebiel; Desert Research Institute, Reno
Nevada

K. Kelly, D. Wagner, A. Sarofim, and J. Lighty; University of Utah, Salt Lake City UT.

G. Palmer, Hill Air Force Base, Ogden UT.

ABSTRACT

A series of measurements have been performed at Hill Air Force Base to evaluate instruments that provide continuous measurements of black carbon aerosol and particle bound PAH's emitted from military vehicles. During the first series, gasoline and diesel powered vehicles were operated at idle or fast idle, though they were placed under load on a dynamometer during the second series. Photoacoustic instruments were developed that operated at a wavelength of 1047 nm where gaseous interference is not a problem, though sensitivity to black carbon is good. Compact, efficient, solid-state lasers with direct electronic modulation capability are used in these instruments. Black carbon measurements are compared with samples collected on quartz fiber filters that were evaluated using the thermal optical reflectance method. A measure of total particle-bound PAH was provided by photoelectric aerosol sensors (PAS) and is evaluated against a sum of PAH mass concentrations obtained with a filter-denuder combination. The photoacoustic instrument (PA) withstood the vigors of the field environment quite well, and provided sensitive measurement of black carbon mass concentration that agrees acceptably with thermal optical reflectance measurements of elemental carbon. The PAS had to be operated with

a dilution system held at approximately 150 C for most of the source-sampling to prevent spurious behavior, thus perhaps compromising detection of lighter PAH's. PA and PAS measurements were found to have a high degree of correlation, perhaps suggesting that the PAS can respond to the polycyclic nature of the black carbon aerosol, and perhaps that the detected particle-bound PAH's are produced in proportion, and are adsorbed to, the black carbon aerosol.

Introduction

Quantification of black carbon aerosol is important for both health and for the Earth's radiation balance (Andreae 2001; Lighty, Veranth et al. 2001) so the accurate, rapid assessment of these aerosols is needed, both in direct analysis of source emissions as well as in cities or remote locations. Black carbon aerosol is produced by combustion of fossil fuels and biomass with regional emissions being of sufficient magnitude to cause disruptions of atmospheric heatings and possibly large scale perturbations of the Earth's hydrological cycles (Ramanathan and Crutzen 2003). Historical trends point towards increasing levels of BC production (Novakov, Ramanathan et al. 2003). It is unhealthy to breath the polycyclic aromatic hydrocarbons that may exist in the vapor phase, may be absorbed in liquid phase aerosol, or may be adsorbed to the surface of black carbon aerosol (Mader and Pankow 2002; Naumova, Eisenreich et al. 2002; Naumova, Offenbergl et al. 2003; Pankow 2003; Zielinska, Sagebiel et al. 2003). PAHs as a group are reasonably anticipated to be carcinogenic (NTP 2003), and a few individual PAHs, such as benz[a]anthracene and benzo[a]pyrene, are probably carcinogenic (IARC 2003). Diesel exhaust has also been linked with allergic inflammation (Nel, Diaz-Sanchez et al. 1998). This paper provides an assessment of real time instruments for measurement of BC and particle-bound PAH's for use in sampling combustion sources.

Methods for quantifying black carbon mass concentration can be divided into two categories; those that do and do not require a filter substrate. Examples of filter-based techniques include both thermal and optical methods, and both laboratory and real-time instruments exist for each. Thermal methods start with the collection of aerosol on a filter, followed by measurement of the carbon atoms evolved when the filter is heated, with elemental carbon being defined as the carbon mass observed in some temperature range. Filter-based optical methods measure the optical attenuation across a filter as aerosol are deposited, and exploit the observation that most particulate light absorption in the atmosphere is due to thusly defined black carbon aerosol. Accurate mass flow meters are vital for quantifying the volume of air sampled to obtain the observed aerosol accumulation on a filter. Filter methods have limitations with respect to dynamic range, lack of a common definition of elemental carbon, and scattering aerosol interferences in the black carbon measurement (Horvath 1997). Photoacoustic instruments also are used to measure BC and they overcome deficiencies of the filter-based sampling methods.

The photoelectric aerosol sensor (PAS) utilizes an ultraviolet lamp to ionize particles containing PAH's. The charged particles are collected on a filter and the charge is measured with an electrometer. The PAS signal was originally correlated to seventeen individual PAHs from several sources, with a universal conversion factor of $1-3 \text{ ng m}^{-3} \text{ femtoamp}^{-1}$ (Wilson and Chuang 1991; Wilson and Barbour 1994; EPA 1997). Because PAH's are such a complex mix of vapor and particle-phase compounds, the PAS responds differently to each type of source, and the sensitivity varies in comparison to extractive methods (Agnesod, Maria et al. 1996). Furthermore, independent evaluations of the PAS are limited, and investigators report widely varying conversion factors (EPA 1997; Chuang, Callahan et al. 1999; Chetwittayachan,

Shimazaki et al. 2002). A chronicle is provided in this paper of the efforts employed to successfully use the PAS in source sampling, as well as a comparison of results from the PAS as compared to with measurements from a filter and denuder sampler followed by extraction and laboratory quantification of individual PAH's. Excellent correlation is found between BC and PAS measurements raising the issue, does the PAS respond to the polycyclic nature of the black carbon aerosol? This question takes on particular relevance since the laboratory extractions of PAH's showed only a weak correlation with BC (Zielinska, Sagebiel et al. 2003). The tubing inlet for the had to be heated to approximately 150 C to remove offending species, and, in the process, may have also greatly affected the gas to particle phase partition.

Photoacoustic Measurements of Aerosol Light Absorption and the Definition of Black Carbon

Photoacoustic instruments have been used in source sampling of black carbon aerosol. Sample air is pulled continuously through an acoustical resonator and is illuminated by laser light that is periodically modulated at the acoustical resonance frequency. Light absorption is manifested in particle heating and this heat transfers rapidly to the surrounding air, inducing pressure fluctuations that are picked up with a microphone on the resonator. Microphones have a very large dynamic range (at least 6 orders of magnitude), so black carbon measurements can be made over a large dynamic range with these instruments. The advancement that has been very important for the continued success of these instruments is the ability to measure very low levels of light absorption. Incidentally, aerosol light absorption occurs throughout the entire particle volume for combustion particles, so black carbon aerosol mass concentration is found to vary in direct proportion with light absorption. Vehicle manufactures pursued these methods in the 1970's and 1980's using bulky Argon Ion lasers and dye lasers (Terhune and Anderson 1977;

Japar and Killinger 1979; Japar and Szkarlat 1981; Japar and Szkarlat 1981; Japar, Szkarlat et al. 1984; Roessler 1984), and a resurgence of interest has emerged in research laboratories that coincides with technological developments in compact, efficient laser sources (Petzold and Niessner 1994; Petzold and Niessner 1995; Arnott, Moosmüller et al. 1999; Moosmüller, Arnott et al. 2001).

The photoacoustic instrument developed for this work operates at a convenient wavelength of 1047 nm where gaseous interference is not a problem and where a laser source is available that allows for direct electronic modulation of the power at the resonator frequency. Figure 1 shows calculated light absorption for a standard atmosphere containing only gases, for it is gaseous interference that could potentially limit black carbon particle detection. Figure 1a shows that a number of micro-windows are available where relative minima of gaseous absorption occur. Figure 1b shows details around a commonly used wavelength of 532 nm. The chief interfering gas at this wavelength is NO₂, giving rise for a need to denude this common combustion gas for practical applications (Adams, Japar et al. 1986). Figure 1c shows that the laser wavelength of 1047 nm is ideal because of the relatively broad range over which gaseous interference is a minimum. NO₂ is not an interferent at 1047 nm, but can be useful in cross-calibrating instruments (Arnott, Moosmüller et al. 2000).

The acoustical resonator, shown schematically in Fig. 2, was designed for compactness, ease of reproducibility in manufacture, and robustness with respect to use of the instrument in very noisy, dirty sampling environments. . The instrument comprises two identical coupling sections, and a third resonator section. These parts are manufactured out of aluminum. The coupling sections allow the laser beam to enter the instrument through windows well separated from the resonator section. The sample inlets and outlets are followed by cavities that are tuned

to reduce the coupling of noise into the resonator section. The resonator section has a horizontal tube that is $1/2$ of an acoustic wavelength long, and two vertical tubes that are $1/4$ of an acoustic wavelength long. In previous designs (Arnott, Moosmüller et al. 1999), the vertical tubes were at an angle of 45 degrees to the horizontal instead of 90 degrees as they are now, and the tubes were formed from pipe rather than machined with precision. The 90 degrees angles allow for symmetry when deciding where the holes in the resonator are placed to allow for laser beam and sample air passage. The piezoelectric transducer is used as a sound source to occasionally scan the resonator resonance frequency and quality factor for use in calibrating the instrument from an acoustical perspective. The microphone and piezoelectric transducer sit at pressure antinodes of the acoustic standing wave, and the holes in the resonator are at pressure nodes. The instrument is bolted together in three parts for easy disassembly in case it needs to be cleaned. The laser beam passes through the windows and the holes in the resonator section. The laser beam pumps the acoustic wave through light absorption, and the transfer of the associated heat to the surrounding air, in the resonator section.

The truth of the matter is that the photoacoustic instrument measures the aerosol light absorption coefficient (Arnott, Moosmüller et al. 1999; Arnott, Moosmüller et al. 2000), and then a quantity defined as black carbon (BC) is computed from the absorption coefficient. The ‘elemental’ carbon (EC) part of the exhaust absorbs light at 1047 nm much more strongly than any other common particulate aerosol in exhaust and in the atmosphere so that it is reasonable to associate elemental carbon with aerosol light absorption. Why is it reasonable to associate aerosol light absorption with a black carbon mass concentration (BC)? Because aerosol light absorption occurs throughout the entire particle volume, giving rise to a direct proportionality between the absorption measurement and the aerosol mass. It is perhaps inevitable to speculate

that the aerosol complex refractive index could vary with combustion source [(Dalzell and Sarofim 1969) (Fuller, Malm et al. 1999)], so that the black carbon measured values could be different for particles actually having the same numbers of carbon atoms in them. And it is possible to postulate that aerosol coatings or adsorbents, or particle morphology, could also give rise to different absorption coefficients than one would observe for uncoated particles.

Experiences to date have shown that for an emission source such as a late model diesel that is rich in EC, the Improve protocol method of quantifying EC (Chow, Watson et al. 1993) correlates well with the aerosol light absorption measurement at 1047 nm. Figure 3 shows comparisons of aerosol light absorption at 1047 nm with EC and organic carbon (OC) from data acquired on quartz fiber filters and analyzed by the thermal optical reflectance method, Improve protocol. The vehicles were operated at idle or advanced idle with no load (Rogers, Sagebiel et al. 2003). Note the good correlation EC with BC (Fig. 3a), and the relatively poor correlation of OC with BC (Fig. 3b). The offset between EC and BC measurements is negligible, but is substantial between BC and OC. The lack of offset in the EC case indicates that the photoacoustic instrument has a negligible response to the various exhaust gases. The EC to total carbon ratio ranged from 0.1 to 0.4, and yet no systematic influence was seen on the correlation of BC with EC, addressing at least in a cursory manner the issues of particle coatings and refractive index variations. The photoacoustic instrument used for this work in 1999 was not actually the one shown schematically in Fig. 2, but was a previous prototype that was modified to allow use with the 1047 nm laser (Arnott, Moosmüller et al. 1999). The data in Fig. 3a gave the impetus to accept the 1047 nm laser operation as ideal, and to move forward with the improved resonator design shown in Fig. 2. The prototype resonator was operated at both its fundamental acoustic frequency of 500 Hz, and in exploration of the noise reduction potential at

the next available harmonic at 1500 Hz, even though the resonator coupling efficiency at the higher frequency is only 1/3 of its value at 500 Hz. A significant reduction in effects of ambient noise were noted in the 1500 Hz operation, and so the resonator design shown in Fig. 3 was made with dimensions essentially 1/3 those of the prototype so that it operates in its fundamental mode of 1500 Hz.

From this point forward, the following relationship was used to obtain black carbon concentration from the aerosol light absorption measurement at 1047 nm:

$$\text{BC } (\mu\text{g m}^{-3}) = 5 (\text{m}^2 \text{g}^{-1}) B_{\text{abs}} (\text{Mm}^{-1}) [\text{measured at } 1047 \text{ nm}] . \quad (1)$$

Most of the consequential data in Fig. 3 represents diesel emissions. EC from diesels provide a relatively unambiguous measurement from the various protocols and methods that have been developed though ambient and wood smoke samples have substantial differences (Watson, Chow et al. 1994; Chow, Watson et al. 2001). For these reasons it is good to use diesel emissions as a starting point to establish essentially an EC standard, and to use the BC measurement by the photoacoustic method as a standard for other types of sources.

BC and EC measurements for gasoline and diesel vehicles used in ground support at Hill Air Force Base were obtained in 2000 (Kelly, Wagner et al. 2003), and are shown in Fig. 4. The EC fraction ranged from 2.5% to 35% of the total carbon in these measurements, and the vehicle engine load ranged from idle to 93%. The photoacoustic instrument used in these measurements is the one shown schematically in Fig. 2. This time the EC measurements were made on the aluminum substrates used in a Moudi sequential analyzer. TOR analysis for these substrates simply skips the pyrolysis correction stage and moves directly from OC4 to EC1. Most EC from diesel sources is contained in the EC2 phase (Watson, Chow et al. 1994) so the pyrolysis correction is not so important to the data shown in Fig. 4. It should be noted that the EC from

Moudi analysis correlated well with that obtained in by the quartz filter analysis for the data shown in Fig. 3; however, the quartz filter sampler had a leak in the 2000 SERDP experiment.

The Photoelectric Aerosol Sensor

The photoelectric aerosol sensor 2000 (PAS2000 EcoChem Messtechnik GmbH) qualitatively measures the concentration of particle-bound polycyclic aromatic hydrocarbons (pPAHs). Figure 5 shows a schematic of the PAS, and additional instrument details can be found in (EPA 1997) and (Burtscher 1992) and in (Burtscher and Siegmann 1994). Briefly, the PAS uses a KrCl excimer lamp operating at 222 nm as a photoionization source; the photon energy of the lamp is chosen so that gas-phase molecules are negligibly ionized. Samples flow continuously into the excimer-lamp ionization region, where particle-bound PAH molecules are ionized and lose an electron. The positively charged particles collect on a filter where charge is measured with an electrometer. The charge is integrated over time to give the photoelectric current (in femto- or picoamps), and this current should be proportional to the PAH loading on particles.

During the course of this study, temperature and exhaust concentration were identified as important factors governing the response and reproducibility of PAS readings. Other studies found little effect from temperature or humidity (EPA, 1997; Dubowsky et al., 1999; Lee et al., 1999); however, these studies focused on indoor air, ambient samples, or cigarette smoke and thus lower pPAH concentrations. For sampling exhaust from vehicles or aircraft, a PAS inlet temperature of at least 120 C produced more stable results than lower inlet temperatures. Even with dilution, it is possible that vehicles and aircraft contain enough vapor-phase hydrocarbons and water vapor in their exhaust to condense inside the PAS and produce erratic results, as illustrated for example in Fig. 6 data from the 1999 SERDP project (Rogers, Sagebiel et al.

2003). In addition, exposing the PAS directly to undiluted exhaust caused spurious negative signals. In order to maintain stable PAS readings during this study, the PAS inlet was heated to a constant temperature 150 C; the exhaust was diluted with dry, particle-free air; and the PAS response was generally maintained in the femtoamp range.

Figure 7 shows the times series of emissions from a FA18a jet aircraft obtained with the PAS and PA. The aircraft was in for repairs at the Navy base on North Island, San Diego CA, and an eductor system was used to dilute the exhaust with a dilution ratio of about 1:15. The aircraft was brought from idle to 80% of full power. Exhaust emissions become more diluted by ambient air as the aircraft power setting increases. Note that the PAS curve is everywhere positive, and at times, matches the form of the BC curve quite well. Of course it is not expected necessarily that the PAS and BC curves should be in 1:1 correspondence, as the PAH emission rate may be different than that of the BC. Also note that Fig. 7 shows that the photoacoustic instrument can provide useful data even in a very loud environment.

Figure 8 shows measurements of emissions from gasoline and diesel vehicles from SERDP 2000 (Kelly, Wagner et al. 2003). Two PAS instruments were used, with one behind the DRI dilution system (described in (Rogers, Sagebiel et al. 2003), and one behind the so-called Matter dilution system (Hueglin, Scherrer et al. 1997). The Matter dilution system samples directly from the tail pipe. Note that in both cases, Figs. 8a) and 8b), the correlation of PAS signals with BC measurements is quite high, perhaps suggesting that PAH production is correlated highly with BC production, and/or that the PAS responds directly to BC. It could also be that the need to operate the PAS with an inlet at 150 C favors PAH's being in the vapor phase.

However, extractive measurements of PAH's do not show a strong correlation of black carbon with the ratio of particle to gas phase concentrations of pyrene and fluoranthene for the

vehicles whose emission is reported in Fig. 8 (Zielinska, Sagebiel et al. 2003). The so-called Seigmann sum of particle-bound PAH's are shown in Figs. 8c and 8d against BC and the PAS, respectively. Note in Fig. 8c) that the data tends to clump into two super data points, and the wide spread of values at the low end, likely due to the uncertainty in the PAH measurement as well as due to the variations of emissions from different sources. The substantial offset is perhaps suggestive that the particle bound PAH's are not exclusively associated with BC. Note that the slope of the linear curve fit implies around 1.25 ng of particle-bound PAH produced per 1 ug of BC. A ratio of around 1 (and for gasoline vehicles, 3) ng particle-bound PAH per ug BC can be calculated from the tunnel study data reported in (Miguel, Kirchstetter et al. 1998).

The PAS versus extractive PAH measurements are shown in Fig. 8d. The data clumping is not as severe as in Fig. 8c), and the correlation is modest. The slope of the curve, $0.11 \text{ ng m}^{-3} / \text{femtoamp}$ is consistent with values found in an ambient study in Italy where traffic and meteorological inversions contributed to the observed levels of air pollutants. Some fraction of the pPAH is absorbed into the organic carbon particulate in the exhaust, particularly the lower molecular weight higher vapor pressure molecules; not all pPAH is adsorbed to the surface of elemental carbon aerosol (Allen, Sarofim et al. 1997). Much of the organic carbon fraction may be volatilized by the use of the 150 C inlet on the PAS necessary to avoid negative signals such as those shown in Fig. 6. These negative signals may be due to charge separation occurring during evaporation of relatively volatile aerosol from the PAS filter, just as happens with water droplets in the atmosphere (Dong and Hallett 1992). PPAH's adsorbed or absorbed in a film thicker than a single molecular level would very likely have their charge separation from the UV lamp quenched so as not to contribute to the PAS signal anyway (Burtscher and Siegmann 1994). From the outstanding correlation of PAS and BC measurements as shown in Figs. 8a and 8b, it is

to be concluded that the PAS responds to pPAH's that are produced in combustion at the same rate as BC, or that a good portion of the PAS response can be to the BC itself.

Acknowledgments

This research was supported by the Strategic Environmental Research and Development Program, Project CP-1106. We thank Bob Armstrong of HAFB for his assistance with the vehicles; John Walker of DRI for his assistance with some mechanical aspects of the photoacoustic instrument design; and Hans Moosmüller of DRI for conversations concerning the choice of laser wavelength to use for the photoacoustic instrument. James B. Griffin, Jacob D. McDonald, and Dana Overacker contributed to the conduct of the first SERDP experiment in 1999, and thus to the laying of the groundwork for what was to follow in subsequent experiments.

FIGURES

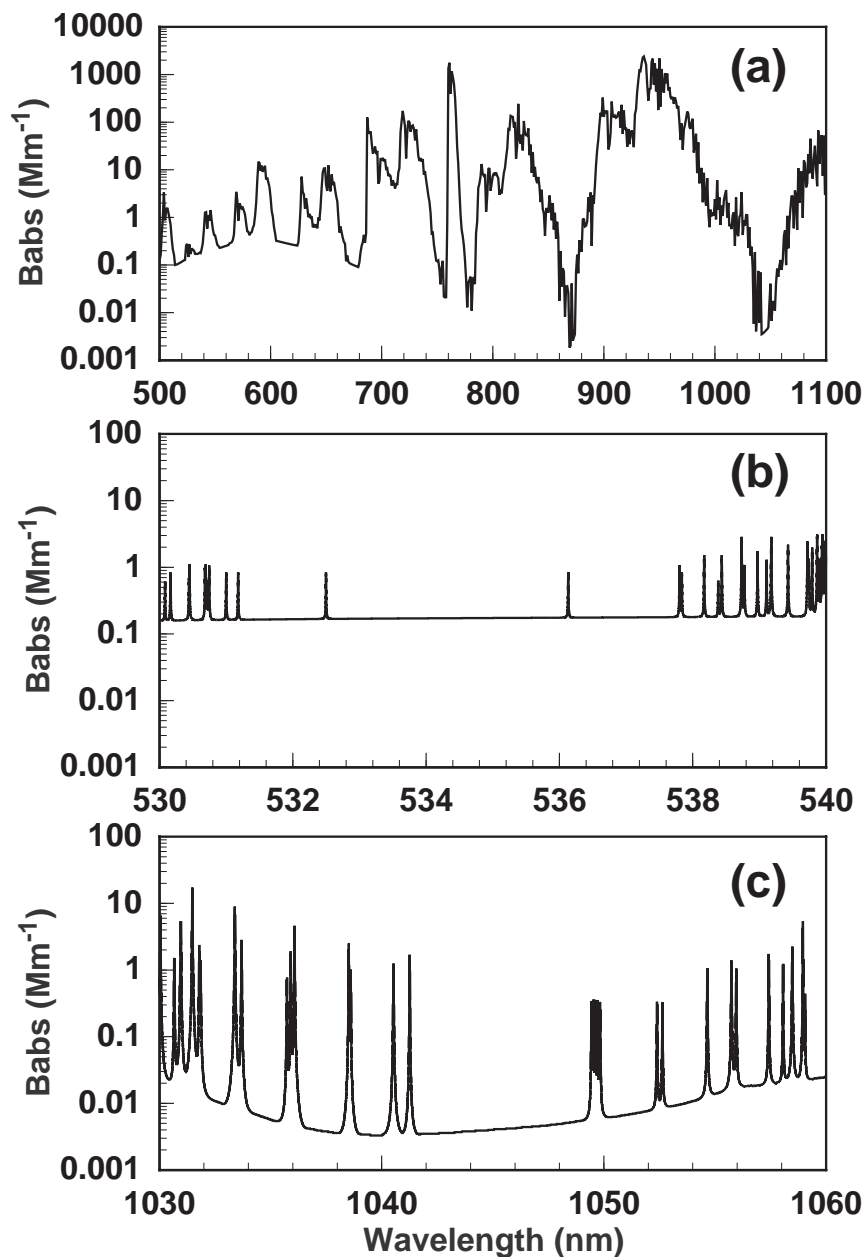


Figure 1. Calculation of light absorption by gases in a standard atmosphere for most of the visible and near IR spectrum (a), and near wavelengths where convenient laser sources are available at 532 nm (b), and 1047 nm (c). Note that gaseous interference is especially low at 1047 nm. The main interfering gas at 532 nm is NO₂, a common gas produced in combustion.

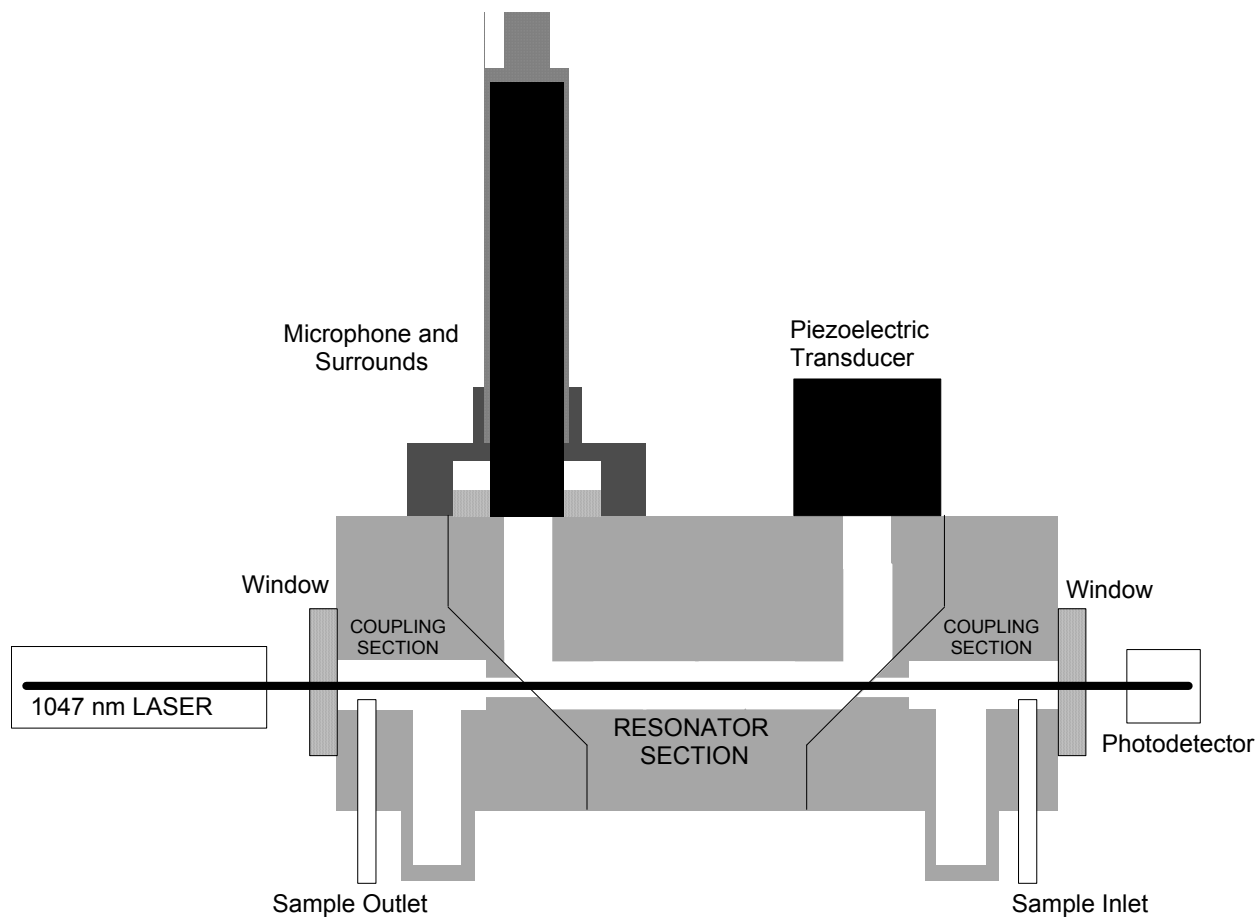


Figure 2. Schematic representation of the new acoustical resonator used in the photoacoustic instrument.

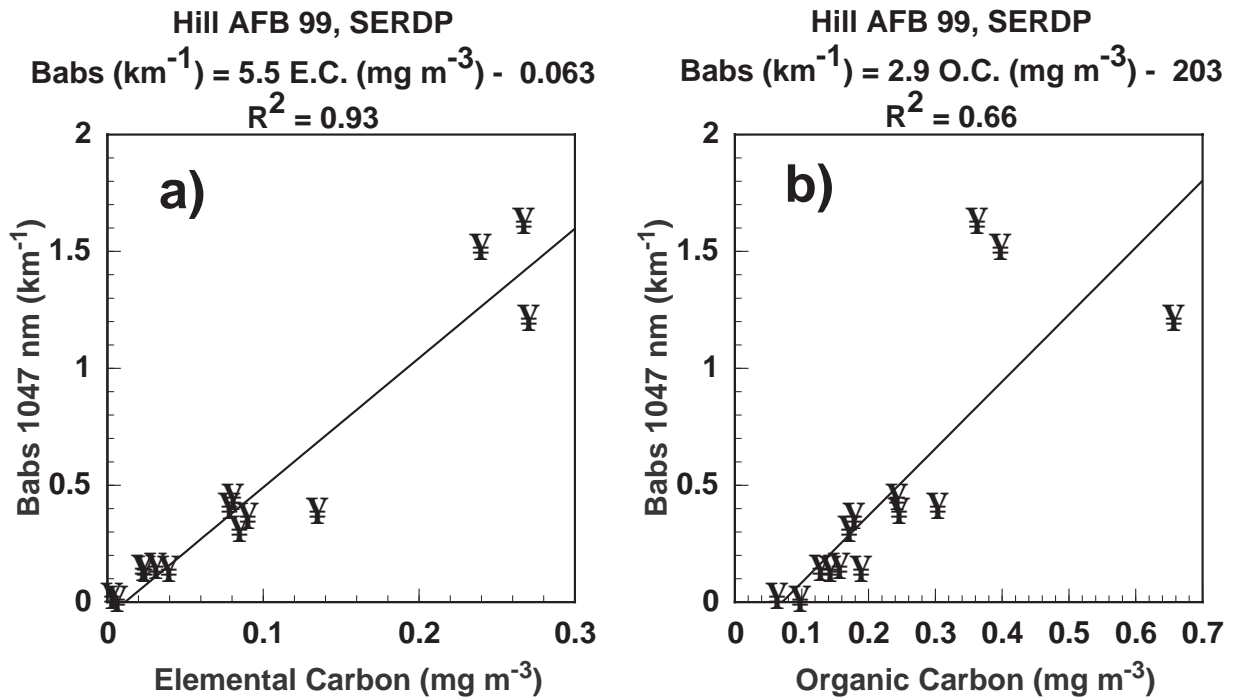


Figure 3. Aerosol light absorption measurements for gasoline and diesel vehicles at Hill Air Force Base. Comparison with elemental and organic carbon measurements are shown in a) and b) respectively. The two left most data points on each figure are from gasoline vehicles. Vehicles were either idling or were elevated idling, and were not under any other load.

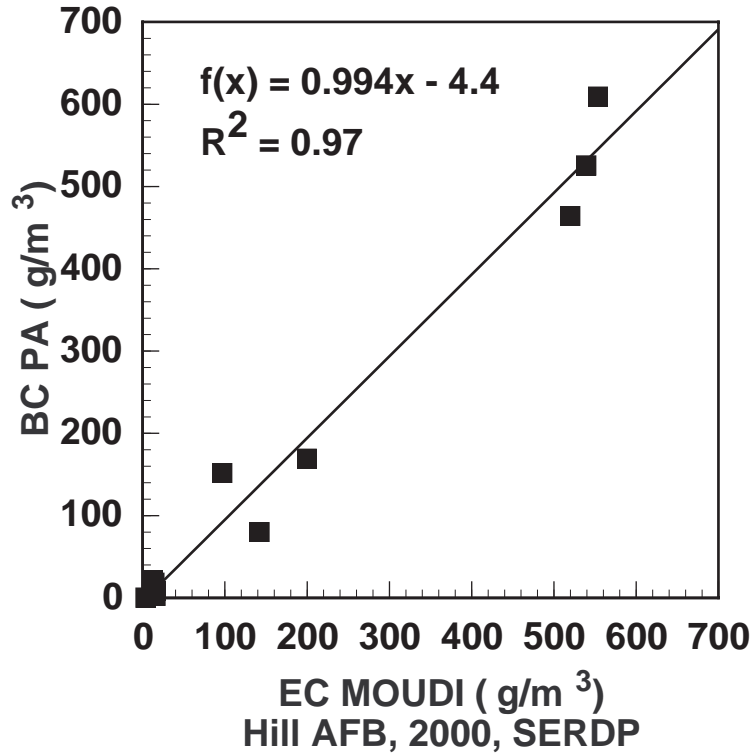


Figure 4. Black carbon and elemental carbon measurements for gasoline and diesel vehicles operated under load. The gasoline vehicles were particularly clean, and provided the left most data points. These measurements were made using the photoacoustic instrument shown schematically in Fig. 2.

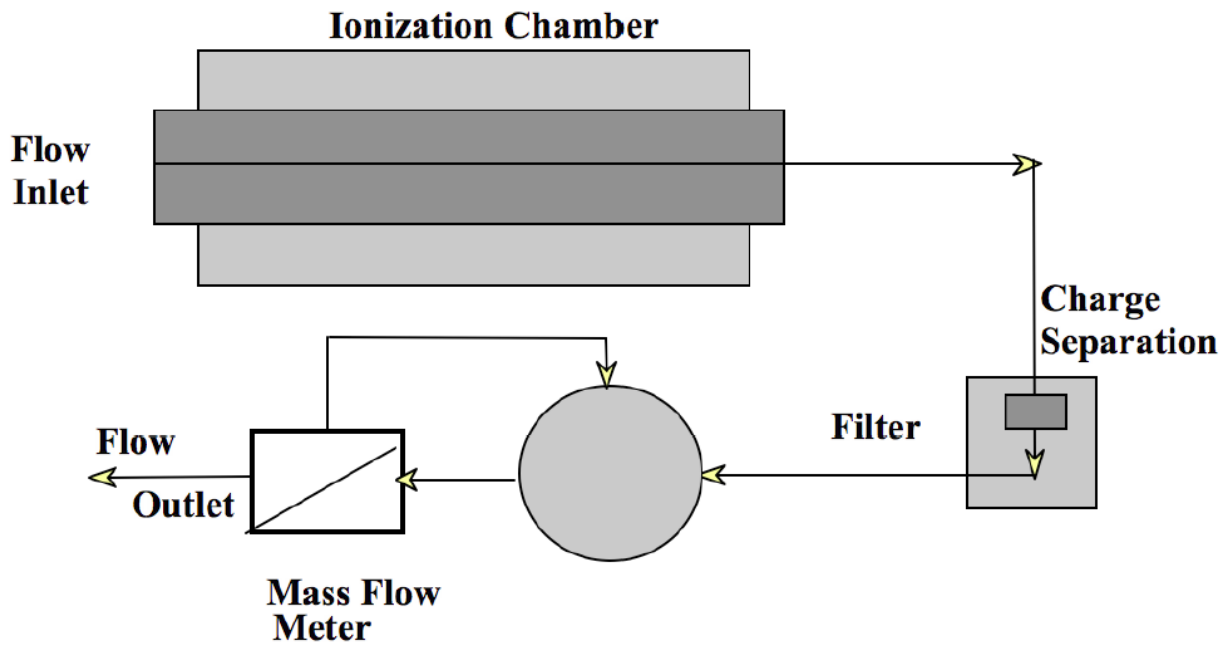


Figure 5. Schematic of the photoelectric aerosol sensor (PAS).

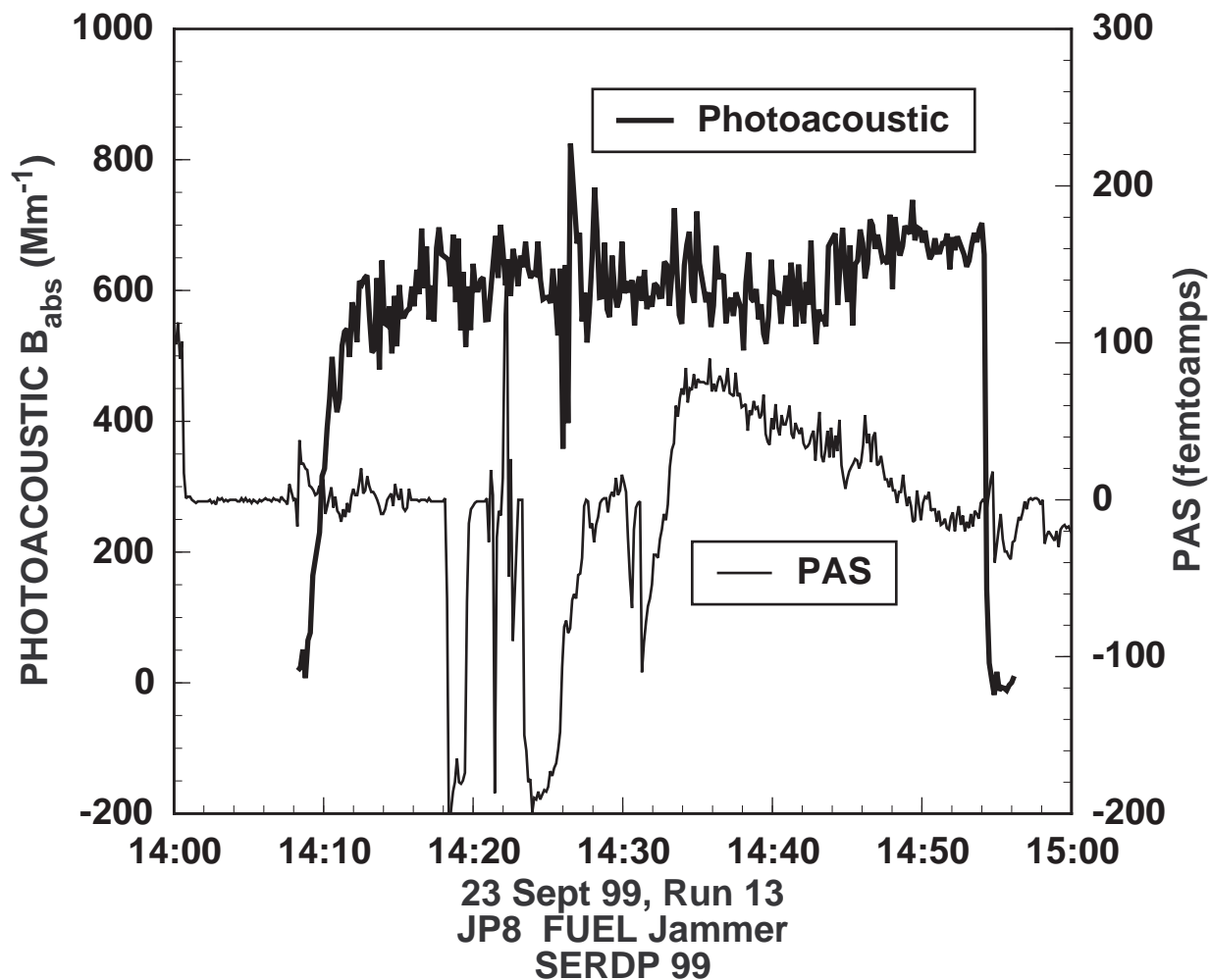


Figure 6. Time series showing aerosol light absorption on the left axis and photoelectric aerosol sensor current on the right axis, for a ‘Jammer’ vehicle operated on JP8 fuel. Note the substantial periods when the PAS signal is negative, and the perhaps unexpected decay of the PAS signal around time 14:40. This is a typical series for the PAS before the instrument was thoroughly cleaned, and before the PAS inlet was heated to 150 C.

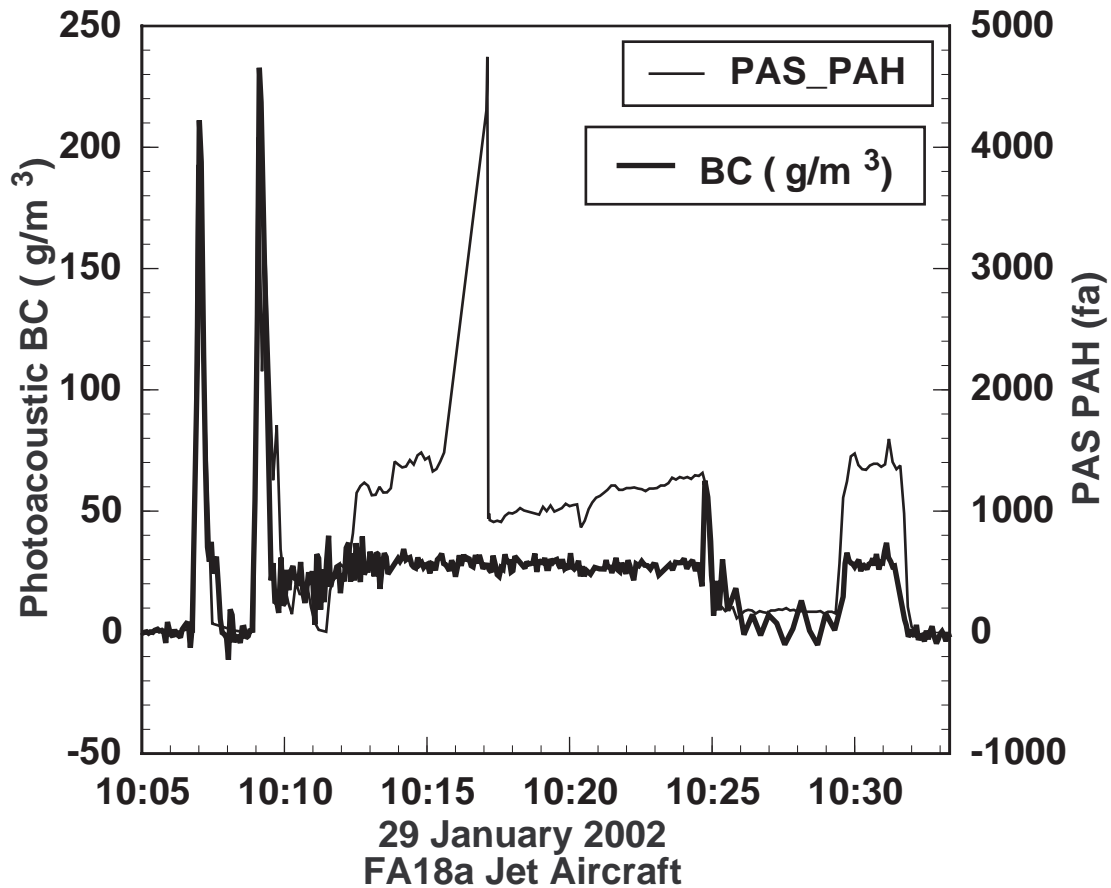


Figure 7. Time series for photoacoustic black carbon and photoelectric aerosol sensor measurements from a tethered FA18a jet aircraft under variable load. Curves nearly overlap after crank-up, between 10:05 and 10:10. The time interval 10:25 – 10:30 had the greatest load (80% full power) and lowest emission concentrations, as the aircraft was pulling in more dilution air at this time. Data is from SERDP 2002.

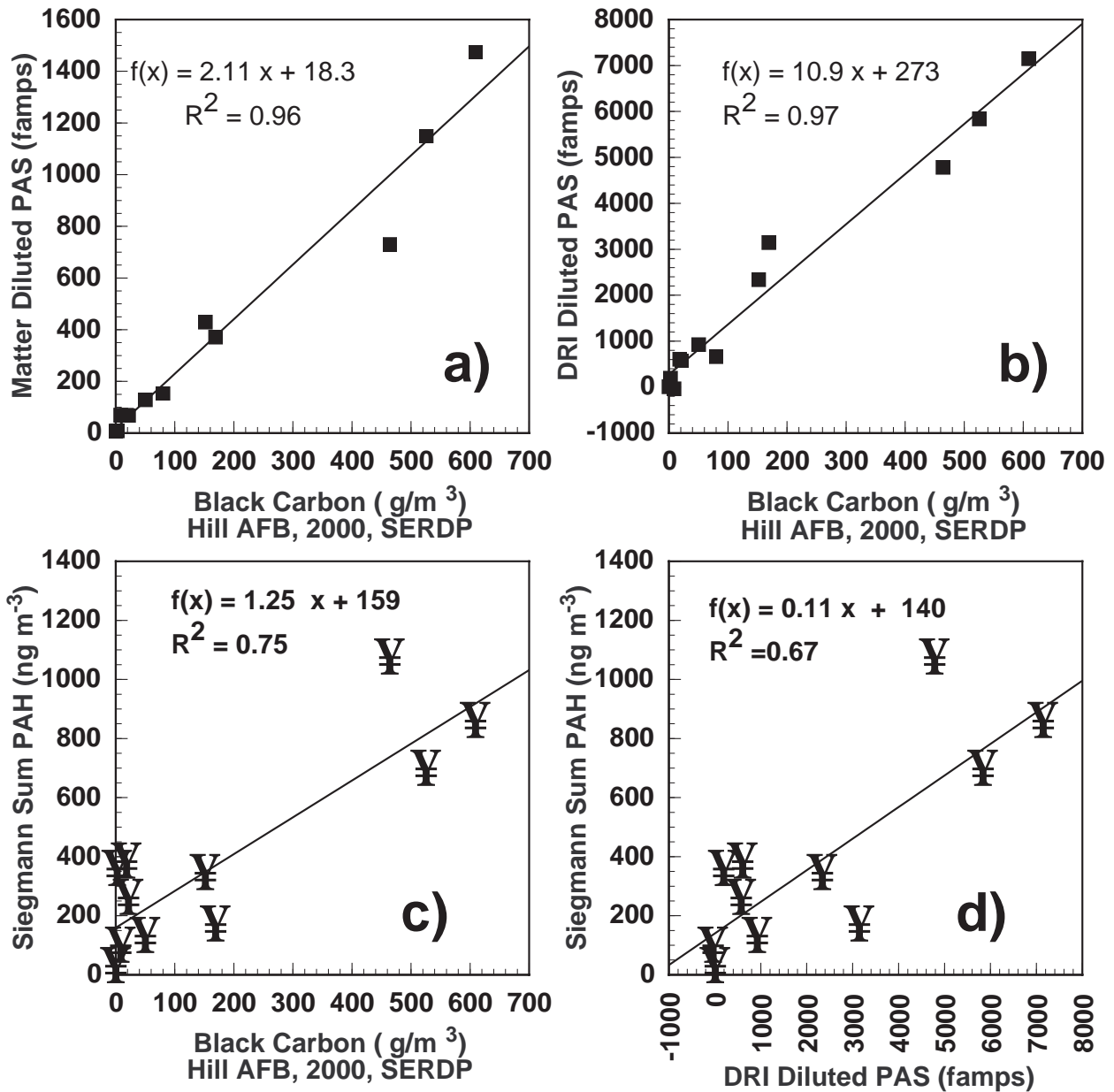


Figure 8. Scatter plot of black carbon and PAS measurements of emissions from gasoline and diesel vehicles during SERDP 2000. In a), PAS sampled behind the so-called Matter dilution system, and in b), a second PAS sampled behind the DRI dilution tunnel. In both cases the BC measurements were obtained behind the DRI dilution tunnel. Note the high degree of correlation of PAS and BC data. Extractive PAH's are shown in c) and d) against BC and the PAS. Linear regressions in c) and d) are subject to substantial data clumping around the lowest and highest values, and to the uncertainty in the PAH measurements. Particle-bound PAH blanks were around 30 ng m⁻³, and can be viewed as one measure of the uncertainty in the PAH measurement.

References

- Adams, K. M., S. M. Japar and W. R. Pierson (1986). "Development of a MnO₂-Coated, Cylindrical Denuder for Removing NO₂ from Atmospheric Samples." Atmospheric Environment **20**(6): 1211-1215.
- Agnesod, G., R. D. Maria, M. Fontana and M. Zublena (1996). "Determination of PAH in airborne particulate: Comparison between off-line sampling techniques and an automatic analyser based on a photoelectric aerosol sensor." The Science of the total environment **189-190**: 443-449.
- Allen, J. O., A. F. Sarofim and K. A. Smith (1997). "A critical evaluation of two proposed atmospheric partitioning mechanisms, adsorption and absorption, using atmospheric data for polycyclic aromatic hydrocarbons." Journal of Aerosol Science **28**: S335-S336.
- Andreae, M. O. (2001). "The dark side of aerosols." Nature **409**: 671-672.
- Arnott, W. P., H. Moosmüller, C. F. Rogers, T. Jin and R. Bruch (1999). "Photoacoustic spectrometer for measuring light absorption by aerosols: Instrument description." Atmospheric Environment **33**: 2845-2852.
- Arnott, W. P., H. Moosmüller and J. W. Walker (2000). "Nitrogen dioxide and kerosene-flame soot calibration of photoacoustic instruments for measurement of light absorption by aerosols." Review of Scientific Instruments **71**(7): 4545-4552.
- Burtscher, H. (1992). "Measurement and characteristics of combustion aerosols with special consideration of photoelectric charging and charging by flame ions." J. Aerosol Science **23**(6): 549-595.
- Burtscher, H. and H. C. Siegmann (1994). "Monitoring PAH-Emissions from combustion processes by photoelectric charging." Combustion Science and Technology **101**: 327-332.
- Chetwittayachan, T., D. Shimazaki and K. Yamamoto (2002). "A comparison of temporal variation of particle-bound polycyclic aromatic hydrocarbons (pPAHs) concentration in different urban environments: Tokyo, Japan, and Bangkok, Thailand." Atmospheric Environment **36**: 2027-2037.
- Chow, J., J. Watson, D. Crow, D. Lowenthal and T. Merrifield (2001). "Comparison of IMPROVE and NIOSH Carbon Measurements." Aerosol Science and Technology **34**(1): 23-34.
- Chow, J. C., J. G. Watson, L. C. Pritchett, W. R. Pierson, C. A. Frazier and R. G. Purcell (1993). "The DRI thermal/optical reflectance carbon analysis system: Description, evaluation and applications in U.S. air quality studies." Atmospheric Environment **27A**: 1185-1201.
- Chuang, J. C., P. J. Callahan, C. W. Lyu and N. K. Wilson (1999). "Polycyclic aromatic hydrocarbon exposures of children in low-income families." J. Exposure Analysis and Environ. Epid. **2**: 85-98.
- Dalzell, W. H. and A. F. Sarofim (1969). "Optical constants of soot and their application to heat flux calculations." Journal of Heat Transfer: 100-104.
- Dong, Y. and J. Hallett (1992). "Charge Separation by Ice and Water Drops During Growth and Evaporation." Journal of geophysical research **97**(D18): 20,361.
- EPA (1997). Field and Laboratory Analyses of a Real-Time PAH Analyzer, EPA Office of Research and Development.

- Fuller, K. A., W. C. Malm and S. M. Kreidenweis (1999). "Effects of mixing on extinction by carbonaceous particles." Journal of geophysical research **104**(D13): 15941-15954.
- Horvath, H. (1997). "Systematic deviations of light absorption measurements by filter transmission methods." Journal of Aerosol Science **28**: S55-S56.
- Hueglin, C., L. Scherrer and H. Burtscher (1997). "An accurate, continuously adjustable dilution system (1:10 to 1:10⁴) for submicron aerosols." Journal of aerosol science **28**(6): 1049-1055.
- IARC (2003). International Agency for Research on Cancer.
- Japar, S. M. and D. K. Killinger (1979). "Photoacoustic and absorption spectrum of airborne carbon particulate using a tunable dye laser." Chemical Physics Letters **66**: 207-209.
- Japar, S. M. and A. C. Szkarlat (1981). "Measurement of Diesel Vehicle Exhaust Particulate Using Photoacoustic Spectroscopy." Combustion Science and Technology **24**: 215-219.
- Japar, S. M. and A. C. Szkarlat (1981). Real-time measurements of diesel vehicle exhaust particulate using photoacoustic spectroscopy and total light extinction. Fuels and Lubricants Meeting, Tulsa OK, SAE.
- Japar, S. M., A. C. Szkarlat and W. R. Pierson (1984). "The determination of the optical properties of airborne particle emissions from diesel vehicles." The Science of the Total Environment **36**: 121-130.
- Kelly, K. E., D. A. Wagner, J. S. Lighty, A. F. Sarofim, C. F. Rogers, J. Sagebiel, B. Zielinska, W. P. Arnott and G. Palmer (2003). "Characterization of Exhaust Particles from Military Vehicles Fueled with Diesel, Gasoline, and JP-8." Journal of the Air & Waste Management Association **53**(3): 273-282.
- Lighty, J. S., J. M. Veranth and A. F. Sarofim (2001). "Combustion aerosols: Factors governing their size and composition and implications to human health." Journal of Air and Waste Management Association **50**: 1565-1618.
- Mader, B. T. and J. F. Pankow (2002). "Study of the Effects of Particle-Phase Carbon on the Gas/Particle Partitioning of Semivolatile Organic Compounds in the Atmosphere Using Controlled Field Experiments." Environmental science & technology **36**(23): 11.
- Miguel, A. H., T. W. Kirchstetter, R. A. Harley and S. V. Hering (1998). "On-Road Emissions of Particulate Polycyclic Aromatic Hydrocarbons and Black Carbon from Gasoline and Diesel Vehicles." Environmental science & technology **32**(4): 6.
- Moosmüller, H., W. P. Arnott, C. F. Rogers, J. L. Bowen, J. A. Gillies, W. R. Pierson, J. F. Collins, T. D. Durbin and J. M. Norbeck (2001). "Time resolved characterization of particulate emission: 2. Instruments for elemental and organic carbon measurements." Environmental Science & technology **35**: 1935-1942.
- Naumova, Y. Y., S. J. Eisenreich, B. J. Turpin, C. P. Weisel, M. T. Morandi, S. D. Colome, L. A. Totten, T. H. Stock, A. M. Winer, S. Alimokhtari, J. Kwon, D. Shendell, J. Jones, S. Maberti and S. J. Wall (2002). "Polycyclic Aromatic Hydrocarbons in the Indoor and Outdoor Air of Three Cities in the U S." Environmental science & technology **36**(12): 8.
- Naumova, Y. Y., J. H. Offenberg, S. J. Eisenreich, Q. Meng, A. Polidori, B. J. Turpin, C. P. Weisel, M. T. Morandi, S. D. Colome, T. H. Stock, A. M. Winer, S. Alimokhtari, J. Kwon, S. Maberti, D. Shendell, J. Jones and C. Farrar (2003). "Gas/particle distribution of polycyclic aromatic hydrocarbons in coupled outdoor/indoor atmospheres." Atmospheric environment **37**(5): 18.
- Nel, A. E., D. Diaz-Sanchez, D. Ng, T. Hiura and A. Saxon (1998). "Updates on cells and cytokines - Enhancement of allergic inflammation by the interaction between diesel

- exhaust particles and the immune system." The journal of allergy and clinical immunology : official organ of American Academy of Allergy **102**(4 1): 539-554.
- Novakov, T., V. Ramanathan, J. E. Hansen, T. W. Kirchstetter, M. Sato, J. E. Sinton and J. A. Sathaye (2003). "Large historical changes of fossil-fuel black carbon aerosols." Geophysical Research Letters **30**: doi:10.1029/2002GL016345.
- NTP (2003). 10th Report on Carcinogen, National Toxicology Program. U.S. Department of Health and Human Services, National Toxicology program.
- Pankow, J. F. (2003). "Gas/particle partitioning of neutral and ionizing compounds to single and multi-phase aerosol particles 1 Unified modeling framework." Atmospheric environment **37**(24): 12.
- Petzold, A. and R. Niessner (1994). The Photoacoustic Soot Sensor for Black Carbon Monitoring. Fifth International Conference on Carbonaceous Particles in the Atmosphere, Berkeley, CA.
- Petzold, A. and R. Niessner (1995). "Novel Design of a Resonant Photoacoustic Spectrophone for Elemental Carbon Mass Monitoring." Applied Physics Letters **66**(10): 1285-1287.
- Ramanathan, V. and P. J. Crutzen (2003). "New Directions: Atmospheric Brown 'Clouds'." Atmospheric Environment **37**: 4033-4035.
- Roessler, D. M. (1984). "Photoacoustic Insights on Diesel Exhaust Particles." Applied Optics **23**(8): 1148-1155.
- Rogers, C. F., J. C. Sagebiel, B. Zielinska, W. P. Arnott, E. M. Fujita, J. D. McDonald, J. B. Griffin, K. Kelly, D. Overacker, D. Wagner, J. S. Lighty, A. Sarofim and G. Palmer (2003). "Characterization of Submicron Exhaust Particles from Engines Operating Without Load on Diesel and JP-8 Fuels." Aerosol Science & Technology **37**(4): 355-368.
- Terhune, R. W. and J. E. Anderson (1977). "Spectrophone Measurements of the Absorption of Visible Light by Aerosols in the Atmosphere." Optics Letters **1**(2): 70-72.
- Watson, J. G., J. C. Chow, D. H. Lowenthal and L. C. Pritchett (1994). "Differences in the carbon composition of source profiles for diesel- and gasoline-powered vehicles." Atmospheric environment **28**(15): 2493-2505.
- Wilson, N. K. and R. K. Barbour (1994). "Evaluation of a real-time monitor for fine particle-bound PAH in air, Polycyclic Aromatic Compound." Polycyclic Aromatic Compounds **5**: 167-174.
- Wilson, N. K. and J. C. Chuang (1991). "Sampling polycyclic aromatic hydrocarbons and related semivolatile organic compounds in indoor air." Indoor Air **4**: 512-513.
- Zielinska, B., J. Sagebiel, W. P. Arnott, C. F. Rogers, K. E. Kelly, D. A. Wagner, J. S. Lighty, A. F. Sarofim and G. Palmer (2003). "Phase and size distribution of polycyclic aromatic hydrocarbons in diesel and gasoline vehicle emissions." environmental Science & technology submitted in 2003.

APPENDIX 3:

PHASE AND SIZE DISTRIBUTION OF POLYCYCLIC AROMATIC HYDROCARBONS IN DIESEL AND GASOLINE VEHICLE EMISSIONS

Phase and Size Distribution of Polycyclic Aromatic Hydrocarbons in Diesel and Gasoline Vehicle Emissions

B. Zielinska^{1*}, J. Sagebiel¹, W. P. Arnott¹, C.F. Rogers¹, K.E. Kelly², D.A. Wagner², J. S. Lighty², A.F. Sarofim², and G. Palmer³

¹ *Desert Research Institute, Division of Atmospheric Sciences, University and Community College System of Nevada, 2215 Raggio Parkway, Reno, NV 89512*

² *Department of Chemical and Fuels Engineering, University of Utah, Kennecott Research Center, 100 S. 1495 E., Salt Lake City, UT 84112*

³ *Hill Air Force Base, Ogden, UT*

Abstract

Emission measurements were made for aircraft ground support equipment (AGE) vehicles at Hill Air Force Base (HAFB, Ogden, UT) as part of a Strategic Environmental Research and Development Program, using chassis dynamometers. The exhaust from the tested vehicle was passed to a dilution tunnel where it was diluted 30 to 40 times, and collected using Micro-Orifice Uniform Deposit Impactor (MOUDI), a XAD-coated annular denuder, and a filter followed by a solid adsorbent. MOUDI substrates were analyzed for mass and for organic (OC) and elemental (EC) carbon, by the thermal/optical reflectance (TOR) method and for polycyclic aromatic hydrocarbons (PAH) by GC/MS. The denuder and filter/solid adsorbent samples were analyzed for PAH. Overall, there is more mass and higher EC contribution when the vehicle is run under higher load in comparison with the low load. Older vehicles generally show more mass and EC emissions than newer vehicles, and there is a shift toward smaller particle sizes for the low load, which is most pronounced for newer vehicles. PAH are present predominantly on the sub-micron particles collected on MOUDI stages 0.18-0.32 μm , 0.32-0.56 μm and 0.1-0.18 μm . For the low-load runs, the distribution of PAH seems to be shifted towards smaller size particles. The gas-particle phase distribution of semi-volatile PAH depends also on the engine loading. For idle, not only two- three-ring PAH are retained on the denuder segment, but also less volatile 4-ring PAH are retained at the 80–90% range, which implies that they are present predominantly in the gas phase. In contrast, for engines under high loads a much larger portion of 3 and 4-ring PAH are partitioned to the particle phase.

Introduction

Polycyclic aromatic hydrocarbons (PAH) constitute a broad family of compounds that are sometimes described as semi-volatile organic compounds (SVOC). This term refers to the fact that PAH are distributed between gas and particle phases. The factor of $\sim 10^7$ in the range of their vapor pressures is reflected in the fact that, at equilibrium at ambient temperature, two-ring naphthalene exists almost entirely in the gas phase, whereas benzo[*a*]pyrene (B[*a*]P), other five-ring PAHs, and higher-ring PAHs are predominantly adsorbed on particles. The intermediate three- and four-ring PAHs are distributed between the two phases. However, the gaseous concentrations of these intermediate

PAHs can be significantly reduced by their adsorption and absorption on various types of surfaces. Because of this phenomenon, the amount and type of particulate matter play an important role, together with temperature, in the vapor-particle partitioning of semi-volatile organic compounds^{1,2,3,4}. Thus, the phase distribution of the PAH in the atmosphere is determined by the liquid phase (or sub-cooled liquid phase) vapor pressure of the individual species, by the amount and chemical nature of the particulate matter present (adsorption onto the aerosol surface and absorption into the aerosol organic matter), and by the temperature.

Diesel and gasoline-powered engines emit significant amounts of PAH distributed between the gas- and particle phases. However, the distribution of these PAH in the diluted exhaust in relation to the engine work cycle (i.e. running under different loads or at idle) is not well characterized. Since the amount and chemical nature of particulate matter (PM) produced by the given engine changes according to the work cycle, is the PAH phase and particle size distribution also cycle dependant? Are PAH emitted by spark-ignition vehicles phase and particle size distributed at the same way as those emitted by diesel? This paper attempts to evaluate these questions.

Experimental

Sample collection. The emission measurements were obtained for a variety of military vehicles at Hill Air Force Base (HAFB, Ogden, UT) in November 2000, as part of a Strategic Environmental Research and Development Program, SERDP^{5,6}. The selection of aircraft ground support equipment (AGE) vehicles is shown in Table 1, along with fuel type.

AGE vehicles, with exception of the Jammer were tested using chassis dynamometers under pre-determined load. It was not possible to operate the Jammer on a dynamometer; therefore, it was only tested under idle conditions. The experimental conditions are presented in Table 2. The exhaust from the tested vehicle was passed to the DRI dilution tunnel based on the design of⁷. The inlet to the dilution sampler was a 3.2m long line heated to 150°C. The sample stream was diluted by air that had passed through a HEPA filter, desiccant and activated carbon beds. The dilution ratios for each run are shown in the third to last column of Table 2. The diluted sample was allowed to equilibrate in the residence chamber for approximately 80 seconds before being passed to the aerosol characterization instruments. The temperature and the relative humidity in the dilution sampler ranged from 18°C to 33°C and from approximately 5% to 31%, respectively, depending on engine and ambient conditions. The dilution sampler flow supplied four sampling trains, two of which (No. 1 and 2) were fitted with Bendix-Unico 240 cyclones⁸, which provide a 50% cut-point of 2.5 micrometers aerodynamic diameter at a volumetric flow rate of 113 liters/minute (LPM). The remaining two sampling trains (No. 3 and 4) did not contain size-classifying devices. Sampling train No. 1 and 2 supplied the DRI fine particulate/semi volatile organic compound sampler (FP/SVOC) and an annular denuder (both described below), respectively. A Micro-Orifice Uniform Deposit Impactor (MOUDI) was connected to sampling train #4.

Sampling Methods. The semi-volatile polycyclic aromatic hydrocarbons (PAH) were collected using a sorbent-coated annular denuder⁹. The denuder sampler, purchased from the University Research Glassware Corporation (URG, Chapel Hill, NC), consisted of

three stages; the first stage was an 8-channel denuder section (52 mm OD, 600 mm length) coated with polystyrene-divinylbenzene resin XAD-4, which strips the gas-phase species from the airstream before collection of the particles on a second stage, consisting of a 47 mm Teflon-impregnated glass fiber (TIGF, T60X20) filter. The third stage consisted of polyurethane foam plugs (1" diameter) in combination with the 5 g of adsorbent resin XAD-4 (PUF/XAD/PUF "sandwich" cartridge) that were placed downstream of the filter to assess "blow off" or volatilization loss of semi-volatile PAH from the particles. The denuder XAD coating was performed by Dr. Lara Gundel of the University of California, Berkeley. In parallel, a medium-volume DRI fine particulate/semi volatile organic compound (FP/SVOC) sampler, using 90 mm TIGF (T60X40) filters backed by the PUF/XAD/PUF "sandwich" cartridge (10 g of XAD-4 resin between two 2" PUF plugs) was employed. The flow was set at approximately 90 L/min for the denuder and at 100 L/min for the FP/SVOC sampler.

Prior to sampling, the XAD-4 resin was cleaned by Soxhlet extraction with methanol followed by dichloromethane (CH_2Cl_2), each for 48 hours. The cleaned resin was then dried in a vacuum oven heated at 40 °C and stored in sealed glass containers in a clean freezer. The PUF plugs were cleaned by Soxhlet extraction with acetone followed by extraction with 10% diethyl ether in hexane, as described in U.S. EPA Method TO-13. Prior to sampling, XAD-4 resin and PUF plugs were loaded into the glass sampling cartridges. The TIGF filters were cleaned by sonication in methanol for 10 minutes (twice), followed by two more 10-minute sonications in CH_2Cl_2 . The filters are then dried, placed in clean aluminum foil, and labeled. Each batch of precleaned XAD-4 resin and ~10% of precleaned PUF plugs and TIGF filters was checked for purity by solvent extraction and GC/MS analysis of the extracts. The sampling flow rates were checked before and after sampling. After sampling, the filters were placed in clean aluminum foil and the PUF/XAD/PUF sandwich cartridges were also wrapped in aluminum foil and stored at ice temperature until transported to a laboratory freezer.

Micro-Orifice Uniform Deposit Impactor (MOUDI). A MOUDI sampler was used in this sampling campaign; it was fitted with aluminum media for thermal/optical reflectance (TOR) carbon analyses. The MOUDI is an inertial cascade impactor with multiple nozzles. At each stage, jets of particle-laden air are impinged upon an impaction plate and particles larger than the cut size of each stage are collected on the impaction plates. Smaller particles with less inertia follow the air streamlines and proceed onto the next stage. The nozzles of each succeeding stage are smaller than the prior stage, giving a higher velocity through the nozzles, and a smaller particle size cut. The airflow continues through a series of eight impactor stages until the smallest particles are removed by the after-filter. In the configuration we used, the top stage (which would nominally be 5.6 μm) was greased with high vacuum grease to remove any larger particles and prevent particle bouncing. The stages at 3.2, 1.8, 1.00, 0.53, 0.32, 0.18, and 0.096, 0.049 μm were used in the normal manner, with the after-filter collecting particles smaller than 0.049 μm . The MOUDI operated at a flow rate of 30 LPM.

Analysis Methods. The SVOCs collected on each denuder-filter-PUF/XAD/PUF sampling train were extracted separately with high purity, HPLC grade solvents. The denuder portion was extracted with cyclohexane immediately following the sample collection. Approximately 200 ml of cyclohexane was poured into the denuder section, which had been capped at one end. The other end was capped and the denuder manually inverted about 10 times. The solvent was drained and the procedure repeated two more times, using n-hexane for the last extraction. The PUF/XAD plugs were microwave-extracted with 10% diethyl ether in hexane¹⁰ and the filters were microwave-extracted with dichloromethane. Prior to extraction, the following deuterated internal standards were added to each PUF, filter, and XAD sorbent: naphthalene-d₈, acenaphthylene-d₈, phenanthrene-d₁₀, anthracene-d₁₀, chrysene-d₁₂, fluoranthene-d₁₀, pyrene-d₁₀, benz[a]anthracene-d₁₂, benzo[e]pyrene-d₁₂, benzo[a]pyrene-d₁₂, benzo[k]fluoranthene-d₁₂ and benzo[ghi]perylene-d₁₂. The extracts were concentrated by rotary evaporation at 20 °C under gentle vacuum to ~1 ml and filtered through 0.20 µm Anatop (Whatman International, Ltd.), rinsing the sample flask twice with 1 ml CH₂Cl₂ each time. Approximately 50 µl of acetonitrile was added to the sample and CH₂Cl₂ was evaporated under a gentle stream of nitrogen. The final volume was adjusted to 1 ml with acetonitrile. The sample was then analyzed by electron impact (EI) GC/MS technique, using an Ion Trap Varian Saturn 2000, operating in the selected ion storage (SIS) mode. Injections (1 µl) were made in the splitless mode onto a 30 m x 0.25 mm ID CPSil 8 fused-silica capillary column (Varian, Inc.). Identification and quantification of the SVOC was made by SIS, monitoring the molecular ion of each SVOC and deuterated SVOC. Calibration curves for the GC/MS/SIS quantification were made for the molecular ion peaks of the SVOC using the corresponding deuterated species (or the deuterated species most closely matched in volatility and retention characteristics) as internal standards. NIST SRM 1647 (certified PAH), with the addition of deuterated internal standards and authentic standards of compounds not present in the SRM, were used to make calibration solutions.

All aluminum MOUDI substrates were analyzed for mass and for organic (OC) and elemental (EC) carbon, by thermal/optical reflectance (TOR) method, as described previously¹¹. The TOR analysis used ¼ of an aluminum substrate and no correction for pyrolysis was applied to these samples. The remaining ¾ of selected MOUDI samples were spiked with deuterated PAH standards, extracted by sonication with dichloromethane (repeated 3 times), concentrated to 25 µl and analyzed for PAH, as described above.

All data discussed below are not corrected for dilution. The phase and size distribution of PAH discussed in this paper relates to the diluted exhaust and may not be valid for tailpipe conditions. Therefore, the correction for dilution might be potentially misleading.

Results and Discussion

MOUDI Mass and Carbon Data. With the exception of the quartz after-filter, all OC/EC data were obtained from aluminum foil by the TOR method¹¹. However, due to the reflective nature of aluminum foil, it was not possible to apply the pyrolysis correction

for these samples. Thus, the concentrations of EC might be slightly overestimated. Although MOUDI EC data correlate very well with black carbon data obtained by the continuous photoacoustic method (W. Arnott, unpublished results) for the same runs (slope = 0.99 and $r^2 = 0.972$) there is a significant difference between BC and EC concentrations for the runs with low mass emissions, as shown later.

Figure 1 shows the distribution of mass, organic carbon x 1.2 (to account for hydrogen mass) and elemental carbon between individual MOUDI stages for the system blank and for the diluted exhaust from the AGS vehicles, run under different conditions (see Table 2 for the run description). Although the system blank sample (Figure 1A) shows some mass, the distribution of mass between different MOUDI stages is different than for the exhaust samples. For the system blank the majority of mass is found on the 1.0 – 1.8 and 1.8 – 3.2 μm stages, indicating that some accumulation mode particles are desorbing from the dilution tunnel walls. The gasoline vehicle diluted exhaust from a run under high (53%) load (Figure 1B) shows very different mass distribution, with the majority of mass collected on 0.32-0.53; 0.18-0.32; 0.05-0.1 and <0.05 μm stages. The mass is composed mostly of organic carbon, with very little elemental carbon present.

For the two diesel vehicles tested on the dynamometer, 1996 Dodge Bobtail and 1986 Jeep Bobtail, there is overall more mass and higher EC contribution when the vehicle is run under higher load (Figure 1C and 1E) in comparison with the low load (Figure 1D and 1F). However, the older vehicle shows in general more mass and EC emissions than the newer vehicle (EC constitutes 35% and 26% of TC for the Jeep tested under high and low load, respectively, as compared with 11% and 3% for Dodge). Also, there is a shift toward smaller particle sizes for the low load, which is the most pronounced for the newer vehicle, 1996 Dodge Bobtail. Figures 1G and 1F show the distribution of mass and OC/EC for the two vehicles running under idle conditions, a 1992 Jammer and 1996 Dodge Bobtail, respectively. The Jammer exhaust contains more mass than the Dodge Bobtail, but the emissions from both vehicles is mostly of OC.

The quartz after filters (<0.056 μm) contain significant amount of mass for all runs. However, since the mass was obtained from the gravimetric analysis of quartz filters, there are two factors that can make these measurements inaccurate: 1) the quartz filter is prone to a positive sampling artifact, i.e. adsorption of gaseous organic compounds on the filter during sampling; 2) some particle bouncing could have occurred during sampling. Since the main constituent of the after filter mass is organic carbon, with very little of elemental carbon, this supports the first assumption.

Table 3 shows the distribution of the particle mass and OC/EC between individual MOUDI stages for runs selected for PAH analysis in the diluted vehicle exhaust. Since two Dodge Bobtail runs under 27% load were replicates, they were combined in order to obtain sufficient mass for these analyses.

MOUDI PAH Data. Figure 2 A, B and C show the distribution of PAH between the MOUDI stages collected from the diluted Dodge Bobtail exhaust run under high load (95, 81, 54, 27%) and Figure 2D, E and F - under constant low load (27%). Although it is generally assumed¹² that the aluminum foil has very low affinity for gaseous organic

compounds and thus is not prone to positive sampling artifacts, it is clear from this figure that the gas-phase PAH (Figure 2A and D) are present in measurable amounts in all stages. Naphthalene, methyl- and dimethyl- naphthalenes are present in very high concentrations in spark-ignition and diesel vehicle exhaust, and are even few orders of magnitude higher than particle-associated four and five ring PAH. These gas-phase PAH are distributed randomly between all stages, which indicates their non-specific adsorption, most likely on the particles collected on the various MOUDI stages (i.e. positive sampling artifact). The particle-associated semi-volatile PAH (Figure 2B and E) and non-volatile 4 through 6-ring PAH (Figure 2C and F) are present predominantly on the sub-micron particles collected on MOUDI stages 0.18-0.32 μm , 0.32-0.56 μm and 0.1-0.18 μm (see Table 4 for the explanation of mnemonics). For the low-load runs (27%), the distribution of PAH seems to be shifted towards smaller size particles, which is consistent with mass and OC distribution. In addition, the concentrations of PAH are much lower in low-load runs.

The system blanks showed very low PAH concentrations, distributed randomly between all stages, in contrast to the diesel runs, as shown in Figure 3.

Denuder PAH Data. Figure 4 shows the percentage of PAH present on the denuder portion (covered with XAD resin) of the annual denuder for 1996 Dodge Bobtail run under idle (Figure 4A), low load (27%, Figure 4B) and high load (Figure 4C) conditions, in relation to total PAH present on denuder+filter+PUF/XAD/PUF cartridge. The PAH are shown according to their elution order from a non-polar capillary column (CPSil 8, 5% phenylmethylsilicone), which separates PAH according to their volatility. It can be seen from this figure that the gas-particle phase distribution for these diesel runs depends on the engine loading. For idle (Figure 4A), the more volatile two-three-ring PAH, from naphthalene to dimethylphenanthrenes, are retained on the denuder portion, and the less volatile 4-ring PAH, such as fluoranthene and pyrene, are retained by the denuder at the 80 –90% range. These results imply that they are present predominantly in the gas phase. In contrast, for engines under high load (Figure 4C) a much larger portion of 3 and 4-ring PAH is partitioned to the particle phase. The low-load results (27%, Figure 4B) are clearly situated between these two extremes. The non-volatile 5 – ring PAH, such as benzo(b+j+k)fluoranthene, BaP, BeP, or benzo(g,h,i)perylene are present predominantly on the filter for all runs.

The most volatile and most abundant PAH (naphthalene and methyl-naphthalenes) shows the significant break through the denuder (approximately 20% and 10%, respectively), as Figure 4 shows. The flow rate through our denuder was calculated based on Possanzini model¹³ to be optimal for phenanthrene (99.5% efficiency) at 92 L/min. Thus, PAH more volatile than phenanthrene might experience a break through the denuder with this flow rate. However, the lower flow rate could have resulted in a particle loss to the denuder walls and evaporative losses of more volatile PAH from particles. The diffusional losses depend on the particle residence time and are important for smaller particles ($d_p < 0.01 \mu\text{m}$). As it can be seen from Figure 2C and 4F, the higher molecular weight (mw) PAH (from BaA to coronene) are present in significant amounts on small particles (0.05-0.1 μm MOUDI cut-off stage), especially for a low load run (27%). Consequently, some diffusional particle losses might have occurred for low load or idle

runs and, as it can be seen in Figure 4, the gas-phase concentrations of some higher mw PAH, such as BeP or benzo(g,h,i)perylene are higher than expected.

Evaporative losses are important for higher volatility compounds that can evaporate from particles during their residence time in the denuder, as surrounding gases are removed and the equilibrium is disturbed¹⁴. Thus, the transit time through the sorbent-coated section should be short enough to limit evaporation of semi-volatile PAH from particles (≤ 0.3 sec recommended). For 92 L/min flow rate and 5.2 cm x 60 cm 8-channel denuder used in this work, the transit time was approximately 0.3 sec.

The mechanism of gas/particle (G/P) partitioning of SVOC, such as PAH, includes adsorption onto the aerosol surface and absorption into the aerosol organic matter layer^{2,3,15,16}. Several investigators have suggested that G/P partitioning is primarily absorptive in nature and can be described by the gas-liquid interaction processes under many conditions^{2,3,17,18,19}. However, it has been recently argued that adsorption onto aerosol soot carbon dominates G/P partitioning of PAH and that absorption may account for less than 10% of total PAH in the particulate phase²⁰. Since our dynamometer measurements include several vehicles and test cycles that produced different amount of soot and organic carbon fractions, it was interesting to compare the G/P partitioning of PAH for these runs.

Table 5 lists OC*1.2, EC and black carbon (BC, obtained by the photoacoustic method) concentrations in the diluted exhaust of all vehicle's runs listed in Table 2. Also, the ratio of particle to gas phase concentrations (C_p/C_g) for fluoranthene and pyrene are listed. C_g values are obtained from the XAD coated denuder section, whereas C_p represents the sum of filter and PUF/XAD/PUF concentrations. As mentioned before, EC and BC are highly correlated for these runs. However, since no correction for pyrolysis was applied to the TOR method (due to the reflective nature of aluminum foil), the EC values might be slightly overestimated, especially for the runs with low EC content and high OC content. Thus, the BC values reflect probably more correctly the emissions soot content than EC values.

Figure 5 shows the relationship between C_p/C_g and BC and C_p/C_g and OC*1.2 for fluoranthene and pyrene in all runs. It is obvious that no correlation exists between these parameters. However, if the runs are sorted according to the BC content in emissions, it can be seen (Figure 6, lower graphs) that the good correlations exist between C_p/C_g and BC for runs with higher BC contents (i.e all 1986 Jeep Bobtail and 1992 Jammer runs) and between C_p/C_g and OC*1.2 for all runs with low BC content (i.e. 1996 Dodge Bobtail and 1993 Ford F350 gasoline runs). The slope of the trend line, which represents a gas-particle partition coefficient, is higher for the C_p/C_g and OC*1.2 relationship than for C_p/C_g and BC relationship, thus implying that the gas-particle phase distribution of these PAH is influenced more by the organic layer than BC content. However, both mechanisms, i.e. adsorptive to BC (if present in sufficient amount) and absorptive to OC, are responsible for the G/P partitioning of PAH under these conditions.

The exhaust from all vehicles tested on the dynamometer was diluted 30 to 40 times and allowed to equilibrate for approximately 80 sec prior to collection (see Table 2). It has been shown²¹ that under warm conditions (as used in this study, see Table 2), the equilibrium between gas- and particle phase PAH is reached very quickly, on the order of several seconds.

Comparison of Denuder and FP/SVOC Sampler. Figure 7 A, B, C, D shows the comparison of samples collected with the denuder and with the DRI FP/SVOC sampler for 1996 Dodge Bobtail idle and high load runs. The PUF/XAD/PUF extract from the FP/SVOC sampler is compared with the denuder extract (Fig 7 B and D) and filter extract from FP/SVOC sampler is compared with denuder filter extract plus the extract from the PUF/XAD/PUF cartridge following the filter (Fig 7 A and C). The most volatile 2-ring PAH are shown on the figure inserts. Their concentrations are approximately an order of magnitude higher than the concentrations of the most abundant 3-ring PAH, and they show approximately 10 to 20% breakthrough the denuder. For semi-volatile 2- 4 rings PAH, the sampling system consisting of a TIGF filter followed by a PUF/XAD/PUF cartridge (FP/SVOC sampler), showed lower concentrations on the filter and higher concentrations on the PUF/XAD/PUF cartridge in comparison with the denuder sampler, which indicates blow-off semi-volatile PAH from the filter (negative sampling artifact) for the FP/SVOC system. The exceptions are combined methyl- and dimethyl-phenanthrene isomers, for which the concentrations are generally higher for the denuder samples. The reason for this phenomenon is not clear – it may indicate breakthrough the PUF/XAD/PUF cartridge of FP/SVOC sampler, or the presence of some interfering compounds on the XAD-coated denuder section of the annular denuder.

Figure 8 shows the same comparison for the gasoline-powered 1993 Ford F-350 run under high (53%) load (Figure 8 A and B) and under variable (from 53% to 11%) load (Figure 8 C and D). This vehicle shows generally low PM emission rates when compared with diesel vehicles tested (see Figure 1) and the total PM concentrations for high load run was approximately 4 times lower than for low load run. Figure 8 shows that the concentrations of the gas-phase 2-ring PAH for these two runs are comparable (or higher) than the diesel vehicle shown in Figure 7, but the concentrations of 3-ring PAH are lower. In addition, the concentration of 5-ring PAH and coronene are higher for gasoline vehicle, especially for high load. This is consistent with the previous reports²². Again, for semi-volatile 2- 4 rings PAH, the sampling system consisting of a TIGF filter followed by a PUF/XAD/PUF cartridge (FP/SVOC sampler) showed lower concentrations on the filter and higher concentrations on the PUF/XAD/PUF cartridge in comparison with the denuder sampler, which indicates blow-off semi-volatile PAH from the filter (negative sampling artifact) for the FP/SVOC system. For diluted gasoline and diluted diesel exhaust, no evidence of positive filter artifact was observed. This indicates that the Teflon coated glass-fiber filters are less susceptible to gas-phase adsorption of volatile organic compounds than glass fiber filters.

In summary, for both diesel and gasoline vehicles there is more mass and higher EC contribution when the vehicle is run under higher load in comparison with the low load. However, the gasoline vehicle shows predominantly OC emissions, with very little EC present. The older diesel vehicles generally show more mass and EC emissions than

newer vehicles, and there is a mass shift toward smaller particle sizes for the low load, which is most pronounced for newer vehicles. The particle-associated semi-volatile PAH and non-volatile 4 through 6-ring PAH are present predominantly on the sub-micron particles collected on MOUDI stages 0.18-0.32 μm , 0.32-0.56 μm and 0.1-0.18 μm . For the low-load diesel vehicle runs, the distribution of PAH seems to be shifted towards smaller size particles. The gas-particle phase distribution of semi-volatile PAH depends also on the engine loading. For idle, the more volatile two- three-ring PAH, from naphthalene to dimethylphenanthrenes are retained on the denuder portion, but also less volatile 4-ring PAH, such as fluoranthene and pyrene are retained by the denuder at the 80 –90% range, which implies that they are present predominantly in the gas phase. In contrast, for engines under high loads a much larger portion of 3 and 4-ring PAH are partitioned to the particle phase.

Particle bound PAH tends to be associated with OC through the process of absorption when the EC content is small. Even when the EC fraction is larger and PAH's are adsorbed to the EC surface, an appreciable fraction of particle-bound PAH is associated with OC. These are the conclusions of direct source sampling with diluted, scrubbed air. Further dilution and transformation may occur in the atmosphere to adjust this picture of the gas- and particle-phase distribution.

Acknowledgements

This research was supported by Strategic Environmental Research and Development Program (SERDP) Project CP-1106, Characterization of Particulate Emission: Size Characterization and Chemical Speciation. We thank Mr. Bob Armstrong of Hill Air Force Base for his assistance.

References

- (1) Ligocki, M. P.; Pankow, J. F. *Environ.Sci.Technol.* **1989**, *23*, 75-83.
- (2) Pankow, J. F. *Atmos.Environ.* **1994**, *28*, 185-188.
- (3) Pankow, J. F. *Atmos.Environ.* **1994**, *28*, 189-194.
- (4) Odum, J. R.; Hoffman, T.; Bowman, F. A.; Collins, D.; Flagan, R. C.; Seinfeld, J. H. *Environ.Sci.Technol.* **1996**, *30*, 2580-2585.
- (5) Rogers, C. F.; Sagebiel, J. C.; Zielinska, B.; Arnott, W. P.; Fujita, E. M.; McDonald, J. D.; Griffin, J. B.; Kelly, K.; Overacker, D.; Wagner, D.; Lighty, J. S.; Sarofim, A.; Palmer, G. *Aerosol Sci.Technol.* **2003**, *37*, 355-368.
- (6) Kelly, V. R.; Lovett, G. M.; Weathers, K. C.; Likens, G. E. *Atmos.Environ.* **2002**, *36*, 1569-1575.
- (7) Hildemann, L. M.; Cass, G. R.; Markowski, G. R. *Aerosol Sci.Technol.* **1989**, *10*, 193-204.
- (8) Chan, T.; Lippmann, M. *Environ.Sci.Technol.* **1977**, *11*, 377-386.
- (9) Gundel, L. A.; Stevens, R. K.; Daisey, J. M.; Lee, V. C.; Mahanama, K. R. R.; Cancel-Velez, H. G. *Atmos.Environ.* **1995**, *29*, 1719-1733.
- (10) Autho, 1998.
- (11) Chow, J. C.; Watson, J. G.; Pritchett, L. C.; Pierson, W. R.; Frazier, C. A.; Purcell, R. G. *Atmos.Environ.* **1993**, *27A*, 1185-1201.

- (12) Offenberg, J. H.; Baker, J. E. *Atmos. Environ.* **2002**, *36*, 1205-1220.
- (13) Possanzini, M.; Febo, A.; Liberti, A. *Atmos. Environ.* **1983**, *17*, 2605-2610.
- (14) Kamens, R. M.; Coe, D. L. *Environ.Sci.Technol.* **1997**, *31*, 1830-1833.
- (15) Pankow, J. F. *Atmos. Environ.* **1987**, *21*, 2275-2283.
- (16) Jang, M.; Kamens, R. M.; Leach, K. B.; Strommen, M. R. *Environ.Sci.Technol.* **1997**, *31*, 2805-2811.
- (17) McDow, S. R.; Sun, Q. R.; Vartiainen, M.; Hong, Y. S.; Yao, Y. L.; Fister, T.; Yao, R. Q.; Kamens, R. M. *Environ.Sci.Technol.* **1994**, *28*, 2147-2153.
- (18) Kamens, R. M.; Odum, J. R.; Fan, Z. H. *Environ.Sci.Technol.* **1995**, *29*, 43-50.
- (19) Jang, M.; Kamens, R. M. *Environ.Sci.Technol.* **1998**, *32*, 1237-1243.
- (20) Dachs, J.; Eisenreich, S. J. *Environ.Sci.Technol.* **2000**, *34*, 3690-3697.
- (21) Kamens, R. M.; Jang, M.; Chien, C. J.; Leach, K. *Environ.Sci.Technol.* **1999**, *33*, 1430-1438.
- (22) Miguel, A. H.; Kirchstetter, T. W.; Harley, R. A.; Hering, S. V. *Environ.Sci.Technol.* **1998**, *32*, 450-455.

Table 1. Aircraft ground support equipment tested in the HAFB experiment

Vehicle Type	Fuel Type	Engine Manufacturer	Engine Displacement	Exhaust Treatment
1993 Ford F-350	Gasoline	Ford	5.8 liter	catalytic converter
1996 Dodge Bobtail	Diesel	Cummins	5.9 liter	none
1986 Jeep Bobtail	Diesel	Nissan	4.4 liter	none
1992 Jammer	JP-8 aviation fuel	HATZ	1.27 liter	none

“Bobtail” vehicles tow aircraft, and “Jammers” lift munitions into aircraft.

Table 2. Vehicle and dilution conditions for HAFB tests.

Run (min)	AGE	Engine speed (rpm)	Engine Load (% /kW)	Torque (N m)	Dilution ratio	RH (%)	Tem (°C)
60	Ford F350	2450	53/72	224	1:34.2	2-31	22-24
60	Ford F350	2450	53, 43,32, 21,11/ 72,58,43,28,14	224,179,134,90, 45	1:37.6	13-32	20-26
60	Dodge Bobtail	700	idle	idle	1:33.5	11-13	27-28
60	Dodge Bobtail	1500	95, 81,54, 27/ 96,72,48,24	759, 616, 411, 206	1:31.7	15-21	24-26
60	Dodge Bobtail	1500	27/24	206	1:30.3	18-22	22-24
60	Dodge Bobtail	1500	27/24	206	1:30.4	23-29	18-22
45	Jeep Bobtail	1700	23/24	411	1:31.8	23-31	19-24
20	Jeep Bobtail	1700	23/24	411	1:31.8	10-22	24-26
20	Jeep Bobtail	1700	23, 9/24, 9	411,164	1:31.1	9-16	26-28
20	Jeep Bobtail	1700*	93, *, 23/ 87, *, 48	1640, *, 822	1:42.0	8-20	24-27
30	Jammer	2500	idle	idle	1:32.1	14-29	16-26
30	Jammer	2500	idle	idle	1:31.3	2-14	27-33

* acceleration during the middle of the test;
RH: relative humidity

Table 3. MOUDI mass, organic mass (OC*1.2) and EC data (ug/m3).

Stage No.	Cut-off (um)	Blank			Dodge Bobtail, High			Dodge Bobtail, Low			Dodge Bobtail, Low*			Jeep Bobtail, Low			Jeep Bobtail, High		
		Mass	OC	EC	Mass	OC	EC	Mass	OC	EC	Mass	OC	EC	Mass	OC	EC	Mass	OC	EC
1	3.2	0.7	4.6	0.4	6.7	3.5	1.2	61.4	31.8	0.5	7.0	4.7	0.2	21.0	11.2	3.4	32.8	21.3	8.1
2	1.8	65.4	26.6	1.9	21.8	8.8	2.4	3.5	4.5	0.2	3.5	3.4	0.1	738.4	274.8	12.0	84.9	44.0	27.2
3	1	104.7	35.3	3.4	7.3	5.6	1.5	1.8	3.3	0.1	3.5	3.9	0.2	36.3	25.6	11.1	271.9	154.8	109.9
4	0.56	5.8	5.2	0.5	20.1	14.1	3.1	4.1	4.6	0.2	4.1	3.6	0.2	291.9	149.1	45.4	345.2	225.6	141.9
5	0.32	0.0	4.7	1.0	315.3	241.5	25.9	28.7	9.5	0.4	5.8	6.3	0.4	469.4	313.7	144.4	798.4	523.0	303.8
6	0.18	0.7	3.2	0.1	736.1	541.5	75.3	127.5	122.1	6.1	158.4	151.3	6.4	1194.5	911.5	278.6	1955.6	1177.7	655.3
7	0.1	0.0	2.4	0.0	309.2	227.0	21.9	132.2	91.5	1.9	142.0	156.3	2.9	173.6	155.0	33.4	152.4	100.7	47.4
8	0.056	0.0	2.6	0.0	82.0	64.8	3.6	88.3	90.3	1.1	101.7	82.7	1.6	47.7	44.4	3.6	30.9	25.0	4.8
AF		53.8	45.9	2.4	83.2	91.8	7.1	142.1	63.9	1.5	47.9	84.2	2.2	158.4	123.0	7.3	129.2	217.3	11.0

*Duplicate run

Table 4. The list of PAH and their mnemonics

Mnemonic	PAH
naphth	Naphthalene
mnaph	Methylnaphthalenes (2 isomers)
biphen	Biphenyl
dmenaph	Dimethylnaphthalene (6 isomers)
mebiph	Methylbiphenyls (3 isomers)
tmenaph	Trimethylnaphthalenes (12 isomers)
acnapy	Acenaphthylene
acnape	Acenaphthene
fluore	Fluorene
phenan	Phenanthrene
meflu	Methylfluorenes (3 isomers)
xanone	Xanthone
acquone	Acenaphthenequinone
mephen	Methylphenanthrene (5 isomers)
anrquone	Anthraquinone
dmephen	Dimethylphenanthrene (7 isomers)
anthra	Anthracene
fluora	Fluoranthene
pyrene	Pyrene
bntiop	Benzonaphthothiophene
mefl/py	MePyrene/MeFluoranthene (6 isomers)
bzcphen	Benzo(c)phenanthrene
baanth	Benz(a)anthracene
chrysn	Chrysene
bzantone	Benzanthrone
baa7_12	Benz(a)anthracene-7,12-dione
chry56m	5+6-methylchrysene
bbjkfl	Benzo(b+j+k)fluoranthene
bepyrn	BeP
peryle	Perylene
bapyrn	BaP
incdpy	Indeno[123-cd]pyrene
bghipe	Benzo(ghi)perylene
dbanth	Dibenz(ah+ac)anthracene
corone	Coronene

Table 5. Mass, EC, BC, OC*1.2 and Cp/Cg data for fluoranthene and pyrene

VEHICLE	Load, %	Mass (ug/m3)	EC (ug/m3)	BC (ug/m3)	OCx1.2 (ug/m3)	Fluoran- thene	Pyrene
Ford F-350	53	218.4	15.7	2.5	69.8	0.27	0.59
Ford F-351	53,43,32, 21,11	40.2	3.5	0.25	54.7	0.02	0.08
Dodge Bobtail	Idle	168.3	16.5	8.5	144.8	0.05	0.07
Dodge Bobtail	95,81,54, 27	1581.6	142.0	79.88	1198.6	1.43	1.95
Dodge Bobtail	27	589.6	12.0	21.67	421.5	0.19	0.41
Dodge Bobtail	27	474.0	14.3	18.39	496.3	0.24	0.53
Jeep Bobtail	23	1686.9	519.8	464.06	1027.0	0.31	0.39
Jeep Bobtail	23	2622.1	553.5	609.21	1604.7	0.38	0.59
Jeep Bobtail	23,9	3131.2	539.2	525.59	2008.3	0.38	0.47
Jeep Bobtail	93,23	3801.2	1309.5	na	2489.5	0.57	1.37
Jammer	Idle	881.7	199.5	169.19	633.6	0.13	0.18
Jammer	Idle	1702.4	96.7	151.79	1154.9	0.11	0.16
Jammer	Idle	na	na	50.24	na	0.08	0.09

List of Figures

Figure 1. The distribution of mass, OC and EC over MOUDI stages for selected runs. A: system blank; B: Ford F350, high load; C: 1996 Dodge Bobtail, high load; D: 1996 Dodge Bobtail, low load; E: 1986 Jeep Bobtail, high load; F: 1986 Jeep Bobtail, low load; G: 1992 Jammer, idle; H: 1996 Dodge Bobtail, idle

Figure 2. The distribution of PAH over MOUDI stages for 1996 Dodge Bobtail runs; A, B, and C high load; D, E, and F – low load

Figure 3. The distribution of PAH over MOUDI stages for system blank. A: gas-phase PAH; B: semi-volatile and particle phase PAH

Figure 4. The percentage of PAH present on the XAD-covered denuder stage for 1996 Dodge Bobtail runs. A: idle; B: low load; C: high load

Figure 5 The relations between C_p/C_g and BC (5A and 5B) and C_p/C_g and $OC*1.2$ (5C and 5D) for fluoranthene and pyrene

Figure 6. The relations between C_p/C_g and $OC*1.2$ for 1996 Dodge Bobtail and gasoline Ford F350 runs (6A and 6B) and C_p/C_g and BC for 1986 Jeep Bobtail and 1992 Jammer (6C and 6D)

Figure 7. Comparison of samples collected with the denuder with samples collected in parallel with FP/SVOC sampler. A: 1996 Dodge Bobtail, idle, denuder filter + denuder PUF/XAD/PUF versus FP/SVOC filter; B: 1996 Dodge Bobtail, idle, denuder XAD portion FP/SVOC PUF/XAD/PUF cartridge C: 1996 Dodge Bobtail, high load, denuder filter +denuder PUF/XAD/PUF versus FP/SVOC filter D: 1996 Dodge Bobtail, high load, denuder XAD portion FP/SVOC PUF/XAD/PUF cartridge

Figure 8. Comparison of samples collected with the denuder with samples collected in parallel with FP/SVOC sampler. A: Ford F350, high load, denuder filter +denuder PUF/XAD/PUF versus FP/SVOC filter; B: Ford F350, high load,, denuder XAD portion FP/SVOC PUF/XAD/PUF cartridge; C: Ford F350, variable load, denuder filter +denuder PUF/XAD/PUF versus FP/SVOC filter; D: Ford F350, variable load, denuder XAD portion FP/SVOC PUF/XAD/PUF cartridge

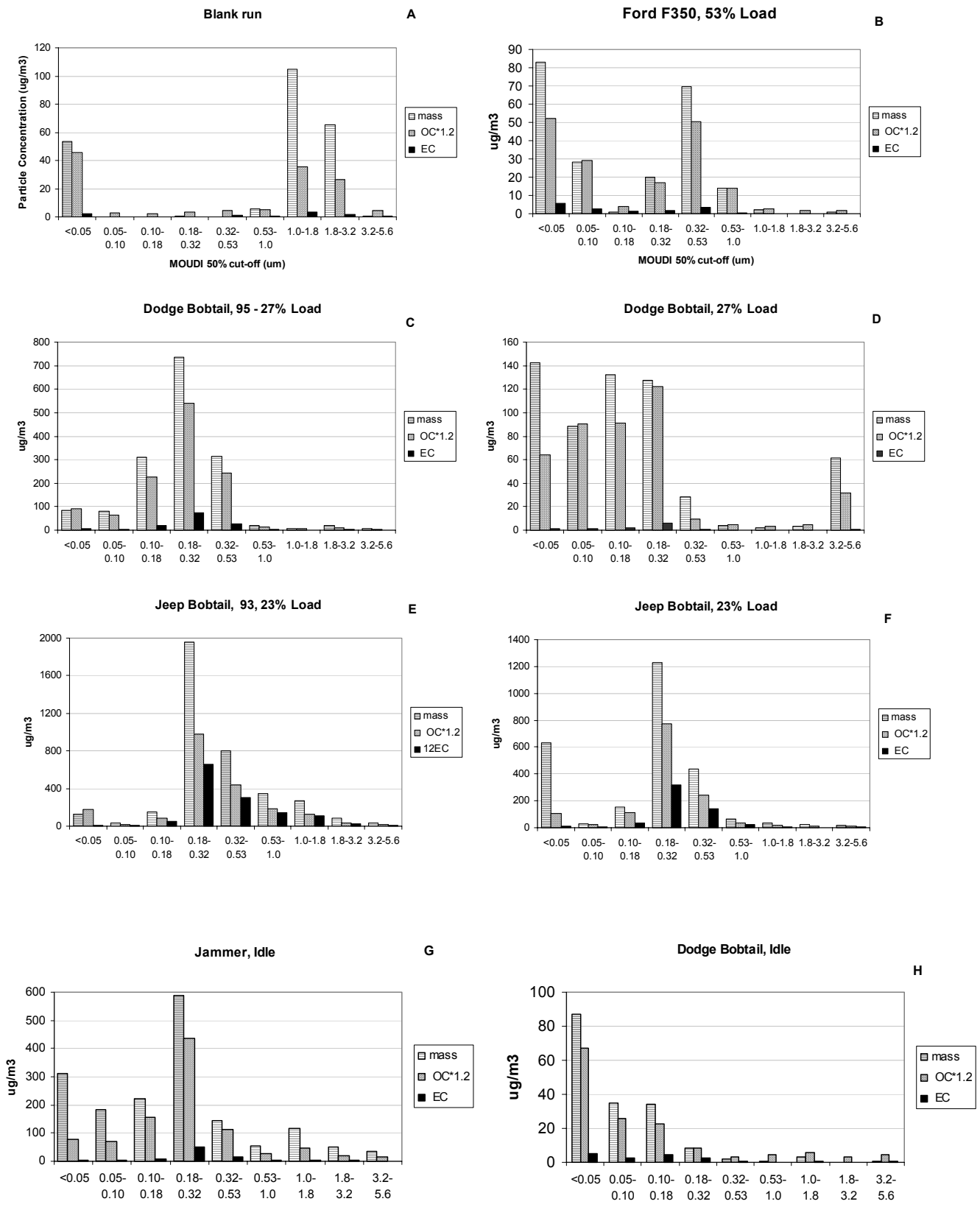


Figure 1

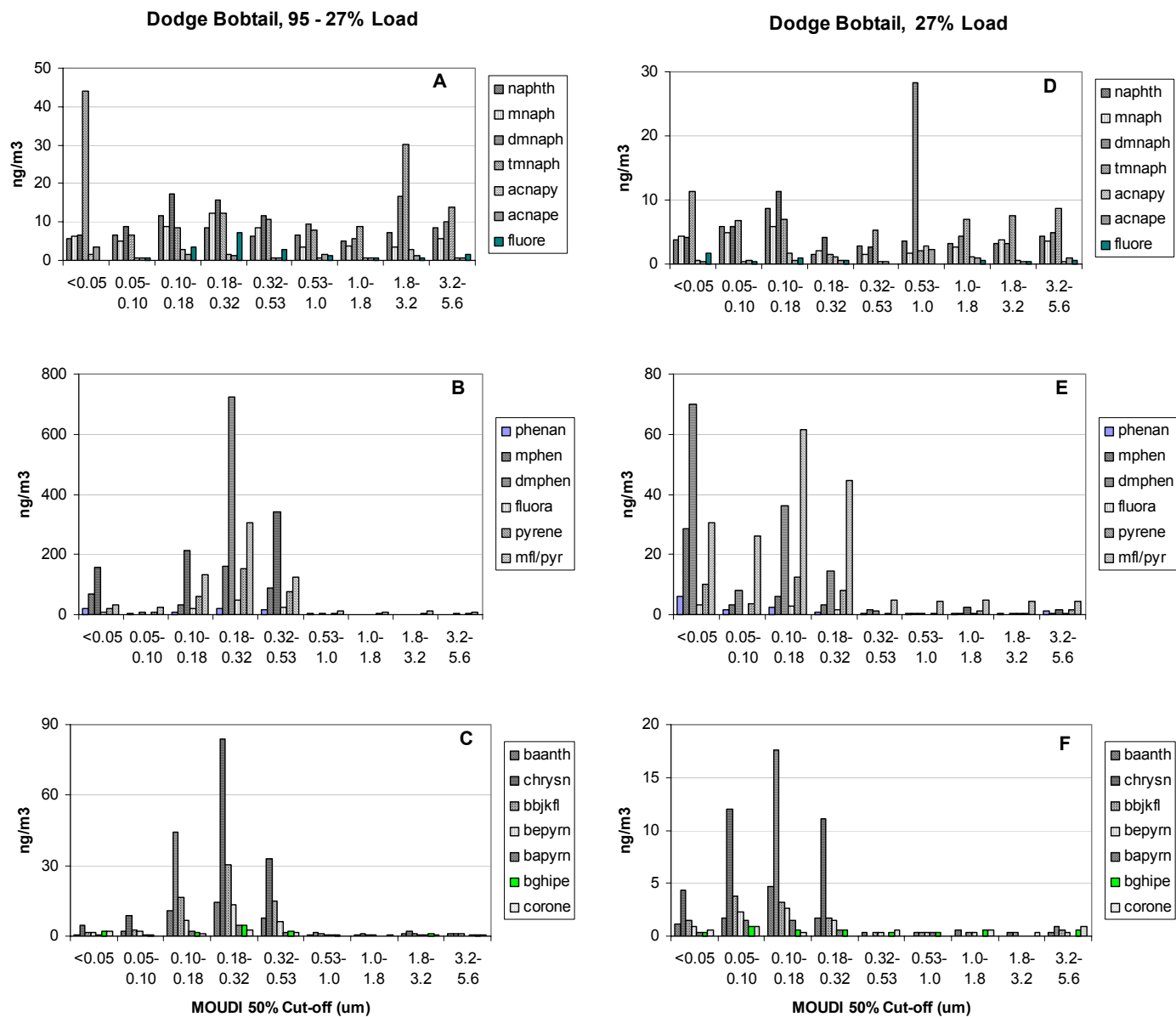


Figure 2

System Blank

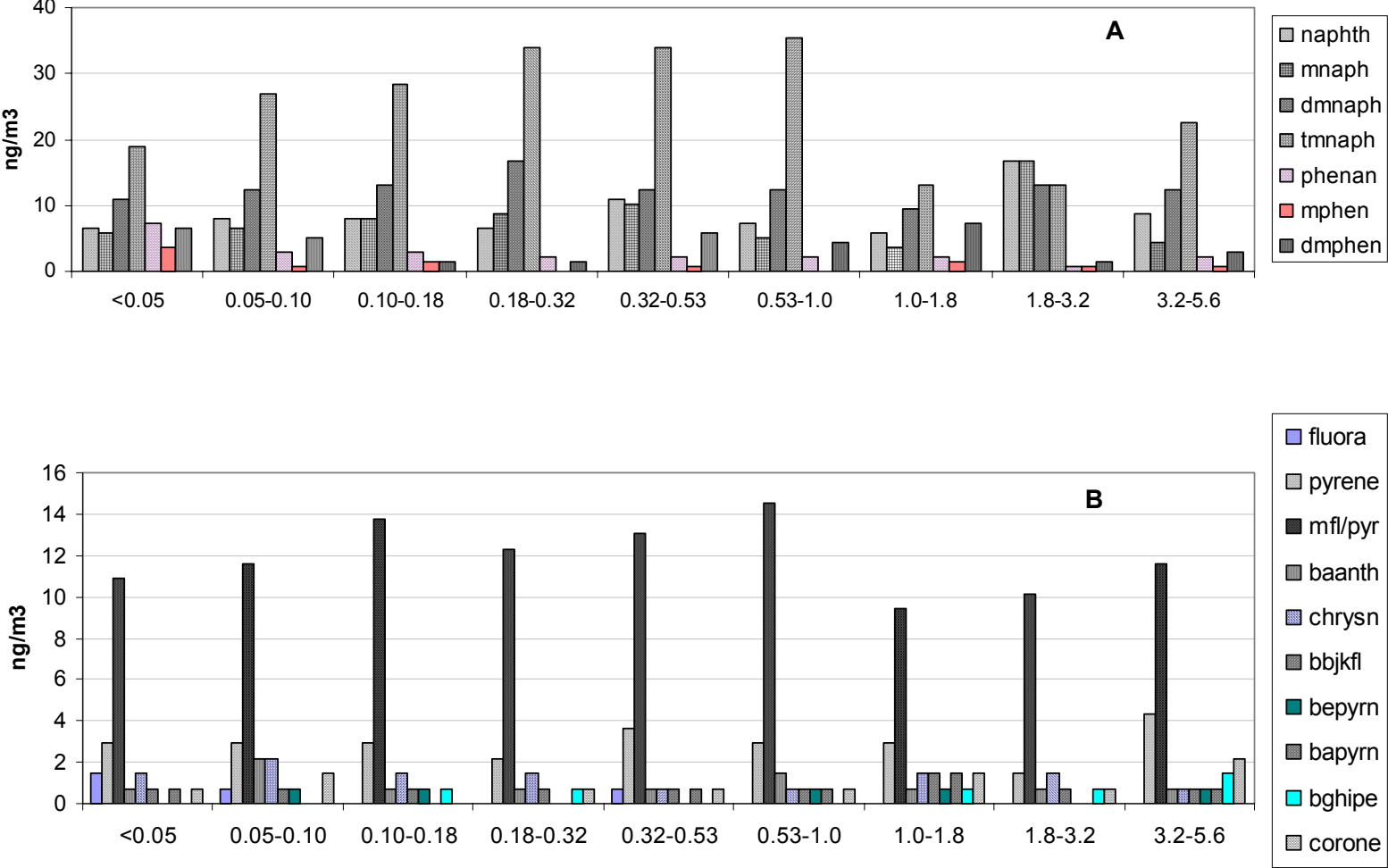


Figure 3

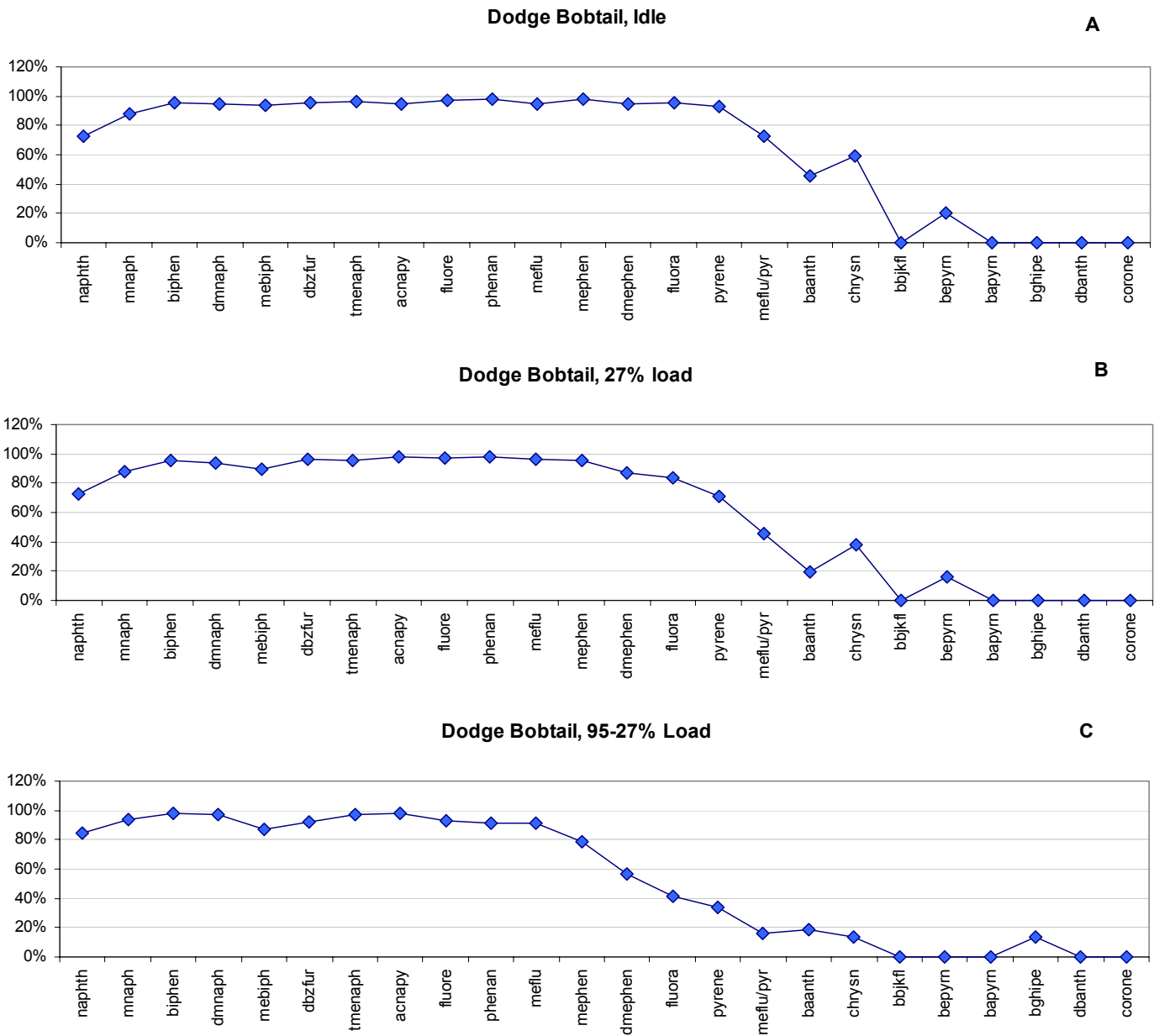


Figure 4

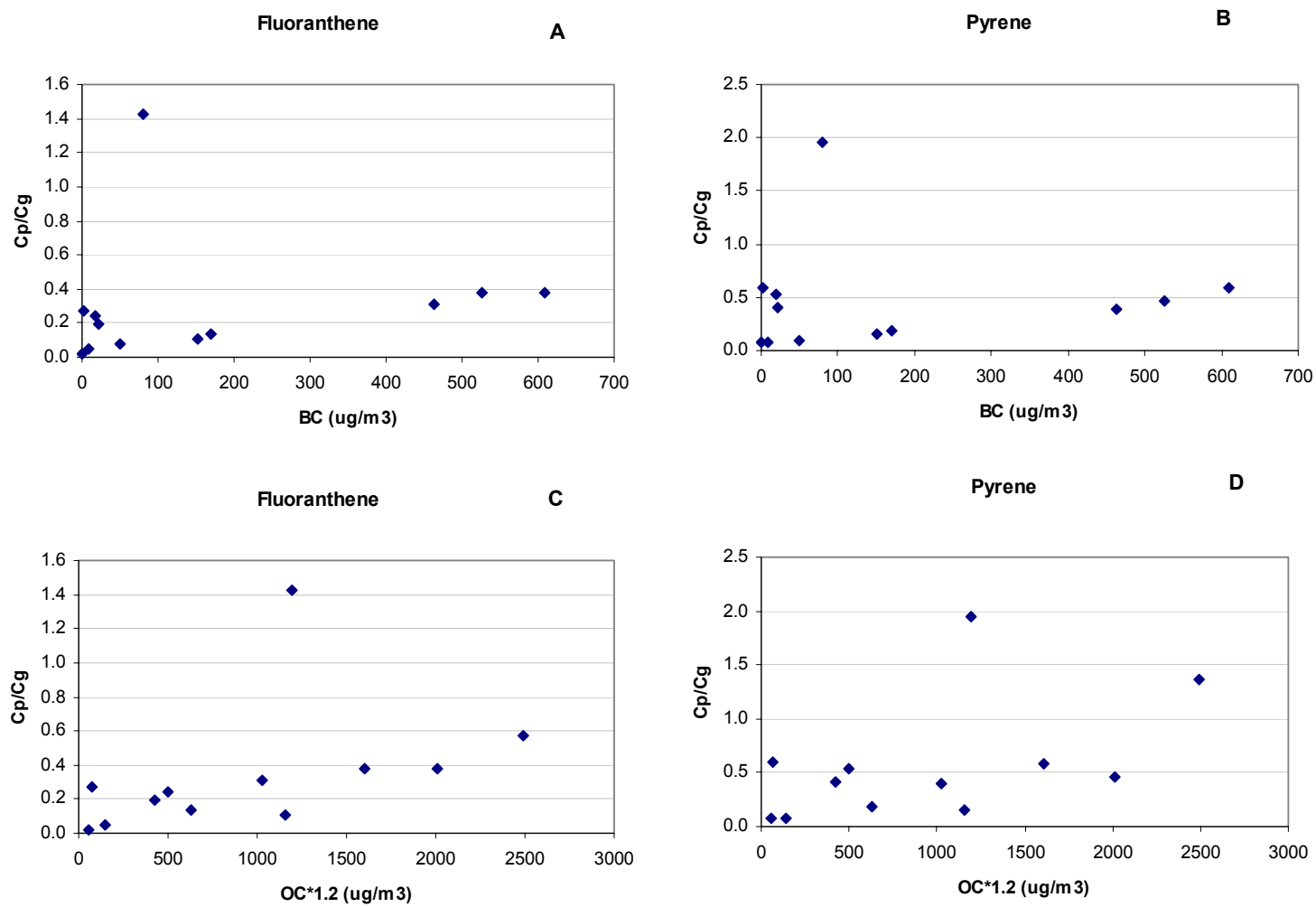


Figure 5

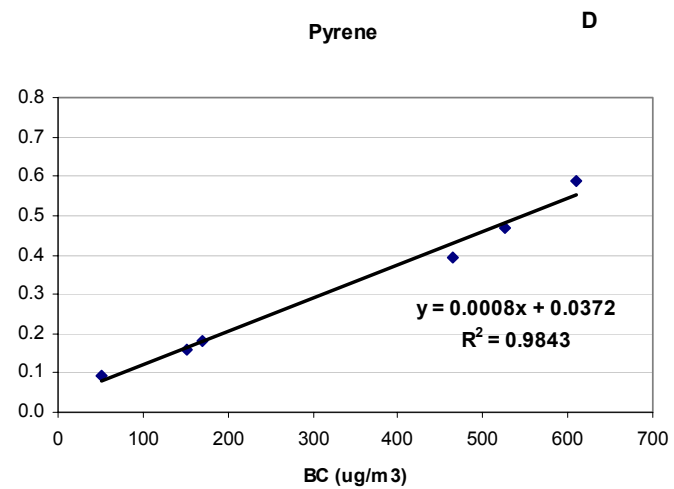
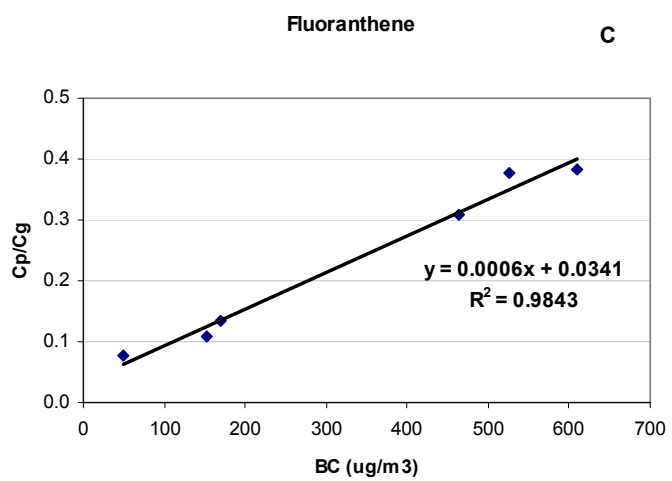
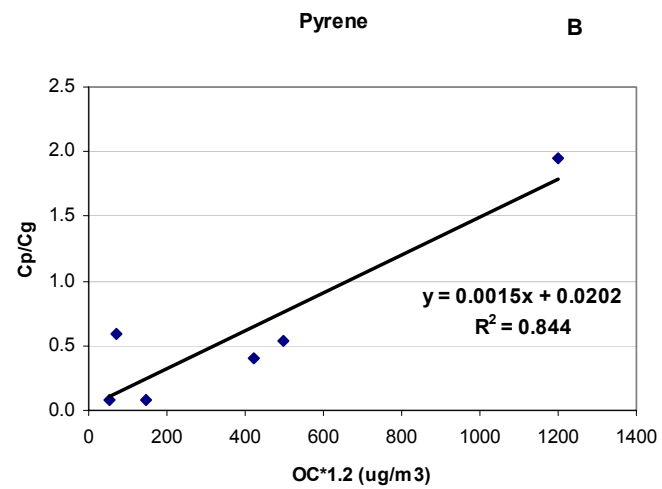
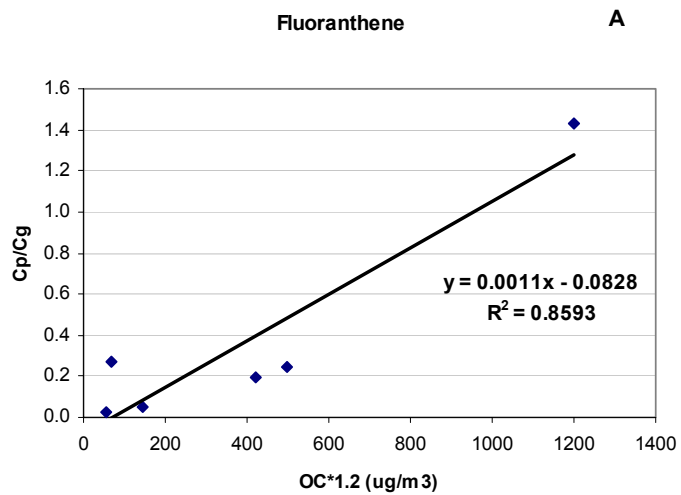


Figure6

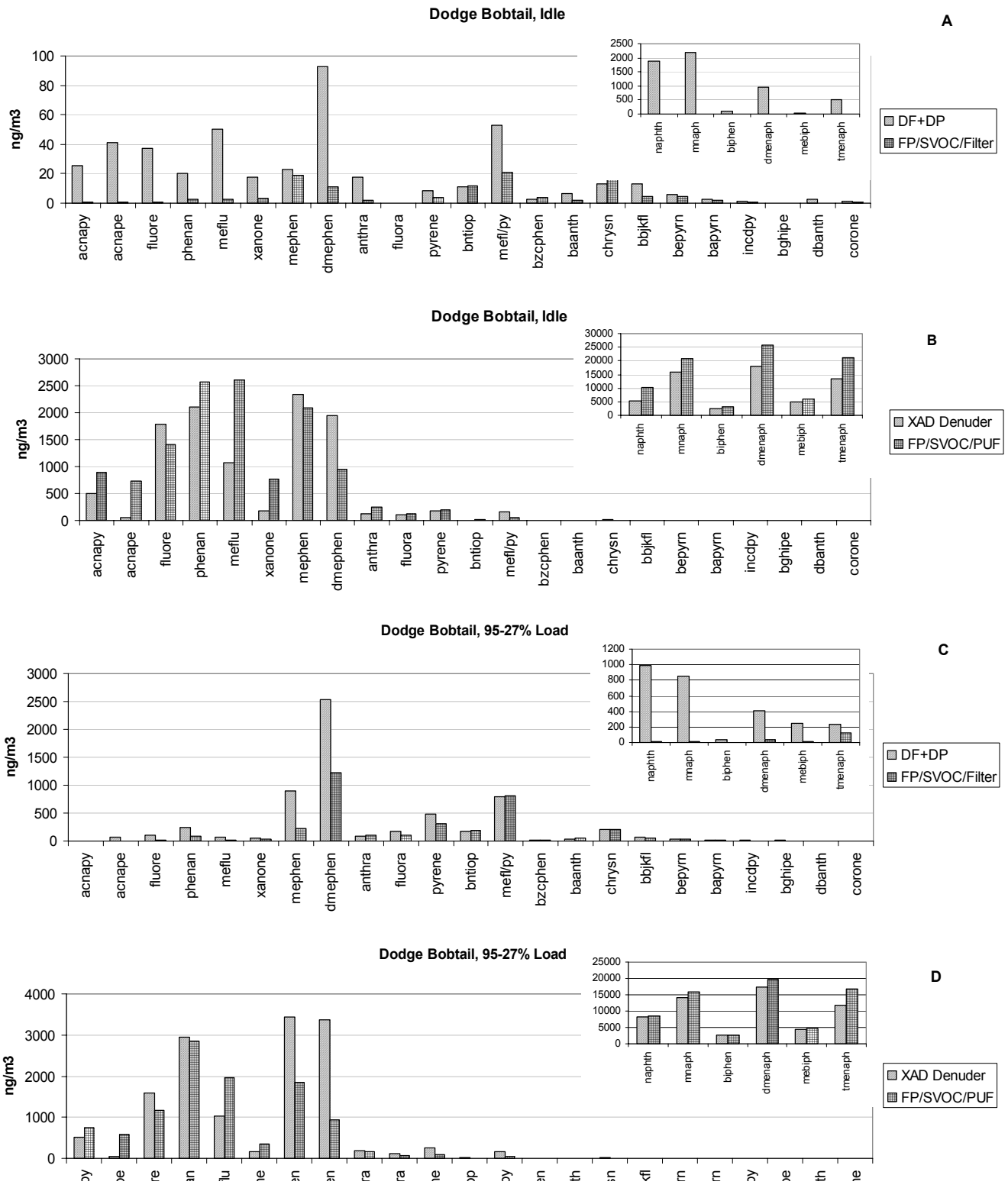


Figure 7

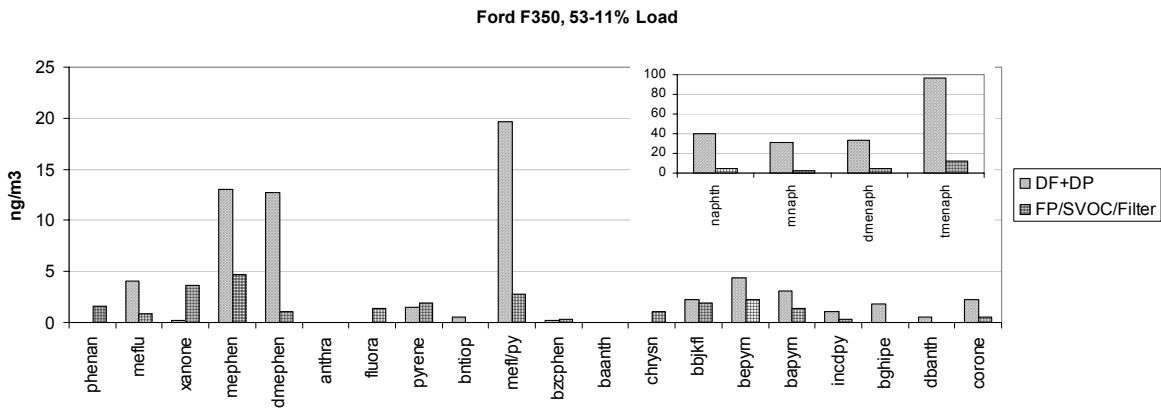
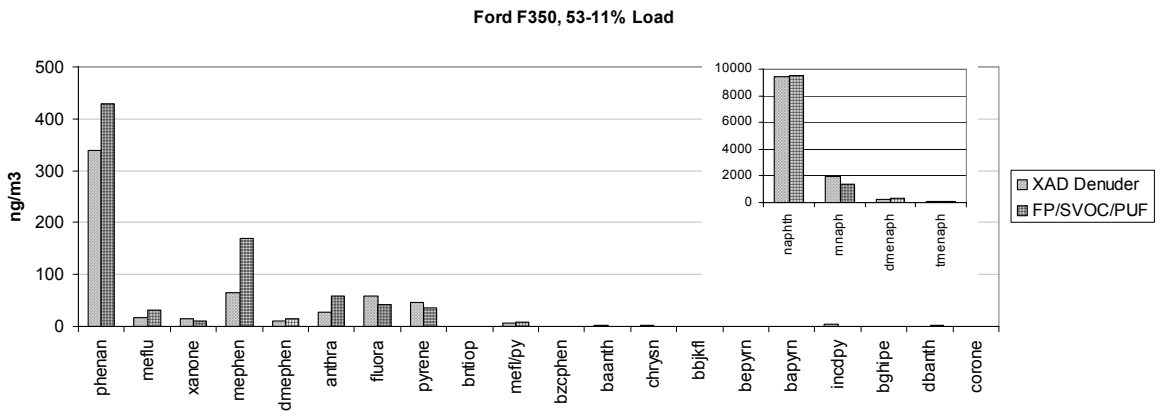
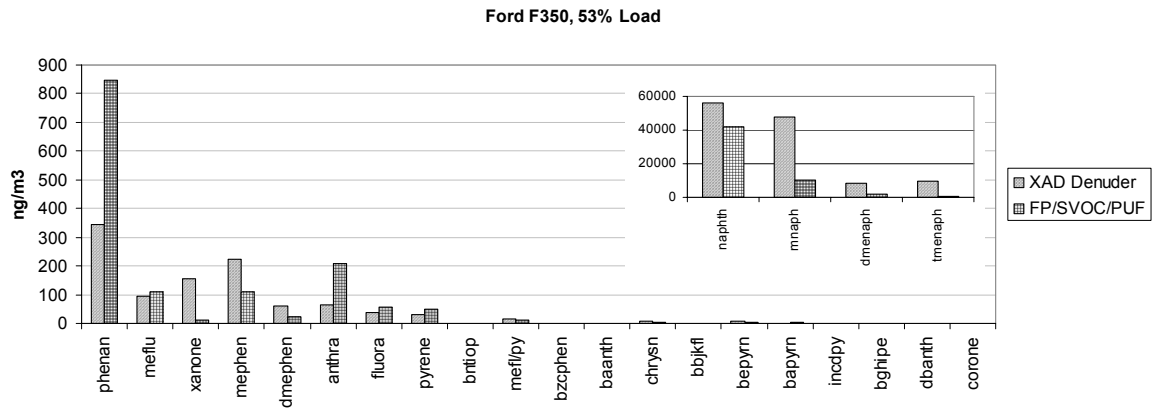
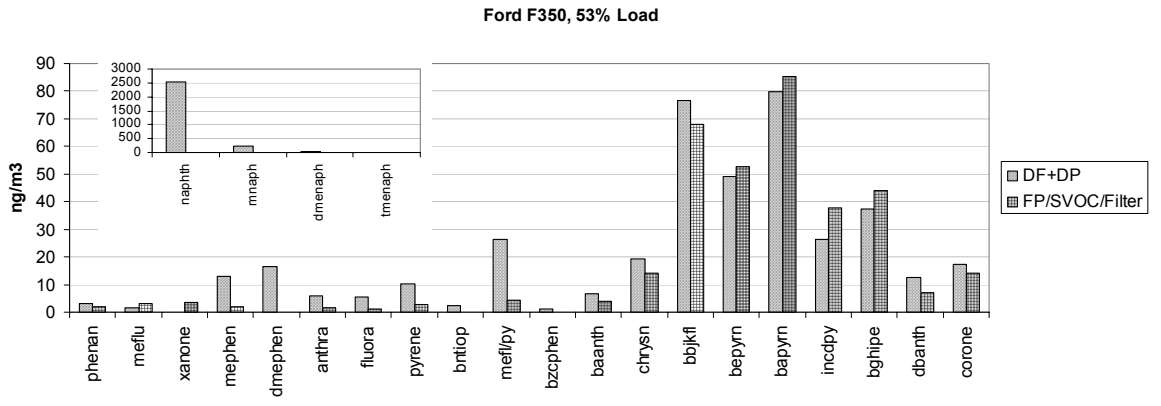


Figure 8

APPENDIX 4:

NORTH ISLAND PAH RESULTS

North Island PAH Results

This Appendix shows the PAH concentrations in the diluted engine exhausts, obtained by the denuder sampling method. Table A4-1 shows the list of PAH quantified for this study and the explanation of their mnemonics. Table A4-2 shows the concentrations of PAH for run 1 through 6 (see Table 4-2 and Section 4 for the description of individual runs). Run 4 was a dynamic blank, i.e. the ambient air was sampled from the discharge chamber, without an engine present. Run # 7 was a field blank of the denuder, collected after the last run. If the average sampling volume (4.5 m^3) is assumed for the field blank, the PAH concentrations are low in comparison with the dynamic blank and the actual runs.

Table A4-2 shows the concentration of the PAH in the gas phase (C_g), in the particle phase (C_p) and the percentage of each PAH present in the gas phase in relation to the total concentration. C_g is equal to the PAH concentrations obtained from the XAD coated denuder section (denuder) and C_p is the sum of the concentration on a filter plus concentration on a PUF/XAD/PUF cartridge (blow-off the filter). For most volatile PAH, i.e. naphthalene, methyl-naphthalenes and dimethyl-naphthalenes, the concentration on the PUF/XAD/PUF cartridge reflect the breakthrough the denuder section rather than the blow-off the filter, since the flow rate was optimized to assure 99% collection efficiency of phenanthrene (Zielinska et al., 2003).

Figure A4-1 shows the percentage of more abundant PAH present in the gas phase. For simplicity, methyl-PAH isomers are summed together (i.e. methyl-naphthalenes, dimethyl-naphthalenes, etc). The phase distribution of semi-volatile PAH is in general consistent with those reported previously by Zielinska et al.(2003), with exception of run 7, helicopter engine. This engine emitted very high amount of PAH and the denuder sampler was clearly overloaded. PAH from naphthalene to phenanthrene show significant breakthrough the XAD coated denuder section. PAH with lower vapor pressure than phenanthrene are present in higher percentage in the gas phase in comparison with run 1, 2, 3, and 5. This could be real, since the helicopter engine showed high PM emission rates with significant amount of organic and elemental carbon (Zielinska et al., 2003).

Table A4-2 shows the concentrations of PAH in the diluted engine exhaust collected on seven MOUDI stages (1.8, 1, 0.53, 0.32, 0.18, 0.096 and 0.049 micron) and quartz after filter (AF) for run 2, 3, 5, and 6. Figure X-2 shows this data graphically. For simplicity, methyl-PAH isomers are summed together. The particle-associated PAH concentrations for runs 2, 3, and 5 are very low, thus highly uncertain. However, as it can be seen from Figure A4-2, the semi-volatile and particle associated PAH are mostly present on lower MOUDI stages (0.18 micron and smaller). This is clearly the case for run 6, for which the concentrations of PAH are significantly higher. This is consistent with the previous observations (Zielinska et al., 2003).

Table A4-1. PAH quantified for this study and their mnemonics

Name	Compound	Name	Compound
NAPHTH	Naphthalene	M_1PHT	1-methylphenanthrene
MNAPH2	2-methylnaphthalene	M_9ANT	9-methylantracene
MNAPH1	1-methylnaphthalene	ANTHRON	Anthrone
BIPHEN	Biphenyl	ANRQUONE	Anthraquinone
ENAP12	1+2ethylnaphthalene	DM36PH	3,6-dimethylphenanthrene
DMN267	2,6+2,7-dimethylnaphthalene	A_DMPH	A-dimethylphenanthrene
DM1367	1,3+1,6+1,7dimethylnaphth	B_DMPH	B-dimethylphenanthrene
D14523	1,4+1,5+2,3-dimethylnaphth	C_DMPH	C-dimethylphenanthrene
DMN12	1,2-dimethylnaphthalene	DM17PH	1,7-dimethylphenanthrene
M_2BPH	2-Methylbiphenyl	D_DMPH	D-dimethylphenanthrene
M_3BPH	3-Methylbiphenyl	E_DMPH	E-dimethylphenanthrene
M_4BPH	4-Methylbiphenyl	FLUORA	Fluoranthene
DBZFN	Dibenzofuran	PYRENE	Pyrene
ATMNAP	A-trimethylnaphthalene	ANTAL9	9-Anthraaldehyde
EM_12N	1-ethyl-2-methylnaphthalene	RETENE	Retene
BTMNAP	B-trimethylnaphthalene	BNTIOP	Benzonaphthothiophene
CTMNAP	C-trimethylnaphthalene	C1MFLPY	1-MeFl+C-MeFl/Py
EM_21N	2-ethyl-1-methylnaphthalene	BMPYFL	B-MePy/MeFl
ETMNAP	E-trimethylnaphthalene	CMPYFL	C-MePy/MeFl
FTMNAP	F-trimethylnaphthalene	DMPYFL	D-MePy/MeFl
TMI235N	2,3,5+I-trimethylnaphthalene	M_4PYR	4-methylpyrene
TM245N	2,4,5-trimethylnaphthalene	M_1PYR	1-methylpyrene
JTMNAP	J-trimethylnaphthalene	BZCPHEN	Benzo(c)phenanthrene
TM145N	1,4,5-trimethylnaphthalene	BAANTH	Benz(a)anthracene
ACNAPY	Acenaphthylene	CHRYSN	Chrysene
ACNAPE	Acenaphthene	M_7BAA	7-methylbenz(a)anthracene
FLUORE	Fluorene	BZANTONE	Benzanthrone
PHENAN	Phenanthrene	BAA7_12	Benz(a)anthracene-7,12-dione
ANTHRA	Anthracene	CHRY56M	5+6-methylchrysene
A_MFLU	A-methylfluorene	BBJKFL	Benzo(b+j+k)fluoranthene
M_1FLU	1-methylfluorene	BEPYRN	BeP
B_MFLU	B-methylfluorene	BAPYRN	BaP
FL9ONE	9-fluorenone	PERYLE	Perylene
XANONE	Xanthone	M_7BPY	7-methylbenzo(a)pyrene
PNAPONE	Perinaphthenone	INCDPY	Indeno[123-cd]pyrene
A_MPHT	A-methylphenanthrene	DBANTH	Dibenzo(ah+ac)anthracene
M_2PHT	2-methylphenanthrene	BGHIPE	Benzo(ghi)perylene
B_MPHT	B-methylphenanthrene	CORONE	Coronene
C_MPHT	C-methylphenanthrene		

*u after the compound name means uncertainty

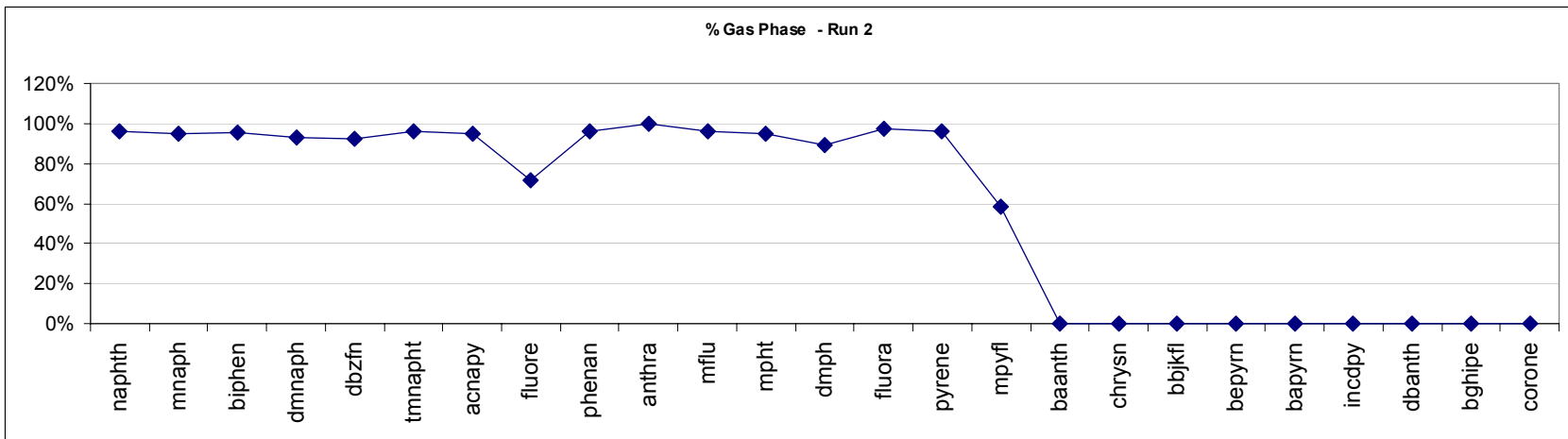
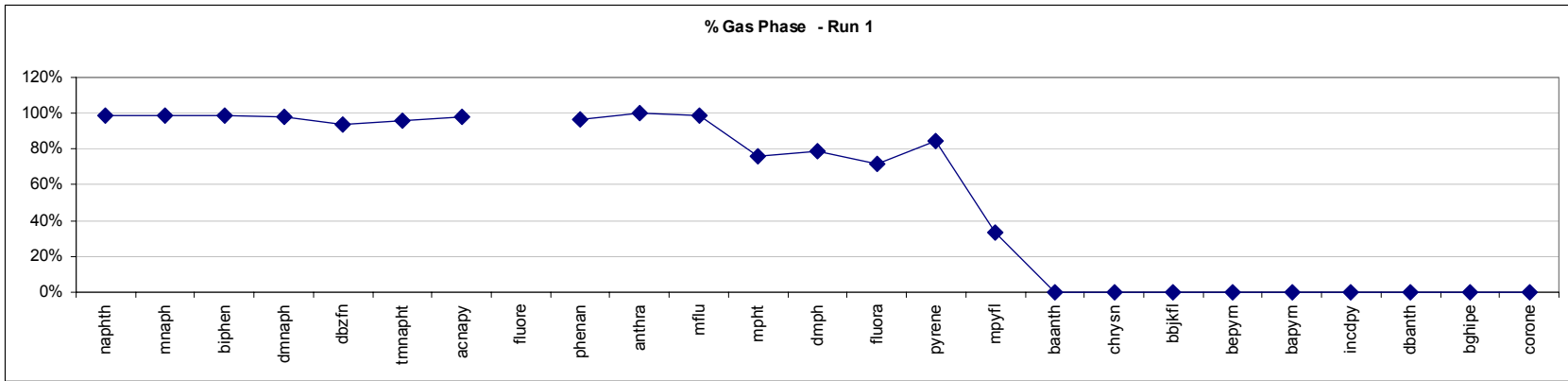


Figure A4-1. Percentage of selected PAHs in the gas phase. Note the MW of compounds increases from left to right.

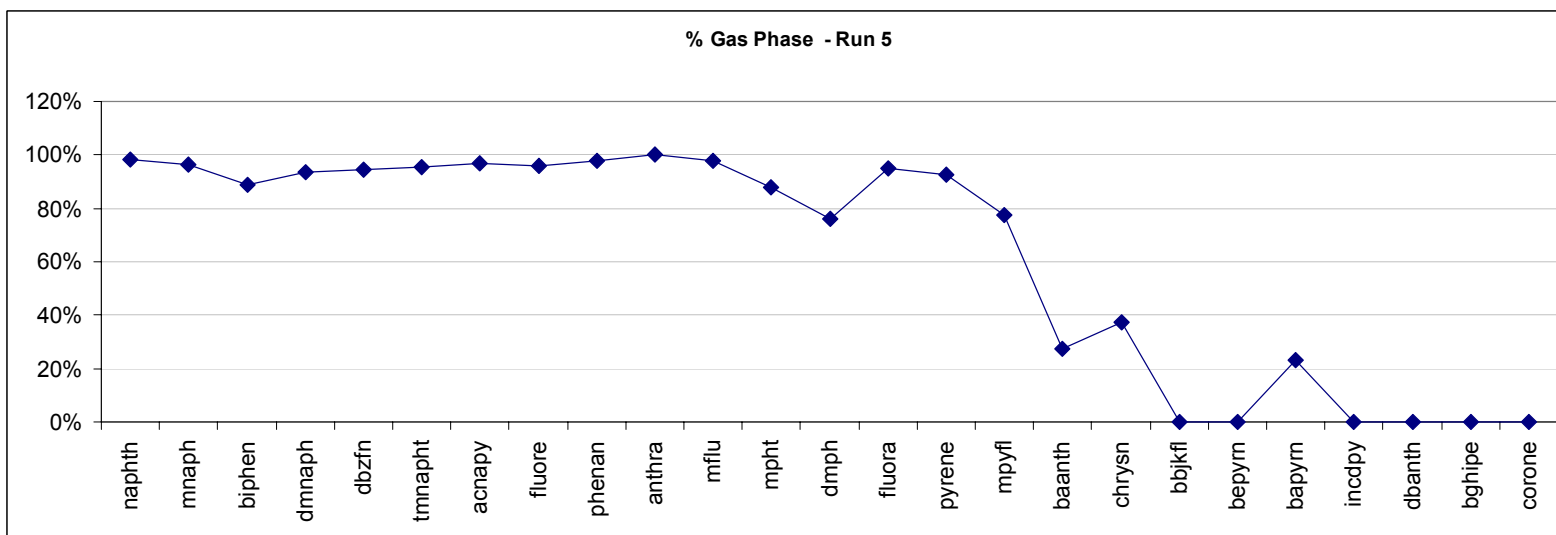
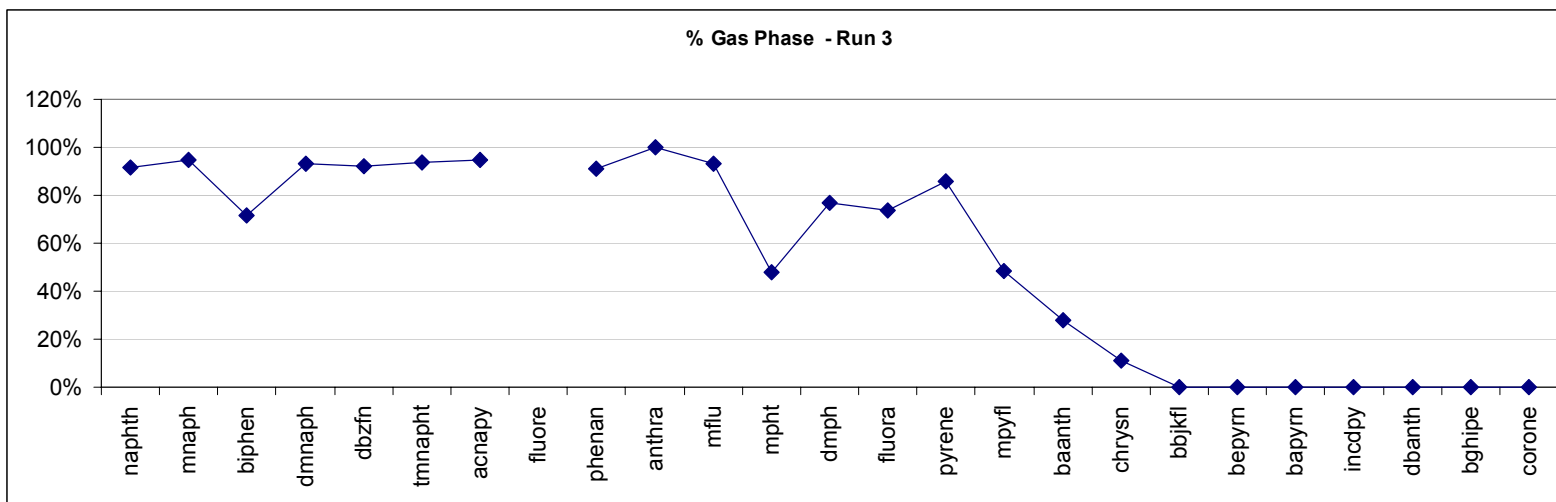


Figure A4-1. Percentage of selected PAHs in the gas phase. Note the MW of compounds increases from left to right.

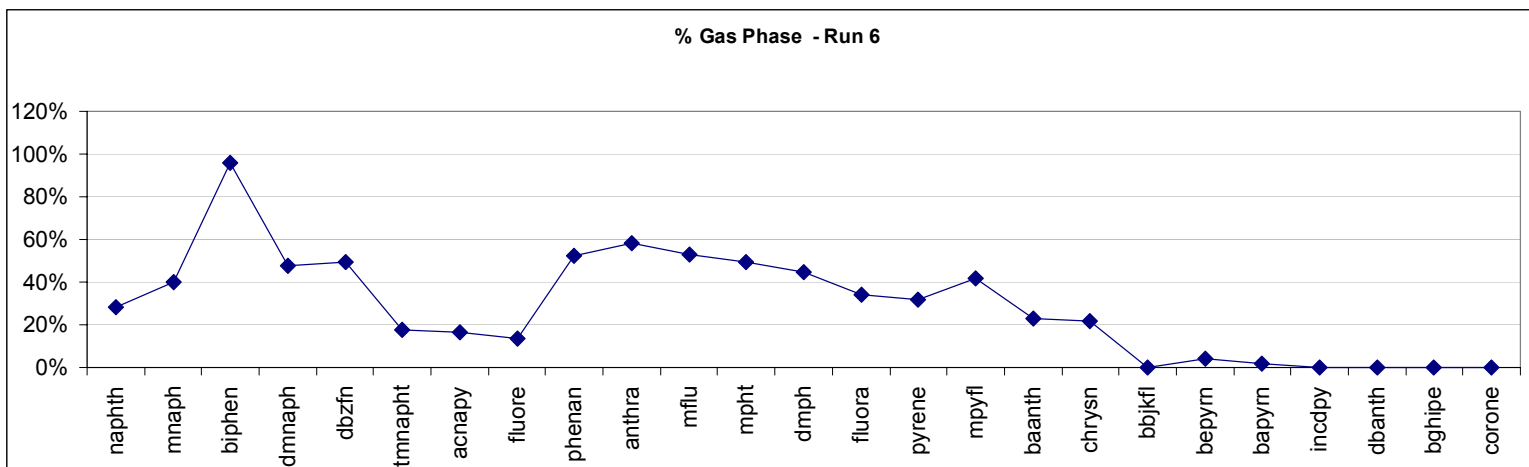


Figure A4-1. Percentage of selected PAHs in the gas phase. Note the MW of compounds increases from left to right.

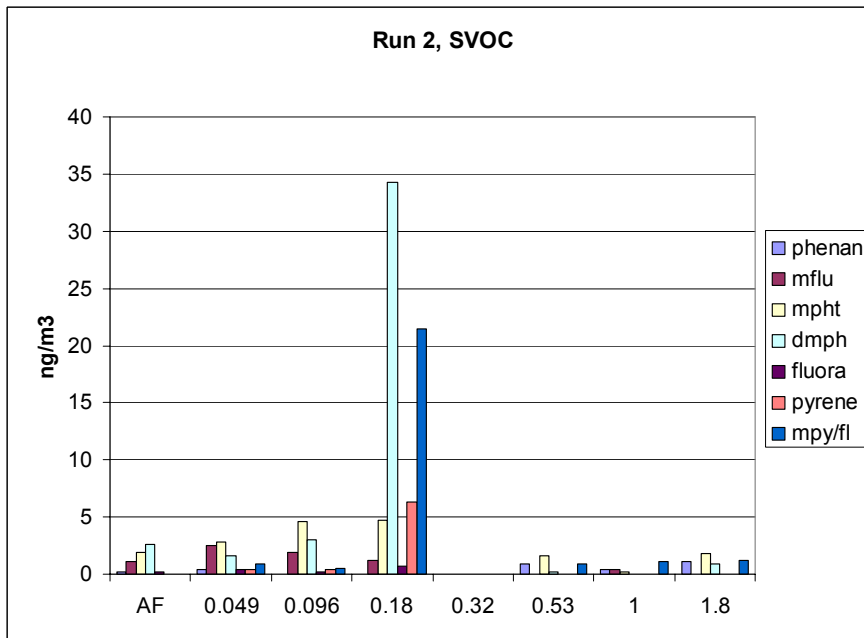
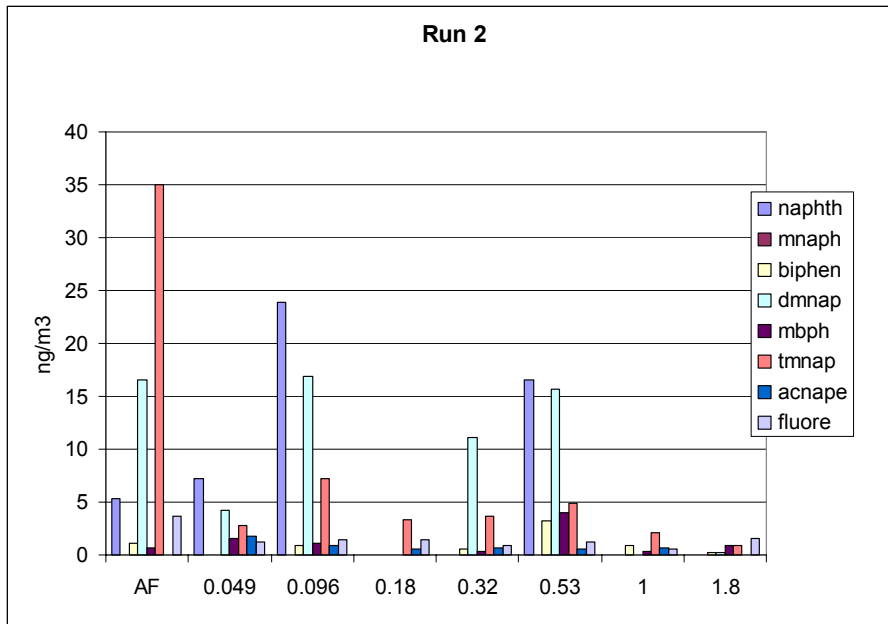


Figure A4-2. MOUDI PAH results.

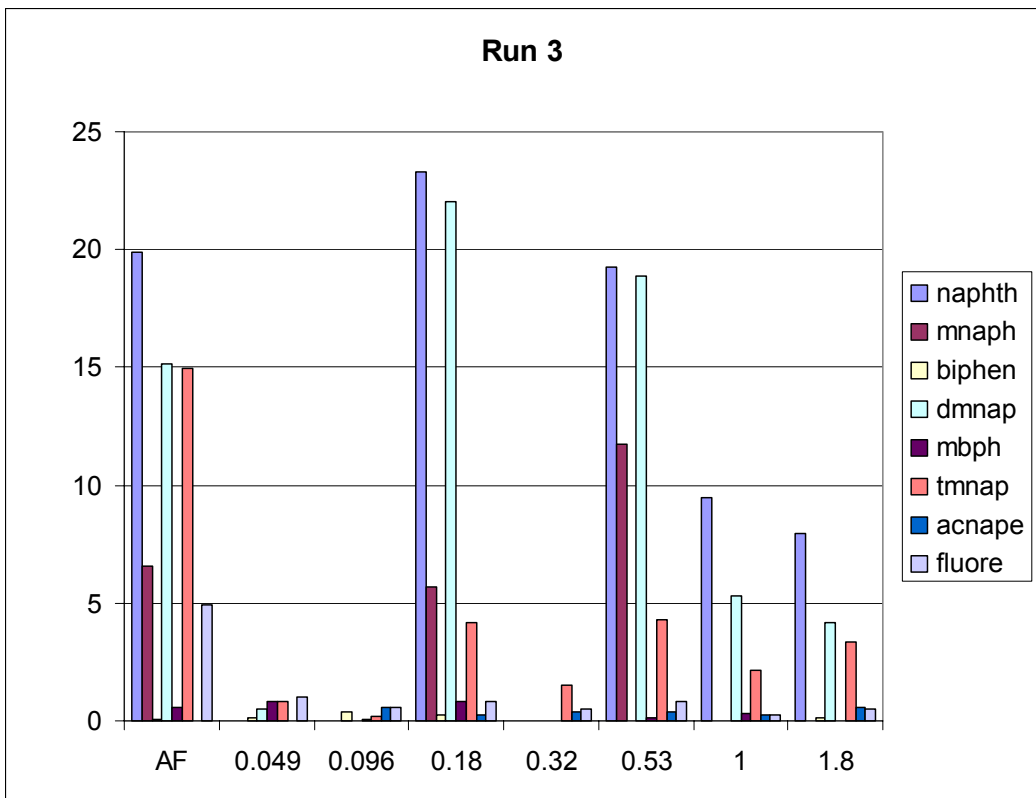
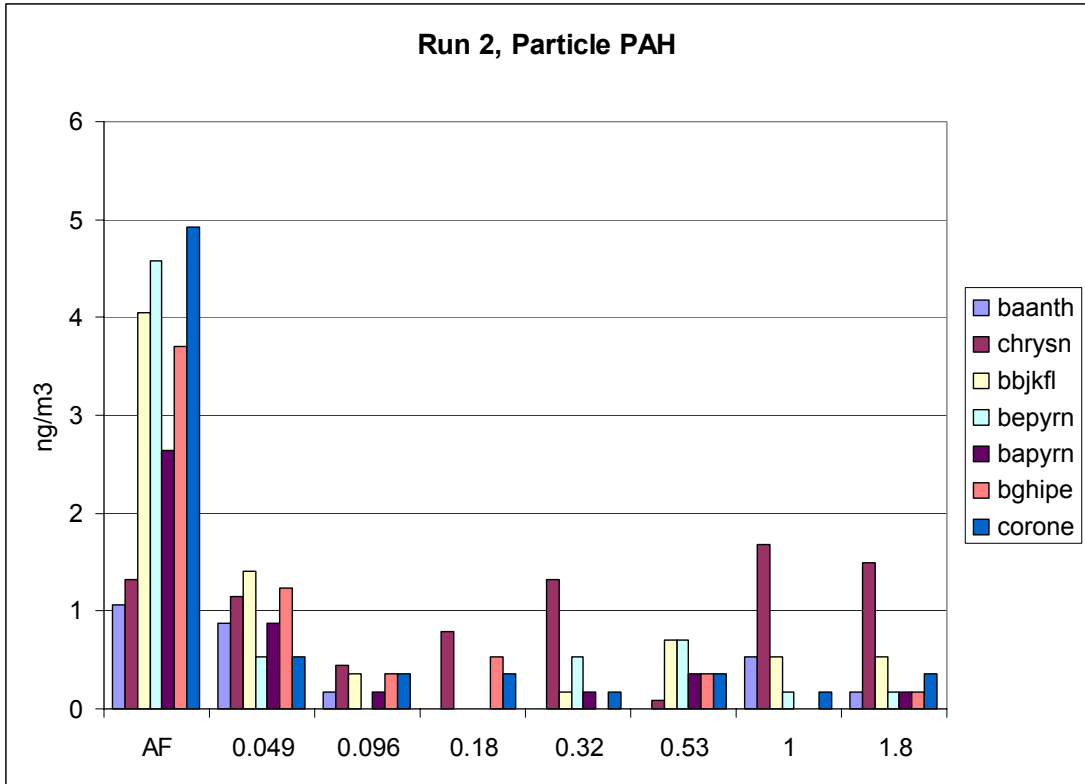


Figure A4-2. MOUDI PAH results.

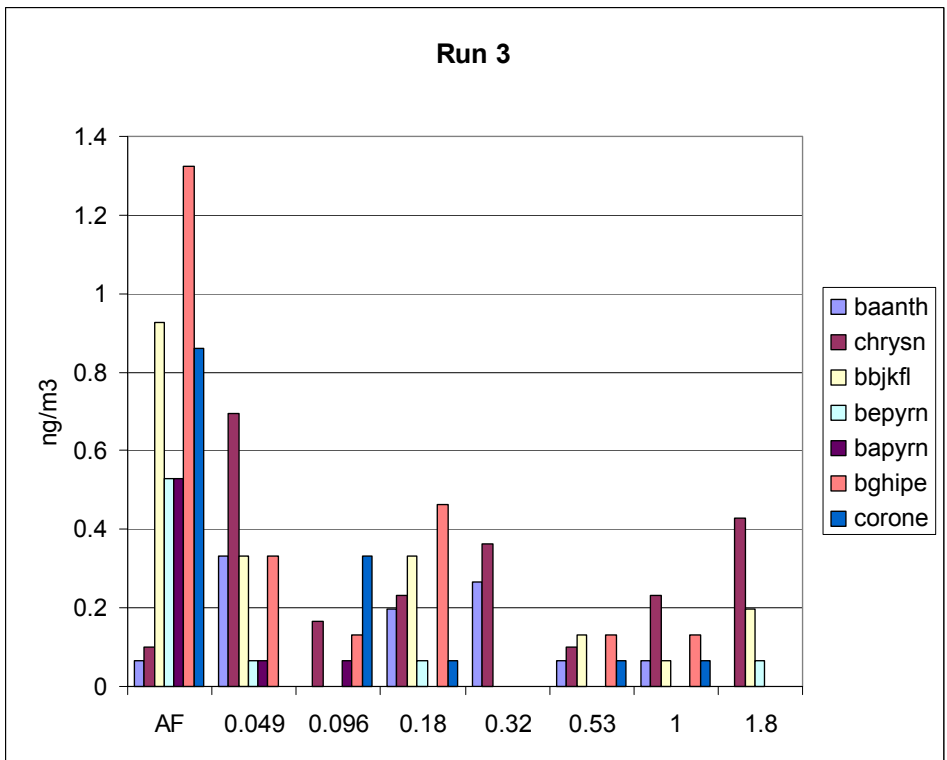
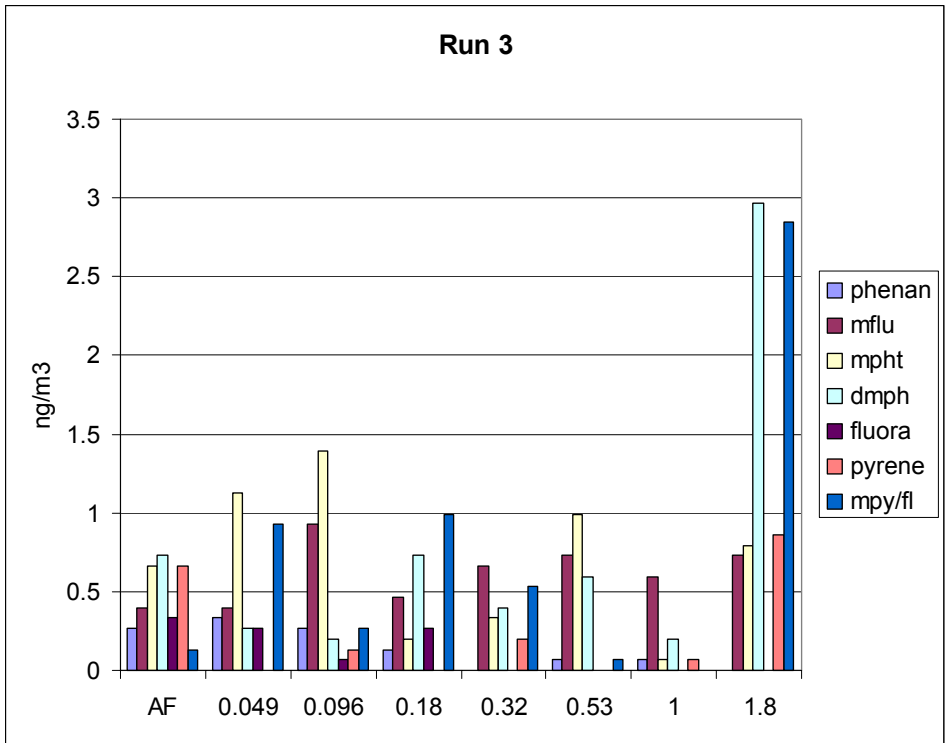


Figure A4-2. MOUDI PAH results.

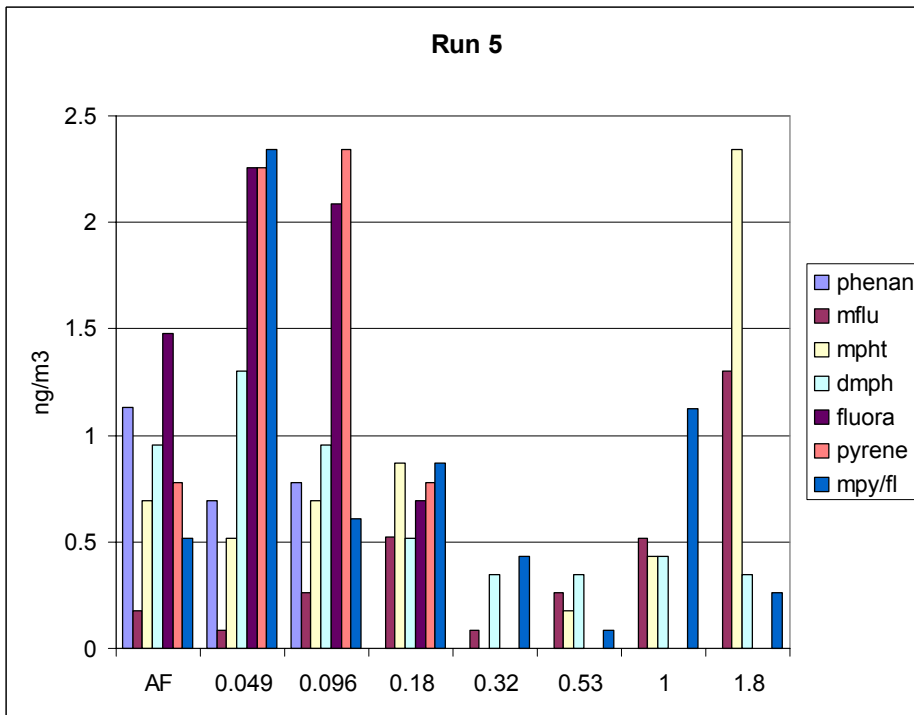
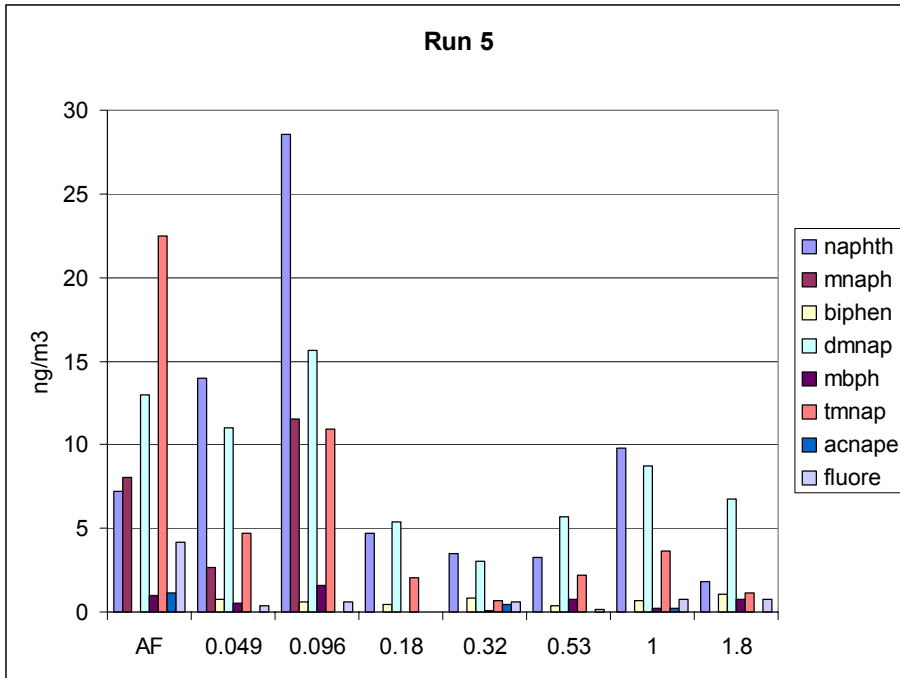


Figure A4-2. MOUDI PAH results.

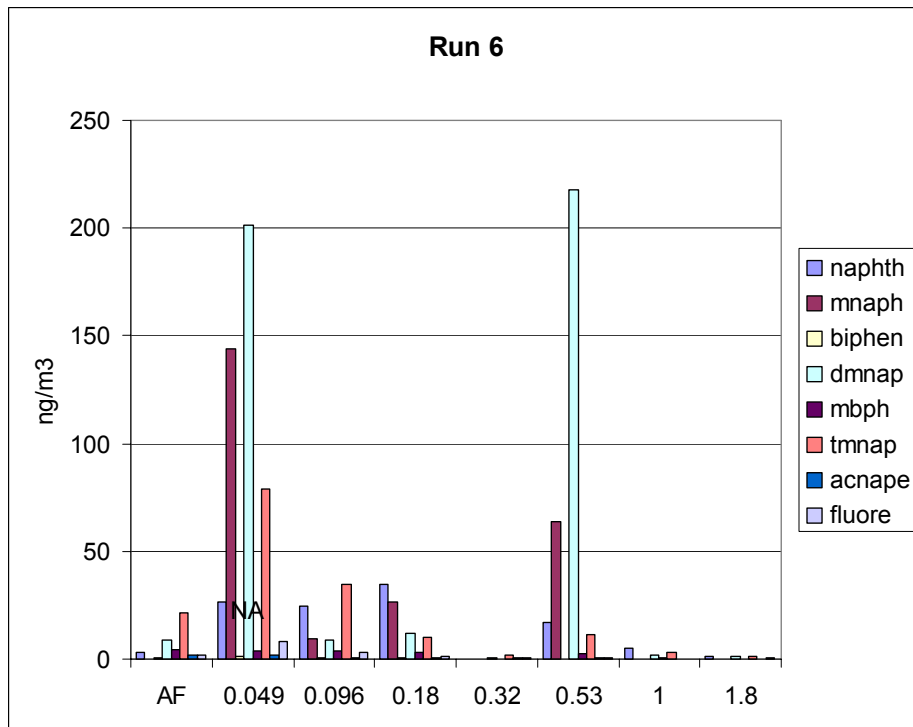
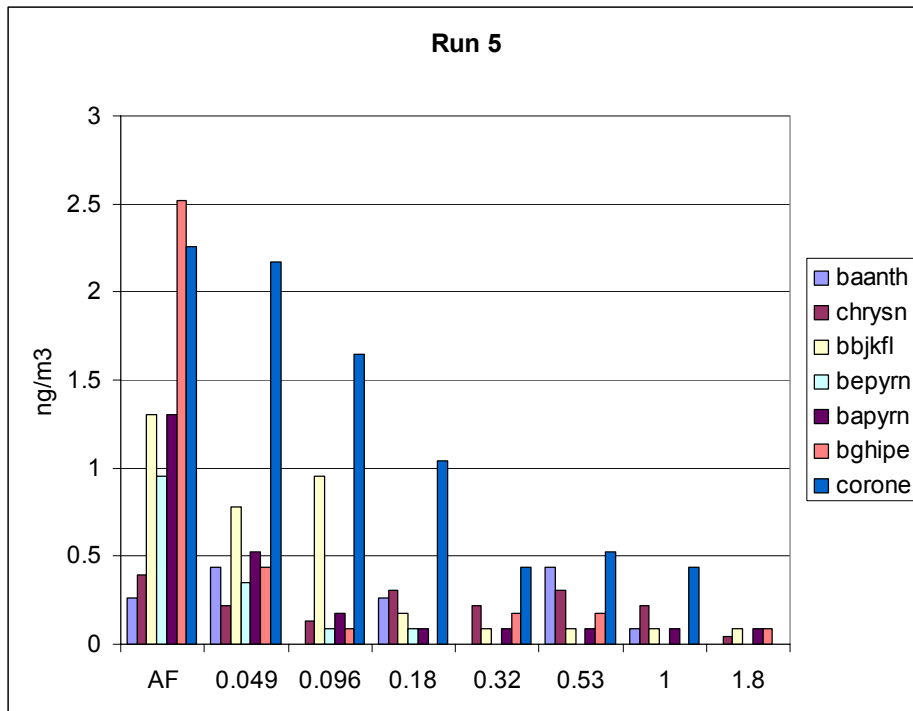


Figure A4-2. MOUDI PAH results.

APPENDIX 5:

EVALUATION OF DIESEL SOOT FILTERS

This article will be published shortly in the Journal of the Air & Waste Management Association.

APPENDIX 6:
SUMMARY OF EMISSION FACTORS

Emission Factor Summary														
Source	Tested	Year	Type	Fuel	Engine load	MOUDI PM* (g/kg)	TEOM PM (g/kg)	MOUDI EC (g/kg)	MOUDI OC (g/kg)	SMPS (#/kg)	PAS** pPAH (mg/kg)	Gundel vapor PAH (mg/kg)	Gundel PM (mg/kg)	Napthalene (mg/kg)
Chevy S-10	1999		AGE	gasoline	idle	3.15				7.08E+13		17.6	14.9	7.7
F-350	2000	1993	F350	gasoline	53%	0.104	0.0845	0.00746	0.0277	7.15E+13	0.0042	122	1.51	24.6
F-350	2000	1993	F350	gasoline	variable	0.017	0.0181	0.00204	0.0263		0.00624	5.89	0.228	4.13
F-350	1999		AGE	gasoline	idle	0.115		0.0347	0.0411	3.43E+14		38.6	1.21	22.7
Dodge Bobtail	2000	1996	Dodge Bot	Diesel	idle, 700 rpm	0.578	1.3	0.0565	0.414	3.24E+15	0.901	31.4	2.72	2.36
Dodge Bobtail	2000	1996	Dodge Bot	Diesel	variable		18.9							
Dodge Bobtail	2000	1996	Dodge Bot	Diesel	27%		4.45							
Dodge Bobtail	1999	1996	AGE	Diesel	idle	1.23		0.162	0.337	3.82E+15		369	18	29
Jeep Bobtail	2000	1986	Jeep Bob	Diesel	23%	2.58		0.641	1.31	9.37E+14	5.5	37.7	4.19	8.11
Jeep Bobtail	2000	1986	Jeep Bob	Diesel	23%,9%	3.45		0.595	1.84		5.4	23.1	3.62	3.83
Jeep Bobtail	2000	1986	Jeep Bob	Diesel	variable	3.69		1.27	2.02		7.03	36.4	2.61	7
Bobtail	1999	1990	AGE	Diesel	idle	4.63		1.92	4.58	4.81E+15		970	588	51
Coleman	1999	1997	AGE	Diesel	idle	0.783		0.158	0.347	3.77E+15		419	14.2	39
Jammer	1999		Jammer	JP8	idle	352		31.2	193.3	3.85E+17		23600	23700	2600
Jammer	2000	1992	Jammer	JP8	idle	3.43		0.13	1.99	1.49E+15	3.88	53.0	4.84	9.1
TF-34	2001	variable	Aircraft	JP5	variable	1.50-154		0.07-8.29	0.46-33.2		0.044-3.05	42.8-223	3.76-15.1	8.36-43.7
T-700	2001	unknown	Helicopter	JP5	variable	0.32		0.18	0.07		0.77	23.4	40.9	1.68
*PM is PM1.8														
pPAH: particle-bound PAH concentration														
** PAS: assuming 1 ftA/ng PAH														
Emission factors were estimated using the method described in Kirchstetter et al., 2001														
All individual PAHs are vapor phase														

Emission Factor Summary						Benz[a]anthracene	benzo[b,j,k]fluoranthene	benzo[a]pyrene	chrysene	indeno[1,2,3-cd]pyrene
Source	Tested	Year	Type	Fuel	Engine load	(ug/kg)	(ug/kg)	(ug/kg)	(ug/kg)	(ug/kg)
Chevy S-10	1999		AGE	gasoline	idle	24.8	0	24.8	0.656	1.66
F-350	2000	1993	F350	gasoline	53%	0.256	0	0	2.64	0
F-350	2000	1993	F350	gasoline	variable	1.04	0	0	0.883	1.85
F-350	1999		AGE	gasoline	idle	4.69	3.74	1.18	5.42	3.7
Dodge Bobtail	2000	1996	Dodge Bob	Diesel	idle, 700 rpm	3.02	0	0	8.59	0
Dodge Bobtail	2000	1996	Dodge Bob	Diesel	variable					
Dodge Bobtail	2000	1996	Dodge Bob	Diesel	27%					
Dodge Bobtail	1999	1996	AGE	Diesel	idle	10.9	0	5.63	40.1	2.82
Jeep Bobtail	2000	1986	Jeep Bob	Diesel	23%	5.04	0	0	2.67	2.95
Jeep Bobtail	2000	1986	Jeep Bob	Diesel	23%,9%	12	0	0	34.7	1.97
Jeep Bobtail	2000	1986	Jeep Bob	Diesel	variable	15.7	0	0	24.4	4.77
Bobtail	1999	1990	AGE	Diesel	idle	64.7	54.4	20.8	103	27.7
Coleman	1999	1997	AGE	Diesel	idle	2.17	1.85	5.38	41.7	5.12
Jammer	1999		Jammer	JP8	idle	2642	3208	189	5239	8490
Jammer	2000	1992	Jammer	JP8	idle	6.92	0	0	1.22	1.49
TF-34	2001	variable	Aircraft	JP5	variable	0-3.22	0	0	0-3.22	0
T-700	2001	unknown	Helicopter	JP5	variable	0.989	0	0	0.206	4.12
*PM is PM1.8										
pPAH: particle-bound PAH concentration										
** PAS: assuming 1 ftA/ng PAH										
Emission factors were estimated using the method described in Kirchstetter et										
All individual PAHs are vapor phase										